FORSCHUNGSZENTRUM ROSSENDORF
Mitglied der Wissenschaftsgemeinschaft Gottfried Wilhelm Leibniz

WISSENSCHAFTLICH-TECHNISCHE BERICHTE
FZR-418
Januar 2005

Bi-Annual Report 2003/2004

The Rossendorf Beamline at ESRF (ROBL-CRG)

Editors: A.C. Scheinost and N. Schell

Preface

The Rossendorf Beamline at the European Synchrotron Radiation Facility (ESRF) is now in operation since 1998. This 4th report covers the period from January 2003 to December 2004. In these two years, more than 40 peer-reviewed papers have been published based on work done at the beamline. 43 different in-house experiments were performed for the FZR and its collaborators, and 16 experiments were performed for the ESRF and its users. Six exemplary highlight reports on pages 3 to 38 should demonstrate the scientific strength and diversity of the experiments performed on the two end-stations of the beamline, dedicated to Materials Research and Radiochemistry. We are proud to have been invited now for three years in a row to contribute highlight articles to the ESRF annual reports.

In May 2003, i.e. after five years of operation, the beamline took the first international review by the ESRF scientific advisory committee quite successfully: the review committee confirmed that both technical and scientific performance are state-of-the-art, and recommended to the ESRF the extension of the CRG contract with the Forschungszentrum Rossendorf for another five-year period (which is the usual contract duration).

A range of technical improvements have been made in the last two years. For the Radiochemistry end-station, the main goal was to lower the detection limit for actinides in environmental samples. A major investment was the new 13-element Ge detector with advanced digital electronics for higher count rates and better energy resolution. At the Materials Research end-station, the pool of sample environment chambers with its control software had continually been up-graded to allow now multiple and fast *in-situ* diagnostics during data collection. The design of a new sputter deposition chamber together with a 100 μm beam focussing optics has been finished and brought into commissioning.

In July 2004 the beamline became a member of the pooled facilities of ACTINET – European Network of Excellence, thus facilitating access to EXAFS experiments involving actinides. The Rossendorf Beamline is still the only beamline in Europe where elaborate safety features make such experiments routinely possible. Up to 25 % of the in-house beamtime will be provided in the next years for collaborations between the FZR and external user groups within this network.

The beamline staff would like to thank all partners, research groups, review panel members and organizations who supported the beamline during the last 24 months. Special thanks to the FZR management, the CRG office of the ESRF with Axel Kaprolat as liaison officer, and to the ESRF safety group headed by Paul Berkvens.

Andreas Scheinost and Norbert Schell

Contents

1. Scientific Highlights

Neptunium(IV) uptake by iron metalloproteins

C. Den Auwer[1], I. Llorens[1], Ph. Moisy[1], C. Vidaud[2], H. Funke[3], C. Barbot[4$], F. Goudard[4]

[1]CEA Marcoule, DEN/DRCP/SCPS, 30207 Bagnols sur Cèze Cedex, France
[2]CEA Marcoule, DSV/DIEP/SBTN, 30207 Bagnols sur Cèze, France
[3]Rossendorf Beamline (BM20), ESRF, 38043 Grenoble, France
[4]Université de Nantes, Fac. Sciences, Biochim. 44322 Nantes, France
[$]now at Laboratoire de Pharmacie galénique, 76000 Rouen, France

Introduction

The chemistry of the actinide family is surprisingly rich because of the large atomic numbers (from Z = 90 for Th) and the relative availability of the valence electrons of these elements. In order to better understand the affinity of “smart” chelates as for ionic selective recognition or uptake by specific biomolecules, it is essential to better understand the intramolecular interactions. Although this has long been done for widely investigated transition metals, very few studies have been devoted to complexation mechanisms of radionuclides by active chelation sites. As a result, the intramolecular interactions of actinide elements with chelation sites that can be encountered either in coordination chemistry or in bioinorganic chemistry are relatively unknown. For instance, the stability of the uranyl cation (UO_2^{2+}) under atmospheric conditions and its ubiquity in the geosphere defines it as a major potential contaminant. Although many studies have been focussing on the complexation mechanisms of uranyl by organic or mineral systems as humic acids, clays or minerals [1-6], few of them have focussed on the sub-molecular level understanding of uptake by metalloproteins of major interests. Oxidation state IV of neptunium has been of particular concern for its relative stability in physiological conditions and reactivity similarities with both Pu(IV), Th(IV) and Fe(III) [7-9].

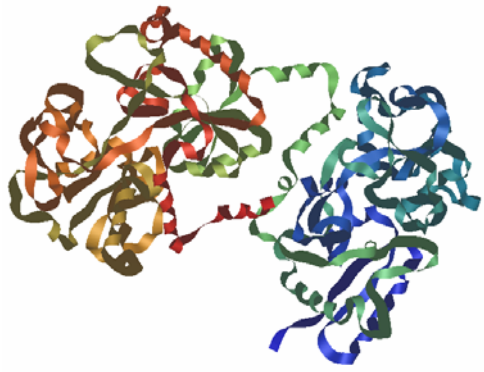

Fig. 1a : Structure of the Equine Apolactoferrin (PDB reference 1I6B [15]).

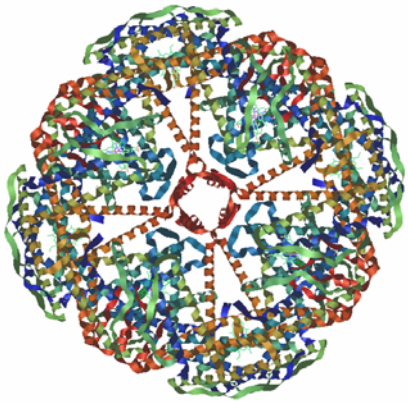

Fig. 1b : Structure of bacterioferritin from E. Coli (PDB reference 1BFR [16]).

Recently, our group has undertaken the investigation of uranyl, neptunium(IV) and plutonium(IV) uptake by ferritin (F) and transferrin (Tf), two metalloproteins that are responsible in advanced eukaryote cell of 15-20% (with haemosiderin) and 10% of iron storage and transport, respectively. Transferrins (Figure 1a) is a regulator of Fe(III) carriage in blood [10]. It is a glycoprotein of 670 amino acids (81 000 Da) with a tertiary structure made of two equivalent lobes (C and N) with one possible complexation site each. The iron metal binding site is made of a distorted octahedron with two tyrosyl phenolates, one histidyl imidazole and one aspartate carboxyl. The requirement of a synergistic anion carbonate has

been confirmed. This anion could coordinate to iron in a bidentate mode. It can bind a wide variety of d-block transition metals, as well as actinides and lanthanides [11]. For instance Taylor *et al.* have suggested that the protein is able to stabilize the tetravalent state and form stable M^{4+}-Tf complexes [12]. This is why transferrin contamination by actinide cations is a critical issue of nuclear human toxicology. Pu(IV) as well as most of the transition metal cations reported to be complexed by transferrin are assumed to be located in the iron sites.[13] Ferritin (Figure 1b) is generally speaking responsible for iron storage inside the cell [14]. The metalloprotein is constituted of a protein coat of 24 elliptic subunits linked by symmetry axis of order 2,3 and 4 which form an inner cavity of 7-8 nm (450 000 Da) containing an iron oxyhydroxyde core associated to phosphate groups (up to 4500 iron atoms).

X ray Absorption Spectroscopy has been extensively used as a structural and electronic metal cation probe. Combination with more traditional spectroscopic techniques as spectrophotometry or vibrational spectroscopy is an ideal tool for the understanding of the chelation mechanism. On the one hand spectrophotometric data provide a fingerprint of the specific complexation mechanism and on the other hand, in the EXAFS regime of XAS, a quantitative description of the cation coordination sphere can be achieved.

Results and discussion

The present experimental report focuses on our work on the Np(IV) cation. To avoid hydrolysis at physiological pH, Np(IV) in initial stock solution was complexed by the synergistic NTA anion as described in the experimental section. Further uptake by apo serum transferrin on the one hand and horse ferritin on the other hand was achieved by total or partial displacement of the NTA ligand.

Spectrophotometric Near InfraRed spectra in Figure 2a show the fingerprint of the complexation of Np(IV) by NTA in the Np(IV)(NTA) and Np(IV)$(NTA)_2$ complexes. The two characteristic aborption bands of Np(IV) in hydrochloric acid (724 nm, not shown and 960 nm) are red shifted upon NTA coordination (731 and 973 for Np(IV)(NTA); 740 and 980 for Np(IV)$(NTA)_2$). In the molecular structure of Nd(III)$(NTA)_2(H_2O)$ [17], the two NTA chelates encapsulate the neodymium cation in a tetradentate fashion : 3 oxygen atoms and 1 nitrogen atom. Based on this model, the adjustment of the Np EXAFS spectrum of Np(IV)$(NTA)_2$ lead to a similar conclusion with two tetradentate NTA molecules per Np cation (R factor = 0.10, Fourier transformed of the EXAFS spectrum displayed in Figure 3). Note that in all the following adjustments a typical coordination number of 8 was assumed for Np(IV). The 6 oxygen atoms are positioned at 2.35 Å (σ^2 = 0.008 $Å^2$) from the cation and the two additional nitrogen atoms are located at 2.63 Å (σ^2 = 0.044 $Å^2$). In the adjustment, contributions from the carbon atoms adjacent to the donor atoms were considered and linked to the first coordination shell. Tentative to add multiple scattering contributions did not lead to an improvement of the fit quality. These distances are slightly shorter (*c.a.* 0.06 Å) than in the neodymium case. Although both cations have a similar ionic radius (CN = 8), shrinking of the Np coordination sphere is expected considering electrostatic interactions because of the larger charge bared by Np(IV) compared to Nd(III).

The evolution of the Tf(Np(IV)$NTA)_2$ complex with the increasing concentration of transferrin is shown in Figure 2b. Upon transferrin titration, both 980 and 740 nm peak decrease and new peaks appear at 995, 747, 732 and 727 nm. This result is a clear fingerprint of the formation of a new Np(IV) complex with both transferrin and NTA. An *a priori* putative model based on the coordination mode of Fe in Fe(III)(NTA)(Tf) [18] with Np in the transferrin iron binding site with one synergistic tetradentate NTA and additional water molecules was tested [19]. The localization of Np in the iron binding site with conccomittant binding by synergistic NTA is a reasonable starting assumption based on previous studies [9,18]. Because the data resolution is large (0.2 Å) and the complexity of the chelation site is high, the model is only indicative of a possible coordination mode. Note also that distinction

between each coordination site of each lobe is impossible to achieve with EXAFS given their structural similarity, as is the exact conformation of the site because the technique averages the signal over all the contributors of similar backscattering factor (*i.e.* O, N, C). Within this model, a satisfactory adjustment (R factor = 0.05) was achieved with single scattering contributions from a first shell with both NTA and Tf (5 O at 2.35 Å, σ^2 = 0.007 Å^2 plus 1 N at 2.63 Å, σ^2 = 0.004 Å^2. Note that the nitrogen contribution has been linked to the oxygen one based on the crystal structure of Nd(III)$(NTA)_2(H_2O)$), a second shell with water molecules (2 O at 2.50 Å, σ^2 = 0.019 Å^2) and a third shell with carbon atoms (8 C at 3.36 Å, σ^2 = 0.008 Å^2). In the crystal structure of Fe(III)(NTA)(Tf), the two tyrosine residues are the only side chain functions available because NTA forces the transferrin lobe to be locked in the open form. Although the site is highly distorted in this structure, the distance of the two tyrosines is on the average 0.1 Å shorter than the one of the oxygen atoms of NTA. In the fit of Tf(Np(IV)$NTA)_2$, only one distance was considered and the average NTA,Tyr-Np(IV) distance is slightly shorter than the one of Nd(III)-NTA in the crystal structure of Nd(III)$(NTA)_2(H_2O)$ (6 O at 2.42 Å and 2 N at 2.67 Å) [17]. Although both cations have comparable ionic radii at coordination number 8, the net electrostatic effect should result in a shorter distance for Np^{4+} than for Nd^{3+}. This short distance is also in agreement with the strong basicity of the phenolate group present in the coordination sphere and agrees with the average value of 2.3 Å displayed in the crystal structure of Ce_2(Tf) [20]. The second shell with water molecules is at a larger distance as it is in Nd(III)$(NTA)_2(H_2O)$. Finally the third shell of carbon atoms (only one Debye Waller factor was used for all the carbon scattering paths) is also consistent with the previous structures. Note that the probable distortion of this shell due to the presence of two types of coordinating groups in the first shell is not accounted in the fit.

Complexation of Np(IV)$(NTA)_2$ by horse ferritin is complicated by the intrinsic intricacy of the ferritin structure made of 12 bundles of four-helical units [13]. Many studies and EXAFS measurements have been devoted to the characterization of the iron oxyhydroxyde core [20-23]; however very little has been done in the field of actinide contamination. Kinetic studies of ^{241}Am incorporation in the hepatopancreas of Homarus gammarus [24,25], have shown that ferritin was the first protein to be contaminated and the last to decorporate the americium ion. Ferritin extracted from digestive mass of ostrea showed similar accumulation [26]. Three fixation sites are possible : sorption onto the iron oxyhydroxy or phosphate groups or binding to the carboxylic groups from the amino acids of the protein, in particular glutamic and aspartic acids. No *a priori* definite chelation or sorption structural model is available. In Figure 3, the FT of the EXAFS spectrum of Np(IV)(NTA)(F) exhibits similar features as for Np(IV)$(NTA)_2$ and Np(IV)(NTA)(Tf). Attempts to fit the second coordination sphere with Np-Fe parameters failed, suggesting that there is no sorption of Np(IV) onto the oxyhydroxy iron core of the protein. A three shell fit (R factor = 0.05) with two oxygen shells for the first sphere and a carbon shell for the second sphere was carried out (with a total Np coordination number fixed to 8) with 5.1 oxygens at 2.35 Å (σ^2 = 0.012 Å^2), 3.9 oxygens at 2.76 Å (σ^2 = 0.028 Å^2) and 8.3 carbons at 3.28 Å (σ^2 = 0.025 Å^2). These results suggest, as in the case of transferrin, that neptunium is partially bounded *via* carboxylate functions to the protein. Concomitant ligation by a NTA ligand is not demonstrated.

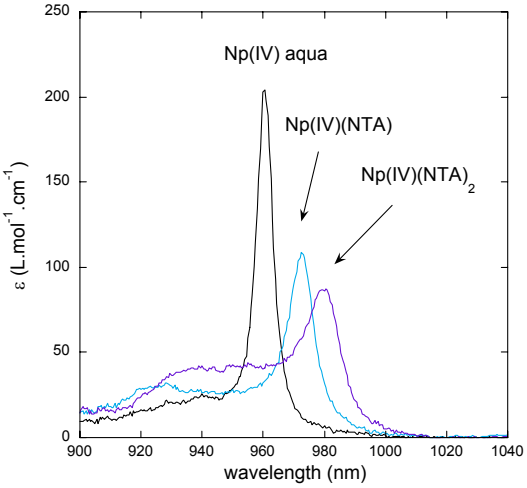

Fig. 2a : NIR Spectrophotometry of aqua Np(IV), Np(IV)(NTA) and Np(IV)$(NTA)_2$.

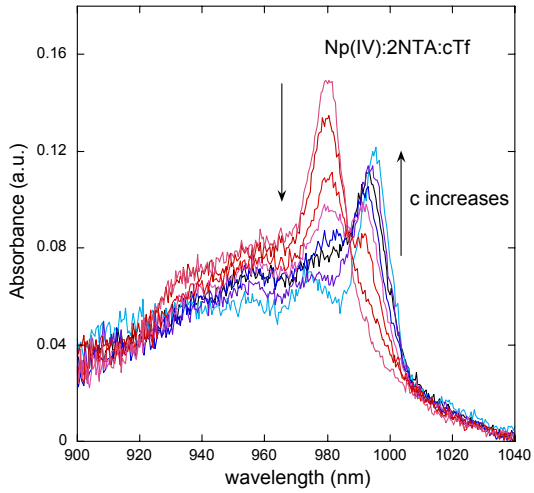

Fig. 2b : NIR Spectrophotometry of Np(IV)(NTA)(Tf) upon transferrin titration at physiological pH.

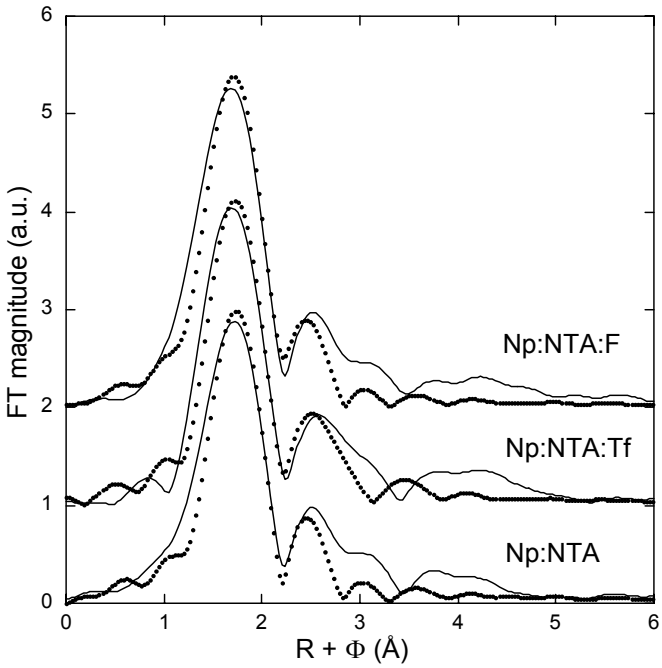

Fig. 3 : Fourier transform (FT) of the EXAFS spectra of Np(IV)$(NTA)_2$, Np(IV)(NTA)(Tf) and Np(IV)(NTA)(F) complexes in aqueous solution at physiological pH. Strait line = data, dots = fit.

Neptunium uptake by two major iron regulation proteins has been investigated by combined X-ray Absorption Spectroscopy and Spectrophotometry. Although definite conclusions on the neptunium coordination sphere are difficult due to the intricacy of the possible metal binding sites, putative models can be tested when available. In both transferrin and ferritin cases, the neptunium cation is partially bounded to carboxylate functions. Additional phenolate functions or water molecules may also enter the coordination sphere as two shells of oxygen atoms were necessary in both adjustments. Further investigation with vibrational spectroscopy should yield a better understanding of the chelation site. Finally, other synergistic or protecting anion than NTA shall be used in order to evaluate their influence on the protein metal binding site.

Experimental

Np(IV):NTA sample preparation

The stock solution of Np(IV) ([Np] = 25 mM) was prepared by hydroxylamine reduction (60°C) of Np(V) obtained by dissolution of $Np(V)O_2OHxH_2O$ in hydrochloric acidic solution. NTA complexation was achieved with 2.8 equivalents of ligand at pH = 4. For spectrophotometric measurements, the $Np(IV)(NTA)_2$ concentration (physiological pH fixed by HEPES buffer) was set to 1.2 mM and increasing amount of free serum transferrin (Sigma-Aldrich, 97 % purity) was added from 0.2 to 2.5 mM. For EXAFS measurements (physiological pH) the $Np(IV)(NTA)_2$ concentration was fixed at 0.28 mM. Transferrin was added with a final concentration of 0.14 mM. Ferritin was added with a final concentration of 0.03 mM.

Near InfraRed Absorption Spectrophotometry

Data acquisition was carried out at room temperature with a Shimadzu 3101 spectrophotometer with a 10 mm path length. In Figure 2a : measurements in HCl. [Np] = 1.5 mM, [NTA] = 20 mM. For Np(IV) aqua, pH = 0; for Np(IV)(NTA), pH = 0; for $Np(IV)(NTA)_2$, pH = 1. In Figure 2b : Transferrin increasing concentration was monitored as follows ([Np]=1.2 mM, [NTA] = 3.4 mM, [HEPES] = 0.4 M, physiological pH) : [Tf] = 0.0; 0.2; 0.4; 0.6; 0.8; 1.0; 1.4; 2.3 mM.

X-ray Absorption Spectroscopy

Neptunium L_{III}-edge EXAFS spectra were recorded at the ROBL beamline (BM20) of the European Synchrotron Radiation Facility. The ring was operated at 6 GeV with a nominal current of 200 mA. The beam line is equipped with a water cooled double crystal Si(111) monochromator. Higher harmonics were rejected by two Pt coated mirrors. A 4-element Ge solid state detector was used for data collection in the fluorescence mode. Dead time corrections were not necessary because of the sample low concentration. Monochromator energy calibration was carried out with yttrium K-edge at 17052 eV. All measurements were recorded at room temperature.

Data treatment was carried out using EXAFS98 code [27]. Background removal was performed using a pre-edge linear function. Atomic absorption was simulated with a cubic spline function. The extracted EXAFS signal was fitted in $k^3CHI(k)$ without any additional filtering using ARTEMIS code [28]. Due to the low signal to noise ratio above 10 $Å^{-1}$ and a glitch at 9 $Å^{-1}$ fitting was carried out between 2.0 and 8.1 $Å^{-1}$, in R space (Kaiser window). Theoretical phases, amplitudes and electron mean free path were calculated with FEFF82 code [29] from the crystal structures of $Nd(NTA)_2H_2O$ and $Ce_2(Tf)$. First sphere oxygen atom contributions and second sphere carbon atom contributions were included in the fit.

Acknowledgements

We thank for financial support the French Nuclear-Toxicology program, CEA/DEN/MRTRA.

References

[1] A. Günther, G. Bernhard, G. Geipel, T. Reich, A. Rossberg, H. Nitsche, *Radiochim. Acta* (2003), **91**, 319.

[2] C. Hennig, P. J. Panak, T. Reich, A. Rossberg, J. Raff, S. Selenska-Pobell, W. Matz, J. J. Bucher, G. Bernhard, H. Nitsche, *Radiochim. Acta* (2001), **89**, 625.

[3] M. A. Denecke, S. Pompe, T. Reich, H. Moll, M. Bubner, K. H. Heise, R. Nicolai, H. Nitsche, *Radiochim. Acta* (1997), **79**, 151.

[4] M. A. Denecke, J. Rothe, K. Dardenne, P. Lindqvist-Reis, *Phys. Chem. Chem. Phys.* (2003), **5**, 939

[5] M. Walter, T. Arnold, T. Reich, G. Bernhard, *Environ. Sci. Technol.* (2003), **37**, 2898.

[6] M. Merroun, C. Hennig, A. Rossberg, T. Reich, S. Selenska-Pobell, *Radiochim. Acta* (2003), **91**, 583.
[7] P. W. Durbin *et al.*, *Health Phys.* (1998), **75**, 34.
[8] M. P. Neu, C. E. Ruggiero, A. J. Francis, in *Avances in Plutonium Chemistry 1967-2000* (Darleane Hoffman, American Nuclear Society, La Grange Park, Il, (2002)) and D. M. Taylor, in *Handbook of Heavy Metals in the Environment* (B. Sarkar, New York, **4**, (2002)).
[9] H. Sun, H. Li, P. J. Sadler, *Chem. Rev.* (1999), **99**, 2817.
[10] see for instance P. Aisen, *Metal Ions Biol. Sys.* (1998), **35**, 585.
[11] K. N. Raymond, V. L. Pecoraro, W. R. Harris, C. J. Carrano, …….(1991), **257**, 571.
[12] D. M. Taylor, *J. Alloys Comp.* (1998), **271**, 6.
[13] W. R. Harris in *Structure and Bonding* (Springer Verlag, Heidelberg) (1998), **92**, 121.
[14] see for instance P. M. Harrison, P. D. Hempstead, P. J. Artymiuk, S. C. Andrews, *Metal Ions in Biological Systems* (1998), **35**, 435.
[15] P. Kumar, J. A. Khan, S. Yadav, T. P. Singh, *Acta Cryst. D* (2002), **58**, 225.
[16] A. Dautant, J. B. Meyer, J. Yariv, G. Precigoux, R. M. Sweet, A. J. Kalb, F. Frolow, *Acta Cryst. D* (1998), **54**, 16.
[17] J. Wang, X. Zhang, *J. Mol. Struct.* (2002), **611**, 39.
[18] K. Mizutani, H. Yamashita, H. Kurokawa, B. Mikami, M. Hirose, *J. Biol. Chem.* (1999), **274**, 10190.
[19] I. Llorens, C. Den Auwer, Ph. Moisy, E. Ansoborlo, C. Vidaud, H. Funke, Chem. Bio. Chem., submitted.
[20] H. M. Baker, C. J. Baker, C. A. Smith, E. N. Baker, *J. Biol. Inorg. Chem.* (2000), **5**, 692.
[21] S. L. Heath, J. M. Charnok, C. D. Garner, A. K. Powell, *Chemical European journal* (1996), **2**, 634.
[22] P. Mackle, C. D. Garner, R. J. Ward, T. J. Peters, *Biochimica et Biophysica acta* (1991), **1115**, 145.
[23] R. Strange, S. Morante, S. Stefanini, E. Chiancone, A. Desideri, *Biochimica et Biophysica Acta* (1993) **1164**, 331.
[24] F. Goudard, F. Paquet, J-P. Durand, M. C. Milcent, P. Germain, J. Pieri, *Biochemistry and Molecular biology International* (1994) **33**, 841.
[25] F. Goudard, J-P. Durand, J. Galey , J. Pieri, *Marine biology* (1991) **108**, 411.
[26] M. C. Milcent, F. Goudard, J-P. Durand, P. Germain, J. Pieri, S. G. George, *Biochemistry and Molecular biology International* (1996) **39**, 137.
[27] A. Michalowicz, *J. Phys. IV C2,* (1997), **7**, 235
[28] M. Newville, *J. Synchrotron Rad.*, **8**, 322 (2001)
[29] J. J. Rehr *et al.*, *Rev. Modern Phys.*, **72**, 621 (2000)

In situ speciation of actinides with a newly developed spectro-electrochemical cell

C. Hennig[1,2], J. Tutschku[2], A. Rossberg[1,2], G. Bernhard[2], A.C. Scheinost[1,2]

[1] The Rossendorf Beamline (BM20), ESRF, 38043 Grenoble, France
[2] Institute of Radiochemistry, Forschungszentrum Rossendorf eV, 01314 Dresden, Germany

Introduction

Natural aquatic and terrestrial environments exert large variations in redox state due to oxygen diffusion on one hand and microbial processes on the other hand. Actinides with their large number of oxidation states are especially susceptible to these redox changes, forming different aqueous complexes which may greatly differ by solubility and mobility. These complexes are often difficult to investigate due to their thermodynamic meta-stability. Therefore, we developed a new spectro-electrochemical cell, which allows to study the structure and speciation of aqueous actinide complexes *in situ* by X-ray absorption spectroscopy, while applying and maintaining a constant potential. Due to the specific safety requirements for handling of radioactive materials the electrochemical cell is gas tight. The spectro-electrochemical cell comprises two safety compartments and a special electrode arrangement. First U L_{III}-edge X-ray absorption spectra have been obtained from aqueous solutions of U(VI) and U(IV) in highly concentrated chloride solutions.

Electrochemistry

A drawing of the spectro-electrochemical cell is shown in Figure 1. The cell body consists of chemically resistant material (polytetrafluorethylene or polyvinylidenfluoride) and is sealed by two independent cover plates using rubber gaskets. These cover plates serve as double confinement against radionuclide release.

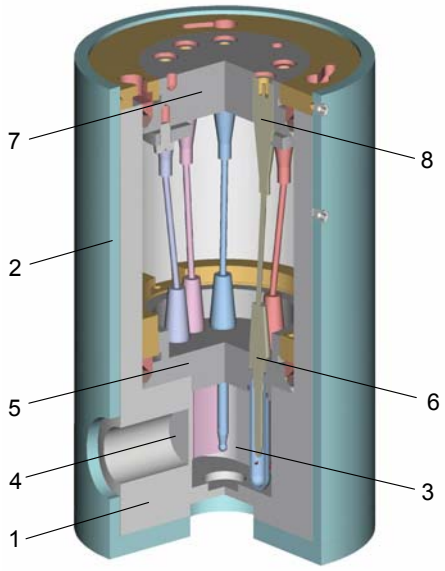

Fig. 1. Drawing of the spectro-electrochemical cell.

1 – Cell body of chemically resistant material
2 – Stainless steel housing
3 – Space for the sample solution
4 – X-ray window
5 – Inner cover plate (first compartment)
6 – Electrode
7 – Outer cover plate (second compartment)
8 – Electrical connector

Each cover plate contains six gas-tight connectors for cables and electrodes. Two X-ray windows were machined directly into the cell walls to avoid additional sealing. The windows are 20 mm apart from each other to allow sufficient X-ray transmission through the chloride solution and to achieve an edge jump of 0.3 at the U L_{III} edge.

The liquid volume of 10 ml was agitated by a magnetic stirrer. All miniaturized electrodes and sensors were machined by KSI Mainsberg and were used in combination with a potentiostat (model PGU 20V-100mA). The working electrode (cathode) was a Pt gauze and the counter electrode (anode) was an Ag wire.

The electrochemical reduction of U(VI) to U(IV) involves an electron transfer and a chemical reaction transforming the trans-dioxo cation. The reaction at the cathode is:

$$UO_2^{2+} + 2e^- + 2H^+ \rightarrow U^{4+} + 2H_2O. \quad (1)$$

At the anode silver is dissolved and precipitates as silver chloride:

$$2Ag + 2Cl^- \rightarrow 2AgCl\downarrow + 2e^-. \quad (2)$$

The dissolved Ag^+ ions are in equilibrium with solid AgCl and the equilibrium potential of the electrode is then determined by the solubility constant of the precipitate. At the experimental conditions chosen, the electrochemical potential was always far away from the decomposition potential of water. In order to avoid a high polarization of the cell, no diaphragm was used. The reduction of 0.01 moles of U(VI) to U(IV) at the cathode is accompanied by a decrease in the chloride concentration due to the precipitation of 0.02 moles of AgCl. The resulting reduction of the chloride concentration is small in comparison to the chloride concentration of the 3, 6 and 9 M Cl^- samples (see next paragraph). In order to enforce the anode reaction in the nominally 0 M Cl^- solution, 0.02 moles of LiCl were added. For both we did not expect an influence on speciation due to the low complex stability of uranium chloride ions. The Ag/AgCl potential was used as reference. Current-potential measurements were applied in order to gain redox potentials of the U(VI):U(IV) couple and appropriate potentials for the reduction process. XANES measurements were performed during the reduction process in situ to monitor the actual oxidation state. An example for the in situ XANES measurement comprising subsequent factor analysis is shown in Figure 2.

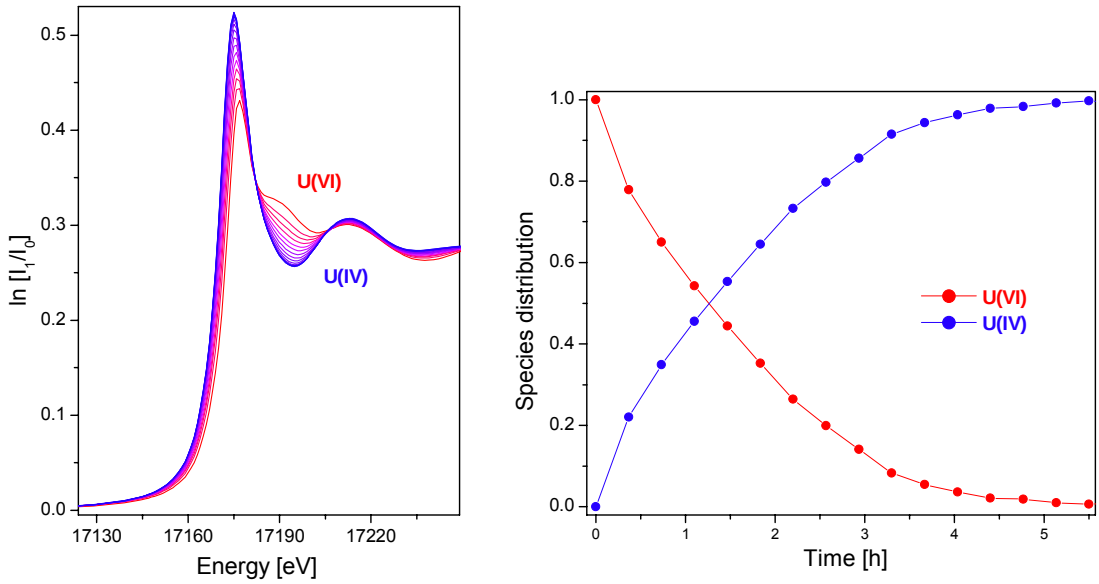

Fig. 2. *In situ* XANES measurements and species distribution in the solution. Left side: U L_{III} edge XANES spectra obtained during the reduction of 0.01M U(VI) in 0.2 M formic acid. The reduction was performed at a constant potential of –350 mV vs. Ag/AgCl. Right side: Distribution of U(VI):U(IV) species extracted by factor analysis.

Experimental

Two stock solutions of 0.1 M U were prepared by dissolving UO_3 either in 0.3 M $HClO_4$ for the chloride-free sample or in 0.3 M HCl for the chloride-containing samples. Four 0.01 M U(VI) aqueous solutions with chloride concentration of 0, 3, 6 and 9 M were prepared. LiCl was dissolved in 2.5 mL U stock solution and 2.5 mL of 1 M HCl obtaining 25 mL of 0.01 M U solutions.

Results and discussion

Comprehensive reviews of thermodynamic data have been reported on U(VI) complexes: a weighted linear regression, using experimental values from different references, yields stability constants of log β_1^0 = 0.17 ±0.02 and log β_2^0 = -1.1 ±0.02 for the reaction $UO_2^{2+} + nCl^- \rightleftharpoons UO_2Cl_n^{2-n}$ [1]. Formation constants log β_n^0 for species with n > 2 have not been published so far. UV-Vis spectroscopy shows significant spectral features which allowed to discriminate the species UO_2^{2+}, UO_2Cl^+ and $UO_2Cl_2^0$ quantitatively [2]. Allen et al. observed the species $UO_2(H_2O)_5^{2+}$, $UO_2(H_2O)_xCl^+$, $UO_2(H_2O)_xCl_2^0$, and $UO_2(H_2O)_xCl_3^-$ recently by EXAFS spectroscopy [3].

In contrast to U(VI), little is known on chloride complexation by U(IV). The formation constant according to the reaction $U^{4+} + nCl^- \rightleftharpoons UCl_n^{4-n}$ extrapolated to an ionic strength I = 0 yields log β_1^0 = 1.72 ±0.13 [1]. Only one experimental value is obtained for n = 2 with a log β_2 = 0.06 (I = 2 M) [4].

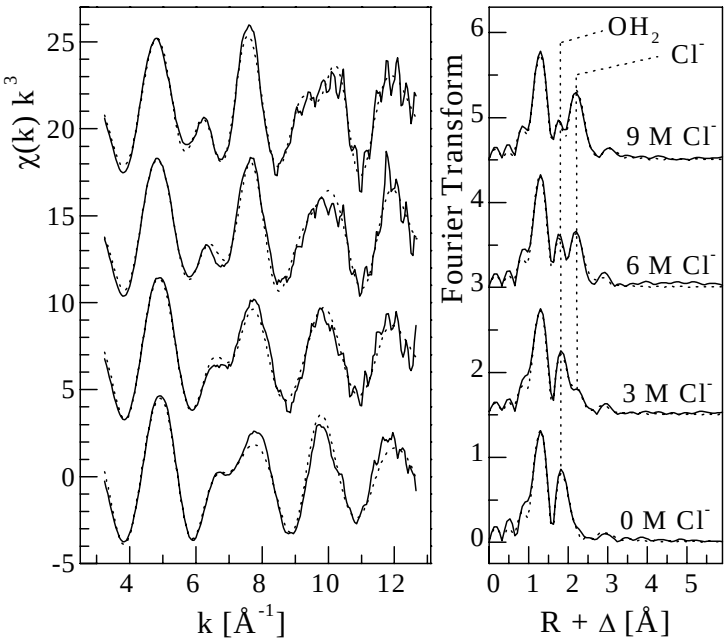

Fig. 3. U L_{III}-edge k^3 weighted EXAFS data (left) and corresponding Fourier transforms (right) taken over k = 3.2-12.7 Å^{-1} for UO_2^{2-} as a function of Cl^- concentration, experimental data (line) and theoretical curve fit (dots).

U L_{III}-edge k^3-weighted EXAFS spectra and the corresponding Fourier transforms (FT) of U(VI) samples are shown in Figure 3. The FT of all samples shows two peaks which arise from two axial oxygen atoms (O_{ax}) at 1.76 ±0.02 Å. The UO_2^{2+} aquo ion (sample 0 M Cl^-) shows 5 equatorial oxygen atoms (O_{eq}) at 2.41 ±0.02 Å. The FTs of the Cl^- solutions show an additional peak at a distance of 2.73 ±0.02 Å indicative of Cl^- in the first coordination sphere. The intensity of this Cl peak increases with increasing Cl^-

concentration. N_{Cl} increases from 1.0 to 2.7 in subsequent EXAFS fits. With increasing Cl^- concentration the dominant FT peak shifts to higher R values indicating a systematic replacement of H_2O by Cl^- in the first coordination sphere.

Possible solution species comprising $UO_2(H_2O)_5^{2+}$ and $UO_2(H_2O)_{5-n}Cl_n^{2-n}$ are averaged to a common radial distribution. However, the structural parameters extracted by EXAFS suggest the species $UO_2(H_2O)_4Cl^+$, $UO_2(H_2O)_3Cl_2^0$ and $UO_2(H_2O)_2Cl_3^-$ according to Figure 4.

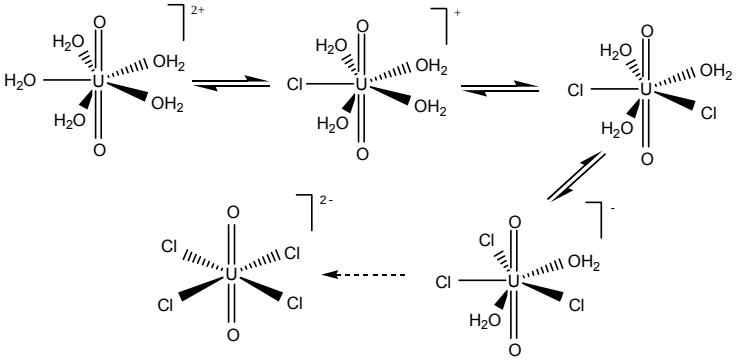

Fig. 4. U(VI) aquo chloro species.

We assume, that in all aquo chloro species the equatorial coordination number remains 5, because in a fourfold coordination as in $UO_2Cl_4^{2-}$ the U-Cl bond length would be reduced to 2.671 Å [5]. With increasing Cl^- concentration the coordination number of Cl increases stepwise. The ligands are coordinated in an inner-sphere fashion. A possible additional outer-sphere coordination could not be verified since EXAFS measurement is not sensitive for the backscattering signals at R+Δ > 3 Å under the used experimental conditions and the outer sphere coordination would most likely be too disordered to be detected.

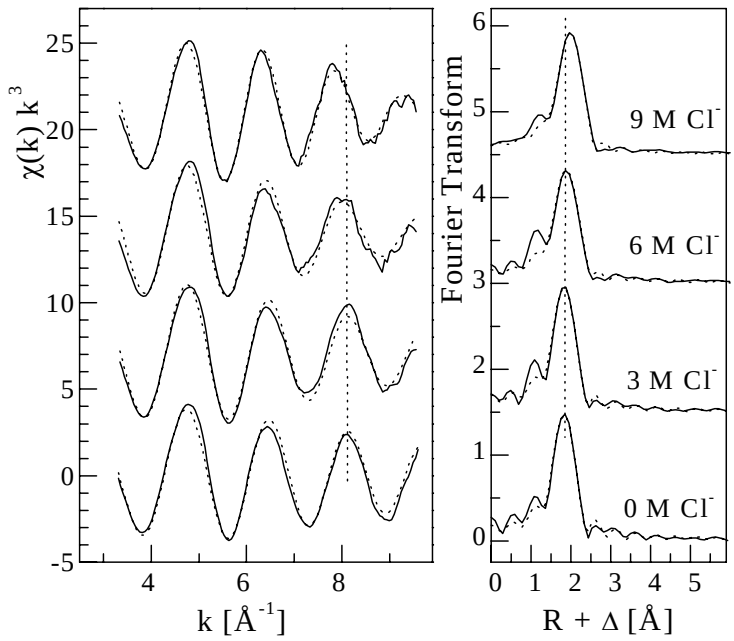

Fig. 5. U L_{III}-edge k^3 weighted EXAFS data (left) and corresponding Fourier transforms (right) taken over k = 3.2-9.6 $Å^{-1}$ for U(IV) as a function of Cl^- concentration, experimental data (line) and theoretical curve fit (dots).

Figure 5 shows the U L_{III}-edge k^3-weighted EXAFS spectra of U(IV). In non-complexing perchloric acid the U(IV) aquo ion shows 8.7 spherically arranged oxygen atoms at a distance of 2.41 Å.

With increasing Cl^- concentration the dominant FT peak shifts to higher R values indicating a systematic replacement of H_2O by Cl^- in a distance of 2.71 Å. During the fits, the σ^2 value of the U-O shell was fixed to 0.0070 $Å^{-2}$, obtained from the U(IV) aquo ion, and that of the U-Cl shell was fixed to 0.0050 $Å^{-2}$ following the value obtained for U(VI). The coordination number N_{Cl} increases from 0.3 to 2.1 and the coordination number N_O decreases from 8.5 to 6.1. The aquo chloro species derived from EXAFS measurements are identified as $U(H_2O)_8Cl^{3+}$, $U(H_2O)_{6\text{-}7}Cl_2^{2+}$ and $U(H_2O)_5Cl_3^{+}$ as shown in Figure 6. The extraction of principal components by factor analysis shows that the coordination number N_{O+Cl} decreases from 9 in $U(H_2O)_8Cl^{3+}$ to 8 in $U(H_2O)_5Cl_3^{+}$.

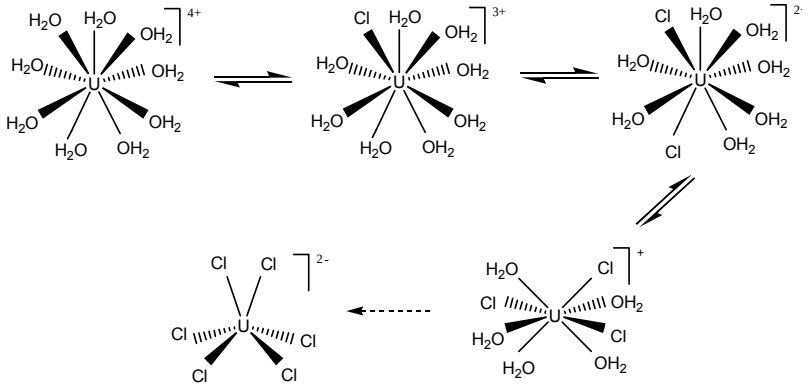

Fig. 6. U(IV) aquo chloro species.

The structure of U(IV) chloride complexes was not investigated up to now. Allen et al. [3] found clear evidence for inner-sphere formation of Np(IV) aquo chloride complexes. Due to the chemical similarity of U(IV) and Np(IV) an equivalent coordination was assumed for U(IV). A comparison of the Cl^- concentrations necessary to reach a coordination number of $N_{Cl} < 1$, which is higher for U(IV) than for Np(IV), confirms that log β_1 follows the trend U(IV) > Np(IV). The similar bond lengths for U-O and U-Cl for the U(VI) and U(IV) aquo chloro species suggests that, despite the difference in formal oxidation state, the effective ionic radii of U(VI) and U(IV) are similar, as has been pointed out in the literature [5].

Acknowledgements

The EXAFS measurements were performed at the Rossendorf Beamline/ESRF. We thank D. Rettig and T. Reich for technical development of a first version and furthermore J. Claußner and D. Falkenberg for their support of the final development of the spectro-electrochemical cell.

References

[1] Grenthe, I.; Fuger, J.; Konings, R.J.M.; Lemire, R.J.; Muller, A.B.; Nguyen-Trung, C.; Wanner, H. In *Chemical Thermodynamics of Uranium*; Wanner, H.; Forest, I., Eds.; Elsevier Science Publishers: Amsterdam, 1992, p. 192.

[2] Paviet-Hartmann, P.; Lin, M.R., *Mat. Res. Soc. Symp. Proc.* 1999, *556*, 977-984.

[3] Allen, P.G.; Bucher, J.J.; Shuh, D.K.; Edelstein, N.M.; Reich, T. *Inorg. Chem.* 1997, *36*, 4676-4683.

[4] Day, R.A., Jr.; Wilhite, R.N.; Hamilton, F.D., *J Am. Chem. Soc.* 1955, *77*, 3180-3182
[5] Watkin, D.J.; Denning, R.G.; Prout, K. *Acta Cryst.* 1991, *C47*, 2517-2519
[6] Denning, R.G. Electronic structure and bonding in actinyl ions, In *Structure and Bonding*, Vol. 79, Springer, Heidelberg 1992.

Quantitative antimony speciation in Swiss shooting-range soils

A.C. Scheinost[1,2], A. Rossberg[1,2], D. Vantelon[3,4], R. Kretzschmar[3], C.A. Johnson[5]

[1] The Rossendorf Beamline (BM20), ESRF, 38043 Grenoble, France
[2] Institute of Radiochemistry, Forschungszentrum Rossendorf eV, 01314 Dresden, Germany
[3] Institute of Terrestrial Ecology, ETH Zurich, 8952 Schlieren, Switzerland
[4] now: Paul Scherrer Institut, Swiss Light Source, 5232 Villigen, Switzerland
[5] Swiss Federal Institute of Environmental Science and Technology (EAWAG), 8600 Dübendorf, Switzerland.

Introduction

Antimony has been used since ancient times, and with 150'000 tons being mined each year, it is the 5th mostly exploited metal. Thus, more Sb is mined and used than As, which has a similar toxicity. Antimony is used for non-metal and metal products in about equal proportions. The non-metal products encompass antimony trioxide (Sb_2O_3) for the fining of glassware and ceramics, and as pigment in paints and lacquers. Non-metal Sb is increasingly used for flame retardants in plastics, textiles and car break pads, as vulcanizing agent in tires, and in semiconductors. Metallic Sb is used to harden Pb alloys for the manufacture of bearings, tubes and ammunition, and is an essential part of lead batteries [1, 2].

Global emission of Sb to the atmosphere from both natural and anthropogenic sources are estimated to 6000 tons per year [3]. High concentrations of Sb have been found in bottom and filter ashes of municipal solid waste incinerator plants. Important sources of uncontrolled release of Sb into the environment are road traffic (dust from break linings and tires), older battery producing plants and shooting ranges. Antimony concentrations up to several thousand mg kg^{-1} have been reported for soils influenced by mining activities [3 and references therein]. In the soils of shooting ranges, Sb concentrations of up to 100 g kg^{-1} have been found, which is 6 orders of magnitude above the natural background of 0.1 mg kg^{-1} [4-7]. Since the Pb cores of bullets contain 1-2 % of Sb and approximately 100,000 tons of bullets are deposited on shooting ranges per year, 1,000-2,000 tons of Sb are deposited, constituting a major emission path.

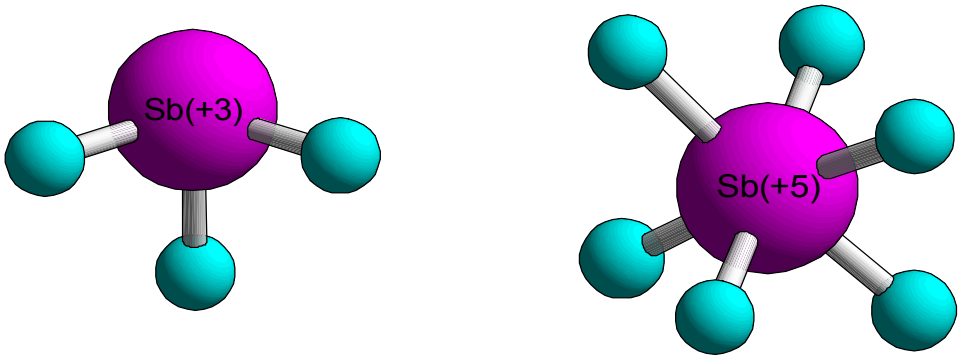

Fig. 1. Coordination of Sb(III) and Sb(V) in oxide minerals. Antimony-oxygen distances vary within similar ranges for both oxidation states (1.92-2.04 Å for Sb^{3+} and 1.98-2.10 Å for Sb^{5+}) [8].

In spite of the common usage and potentially high toxicity, little is known on the geochemical fate of Sb in soils. Superficially deposited Sb seems to be retained in the topsoils, since concentrations rapidly decline with soil depth [4, 9, 10]. Antimony is expected to occur in either trivalent or pentavalent oxidation state in aqueous surface environments,

being coordinated to 3 or 6 oxygen atoms, respectively (Fig. 1). The most important pentavalent aqueous species is $Sb(OH)_6^-$, which prevails above pH 2.5. Below pH 7, this oxyanion may be bound by ubiquitous Fe oxides. In neutral soils, however, i.e. above the point of zero charge of Fe oxides, many soils do not have substantial anion sorption capacity, hence one may expect high susceptibility to leaching. The trivalent aqueous species, $Sb(OH)_3$ sorbs to Fe oxide over a wider pH range, hence is expected to be rather immobile even in neutral soils [11]. Besides the difference in sorption behavior and mobility, a discrimination of both oxidation is important from an ecotoxicological point of view, since Sb(III) is 10 times more toxic than Sb(V). Both oxidation states are discriminated by their oxygen coordination, which can be determined by EXAFS spectroscopy. Furthermore, at sufficiently high Sb concentrations EXAFS can be used to identify the complete short range structure, and hence identify aqueous, sorbed and solid species. Finally, newly developed statistically methods should make it possible to decipher the Sb speciation quantitatively [12, 13]. We selected shooting range soils, because Sb concentrations are sufficiently high for EXAFS analysis, and because shooting activities are an important emitter of Sb into the environment.

Materials and methods

Samples were collected at six shooting ranges in Switzerland, representing a wide range of geochemical conditions including pH, organic and inorganic carbon content and mineralogy, and representing a range of Sb (and Pb) pollution levels (Table 1). The predominant ammunition used at these sites are two calibers of rifle bullets, 6.5 mm (GP11) and 7.5 mm (GW Pat 90), consisting of a metallic core of Pb hardened with 2 to 4 % Sb, encased in a cupronickel-clad steel jacket. Soil samples were collected at the stop butts in various depths, air dried and sieved (< 2 mm). The elemental composition was determined by energy-dispersive X-ray fluorescence spectrometry (Spectro X-LAB 2000).

Antimony K-edge EXAFS spectra were collected at the Rossendorf Beamline (BM20) at the ESRF in fluorescence mode. Sample cooling to 20 K using a He cryostat greatly improved spectra quality due to reduction of the thermal contributions to the Debye-Waller factors, and was applied to all samples. Quantitative speciation was performed by applying iterative target transformation factor analysis (ITFA) to the set of k^3-weighted chi spectra [12, 13]. To determine the short-range structure of extracted species, shell fitting was performed with FEFF 7 and WinXAS.

Table 1. Sample properties.

Sample	Depth	pH	$CaCO_3$	Corg	Sb	Pb	Cu
	cm		---------g/kg---------		----------mg/kg----------		
Goldau B	0-5	8.2	335	29	6000	111000	3050
Zuchwil AhnB	0-5	5.8	0	50	1600	21000	2750
Oberuzwil 0-5	0-5	6.9	0	300	8000	171000	2720
Oberuzwil 5-15	5-15	7.1	13	220	3400	76000	2080
Oberuzwil nB	25-45	7.1	53	220	8600	175000	5100
Quartino A	0-5	9.4	73	72	17500	(516000)	4450
Davos E	0-5	7.8	133	6	1900	35000	920
Losone J-1	1	3.2	0	330	4000	80900	189
Losone N4	16	3.6	0	150	1300	21300	43

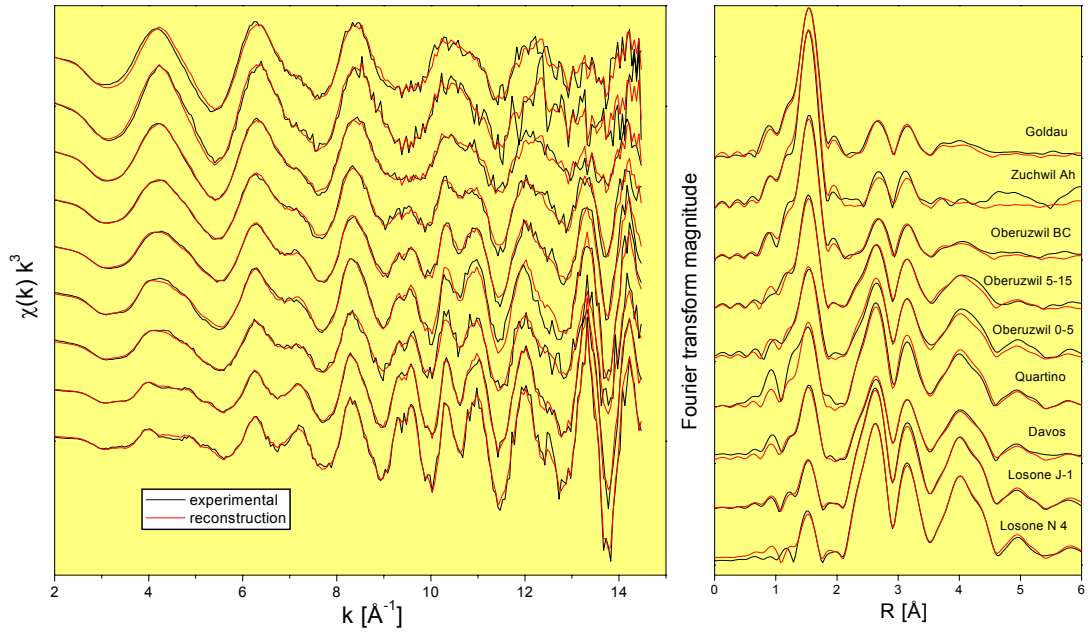

Fig. 2. Antimony K-edge EXAFS spectra of soil samples from 6 different shooting ranges (black lines), and their reconstruction with 2 principal components (red lines).

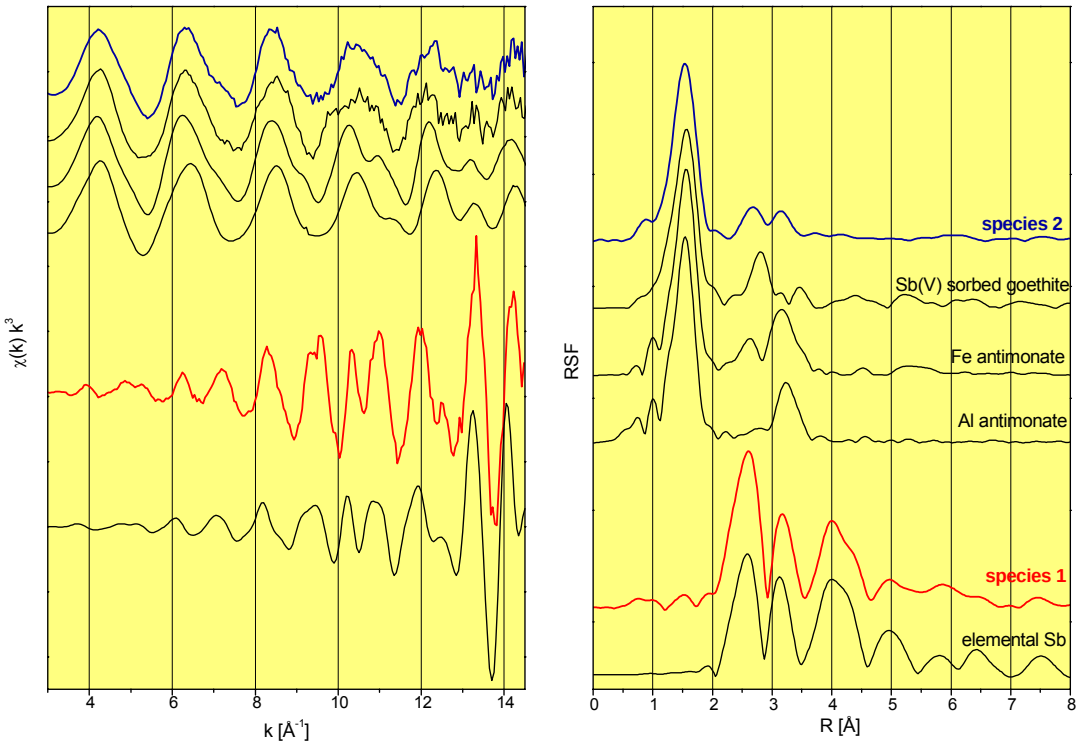

Fig. 3. Antimony K-edge EXAFS spectra of the two Sb species isolated from the sample spectra in Fig. 2 by iterative target transformation factor analysis. Selected reference species are shown for comparison.

Results and discussion

Antimony and Pb concentrations of the samples are closely correlated (R^2=0.988***), revealing their common deposition history (Table 1). The regression line has a slope of 0.0462 which is above the range of 0.02-0.04 expected from the bullet composition. This slight enrichment of Sb may suggest a higher mobility of Pb as compared to Sb. Note that the highest Pb concentration of 516 g kg^{-1} was omitted from the regression, since this concentration exceeded the calibration range of the fluorescence analysis.

Due to the use of a cryostat for sample cooling to 20 K, high quality EXAFS spectra to $\geq$ 15 $Å^{-1}$ could be collected out to 14.5 $Å^{-1}$ (Fig. 2, black lines). The spectra were treated with iterative transformation factor analysis. All spectra are reconstructed with only 2 factors (Fig. 2, red lines), suggesting that Sb speciation is dominated by only two species. The spectral components of these species are shown in Fig. 3 along with the measured spectra of selected references. The short range structure of the two spectral components was determined by multi-shell fitting using paths calculated by FEFF7 (Table 2).

Table 2. Local structure of species 1 and 2 and of selected references.

	Coordination shell			Further shells				
Sample	CN* and element	R [Å]†	σ^2 [$Å^2$]‡	CN and element	R [Å]	σ^2 [$Å^2$]	ΔE_0 [eV]§	$\chi^2_{res\ \%}$**
Species 1	2.1 Sb	2.90	0.0013	2.1 Sb 6.7 Sb 6.1 Sb	3.35 4.30 4.51	0.0027 0.0045 0.0039	6.6	7.5
Species 2	5.3 O	1.98	0.0033	1.1 Fe 1.4 Sb	3.10 3.35	0.0026 0.0053	8.1	3.3
Sb metal	2.2 Sb	2.91	0.0013	1.8 Sb 6.9 Sb 6.3 Sb	3.34 4.29 4.49	0.0021 0.0047 0.0056	9.5	13.0
Sb(V) sorbed goethite	6.1 O	1.99	0.0042	1.0 Fe	3.08	0.0030	7.7	9.2
Sb(V) antimo-nate	6.1 O	1.98	0.0043	2.4 Fe 2.9 Sb 2.3 Sb	3.08 3.37 3.62	0.0080 0.0070 0.0070	5.6	7.4

In species 1, each Sb is surrounded solely by other Sb atoms at distances, which are consistent with Sb metal (Table 2). Furthermore, the spectral component is almost identical with the low-temperature spectrum of Sb foil (Fig. 3). Hence there is no doubt that species 1 is metallic Sb.

* Coordination number
† Radial distance
‡ Debye-Waller factor
§ Phase shift
** Fit error

In species 2, Sb is octahedrally coordinated to O, indicative of the pentavalent oxidation state (Fig. 1, Table 2). Small backscattering peaks in the Fourier transform at distances above 2 Å (Fig. 3, uncorrected for phase shift) were fit with one Fe (or Mn) atom at 3.10 Å and one Sb atom at 3.35 Å. Such an arrangement could indicate that Sb(V) is bound to the surface of Fe (or Mn) oxides as polynuclear inner-sphere surface complex. For comparison, we investigated the spectrum of a Sb(V) sorbed goethite (Fig. 3), which was fit with one Fe atom at a distance of 3.08 Å. While the Fe distance is similar, no Sb atom was observed. An alternative interpretation would be formation of an Fe antimonate. The spectrum of a crystalline Fe antimonate reference phase is shown in Fig. 3. It was fit with 2.4 Fe atoms at 3.08 Å, 2.9 Sb atoms at 3.37 Å and 2.3 Sb atoms at 3.62 Å. The distances of the Fe shell and of the first Sb shell are in line with that of species 2; however, the coordination numbers of species 2 are significantly smaller, and the second Sb shell is missing. These differences may be explained by formation of small Fe antimonate-like clusters with incomplete coordination within 3.37 Å, and the lack of any structure beyond 3.37 Å. Therefore, the most consistent interpretation of species 2 is formation of an amorphous Fe antimonate phase, which may have formed as surface-induced precipitate on Fe oxides.

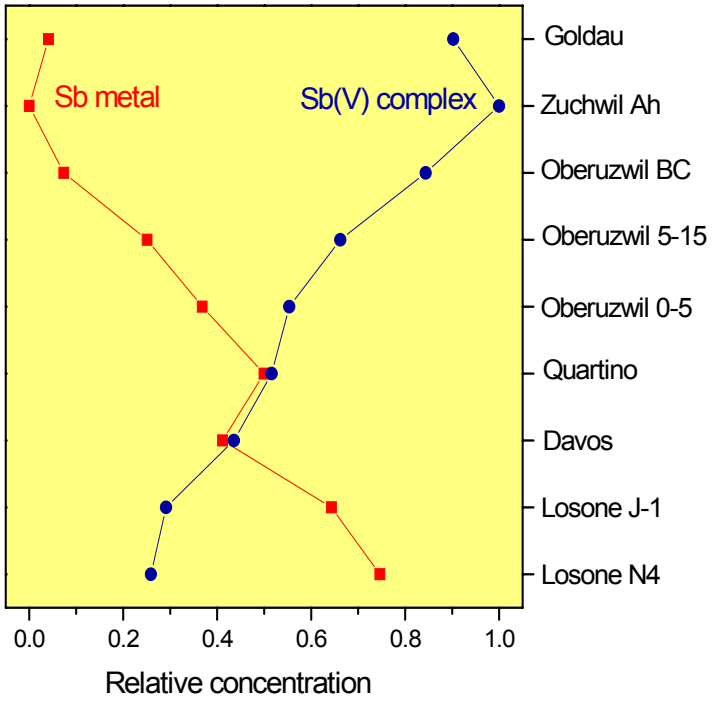

Fig. 4. Quantitative Sb speciation derived by iterative target transformation factor analysis (ITFA).

The relative concentration of the two species as derived by iterative target transformation factor analysis is shown in Figure 4. The highest fraction of Sb metal occurs in the Losone samples. The soil of this site is very acidic, organic matter-rich, and has very low density. Only one bullet was found in the topsoil of a 2 x 2 m^2 area, which had Pb concentrations as high as 80.9 g kg^{-1} [7]. The surface of this bullet was bright-metallic from surface dissolution, and it did not show a weathering crust. No other bullets were found in spite of the high total Pb content of the soil. Furthermore, Pb L_3-edge EXAFS spectroscopy showed only Pb^{2+}, but no Pb(0) at this site (data not shown). Hence soil chemical characteristics, the lack of bullet residues and Pb L_3 EXAFS spectroscopy all strongly suggest that bullet weathering is rapid and complete in this soil. Therefore, the metallic Sb(0) either must have remained unoxidized during Pb oxidative dissolution, or the Sb(0) has formed by reduction from oxidized species.

The general trend from a high amount of Sb(0) in the Losone samples to the prevalence of Sb(V) species in the Zuchwil sample with neutral pH and sandy texture is not related to any of the monitored parameters (pH, texture, concentration of Corg, $CaCO_3$, Pb, Sb, Cu, history of the shooting ranges, etc.). Hence no explanation for the variable speciation can be given.

At some of the sites, Sb(III) was found in soil solution [6]. However, we did not find any evidence for Sb(III) in the bulk soil samples. Since the lower detection limit of the employed combination of EXAFS spectroscopy and factor analysis is about 5 %, trivalent species represent less than 5 %. This indicates that Sb(III) is rapidly oxidized to Sb(V), a process most likely taking place at the surface of Fe or Mn (hydr) oxides.

Conclusion

In spite of a wide variation of geochemical parameters, only two Sb species were found in soils of shooting ranges: Sb metal and Fe antimonate-like clusters. Species with the most toxic trivalent oxidation state were not found. No causal relationship between the speciation and geochemical parameters or shooting range history can be offered. To the best of our knowledge, this is the first time that Sb species have been determined *in situ* in environmental samples.

Acknowledgements

This study was funded in part by the Swiss National Science Foundation. We would like to thank Mr. V. Schärer, Ms. V. Galbier, Mr. G. Tognina and Mr. A. Tremp for their effort to make the sampling possible.

References

[1] D.C. Adriano, Trace Elements in the Terrestrial Environment, Springer Verlag, New York, 1986.
[2] M. Krachler, H. Emons and J. Zheng, Trends in Analytical Chemistry 20 (2001) 79-90.
[3] M. Filella, N. Belzile and Y.-W. Chen, Earth-Science Reviews 57 (2002) 125-176.
[4] C. Fahrenhorst and M. Renger, VDLUFA Kongressberichte 32 (1990) 827-830.
[5] S. Basunia and S. Landsberger, Journal of the Air & Waste Management Associationement Association 51 (2001) 1428-1435.
[6] C.A. Johnson, H. Moench, P. Wersin, P. Kugler and C. Wenger, Journal of Environmental Quality (2004) submitted.
[7] L.A. Knechtenhofer, I.O. Xifra, A.C. Scheinost, H. Flühler and R. Kretzschmar, Journal of Plant Nutrition and Soil Science 166 (2003) 84-92.
[8] Inorganic Crystal Structure Database 2004-02, National Institute of Standards and Technology 2004.
[9] N. Ainsworth, J.A. Cooke and M.S. Johnson, Environmental Pollution 65 (1990) 65-77.
[10] L. Knechtenhofer, PhD Thesis, Dept. of Environmental Sciences, ETH Zurich (2002) 62.
[11] E.A. Crecelius, M.H. Bothner and R. Carpenter, Environmental Science & Technology 9 (1975) 325-333.
[12] A. Roßberg, T. Reich and G. Bernhard, Analytical and Bioanalytical Chemistry 376 (2003) 631-638.
[13] A.C. Scheinost, A. Rossberg, S. Pfister, R. Kretzschmar and M. Marcus, Physica Acta in press (2004).

In-situ studies of ITO film properties and structure during annealing in vacuum

A. Rogozin[1], N. Shevchenko[1], F. Prokert[1], V. Cantelli[1], A. Kolitsch[1], W. Möller[1], M. Vinnichenko[2]

[1] Institute of Ion Beam Physics and Materials Research, Forschungszentrum Rossendorf, P.O. Box 510119, 01314 Dresden, Germany

[2] Kyiv National Taras Shevchenko University, Kyiv 01033, Ukraine

Introduction

Tin-doped indium oxide (ITO) films are highly degenerate wide band gap semiconductors with high conductivity and transparency in the visible region of the spectrum. The preparation of low-resistivity ITO films by reactive magnetron sputtering normally requires deposition on heated substrates or post-deposition annealing.

So far, the annealing processes for reactively sputtered ITO [1, 2] have only been studied for metal-rich films, in contrast to studies after magnetron sputtering from ceramic targets [3-8]. Moreover, mainly isothermal heat treatment is considered in the literature, although annealing using a temperature ramp is of more relevance for practical application. Several investigations report on real-time *in-situ* monitoring of the ITO film resistivity and reflectivity [7, 8], which is used for an *indirect* characterisation of the crystalline structure of the films. This approach requires simplifying assumptions on the linear dependence of the resistivity or light reflectivity on the crystalline fraction, and the stability of the film roughness during annealing. *Direct* investigations of the influence of heat treatment on the ITO film structure are so far limited to post-annealing studies by x-ray diffraction (XRD) and scanning or transmission electron microscopy [1-3, 5, 6, 9].

Annealing of ITO is known to be very efficient in increasing the carrier concentration. It can be quite reasonably explained by the Frank–Köstlin model [10], which accounts for tin donor activation at elevated temperatures. However, this model is valid only for crystalline ITO. The amorphous-to-crystalline transition in ITO during annealing is often assumed as the reason for this activation, but the physics behind the experimental observation is not clear. Here we report the results of a real-time *in-situ* investigation of the film properties and the structure evolution during annealing in vacuum.

Experimental

The films are produced by reactive pulsed middle frequency magnetron sputtering using the facility and procedure described in Ref. 11. The films are grown on Si(100) substrates covered with SiO_2, which were *not* heated intentionally during deposition. The average thickness of the deposited films is 130 nm. The as-deposited films show no crystalline peaks in the XRD patterns and are considered as amorphous.

The post-deposition annealing of identical ITO samples was carried out at two different experimental setups, the materials research station of ROBL at ESRF in Grenoble [12], and the ITO deposition facility at FZR [11]. In both cases the total pressure of the residual gas was below $6\ 10^{-4}$ Pa. The annealing temperature T_a was gradually increased from 20 to 330°C at a constant rate of approximately 5 °C/min. In both experimental setups, the resistivity of the ITO films was monitored *in situ* by the four point probe technique.

In order to study the evolution of the ITO film structure in real time, a UHV annealing chamber, equipped with an x-ray transparent beryllium dome, was mounted on a six-circle goniometer. The x-ray diffraction experiment was performed in Bragg–Brentano geometry within the range of scattering angles of 27-37°. The incident x-ray beam was mono-chromatized to 8.048 keV (λ = 0.154 nm). A multi-channel linear position sensitive detector (PSD) allowed a fast scan acquisition time of 100 s. A spectroscopic rotating compensator ellipsometer (M-2000, J.A Wollam Inc., USA) was used at FZR for *in-situ* monitoring of the film optical properties. The ellipsometer is installed at the deposition chamber which is equipped with fused silica windows at an angle of light incidence of 70.7° with respect to the sample surface normal.

Results and discussion

After increasing the annealing temperature T_a up to 250 $\pm$ 10°C, the XRD patterns show only a broad amorphous peak around 32°, indicating the absence of any structural changes below this temperature. The evolution of the XRD patterns with annealing temperature within the range 200-320°C is shown in Fig. 1. At $T_a \approx 250$°C, the (222) and (400) peaks of crystalline In_2O_3 phase start to appear. Their intensity increases strongly as T_a increases by approximately 30°C, pointing to a rapid crystallization of the ITO film. The film becomes completely crystalline at $T_a \geq 280$°C with a stable structure above. The calculation of the texture coefficient by known equations shows that the film exhibits a weak (222) fiber texture in this state. The size of coherently diffracting domains was estimated by the Scherrer formula to be 65 $\pm$ 4 nm.

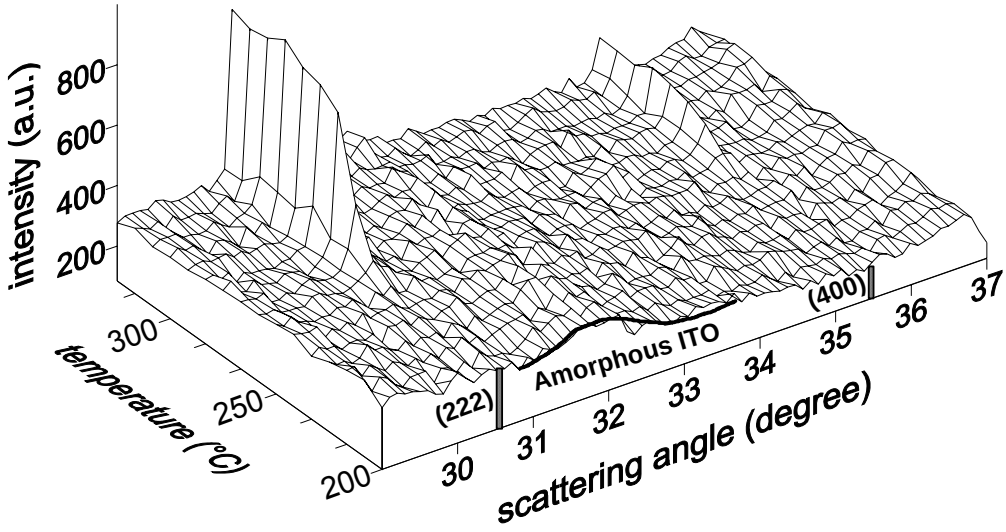

Fig. 1: Evolution of XRD patterns during annealing in vacuum.

The observed temperature of crystallization of 250°C is significantly larger than published values ranging from 150 to 200°C, which are often cited [7, 8]. However, the latter are deduced from post-deposition XRD studies of ITO layers produced on heated substrates [13]. During deposition, additional activation may occur due to plasma-surface interaction including fast ion bombardment, which might promote the crystallization at lower temperatures.

The temperature dependence of XRD integral intensity of the In_2O_3 (222) peak [$I_{(222)}$] [Fig. 2(a)] has the typical S-like shape, being characteristic for the enhancement of the

crystalline fraction during the amorphous-to-crystalline transition. The observed EMA roughness enhancement can be mainly related to the film crystallization because it occurs within the identical temperature range of 250-280°C.

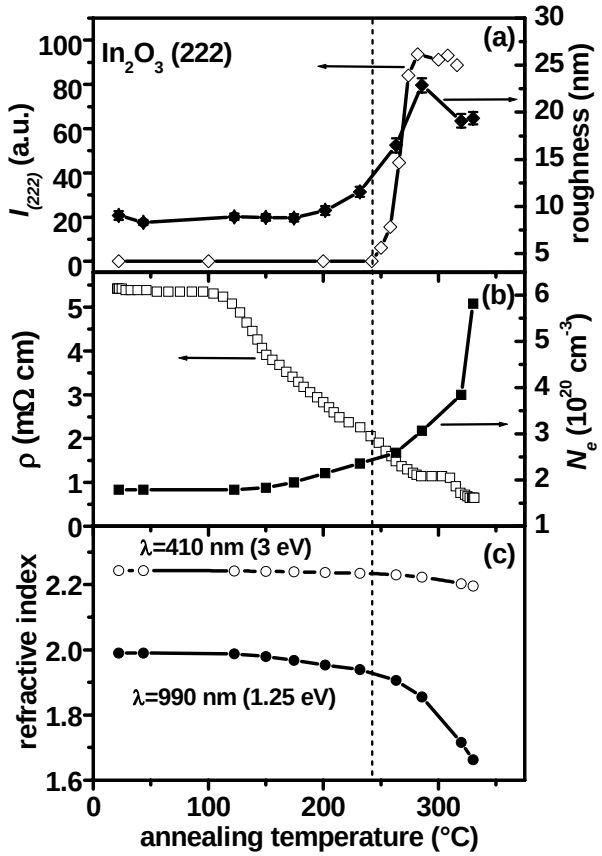

Fig. 2: Temperature dependence during annealing of XRD integral intensity of the In_2O_3 (222) peak [$I_{(222)}$] along with the roughness (a), resistivity and free electron density N_e (b), and refractive index at two wavelengths (c).

Defining the degree of crystallization by $f = I_{(222)}/I_{C(222)}$, where $I_{C(222)}$ is the integral intensity measured at complete crystallization, its time dependence is analyzed by using the Kolmogorov–Johnson–Mehl–Avrami equation [14-16]

$$f = 1 - \exp(-K\ t^n) \qquad (1)$$

where n is a kinetic exponent and K is a rate constant. A linear fit of the function $-ln(1-f)$ plotted *versus* the acquisition time on a double-logarithmic scale, yields $n = 2.99 \pm 0.23$. Under the condition that the coherently diffracting domain size is smaller than the film thickness, this kinetic exponent indicates a 3-dimensional crystallization process.

The observed temperature dependence of the resistivity in Fig. 2(b) indicates several stages with features at T_a = 110, 150, 280 and 310°C, in contrast to the more simple two-stage behavior of the resistivity and single-stage behavior of the reflectivity observed during isothermal annealing [7, 8]. The temperature behavior of the free electron density N_e in Fig. 2(b) qualitatively agrees with a decrease of the resistivity, excepting the temperature range of 280-310°C. The refractive index in Fig. 2(c) decreases at increasing annealing temperature that relates to the free electron density behavior. From the stability of the film resistivity and refractive index at a temperature below T_a ~ 120°C it can be concluded that neither the free electron density nor the structure of the ITO films change during the first

annealing period. At higher temperatures (120-240°C) the free electron density increase in the amorphous ITO can be attributed to the creation of oxygen vacancies due to relaxation of distorted In-O bonds in the amorphous phase. As the resistivity decreases faster than N_e increases, the free electron mobility can be assumed to be enhanced.

The fast enhancement of the free electron density, N_e after the beginning of crystallization (T_a ~ 250°C) can be explained by the onset of Sn donor activation [7, 8, 17] in a growing crystalline phase. However, the spectroscopic ellipsometry is sensitive to the free electron density enhancement even in crystalline grains which are electrically insulated or have bad contact to each other [18]. These grains do not contribute to resistivity decrease until they are electrically connected. Possibly such connections are a reason for the drop of resistivity (T_a > 310 °C) after a plateau observed at increasing N_e within the temperature range 280-310°C.

The comparison of the graphs in Fig. 2 clearly shows that at constant heating rate the resistivity and optical properties depend non-linearly on the crystalline fraction. This is in contrast to the linearity which is often assumed in the literature. A reason for this discrepancy might be the change of surface roughness in this particular case, which renders reliable monitoring of the film structure evolution by indirect techniques extremely difficult.

Summary

The structure and properties of ITO films deposited by reactive magnetron sputtering have been monitored in real time during annealing in vacuum, using three complementary *in-situ* techniques. The direct observation of the structure yields a crystallization temperature of 250°C. Even in the amorphous state the film resistivity decreases significantly at increasing temperature, probably due to relaxation of distorted In-O bonds in the amorphous phase, which leads to a free electron density enhancement by the creation of oxygen vacancies. The rapid crystallization is accompanied by film roughening and leads to a further decrease of the resistivity due to Sn donor activation.

References

[1] A.J. Steckl, G. Mohammed, J. Appl. Phys. **51** (1980) 3890
[2] S. Chaudhuri, J. Bhattacharyya, A.K. Pal, Thin Solid Films **148** (1987) 279
[3] Y. Shigesato, S. Takaki, T. Haranoh, J. Appl. Phys. **71** (1992) 3356
[4] Y. Shigesato, D.C. Paine, Appl. Phys. Lett. **62** (1993) 1268
[5] M. Higuchi, S. Uekusa, R. Nakano, K. Yokogawa, Jpn. J. Appl. Phys. **33** (1994) 302
[6] S. Takayama, T. Sugawara, A. Tanaka, T. Himuro, J. Vac. Sci. Technol. A **21** (2003) 1352
[7] C.W. Ow-Yang, D. Spinner, Y. Shigesato, D.C. Paine, J. Appl. Phys. **83** (1998) 145
[8] D.C. Paine, T. Whitson, D. Janiac, R. Beresford, C. Ow Yang, B. Lewis, J. Appl. Phys. **85** (1999) 8445
[9] H. Morikawa, M. Fujita, Thin Solid Films **339** (1999) 309
[10] G. Frank, H. Köstlin, Appl. Phys. A: Solids Surf. **27** (1982) 197
[11] A.I. Rogozin, M.V. Vinnichenko, A. Kolitsch, W. Möller, J. Vac. Sci. Technol. A **22** (2004) 349
[12] W. Matz, N. Schell, G. Bernhard, *et al.*, J. Synchrotron Rad. **6** (1999) 1076
[13] S. Muranaka, Y. Bando, T. Takada, Thin Solid Films **151** (1987) 355
[14] A. Kolmogorov, Izv. Akad. Nauk SSSR, Ser. Matem. **1** (1937) 355
[15] W. Johnson, R. Mehl, Trans. AIME **135** (1939) 416
[16] M. Avrami, J. Chem. Phys. **7** (1939) 1103
[17] J.R. Bellingham, W.A. Phillips, C.J. Adkins, J. Phys. Condens. Matter **2** (1990) 6207
[18] D. Mergel, Z. Qiao, J. Phys. D: Appl. Phys. **35** (2002) 794

High temperature investigations of Si/SiGe based quantum cascade structures using x-ray diffraction and reflectivity

M. Meduňa[1,2], J. Novák[1,2], G. Chen[1], G. Bauer[1], C.V. Falub[3], S. Tsujino[3], D. Grützmacher[3], E. Müller[3], Y. Campidelli[4], O. Kermarrec[4], D. Bensahel[4], N. Schell[5]

[1] Institute for Semiconductor Physics, Johannes Kepler University, Altenbergerstr. 69, 4040 Linz, Austria

[2] Institute of Condensed Matter Physics, Masaryk University, Kotlářská 2, 61137 Brno, Czech Republic

[3] Laboratory for Micro- and Nanotechnology, Paul Scherrer Institute, 5232 Villigen, Switzerland

[4] STMicroelectronics, 38926 Crolles-cedex, France

[5] Institute of Ion Beam Physics and Materials Research, Forschungszentrum Rossendorf, P.O. Box 510119, 01314 Dresden, Germany

Introduction

High Ge composition $Si/Si_{1-x}Ge_x$ (x = 80%) superlattices are important for design flexibility of SiGe based quantum cascade lasers (QCL). To realize a QCL device based on Si and Ge is quite difficult since the 4 % lattice mismatch between Si and Ge produces a high lattice strain. This strain may induce interface roughness, undulations at the growth front [1] and finally misfit dislocations. That is why the growth of SiGe based QCL structures needs highly stable growth conditions and comparatively low growth temperatures. Moreover, the conditions for electroluminescence and the proper band structure for cascade emitters require a rather complex design of adjacent Si barriers and SiGe quantum wells and a very good control of the layer compositions and thicknesses.

SiGe/Si electroluminescent cascade structures with Ge contents up to 40 %, grown by molecular beam epitaxy (MBE), which exhibited well-resolved electroluminescence in the 10 μm wavelength range with a quite narrow line width of 22 meV were already successfully realized [2]. The structural investigation of these samples was performed by x-ray scattering [3] and demonstrated a very good structural quality of the interfaces. Despite of the large lattice mismatch between the SiGe (40 %) and Si layers, the growth was still pseudomorphic with respect to the Si(001) substrate.

However, in principle, a higher Ge composition in the quantum wells allows a higher design flexibility of SiGe/Si structures but as a drawback induces a lower structural stability due to the extremely high strain values. In order to compensate for the high strain in the system, such structures have to be grown on SiGe relaxed pseudo-substrates. Furthermore, the constituent layers have to be strain-symmetrized with additional cap layers. The strain symmetrization is determined both by the Ge content in the pseudo-substrate and in the layers on top of the structure, grown in reversed order [4]. Dislocations and high interface roughness limit the quality of the strained layers. Furthermore, at elevated temperatures, which might occur during device processing steps, metastable Si/SiGe structures may suffer strain relaxation via dislocation formation and the interface roughness might change as well.

Experimental method and results

In this experiment, we focused on the annealing behavior of strain compensated multiple quantum well (MQW) structures $Si/Si_{1-x}Ge_x$ with high Ge composition (x = 80%), grown on $Si_{0.5}Ge_{0.5}$ pseudo-substrates. Such structures are much more suitable for the analysis of x-ray data and investigations of diffusion processes than QCL devices. These structures have

been investigated by x-ray small angle scattering and high resolution x-ray diffraction (XRD) in a coplanar setup. XRD is sensitive mainly to the strain and x-ray small angle scattering, e.g. x-ray reflectivity (XRR), is only sensitive to the morphology of the interfaces. The superlattices, which are originally designed for their photoluminescence and tunneling properties, remain enormously strained, and they are in a metastable regime. Thus, a study on the temperature dependence of the Ge interdiffusion via XRR measurements is desirable.

The investigated samples contained MBE-grown (300°C) MQW's with 30 periods of $Si_{0.2}Ge_{0.8}$ (83.3 Å) / Si (50 Å) grown on a $Si_{0.5}Ge_{0.5}$ graded relaxed pseudo-substrate (Fig. 1). The superlattices were strain-symmetrized by the system of layers graded up to $Si_{0.2}Ge_{0.8}$ situated below and above the MQW (in reversed order), in order to avoid the formation of misfit dislocations in the MQW. Details on the MBE growth can be found in Refs 5 and 6.

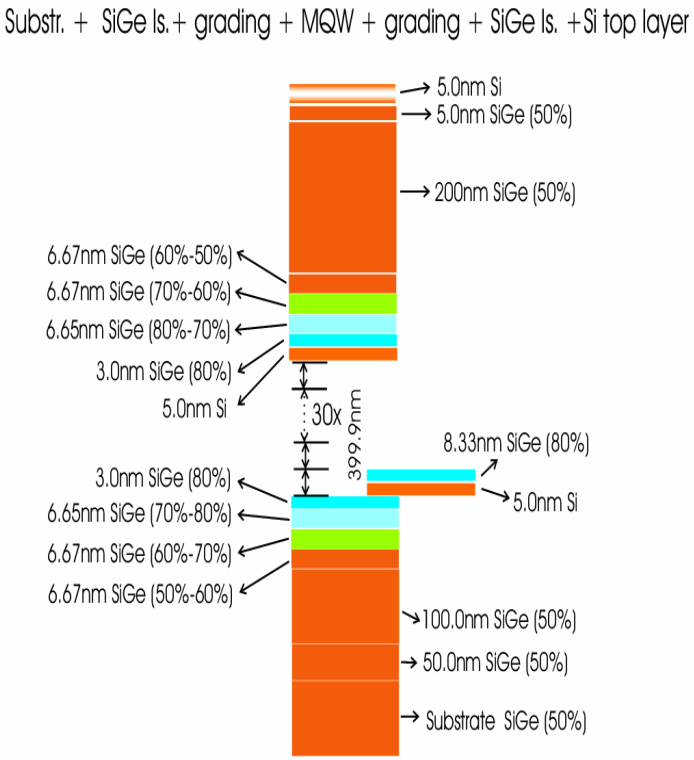

Fig. 1: Scheme of the nominal structure of the investigated SiGe sample K089 (K098ref1, K098ref2 and K098ref3) grown on the $Si_{1-x}Ge_x$ (x = 50 %) pseudo-buffer, which was deposited on Si(001).

We have performed a series of XRR and diffraction reciprocal space maps (RSM) at room temperature and during *in-situ* annealing for temperatures ranging from 600°C up to 830°C for different annealing periods in order to follow the evolution of interfaces during annealing and to find the temperature limit, at which the strain and interdiffusion start to affect the structure. In previous studies, we already found that around a temperature of 810°C the SiGe MQW structure is strongly affected by interdiffusion [6]. In the present, more detailed experiment, we have performed three annealing procedures at different temperatures using three pieces of the same sample structure, taken from the same grown wafer (Fig. 2).

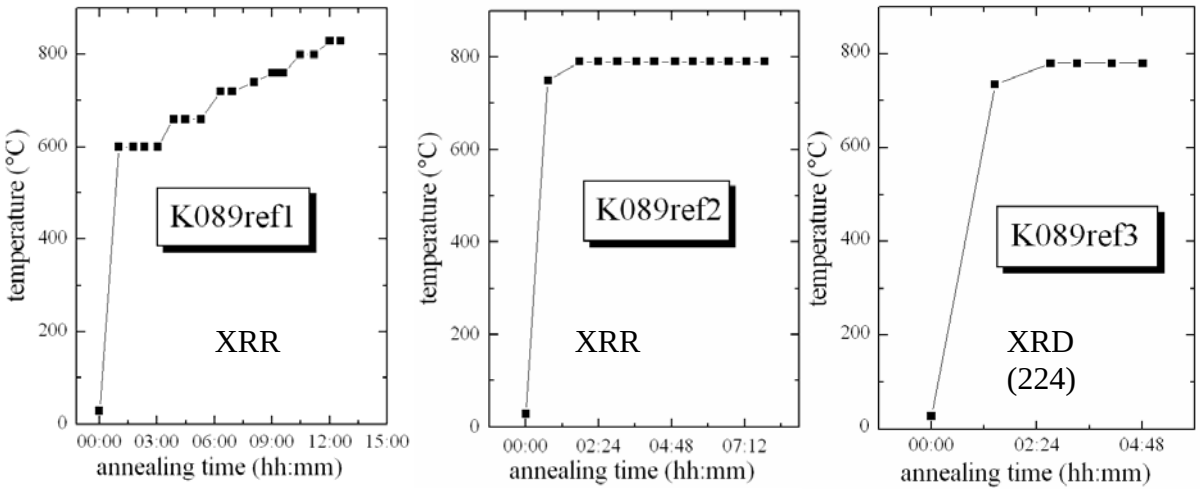

Fig. 2: Temperature *versus* time of the investigated pieces of sample K089 during annealing.

XRR and RSM have been obtained using a wavelength λ = 1.5405 Å. For the annealing experiments we used the small ROBL furnace with a hemispherical Be dome, which allowed to perform the *in-situ* annealing studies both in low and high incidence angle geometry. The annealing itself was performed in vacuum at a pressure of 2.7 x 10^{-5} Pa. Two temperature sensors were used during the experiment to control the sample temperature: one thermocouple measured the temperature at the sample surface and the other one measured the temperature of the heater below the sample. The temperature of the heater was usually about 5-9 % higher than the temperature of the sample surface. The temperature sensors were calibrated before the measurements. A position sensitive detector (PSD) was used to record the scattering signal in a reasonable short data-collection-time (~30 min per RSM).

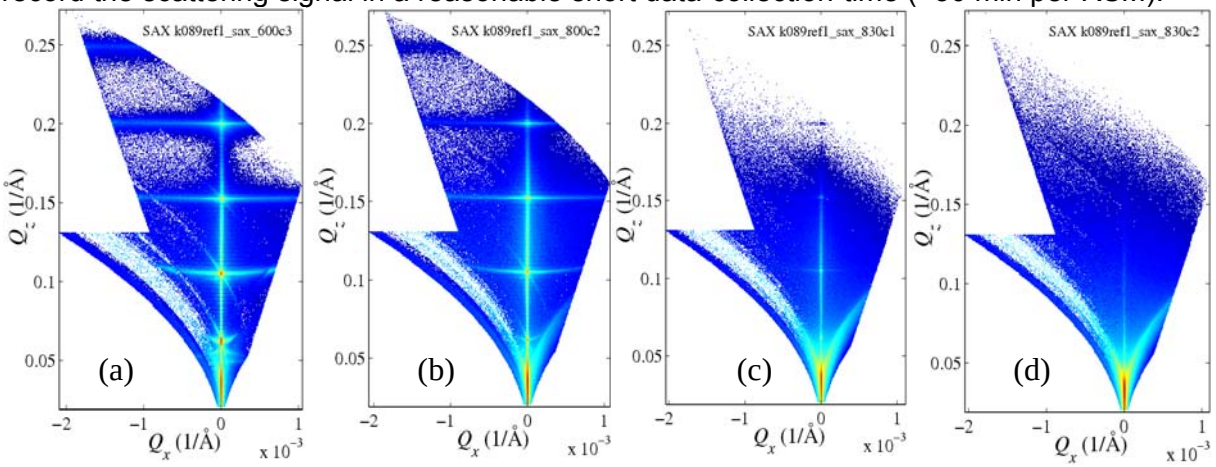

Fig. 3: Series of examples of XRR RSMs during annealing at 600°C (a), 800°C (b), 830°C (c) and 830°C after 35 min (c). The measurement interval between (b) and (c) was about 50 min.

We found that significant changes in reflectivity RSMs start to appear around a temperature of 790°C. At lower temperatures (< 700°C), we did not observe very significant changes in the reflectivity for 4 hrs. However, the change in scattered intensity in RSM was so fast when the temperature was reaching 830°C, that only two maps could be measured. Fig. 3 shows a set of reflectivity RSMs from sample K089ref1 corresponding to different annealing temperatures and time, i.e. 600°C (a), 800°C (b), 830°C (c), and 830°C for 35 min (d), where the periodical structures in the XRR data had vanished.

The annealing and reflectivity measurement of the second piece of the sample K089 (K089ref2) was started immediately at 750°C and continued at the constant temperature of

790°C for more than 6 hrs until the MQW structure disappeared. Thus, the temporal evolution of the MQW structure at the constant temperature was obtained. Examples of RSMs obtained with the PSD at room temperature and at various phases of annealing at 790°C are shown in Fig. 4. At this temperature, the intensity of the superlattice (SL) peaks in XRR RSMs was slowly decreasing in time and the MQW structure disappeared after 6 hrs of annealing at 790°C. Thus, we could record about nine reflectivity maps at different periods after the start of the annealing experiment, in which the clear SL multilayer peaks in RSMs are still observable.

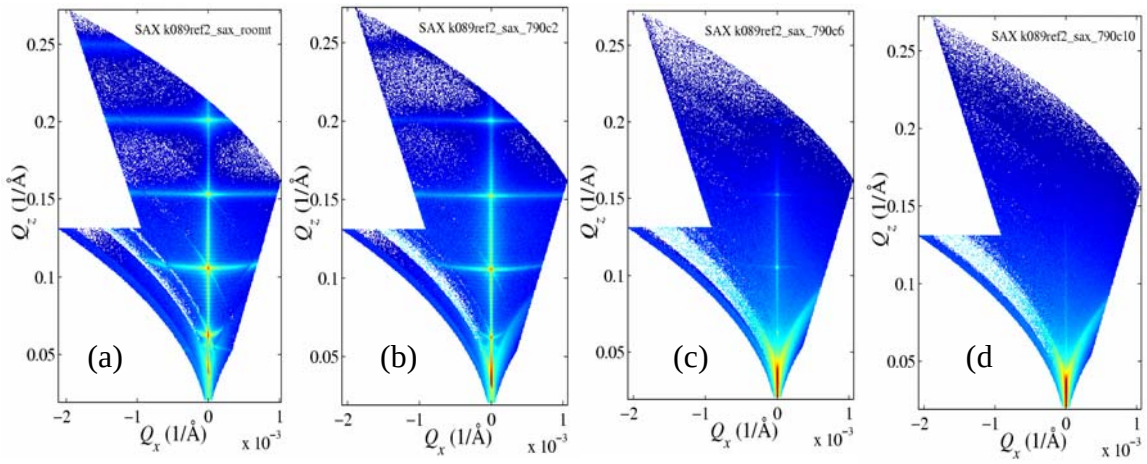

Fig. 4: Series of examples of XRR RSMs obtained for room temperature and during annealing at 790°C (a), after 75 min (b), 190 min (c) and 330 min (d).

Discussion

Since the diffusion processes which are responsible for the stability of the structures occur mainly across the Si/SiGe interfaces, the most important information is included in the specular reflectivity, which is sensitive only to the vertical structure averaged across the horizontal plane parallel to the sample surface. Thus, we have extracted Q_z scans from all RSMs at position $Q_x = 0$ and performed simulations of these specular reflectivity curves. The temporal evolution of specular reflectivity measurements during annealing of sample K089ref2 together with the simulations and the corresponding model of electron density is depicted in Fig. 5.

From the specular reflectivity curves in Fig. 5 (left panel), one can clearly see the slow gradual decrease of the SL multilayer peaks with increasing time. This corresponds to the slow but observable decrease of the relative electron density contrast $\Delta\rho$, as can be seen from the plots in Fig. 5 (right panel). The profile of the relative electron density was obtained from the specular reflectivity simulations. Since the value $\Delta\rho$ becomes very small towards the end of annealing, some of the relative electron density profiles for larger annealing periods were plotted in the insets of Fig. 5 (right panel). It is evident from these insets that the MQW structure can still be detected after 5 hrs of annealing. However, the results of $\Delta\rho$ for the last two measurements have a rather large error since the SL multilayer peaks cannot be clearly observed in the measurement. The relative electron density was normalized to the electron density of the substrate.

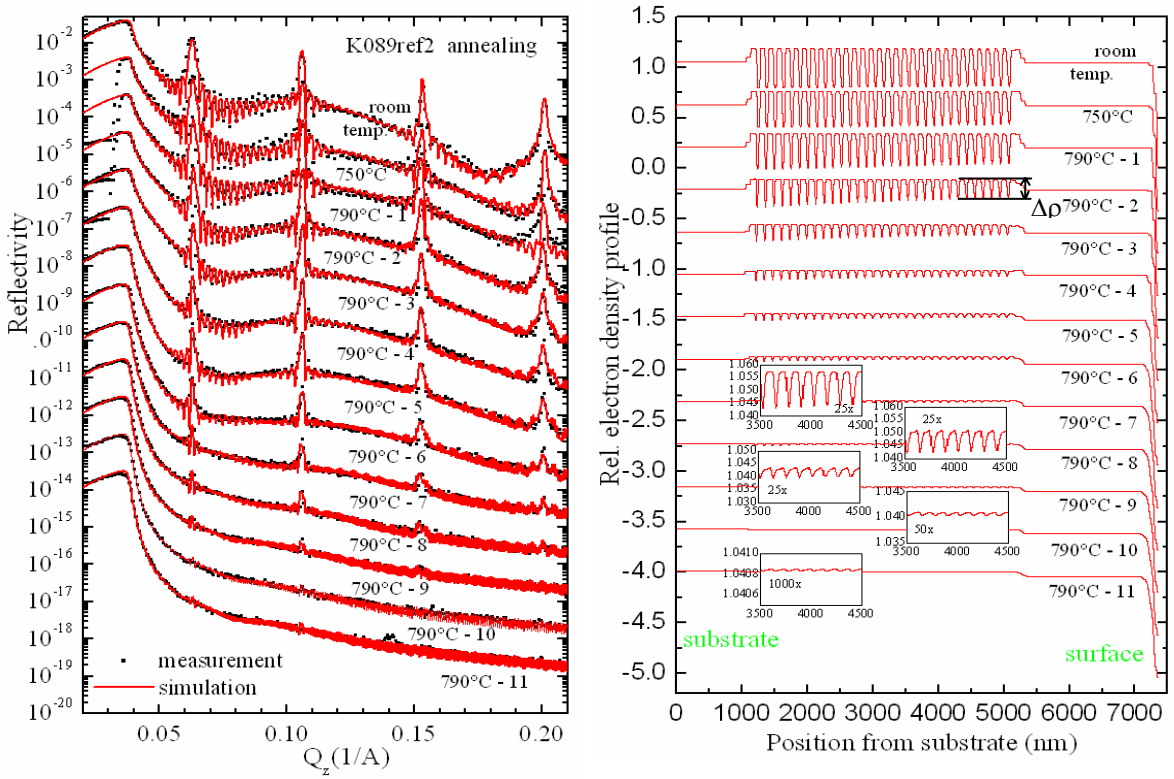

Fig. 5: Evolution of the specular reflectivity curves (left panel) and the corresponding relative electron density obtained from simulations (right panel) of sample K089ref2 during the second annealing experiment reaching the temperature 790°C. The results show the slow disappearance of the SL structure at 790°C. Neighboring reflectivity curves are shifted with respect to each other by a factor 0.1, the shift between neighboring electron density profiles is 0.42.

In the specular reflectivity simulations, we have used a standard matrix optical formalism [7] with modified Fresnel coefficients for ideal interfaces; multiplied by an exponential factor $\exp(-2\sigma_j k_{zj} k_{zj+1})$, see Ref. [8], where σ_j is the roughness of the j-th interface and k_{zj} are the z-components of the wave vectors in the layers. For the roughness replication model we have used the following assumptions [6]: a maximum replication and non-zero intrinsic roughness, a different and independent roughness profile at the Si/SiGe and SiGe/Si interfaces in the MQW and also in the graded regions below and above the MQW. The interface rms roughness σ was increasing within the interval from 0.4 to 2.1 nm from the bottom to the top of the structure for the reference sample, measured at room temperature.

Since the temporal evolution of the MQW structure K089ref2 was very slow with respect to the data collection time of one reflectivity RSM, we could carefully monitor the interface changes occurring in the MQW structure during annealing. The temporal evolution of the electron density contrast $\Delta\rho$, obtained from Fig. 5 (right panel) as an averaged value of contrasts $\Delta\rho$ from the top 15 layers of the MQW, is plotted in a logarithmic scale in Fig. 6 (right panel). It is clearly evident that the changes of $\Delta\rho$ at 790°C fulfill very well an Arrhenius dependence. In Fig. 6 (right panel), we have plotted only the first 9 points corresponding to the temperature 790°C since only these represent the remaining periodicity in MQW with a sufficiently good precision. The $\Delta\rho$ values were used for the exponential fit of the Arrhenius function $\Delta\rho = \rho_0 \exp(-t/t_0)$ in order to obtain the interdiffusion coefficient $D = d^2/4\pi^2 t_0$, where d denotes the multilayer period. We found for the interdiffusion coefficient $D = (1.01 \pm 0.03) \times 10^{-21}$ m^2/s for $Si/Si_{0.2}Ge_{0.8}$ at the temperature 790°C.

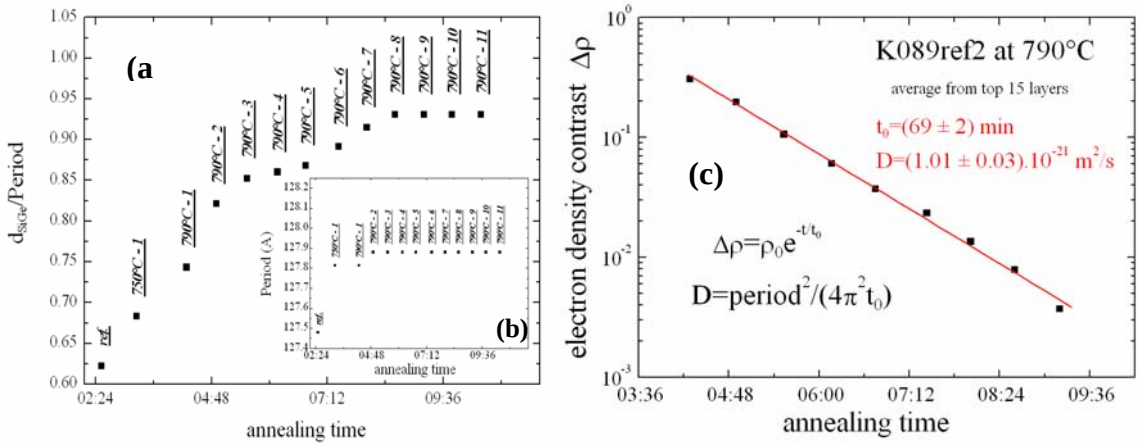

Fig. 6: Temporal evolution of (a) the SiGe layer thickness normalized to the period of the MQW during annealing of sample K089ref2, and inset (b) the SiGe/Si period of MQW, likely caused only by thermal expansion of the material. (c) shows the determination of the diffusion coefficient D at the temperature of 790°C, where the points of the electron density contrast $\Delta\rho$ taken from the average of the top 15 layers, were fitted by an Arrhenius dependence. The obtained interdiffusion coefficient was D = (1.01±0.03) x 10^{-21} m^2/s. The data were obtained from the specular reflectivity simulations, shown in Fig. 5.

From the specular reflectivity simulations, we have also detected a small change of the multilayer period during the annealing, which is only due to the thermal expansion of the multilayer. Thus, the MQW period can be considered as being constant during the annealing. Actually, the thickness of the SiGe layer was found to increase during annealing, see Fig. 6 (left panel). We observed this effect both for the sample K089ref2 at 790°C as well as for the annealing experiment of sample K089ref1. This implies that Si/Ge intermixing plays an important role at a temperature of 790°C and that indeed the Si diffusion into the SiGe layers is more important than the out-diffusion of Ge into the Si layers.

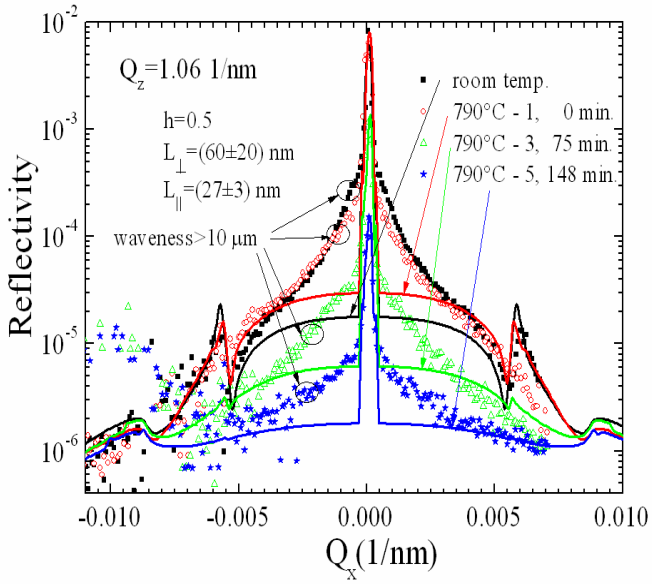

Fig. 7: Temporal evolution of the diffuse scattering within the Q_x scans during annealing of sample K089ref2 at the temperature 790°C. Dot-lines show the measurements and solid-lines show the simulations, assuming only fractal roughness. h is the fractal scaling exponent, $L_{||}$ is the lateral correlation length, $L_{\perp}$ is the vertical correlation length of the interfaces.

To get information on the lateral morphology of the interfaces from the x-ray data, an analysis of non-specular reflectivity is necessary. Thus, we have performed simulations of diffusely scattered intensity along Q_x scans at the position of the second SL peak using a DWBA theory [9, 10] and assuming the simple fractal interface roughness in the MQW. From the measurements and also from the simulations (Fig. 7), it follows that the lateral morphology of the interfaces in the MQW stays statistically preserved and only the roughness is changing during annealing. A lateral correlation length $L_{||}$ = (60±20) nm and a fractal scaling exponent h = 0.5 with a correlation function $C(x) = \sigma^2 \exp(-(|x|/L_{||})^{2h})$ of the interfaces were assumed for all Q_x scans. Since the intensity decreases almost by a constant factor only, the correlation properties of the interfaces are preserved during annealing.

We have also performed a series of XRD RSMs at the reciprocal lattice points (004) and (224) at different temperatures. The evolution of the diffraction signals around (224) is depicted in Fig. 8. It is evident that significant changes in the diffraction RSMs already start to appear at a temperature of 735°C, but the MQW structure stays pseudomorphic during annealing. This means that changes in the strain status precede the interdiffusion processes, considering the fact that the structure has almost disappeared in diffraction after 2 hrs at 780°C, while in XRR the signal from the periodical structure is still observable. From the RSMs in Fig. 8, one also notices that a new diffraction peak from the interdiffused multilayer appears around the position Q_z = 4.49 Å^{-1} at 780°C (marked by a red arrow). The position of this peak is continuously shifting towards the SL0 peak, while the position is the same as the one of the maximum of the envelope curve from MQW peaks in the Q_z direction.

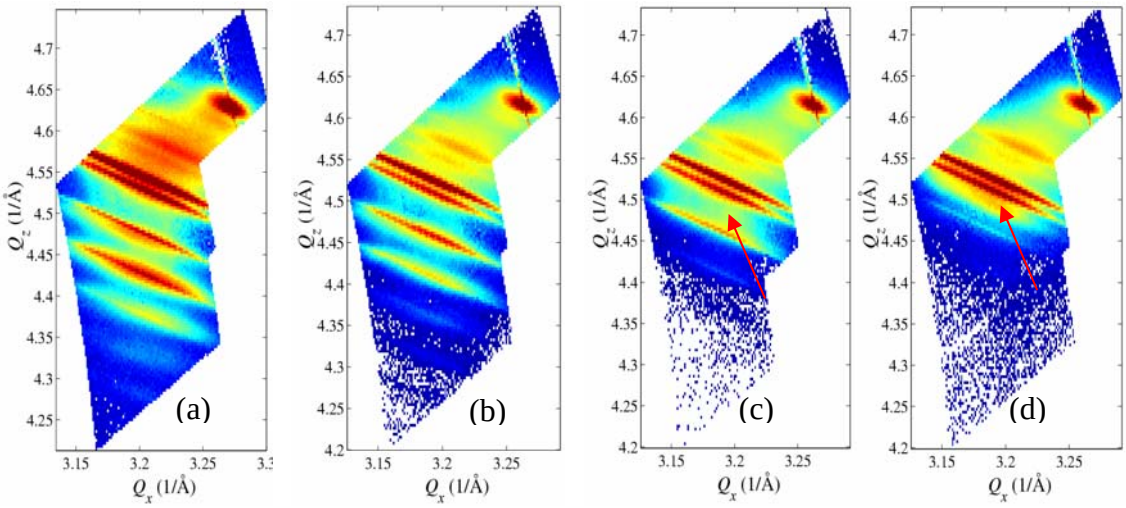

Fig. 8: Series of (224) XRD RSMs: (a) at room temperature, (b) during annealing at 735°C, (c) at 780°C, and (d) at 780°C after 125 min. Around Q_z = 4.49 Å^{-1} one notices the appearance of new diffraction peaks from the interdiffused multilayer, marked by an arrow, starting at 780°C and following within the increase and shift towards the SL0 peak for longer annealing periods. The position of this peak is identical with the envelope maximum of MQW peaks in the Q_z direction.

Summary

We have investigated the structural properties of $Si/Si_{0.2}Ge_{0.8}$ multiple quantum wells during *in-situ* annealing. For the investigation of interdiffusion we used x-ray specular and non-specular reflectivity. From the *in-situ* annealing experiments, we determined the interdiffusion coefficient for $Si/Si_{0.2}Ge_{0.8}$ at the temperature of 790°C for a multilayer period 13.33 nm. Its value of $D = (1.01 \pm 0.03) \times 10^{-21}$ m^2/s is in agreement with the one obtained by Liu *et. al* [11], who used Raman scattering for *ex-situ* investigations of Si/SiGe MQW structures with x = 0.5, and also with the interdiffusion coefficient obtained by extrapolation of data from Holländer *et. al* [12], who used Rutherford backscattering for investigations of strain-symmetrized Si/SiGe MQW structures with x = 0.68. Our observed increase of the SiGe layer thickness during annealing was also detected in previous measurements [6] and seems to be in qualitative agreement with previously published results [13, 14]. The results of this experiment and interdiffusion in cascade structures are discussed in more detail in [15].

References

[1] D.E. Jesson, S.J. Pennycook, J.M. Baribeau, D.C. Houghton, Phys. Rev. Lett. **71** (1993) 1744

[2] G. Dehlinger, L. Diehl, U. Gennser, H. Sigg, J. Faist, K. Ensslin, D. Grützmacher, E. Müller, Science **290** (2001) 2277

[3] T. Roch, M. Meduňa, J. Stangl, A. Hesse, R.T. Lechner, G. Bauer, G. Dehlinger, L. Diehl, U. Gennser, E. Müller, D. Grützmacher, J. Appl. Phys. **91** (2002) 8974

[4] L. Diehl, S. Mentese, E. Müller, D. Grützmacher, H. Sigg, T. Fromherz, J. Faist, U. Gennser, Y. Campidelli, O. Kermarrec, D. Bensahel, Physica **E 16** (2003) 315

[5] C.V. Falub, M. Meduňa, D. Grützmacher, S. Tsujino, E. Müller, A. Borak, T. Fromherz, H. Sigg, G. Bauer, *to be published*

[6] M. Meduňa, J. Novák, G. Bauer, V. Holý, C.V. Falub, S. Tsujino, E. Müller, D. Grützmacher, Y. Campidelli, O. Kermarrec, D. Bensahel, Z. Kristallogr. **219** (2004) 195

[7] M. Born, E. Wolf, *Principles of Optics*, New York, Pergamon Press (1964)

[8] P. Croce, L. Nevot, Revue Phys. Appl. **11** (1976) 113

[9] S.K. Sinha, E.B. Sirota, S. Garoff, H.B. Stanley, Phys. Rev. **B38** (1988) 2297

[10] V. Holý, J. Kuběna, I. Ohlídal, K. Lischka, W. Plotz, Phys. Rev. **B47** (1993) 15896

[11] X. Liu, D. Huang, Z. Jiang, X. Wang, Phys. Rev. **B53** (1996) 4699

[12] B. Holländer, R. Butz, S. Mantl, Phys. Rev. **B46** (1992) 6975

[13] J.M. Baribeau, J. Vac. Sci. Technol. **B16** (1998) 1568

[14] P. Zaumseil, J. Phys. D: Appl. Phys. **B32** (1999) A75

[15] M. Meduňa, J. Novák, C.V. Falub, G. Chen, G. Bauer, S. Tsujino, D. Grützmacher, E. Müller, Y. Campidelli, O. Kermarrec, D. Bensahel, N. Schell, *to be published*

In-situ characterization of stress states in copper dual inlaid interconnects at high temperatures by synchrotron x-ray diffraction

H. Prinz[1], J. Rinderknecht[1], I. Zienert[1], H. Geisler[1], E. Zschech[1], N. Schell[2]

[1] AMD Saxony LLC & Co. KG, Wilschdorfer Landstrasse 101, 01109 Dresden, Germany
[2] Institute of Ion Beam Physics and Materials Research, Forschungszentrum Rossendorf, P.O. Box 510119, 01314 Dresden, Germany

Introduction

The continuous increase of transistor density on microelectronic devices requires a proportional shrinking of the on-chip interconnect structures. Modern copper interconnect structures have line widths of less than 150 nm and are built on more than seven different levels (Fig. 1). The complex structure and the small dimensions result in very strict requirements for the mechanical stability of the system. Metal structures that are exposed to mechanical stress may show deformation if the stress increases above a certain level. Under normal production and operation conditions this level is globally not exceeded. However, locally stress gradients may build up and copper migration phenomena can be observed. This migration can lead to void formation and, in the case of thin lines, to interrupted lines, which will cause device failures. Current interpretations and simulations [1] of stress formation and stress driven migration are based on bulk properties and often do not implement parameters that are important for nanoscale structures, e.g. a split of the diffusion rate in grains, grain boundaries and interfaces. Therefore, new models have to be developed and verified with experimental data. Mechanical stress measurements for nanoscale microelectronic devices are mostly unpractical and destructive, like the drill hole method, or not locally sensitive, like the wafer bow method. XRD stress measurements are non-destructive and offer a good spatial resolution below 100 µm.

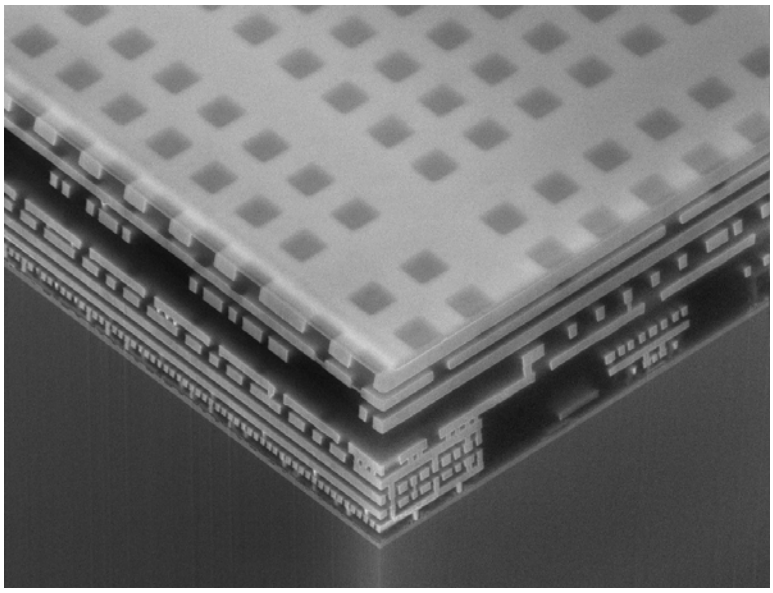

Fig. 1: FIB-Cut of a copper interconnect structure on a modern microprocessor device. The structure scales vary between several µm for power planes and less than 150 nm for high-speed interconnects (courtesy of MALab, AMD Saxony, Dresden).

Experimental

The illuminated area even in µ-XRD is much larger than a single structure, which gives a good averaging of the stress distribution, but also requires specially designed samples. A test mask set allowed the production of large arrays of parallel copper lines with different widths. The different samples were mounted onto a miniaturised heating stage (Anton Paar), that was fixed to the ROBL six-circle diffractometer [2] (Fig. 2). Exact sample positioning was enabled by a newly installed microscope video camera pointing at the diffractometer centre. The small dimensions of the heating stage allow a large degree of freedom for sample rotation in φ (azimutal angle around the sample surface) and χ (Eulerian cradle angle around the incoming beam). For the stress evaluation the Cu(311) reflection at $2\theta = 89.943°$ (for Cu-Kα radiation) was chosen, as the shadowing of the incoming beam by the Eulerian cradle prevents the measurement of higher reflections.

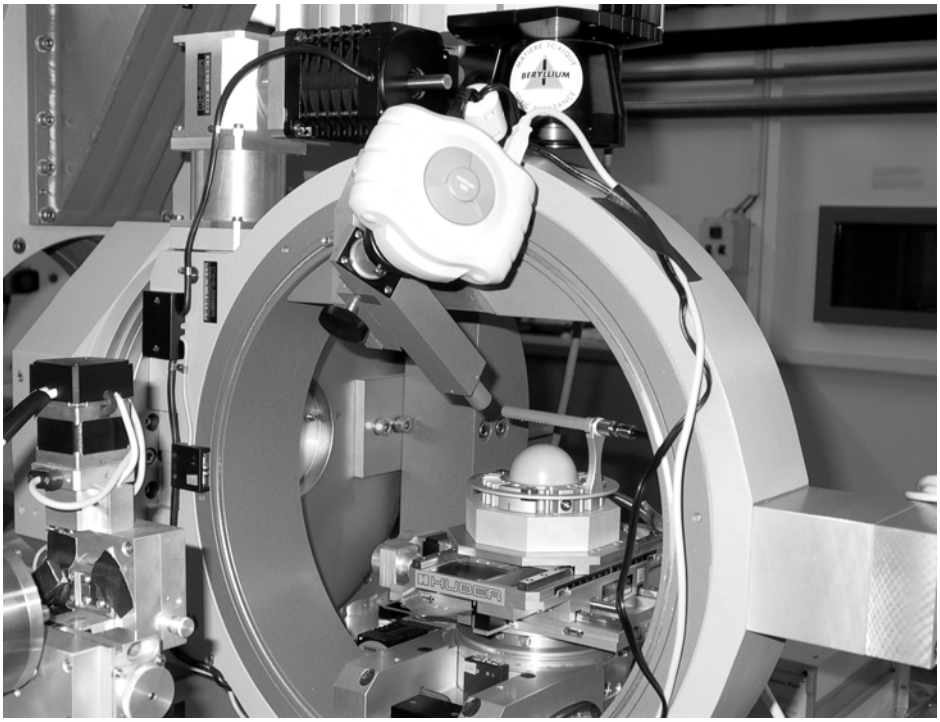

Fig. 2: Experimental set-up for *in-situ* high temperature µ-beam synchrotron radiation stress measurements.

The stress calculations from the experimental data were done with the GADDS software (Bruker-AXS) stress evaluation option. In general, the fundamental stress equation in a 3-dimensional approach has six unknown variables and can be resolved by six independent measurements. XRD stress measurements often try to reduce the necessary data amount by a limitation to a 2-dimensional approach. With the use of synchrotron radiation and the benefits of an area detector, data collection can be extended to a wide range in diffraction space. Instead of a simple solving of the equation, a full fit with 480 data points is used, and gives a representative high precision 3-dimensional stress state. The sample was aligned in a way, that S_{11} represents the stress along the line, S_{22} is the stress across the line and S_{33} stands for out-of-plane stress. Two different arrays with parallel lines were measured, small lines with 0.18 µm line width and wide lines with 1.8 µm line width, respectively. Additionally, two different low-*k* dielectrics were examined as references.

Results and discussion

At first, the general form of a stress-temperature-curve for the in-plane stress S_{11} and S_{22} is discussed: All curves can be divided into three different regions (Fig. 3). In the low temperature regime, the copper structures show tensile stress in the range of 200-350 MPa. With rising temperature the stress decreases nearly linearly and reaches zero-stress at a certain temperature.

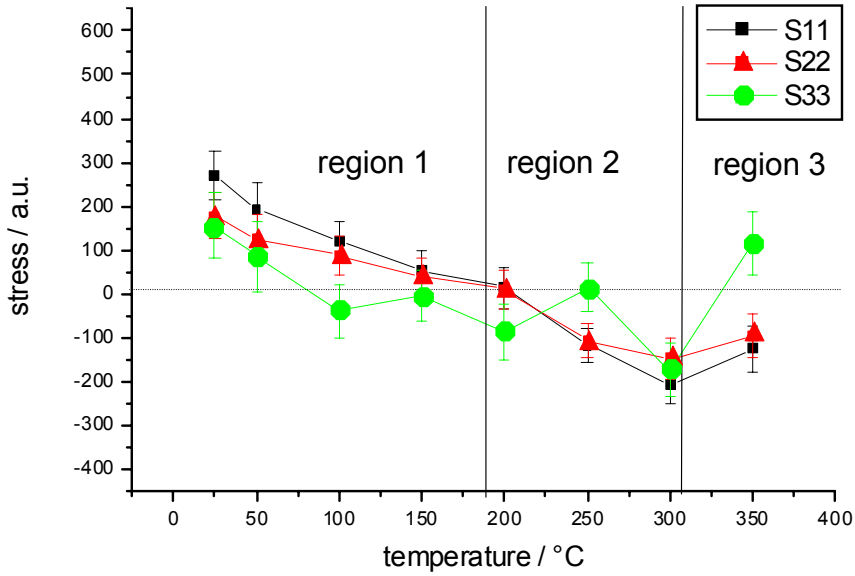

Fig. 3: Stress-temperature curve of an array with 0.18 µm lines in low-*k* copper inlaid interconnect technology.

One point to remark in this first region is the decrease of the error with increasing temperature. This effect is caused by two special conditions unique to this kind of measurements. First, the used method of data evaluation determines that the error is mainly effected by the quality of the experimental data fit, and second, the small spot size of 100 µ-XRD gives a less averaged signal. Strain variations between grains are normally averaged by a wide and higher divergent beam and will only result in peak broadening without any effect on the peak centre. The synchrotron beam has a very low divergence and only grains, that fulfil the Bragg conditions exactly, contribute to the diffraction signal. Also within the µ-beam, the number of grains illuminated is limited and so a variant stress state of some grains can shift the peak centre. The variance of the peak position is then interpreted as a fit error, but in fact gives additional information on the homogeneity of the stress distribution in the sample. This means, that with rising temperature not only the value of the overall stress decreases, but also the differences between the grains is levelling out.

Those effects of the low divergence µ-beam also have a large impact on the measurement set-up. Performing the measurements with a conventional point detector, symbolised in Fig. 4, will only give the strain values of very discrete portions of the sample. In this case, although the resulting stress values are correct, they are certainly not representative for the sample as a whole.

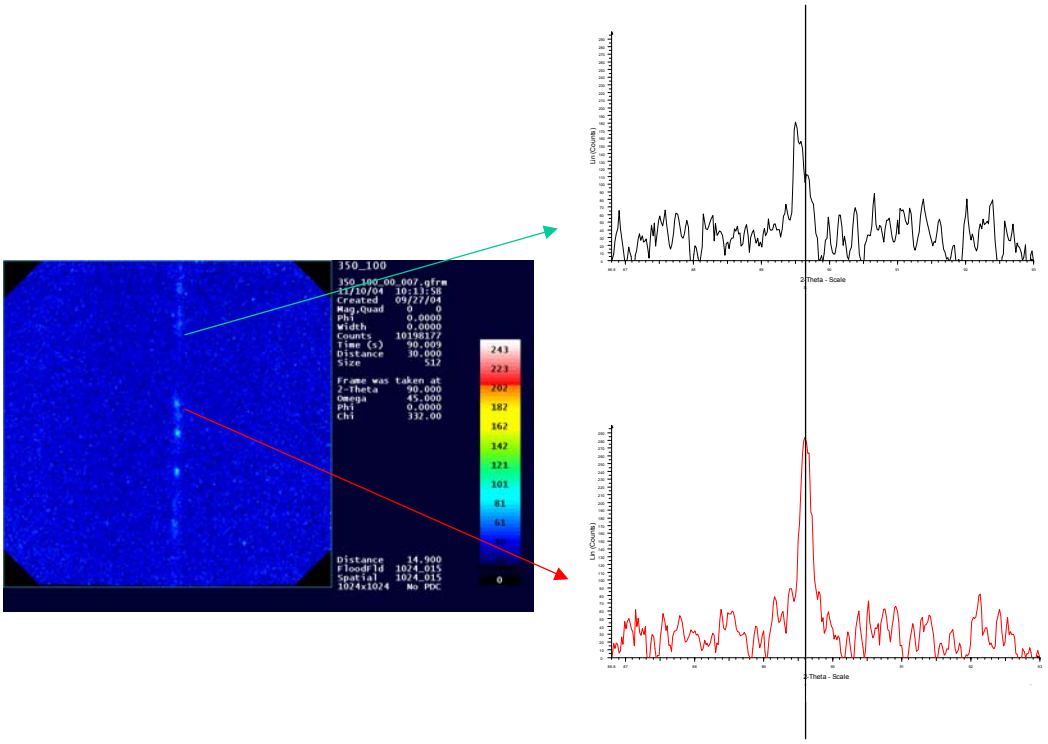

Fig. 4: Raw data from a 2-dimensional detector (left): Small intensity spots (bright spots in the left frame) can show large variations in the scattering angle 2θ when measured by a point detector (symbolised by a vertical cut, right top and bottom) compared to the total signal overviewed by an area detector. Thus, stress evaluation from point detectors may not be representative for a sample as a whole.

The point of zero stress is a parameter characteristic for the material's properties and the process parameters applied to the sample. If a simple mechanical model is used, where a layer is deposited stress free at a specific temperature and then cooled down, the point-of-zero stress should be equivalent to the deposition temperature. A shift of this parameter indicates stress relaxation processes that were induced e.g. by grain growth during an annealing step. Materials properties of the surrounding environment can have a *direct* influence, like a degradation with volume shrinking, or an *indirect* influence, like a change of the copper grain size and texture.

At temperatures above the point-of-zero stress, the stress inside the structures becomes compressive. This second region (i.e. region 2 in Fig. 3) seems to be very appealing with respect to stress migration reliability, as every void formed should be automatically filled under compressive stress and line failures should be impossible. Unfortunately, the compressive stress also has a negative effect. Any weak point in the barrier or cap layer can lead to copper extrusions and can cause a line short-circuit. This is especially a problem for copper lines with current flow, as the current additionally increases the compressive stress locally. For this reason, tensile stress in the copper structures is generally preferred under operating temperatures.

The error-bars of the stress start to increase again in this second region. Inspection of the raw diffraction data shows, that the reason for this increase is different from the first low temperature region. The peaks are broadening significantly with rising temperature as it is expected, but an increase of stress inhomogeneity with clearly separated variations in 2θ for the centre of the Bragg-spots as it is the case for low temperatures was not observed.

At high temperatures (region 3), the slope of the curve starts to flatten out, until finally a constant (compressive) level is reached. In this region, the diffusion of the Cu atoms is fast enough to start stress relaxation processes. As already mentioned, the compressive stress together with the high Cu diffusion can lead to extrusions at those temperatures. Another critical point under these conditions is the stability of the dielectric. Low-*k* materials are organo-silicate glasses and the organic content can degrade at high temperatures leading to shrinking. This will have a very negative impact on the mechanical stability and might corrupt the whole structure.

The out-of-plane stress S_{33} shows a special behaviour: it reaches a point of zero stress much earlier and stops to decrease further. Furthermore, the values start floating around zero and increase again at higher temperatures. There are two main explanations to be considered. First, the measurement geometry and the high degree of texture result in a much lower number of peaks available for the measurements in the S_{33} direction. The error of these values within 60-100 MPa is twice or three times higher. If this high error is taken into account, the slope of the stress-temperature-curve between 50°C and 300°C can be considered to be normal. The high tensile stress at 350°C, however, cannot be explained by a higher error: in this case degradations of the structure seem to cause this effect. The out-of-plane stress S_{33} is most sensitive for degradation phenomena, as the upper interface of the line is covered with SiN/SiO_2 only. This interface shows a lower adhesion strength compared to the Cu/Ta interface on the bottom and sidewalls and has already been identified as a weak point for electromigration [3].

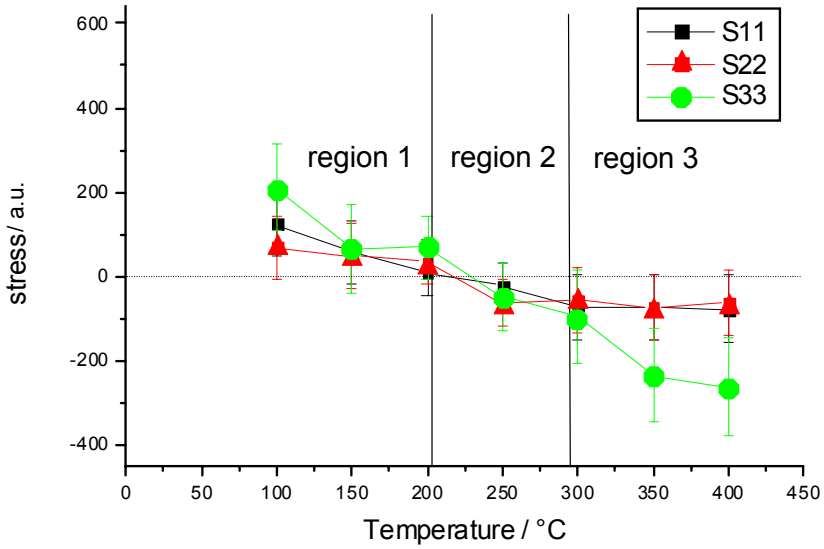

Fig. 5: Stress-temperature curve of an array with 1.8 µm lines in low-*k* copper inlaid interconnect technology.

The line widths have an effect on the room temperature stress state: Wide lines show no significant difference in stress for the in-plane directions S_{11} and S_{22} (Fig. 5). In small lines, however, the value across the line is always lower than along the line (Fig. 3). The measurement of stress-temperature-curves showed, that, additionally, the slope of stress is also lower across small lines, and that in fact the point of zero stress is not affected by the geometry. It also turned out, that at low or only slightly higher temperatures the stress is not identical for the different directions, and that stress gradients due to geometry are present and have to be considered for device reliability.

The effect of different interlayer dielectrics, liner and etch stop layers on the room temperature stress state has already been evaluated [4]. For temperature dependent measurements two different low-k materials with slightly different Young`s modulus and hardness were available. The measurements showed differences between the samples in the low temperature regime, but the effect was too small for a clear interpretation. In general, in low-k structures the liner and capping layer materials have a higher influence on the copper stress state than the low-k materials properties themselves. In the high temperature regime one sample showed less variation in S_{33}, which means less degradation, but for an unambiguous interpretation the number of measured samples was too low.

Summary and conclusion

A new set-up for *in-situ* high temperature stress measurements was tested and successfully used for low-*k* copper inlaid structures. The use of a synchrotron µ-beam (approximately 100 µm) together with a 2-dimensional detector enables *in-situ* measurements of small structures at a reasonable time, which is impossible in any laboratory set-up, and can even be extended to very fast, time dependent experiments in the future. The experimental set-up at ROBL Materials Research with an area detector is ideal for small spot measurements of highly textured samples, as errors due to the lack of proper grain statistics can easily be avoided. The measurements give very important information on the mechanical properties of the device system and processes of stress relaxation or sample degradation at elevated temperatures.

Acknowledgements

The authors wish to thank U. Strauch for his technical support and assistance during the measurements in Grenoble.

References

[1] W. Matz, N. Schell, G. Bernhard, F. Prokert, T. Reich, J. Claußner, W. Oehme, R. Schlenk, S. Dienel, H. Funke, F. Eichhorn, M. Betzl, D. Pröhl, U. Strauch, G. Hüttig, H. Krug, W. Neumann, V. Brendler, P. Reichel, M. A. Denecke, N. Nitsche, *ROBL – a beamline for radiochemistry and materials research at the ESRF*, *J. Synchrotr. Rad.* **6** (1999) 1076

[2] E.S. Ege, Y.-L. Shen, J. Electr. Materials **32** (10) (2003) 1000

[3] V. Sukharev, E. Zschech, *A model for electromigration-induced degradation mechanisms in dual-inlaid copper interconnect structures: Effect of interface bonding strength*, Integrated Reliability Workshop, IEEE 2004, Lake Tahoe, CA, USA, October 18-24, 2004

[4] H. Prinz, I. Zienert, J. Rinderknecht, H. Geisler, E. Zschech, P. Besser, *Micro XRD stress and texture study of inlaid copper lines – influence of ILD, liner and etch stop layer*, 7th Intern. Workshop on Stress-Induced Phenomena in Metallization, Austin, Texas, USA, June 14-16, 2004, AIP Proceedings **741** (2004) 207

2. Technical and Statistical Documentation

2.1. Technical status and developments

Overview and optical characteristics

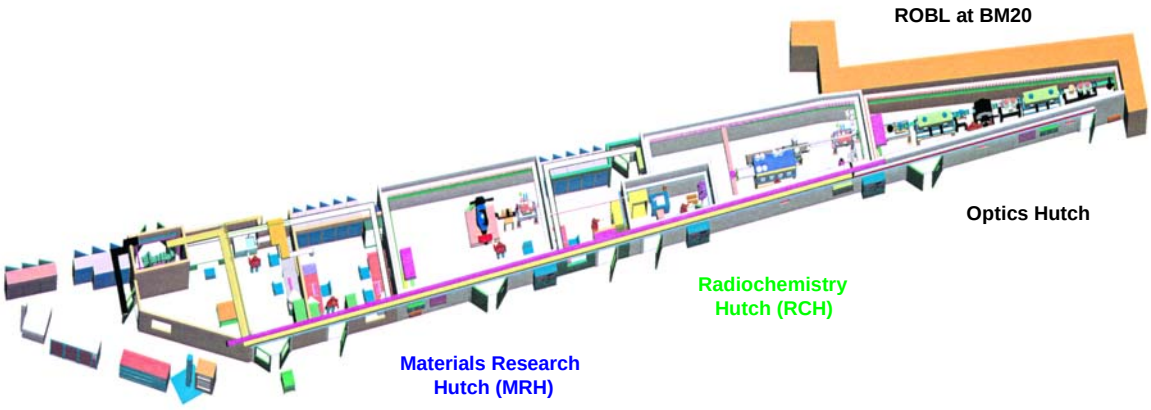

The optics with two mirrors and a double-crystal monochromator in fixed-exit mode provide both a high flux at high angular resolution (for diffraction) and a high flux over a wide energy range with high energy resolution (for EXAFS spectroscopy).

energy range	**5 – 35 keV**
with Si-mirrors	5 – 12 keV
energy resolution Si(111)	1.5 – 2.5 x 10^{-4}
energy resolution Si(311)	0.5 – 1.0 x 10^{-4}
integrated flux (calc.)	**$6 \cdot 10^{11}$ ph./s @ 20 keV at 200 mA**
standard beam size	20 mm (w) x 3 mm (h)
focussed beam size	≤ 0.5 mm x 0.5 mm

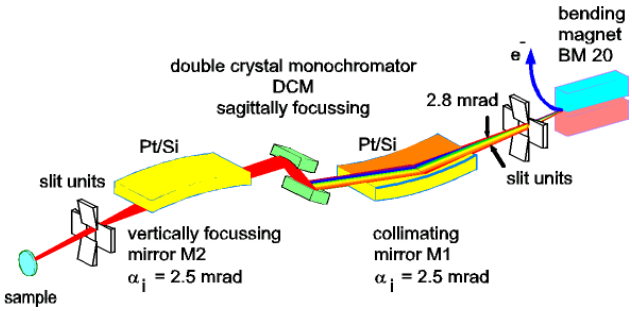

1a	2a	3b	4b	5b	6b	7b	8			1b	2b	3a	4a	5a	6a	7a	0
H																	He
Li	Be											B	C	N	O	F	Ne
Na	Mg											Al	Si	P	S	Cl	Ar
K	Ca	Sc	Ti	V	Cr	Mn	Fe	Co	Ni	Cu	Zn	Ga	Ge	As	Se	Br	Kr
Rb	Sr	Y	Zr	Nb	Mo	Tc	Ru	Rh	Pd	Ag	Cd	In	Sn	Sb	Te	I	Xe
Cs	Ba	La	Hf	Ta	W	Re	Os	Ir	Pt	Au	Hg	Tl	Pb	Bi	Po	At	Rn
Fr	Ra	Ac	Rf	Ha													

Lan	Ce	Pr	Nd	Pm	Sm	Eu	Gd	Tb	Dy	Ho	Er	Tm	Yb	Lu
Act	Th	Pa	U	Np	Pu	Am	Cm	Bk	Cf	Es	Fm	Md	No	Lr

The energy range allows to investigate the elements in yellow by K-edge EXAFS, and those in blue by L-edge EXAFS. Radionuclides permitted at the beamline are shown in red.

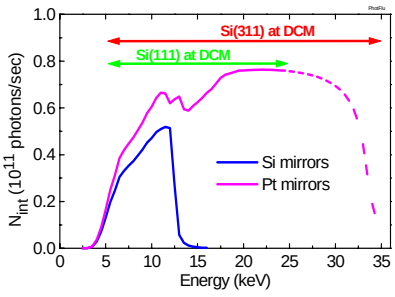

Energy range with different crystals and mirror materials (suppression of harmonics is excellent).

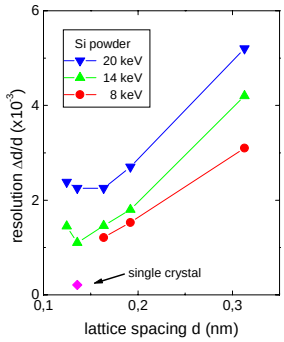

Experimental resolution with Si(111) from silicon powder.

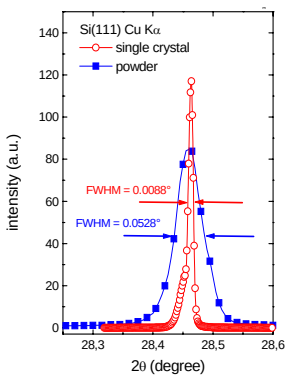

FWHM comparison.

Technical characteristics of the Radiochemistry station

The Radiochemistry experimental station is a highly specialized *unique* **radiochemical laboratory** designed for **radioecological research** (chemical speciation of radionuclides interacting with geological material, organics, and micro-organisms) using x-ray absorption spectroscopy (XAS) in transmission and fluorescence mode for solid and **liquid samples** with an activity of up to 185 MBq (5 mCi). A **multi-barrier safety concept** with separate ventilation, constant radiation monitoring and redundancy of all essential components was developed to satisfy legal requirements.

Tc-99	**Po-208**	**Po-209**	**Ra-226**	**Th-nat**	**Pa-231**
30,000	0.008	0.3	5	10^6	106
U-nat	**Np-237**	**Pu-238**	**Pu-239**	**Pu-240**	**Pu-241**
10^6	7000	0.3	80	22	0.049
Pu-242	**Am-241**	**Am-243**	**Cm-244**	**Cm-246**	**Cm-248**
124	1.4	25	0.062	17	1,156

List of **permitted radionuclides** and their maximum amount in mg (shown in blue).

Spectroscopic glove box with **closed-cycle He cryostat** (in blue) for sample temperatures >15 K. Sample cooling improves EXAFS quality, reduces beam damage of biological samples and reduces beam-induced changes of oxidation state.

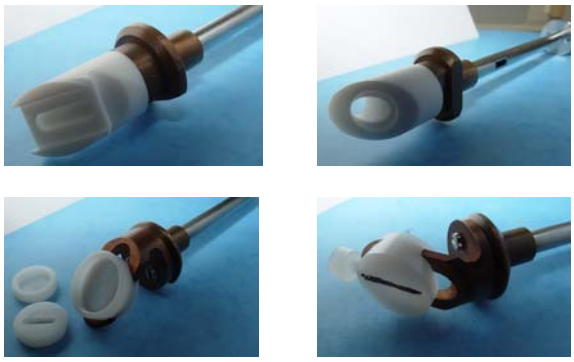

Sample holders fulfilling the necessary safety requirements exist in a wide variety to match different sample states.

13 element LEGe detector with high-rate digital multi-channel analysis spectrometer at the back side of the glove box for high count rates and reasonable energy resolution.

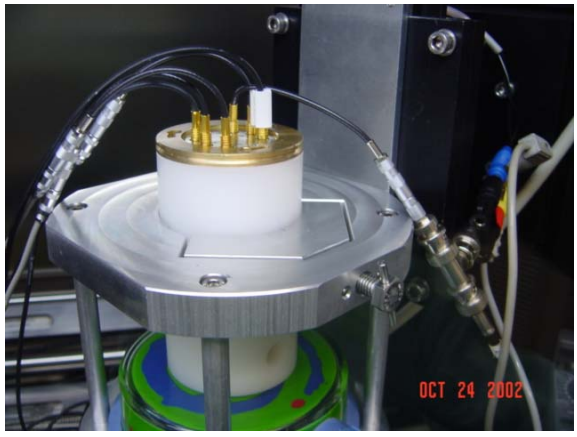

Spectro-electrochemical cell for in-situ redox modifications of aqueous and ionic liquids.

Technical characteristics of the Materials Research station

The materials research hutch MRH is designed for the **structural identification and characterisation of modifications of surfaces and interfaces produced by ion beam techniques** (e.g. hard covers, biocompatible materials, or for semiconductor technology) and the study of interfaces in thin films and nanometer multilayers using various x-ray diffraction techniques (XRD, GIXS) and reflectometry (XRR). A specific reference can be found in [1] and at the website http://www.esrf.fr/UsersAndScience/Experiments/CRG/BM20/.

Detectors

scintillators	(Bede ERD)
PIN-diodes	(AMPTEK XRT-110T)
2-dim. CCD	(Bruker SMART)
x-ray eye	(Photonic Science)
lin. PSD	(Braun)
analyzer	(**C, Ge**)
channel-cut	(**Ge**)

Diffractometer (HUBER)

6 circles	(0.001^{o})
x-y-z table	(±75/75/12 mm; 10/10/1 μm)
15 kg load	(at sample position)
za	(-200 / +50 mm)

ML mirror / deflector
(Osmic W/B4C)

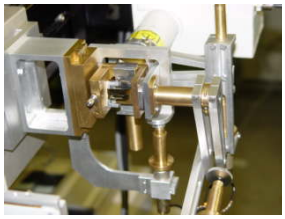

ITME **Ge channel-cut**.

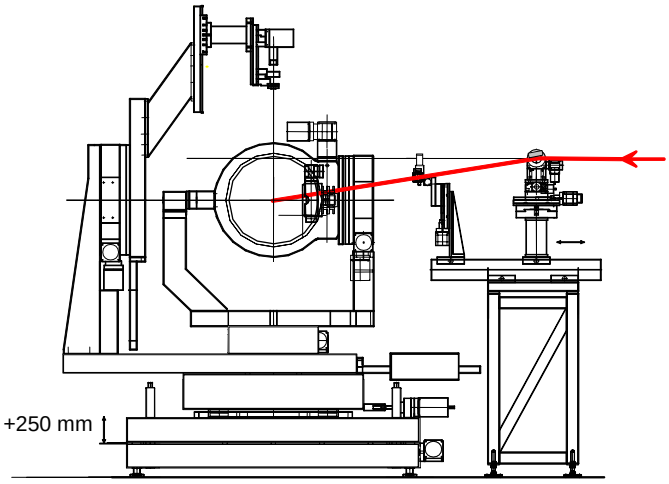

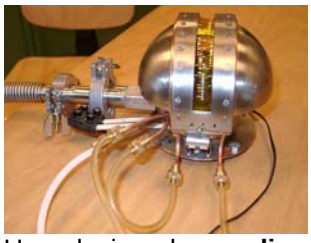

User designed **annealing chamber for reactive gas**.

Sample chambers **annealing** (in reactive gas, for metals, and for semiconductors)
sputter deposition

Commercial **high temperature** chamber (Otto) for annealing up to 2000°C in vertical scattering geometry.

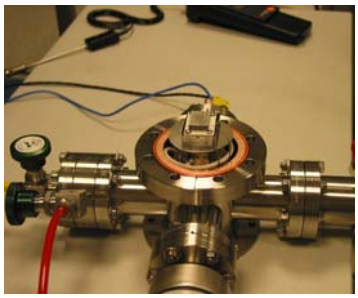

In-house designed chamber for moderate annealing (< 900°C) with **hemispherical Be-window**, i.e. 2π x-ray access for GIXS.

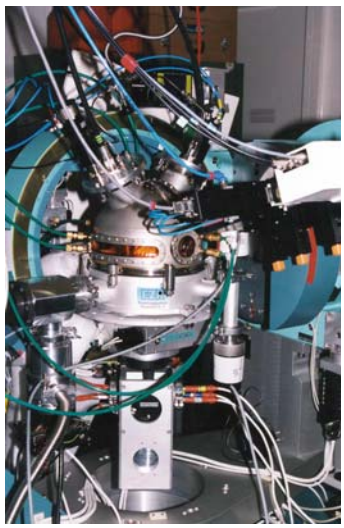

In-situ **two magnetrons sputter deposition** chamber (**Aarhus** collaboration).

[1] N. Schell, W. Matz, F. Prokert, F. Eichhorn, and F. Berberich, *Synchrotron radiation studies of thin films and implanted layers with the materials research endstation of ROBL.* J. Alloys & Comp., **328** (2001) 105-111.

Improving the detection limit of the Radiochemistry end-station

W. Oehme[1], S. Dienel[1], J. Claussner[1], U. Strauch[2], Ch. Hennig[3], A. C. Scheinost[3]
[1] Department of Research Technology
[2] Project Group Rossendorf Beamline at ESRF
[3] Institute of Radiochemistry
Forschungszentrum Rossendorf eV, P.O. Box 510119, 01314 Dresden, Germany

EXAFS spectroscopy is the method of choice for chemical speciation in environmental samples, which are typically characterized by multi-elemental matrices and the presence of aqueous, sorbed and mineral species at the same time. Especially for elements like the actinides, which are toxic at even extremely low concentrations, one demand can never be fulfilled by EXAFS with full satisfaction: lower detection limits. Up to know, we could investigate uranium speciation in simple laboratory samples like kaolinite at concentrations below 100 mg/kg. However, first tests showed that uranium in a soil matrix needed to be present at concentrations above 1000 mg/kg to provide spectral quality sufficient for uranium speciation. The major problem was that the U-L3 fluorescence line in such samples was hidden behind the - often stronger - neighboring K-lines of Rb and Sr. Since many samples of interest contain uranium at maximum concentrations of 50 to 500 mg/kg, EXAFS spectroscopy could not be performed with the existing experimental setup. At this point, it was necessary to acquire a new multi-element detector with higher energy resolution without cutting down on count rate. The installation of this new detector involved not only electronic instrumentation and software development, but - due to the complex radiochemical safety installations at the Radiochemistry end-station - also mechanical engineering. This work which is described in the following has been performed by the Department of Research Technology at the FZR in collaboration with the Institute of Radiochemistry.

The new detector and its electronics

We acquired an advanced hard X-ray, 13-element LEGe detector (Canberra) [3]. Each of the elements has an active thickness of 10 mm and an area of 100 mm2. We have measured average energy resolutions of 156 and 311 eV at shaping times of 3 and 0.25 μs, respectively. The reset periods of the pre-amplifiers are in the range of 250 to 850 ms. The detector is equipped with a custom-designed, small multi-attitude cryostat to allow for multiple detector orientations in the narrow Radiochemistry hutch. The detector is equipped with an automatic LN2 filling station.

The detector is instrumented with a high-rate digital multi-channel analysis spectrometer from X-ray Instrumentation Associates (XIA) [6] which is particularly well suited for EXAFS with multi-element detectors. Each channel operates with a digitally-based X-ray processor (DXP). The DXP offers complete computer control over all amplifier and spectrometer controls including gains, shaping times, and pile-up inspection criteria. The DXP digital filter typically increases throughput by a factor of two over the available analog system at comparable energy resolution but at lower cost per channel.

Software development

The new 13-element Ge detector has been integrated in the measurement program XATROS [5] using the device server XIADS [7] developed at the ESRF. XATROS imports the functionality of this device server. XATROS provides functionality to perform scans and to check these detectors. Checks and settings of the SCAs (single channel analyzer) are supported by visualizations of the statistics parameters and the SCA limits and their contents/counts as text widgets (Fig. 1). Additionally there are mini views of the spectra of each of the thirteen channels. There is also the possibility to get a detailed graphical presentation of each of the thirteen channels. The SCA limits can be set both in the text widgets and in the graphical representation. XATROS is also able to switch easily between the new detector and its electronics and the older one which can be used alternatively.

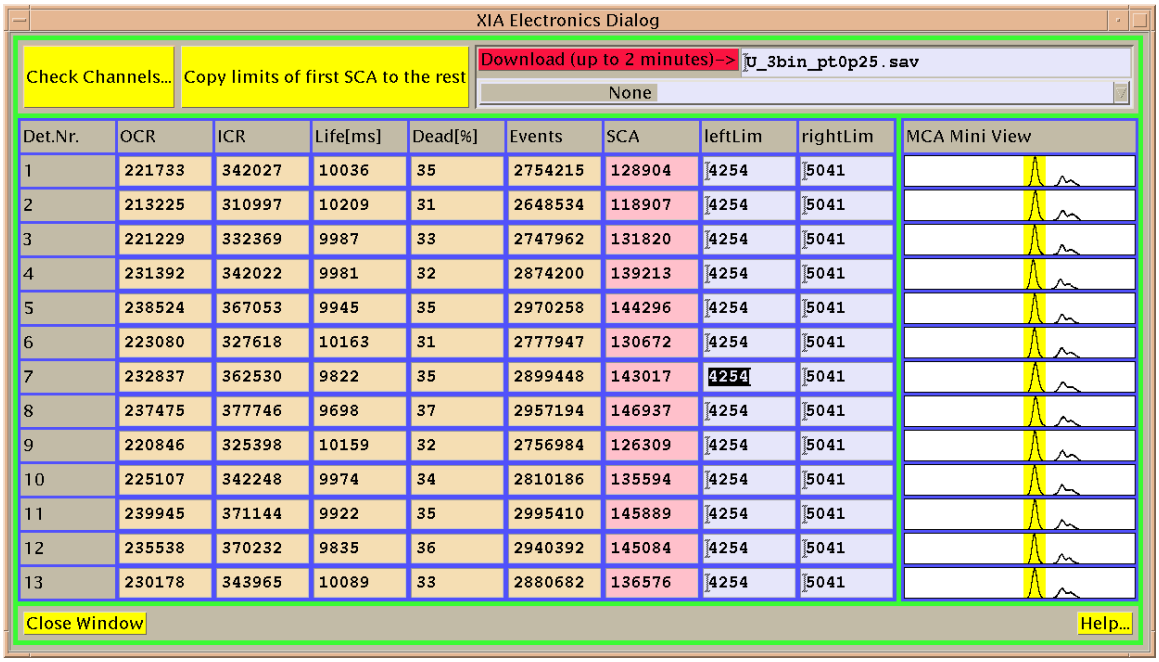

Det.Nr.	OCR	ICR	Life[ms]	Dead[%]	Events	SCA	leftLim	rightLim	MCA Mini View
1	221733	342027	10036	35	2754215	128904	4254	5041	
2	213225	310997	10209	31	2648534	118907	4254	5041	
3	221229	332369	9987	33	2747962	131820	4254	5041	
4	231392	342022	9981	32	2874200	139213	4254	5041	
5	238524	367053	9945	35	2970258	144296	4254	5041	
6	223080	327618	10163	31	2777947	130672	4254	5041	
7	232837	362530	9822	35	2899448	143017	4254	5041	
8	237475	377746	9698	37	2957194	146937	4254	5041	
9	220846	325398	10159	32	2756984	126309	4254	5041	
10	225107	342248	9974	34	2810186	135594	4254	5041	
11	239945	371144	9922	35	2995410	145889	4254	5041	
12	235538	370232	9835	36	2940392	145084	4254	5041	
13	230178	343965	10089	33	2880682	136576	4254	5041	

Fig. 1. Online visualization of the output of each of the 13 detector channels by the application software XATROS.

Upgrade of glovebox and positioning systems

The beamline's central glovebox with its negative air pressure gradient towards the Radiochemistry hutch has to present a safe sample confinement during the EXAFS measurements. This is realized by a bay-window extension of the box, which protrudes into the beam path (pink in Fig. 2). Beam transmission from the first ionization chamber (I0) to the sample inside the glove box, and then from the sample to the second and third ionization chambers again outside of the glove box is realized with Kapton windows. A third Kapton window behind the sample position and normal to the beam enables fluorescence detection by the fluorescence detector.

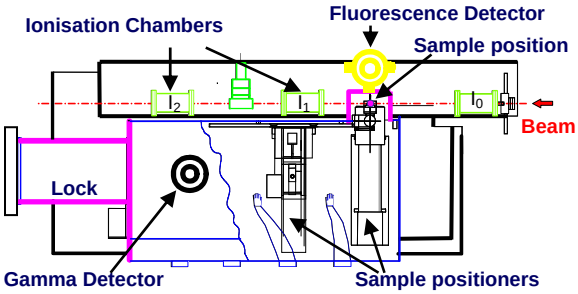

Fig. 2. New glove box design.

The new design had to fulfill several demands. First, simplification of the box interior to ease decontamination in case of a radioactive spill. Second, a larger fluorescence window to allow for an unrestricted, even illumination of all 13 detector elements. Third, a unification of the sample positioning system to ease exchange of the various sample holders, electrochemical cell and the cryostat, and to ease a potential decontamination of the box.

Point 1 was realized by creating a new box extension with a simpler cubic shape and without any further protruding parts. For point 2, we enlarged the diameter of all windows, not only to improve illumination of the fluorescence detector, but also to be able to have the beam and the sample as close as possible to the fluorescence detector for ultra-dilute samples. For point 3, we have extended and unified the control units for the positioning

systems (sample holders and detectors) inside and outside of the glove box. Generally, PEGASUS control units of the MICOS company [1] are now applied. By developing a new software (Device Server PEGASUS [2]) we ensured that these new systems could also be used inside of the existing software systems without the need to change them. A new sample positioning holder is still under development, which will avoid the use of two independent systems, and will be installed in 2005.

Gas flow controllers for the transmission detectors

To improve the sensitivity of the ionization chambers, a new panel with gas flow controllers for the automated and precise adjustment of gas compositions was installed [4]. Using He, N_2 and Ar gas, gas mixtures can be adjusted to have 15-20 % beam absorption in I_0 and 30-40 % beam absorption in I_1 and I_2.

First results

Figure 3 shows typical energy-dispersive XRF spectra of a uranium mine sample collected with the new detector. The uranium L3-line overlaps strongly with the K-line of Rb, and may be even influenced by a strong Sr K-line. Such a situation is quite typical for geological samples where feldspar and other K and Ca-rich minerals contribute to Rb and Sr concentrations in the low g/kg range. The XRF collected at an extended time of 60 s shows that that the U-L_3 line can be separated from the Rb and Sr K-lines using a relatively narrow SCA window. The shoulder can also be separated at a common EXAFS data collection time of 5 s. This is quite remarkable insofar as the shaping time of 0.25 μs represents the condition for optimum count rate, but the worst case in terms of energy resolution.

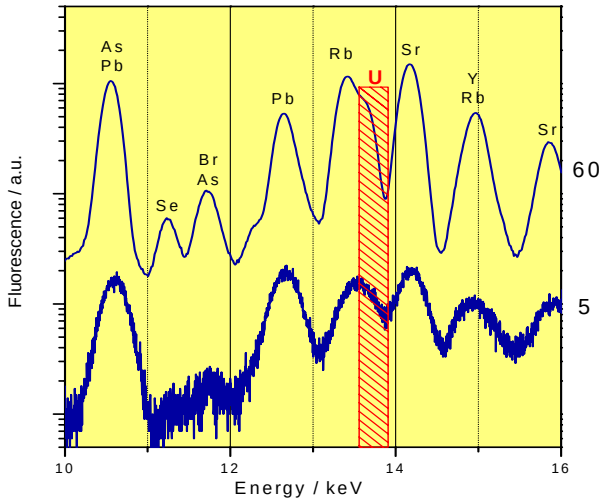

Fig. 3. Typical XRF of Freital mine tailing samples collected with the new detector using a shaping time of 0.25 μs.

The Experimental Report 20-01-626 in this volume demonstrates that EXAFS spectra of several samples from mine tailings and contaminated soils could be successfully collected within a reasonable data collection time (5-8 hours). In such difficult sample matrices we now routinely achieve a lower detection limit of 200 mg/kg uranium.

References

[1] MICOS GmbH: “Manual for SMC-taurus/pegasus”,V1.6, Technical Documentation
[2] W. Oehme: “Description of the PEGASUS Device Server”, ROBL Internal Report, 2003
[3] Canberra Industries: “Germanium Detector - User's Manual”, Technical Documentation, 2001
[4] Bronkhorst HI-TEC: ”Instruction Manual Flow-Bus Interface”,Technical Documentation no.: 9.17.024E, 2003
[5] W. Oehme, T. Reich, Chr. Hennig: “XATROS -User's Guide”, ROBL Internal Report, 2003
[6] X-ray Instrumentation Associates (XIA): “User's Manual Digital X-ray Processor”, Model DXP-2X, Revision A, 2002
[7] E. Papillon: “XIA2X Device Server User Guide”, ESRF/Grenoble, Internal Documentation, 2003

Technical development at the Materials Research end-station

W. Oehme[1], S. Dienel[1], U. Strauch[2], F. Eichhorn[3], N. Schell[3]
[1] Department of Research Technology
[2] Project Group Rossendorf Beamline at ESRF
[3] Institute of Ion Beam Physics and Materials Research
Forschungszentrum Rossendorf, P.O. Box 510119, 01314 Dresden, Germany

Introduction

This report summarizes the most important technical development realized during the last two years in the field of experimental automation at the materials research end-station of ROBL. It has been carried out by members of the Department for Research Technology at the FZR in collaboration with the scientists in Grenoble and comprises special tasks in the fields of mechanical construction, electronic instrumentation and engineering, and particularly, software development. The main goals of these developments were:

- to increase the reliability of the components
- to integrate new equipment into the common experimental concept
- to contribute to a high degree of automation for unattended beamline mode
- to improve the visualization of results in real time.

General infrastructure

The previously used two independent workstations for optics and experimental control in the control cabin E2C were replaced by 2 SunRay-1 terminals each equipped with 18-inch LCD monitors connected to a new centralized workgroup server for the whole beamline (Sun-E250). This increased the reliability of the total system and reduced both noise and necessary space inside the cabin.

Software development

Using the PSD (linear position sensitive detector) a large amount of data is generated (up to 500 * 8k - 32 Bit per scan). This data is stored in a *spec*-typical format [1] which in this form is not easy to analyze *after* and practically impossible to evaluate *during* the experiment. This, however, is important in order to correct any spurious effects for optimization of the experiments in real time. For this reason the following three programs were developed in collaboration with scientists of the Institute of Ion Beam Physics and Materials Research:

1. ***mcaView*** [2]**:** This program is based on a professional XRT/3d-Widget [3] and presents the measured data in a hardware-like manner. The angles of the scan and the channel numbers of the MCA (multi channel analyzer) are taken as the *X*- and *Y*-axes. The counts of the MCA channels are drawn in *Z* direction. The data can be presented in different modes according to the predefined facilities of the XRT/3d-Widget. The most preferable mode is the *contour plot* in a 2D manner with the *Z* values presented in a color scale (see Fig. 1). Since presenting the data in a 3D manner can be very time-consuming, an automatic binning is performed depending on the amount of data to be presented. The program can be used in a *quasi-online* mode and also *offline* (for later data analysis and representation). *Quasi-online* means: The measurement performed by the program spec and *mcaView* are two completely different processes. They only share the same data file. At every time the length of this data file changes, *mcaView* would perform a new presentation.

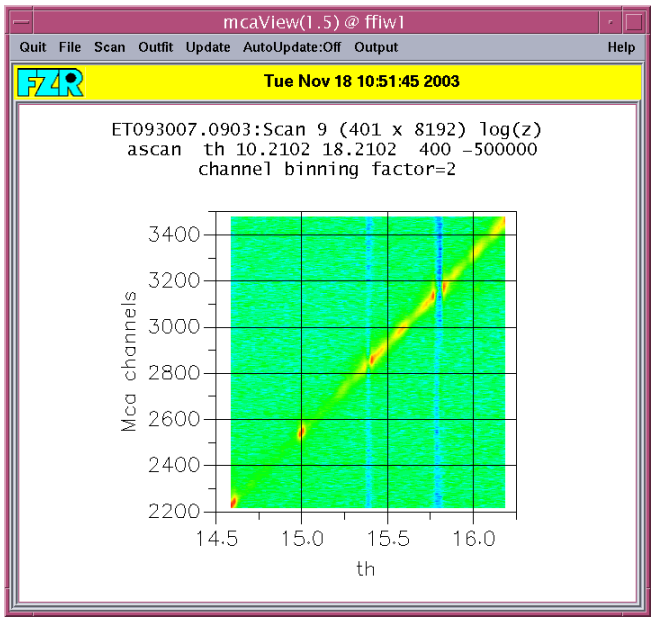

Fig. 1: Example of mcaView's output in contour mode.

2. ***psdView*** [4]: Based on the application *mcaView*, a second application was developed that performs a reciprocal space mapping (RSM). In this way the data can be presented angle-independent often better comparable to literature representations. The data had to be represented as pixel graphics in reciprocal space co-ordinates calculated from the diffractometer scattering angle and predefined calibration parameters of the PSD via

$$tth_{PSD} = tth_{GON} + (PSD_{channel} - PSD_{centre}) / PSD_{slope} \quad \text{and}$$

$$Q_x = 2\pi / \lambda * (\cos th_{GON} - \cos (tth_{PSD} - th_{GON})) \quad [1/nm]$$
$$Q_z = 2\pi / \lambda * (\sin th_{GON} + \sin (tth_{PSD} - th_{GON})) \quad [1/nm]$$

with the zero point PSD_{centre}, the resolution PSD_{slope}, and the wavelength λ taken from a *selection dialogue box*. Each measured value belonging to such a Q_x-Q_z-tuple is transformed into a scale of 100 colors either in a *linear* or in a *logarithmic* manner. Depending on the size of the window on the screen and the chosen clipping, the Q_x and Q_z co-ordinates have to be mapped into pixel positions (since this mapping can lead to some measured values being shown at the same pixel, always the color belonging to the highest measured value is set). The program can be used in a *quasi-online mode*.

An example is shown in Fig. 2. The data come from measurements of a semiconductor superlattice of 100 double layers, each of which consists of 5 nm GaAs and 7 nm $Al_{0.3}Ga_{0.7}As$, deposited by MOCVD (Metal Organic Chemical Vapor Deposition) on GaAs and measured in the neighbourhood of the GaAs(002) reflection. The nearly equidistant points (stripes, respectively) are the SL peaks of increasing interference order (counted from the centre).

3. ***psdConv*** is a Windows program which converts measured data stored in the *spec* dedicated format into text files by performing the same RSM as for *psdView*. It produces 3D-tuples in reciprocal space which can be used as input for a professional 3D program). Additionally, the generated data can be reduced by selecting a low limit value below which the data are not converted.

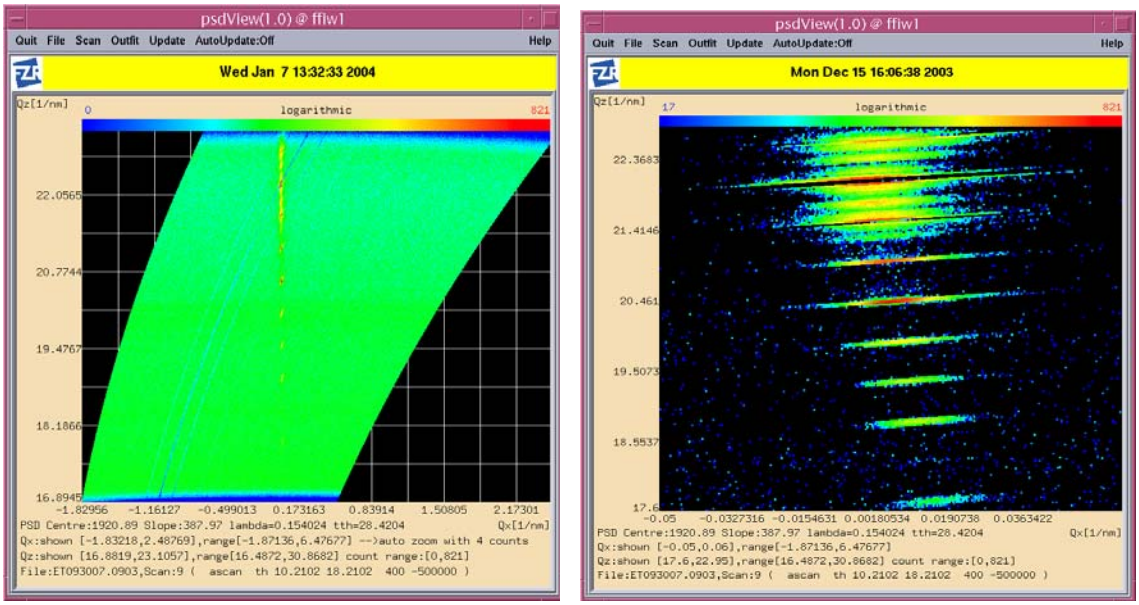

Fig. 2: Run visualization (left) of a rocking curve with the PSD of a GaAs/AlGaAs ML in the neighbourhood of the GaAs(002) reflection. The red and yellow points are SL peaks, the blue stripes are low-intensity artifacts. The zoomed presentation (right) uses 'large' pixels.

Electronic stepper motor controller switch

An example of electronic engineering is shown in Fig. 3. The 6-circle HUBER-diffractometer is controlled via dedicated electronics in *spec*™. But with the 2-dim. CCD detector SMART with its electronics from Bruker, the two systems use different types of stepper motor controllers. As some experiments are easier performed when directly programming the movement of the diffractometer via the SMART software, we have realized an alternative access to four of the axes of the diffractometer (required for the SMART system). We developed a special module drive in a control unit which can be switched between the two types of stepper motor controllers. The four modules offer switchable inputs which provide electronically compatibility to either SMART CONTROL or the VPAP-module in the VME-system and serve the drives of the diffractometer axes at their output. The main difficulty in was to keep the original compatibility to separate communication.

Fig. 3: Axes Switch Unit (left) and one of the controllers (right) developed in the Department of Research Technology of FZR.

References

[1] Certified Scientific Software, *spec*™ *X-Ray Diffraction Software*, User's Manual (2001)
[2] W. Oehme, *mcaView*, Internal Report ROBL (2003)
[3] KL Group Inc., *XRT/3d*™ *for Motif*, Programmer's Guide & Reference Manual, V2.1 (1994)
[4] W. Oehme, *psdView*, Internal Report ROBL (2003)

2.2. Beamline personnel

Head of the beamline / CRG spokesperson:	Andreas Scheinost	(-2462)
Responsible for MRH:	Norbert Schell	(-2367)
Responsible for RCH:	Andreas Scheinost	(-2462)
Responsible for Radiochemical Safety:	Christoph Hennig	(-2005)

	Name (phone)	Position/Education/Research Interests
	Manuela Strauch (-2463)	Secretary *(since 01.02.04)*
	Udo Strauch (-2372)	Beamline Technician
Radiochemistry	Harald Funke (-2339)	Beamline Scientist Ph.D. in Physics (1974), University of Moscow (Russia) application of wavelet analysis to EXAFS
	Christoph Hennig (-2005)	Beamline Scientist Ph.D. in Crystallography (1995), Universität Leipzig structure of uranyl complexes by XRD and EXAFS aqueous chemistry and electrochemistry of actinides
	Andre Rossberg (-2847)	Postdoc Ph.D. in Chemistry (2002), TU Dresden new methods for EXAFS analysis aqueous chemistry and sorption processes of actinides
	Andreas Scheinost (-2462)	Beamline Scientist Ph.D. in Agricultural Engineering (1994), TU München actinide speciation in soils, sediments and aquifers using XAS and complimentary methods
Materials Research	Valentina Cantelli (-2849)	Beamline Scientist (*since 01.10.03)* Masters in Physics (1995), University of Turin (Italy) characterizing of *in-situ* structurally modified thin magnetic materials
	Ana Cardoso (-2463)	Postgraduate student (*01.07.04 to 31.12.04)* Masters in Materials Engineering (2004), New University of Lisbon (Portugal) characterization of sputter deposited NiTi SMAs during annealing
	David Dekadjevi	Postdoc (*01.02.03 to 31.08.03)* Ph.D. in Physics of Condensed Matter (2001), University of Leeds (UK) HRXRD at semiconductor multilayers and quantum dot structures
	Rui Martins (-2872)	Ph.D. student (*since 01.11.03)* Masters in Materials Engineering (2004), New University of Lisbon (Portugal) characterization of the growth process of sputter deposited thin films (TiAlN hard coatings and NiTi shape memory alloys)
	Norbert Schell (-2367)	Beamline Scientist *(CRG spokesperson 01.04.02 to 31.03.04)* Ph.D. in Physics (1994), LMU München XRD *in-situ* film growth characterisation for magnetron sputter deposition

Postal address Rossendorf Beamline
(ROBL-CRG, BM20)
ESRF / sector 21
BP 220
F-38043 Grenoble cedex France

Phone: +33 (476) 88 xxxx
Fax: +33 (476) 88 2505
E-mail: surname@esrf.fr

FZR personnel involved in the scientific and technical programme

Department of Research Technology

Siegfried Dienel	Winfried Oehme	Jürgen Claussner

Institute of Ion Beam Physics and Materials Research

Manfred Beckers	Johannes von Borany	Frank Eichhorn
Jörg Grenzer	Ines Heidel	Joachim Kreher
Friedrich Prokert	Andrea Scholz	Natasha Shevchenko

Institute of Radiochemistry

Thuro Arnold	Gerd Bernhard	Heidemarie Friedrich
Gerhard Geipel	Alix Günther	Astrid Koban
Mandy Leckelt	Mohamed Merroun	Henry Moll
Cordula Nebelung	Johannes Raff	Anette Rumpel
Jörg Tutschku	Markus Walter	Kai-Uwe Ulrich

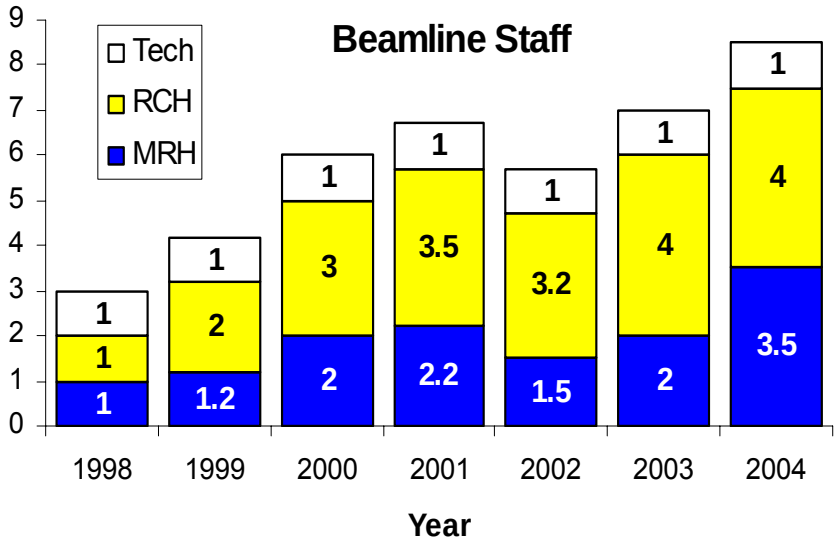

Fig. 3.1. Evolution of beamline personnel since 1998.

2.3. Beamtime allocation and user groups

In the past two years, a total of 74 experiments have been performed at the beamline (Table 4.1). For those experiments, a total of 1092 shifts have been delivered. About 76 % of the beamtime has been used for FZR in-house experiments, 24 % for ESRF experiments. In addition to the experimental shifts, 209 shifts have been used for the commissioning of new equipment and the development of new techniques. A total of 134 different users, including users from the FZR but excluding the beamline staff, have worked at the beamline in the past two years.

Table 4.1. Use of beamtime at the Rossendorf Beamline.

	Year	FZR shifts	ESRF shifts	Technical shifts	Experiments FZR / ESRF	Users
MRH	**2003**	195	72	53	9 / 6 = 15	24 / 8 = 32
	2004	172	69	90	10 / 5 = 15	22 / 13 = 35
RCH	**2003**	227	60	18	17 / 5 = 22	14 / 18 = 32
	2004	231	66	48	16 / 6 = 22	15 / 20 = 35
sum		**825**	**267**	**209**	**52 / 22 = 74**	**75 / 59 = 134**

Figure 4.1 shows the development of shift allocation from the last year of the construction period (1998) up to December 2004. Since 2000, beamtime usage has reached a plateau with the beamline running at full capacity. A higher fluctuation of in-house beamtime at MRH is counterbalanced by the number of technical shifts used for the development of new techniques and short staff experiments. Both end-stations used about the same amount of shifts, in accordance with the agreement between the Institute of Radiochemistry and the Institute of Ion Beam Physics and Materials Research at the FZR, which are the main supporters of the beamline.

267 shifts have been provided for ESRF experiments and 18 more will be provided in February 2005, i.e. within the ESRF scheduling period 2004/II. Thus, ROBL delivered the full maximum of 142 shifts per year agreed upon between the ESRF and the CRG beamlines. The ESRF had assigned three more experiments in 2003 and 2004 to the Radiochemistry end-station, which could not be performed because users were not able to prepare their samples in time for the experiments, or because samples contained traces of such radionuclides, which are not permitted at the beamline (usually strong gamma emitters).

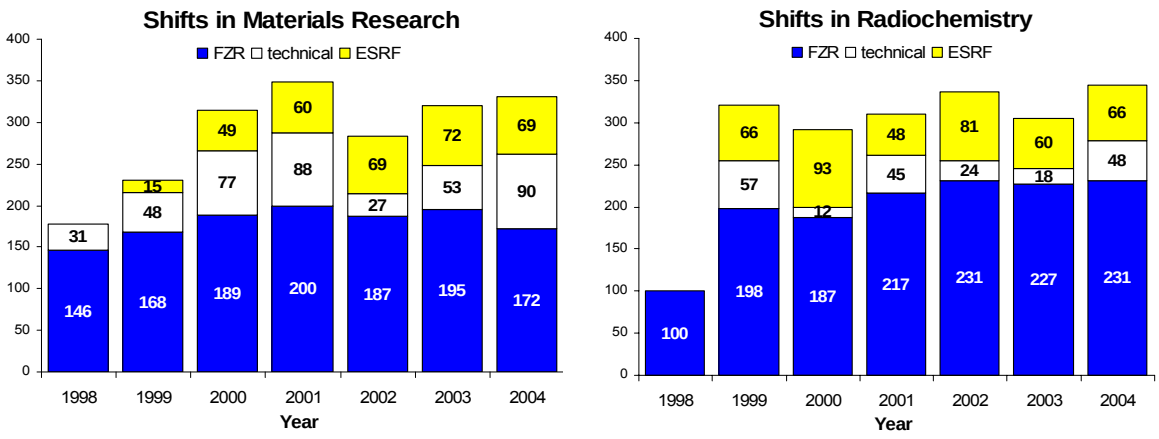

Fig. 4.1. Development of shift allocation for Materials Research and Radiochemistry since 1998.

The figure below shows the beamtime delivery of all CRG beamlines in 2003. The Rossendorf Beamline has delivered the greatest number of shifts per independent experimental station of all CRG beamlines. In the past years it has always been among the top three in terms of shift delivery.

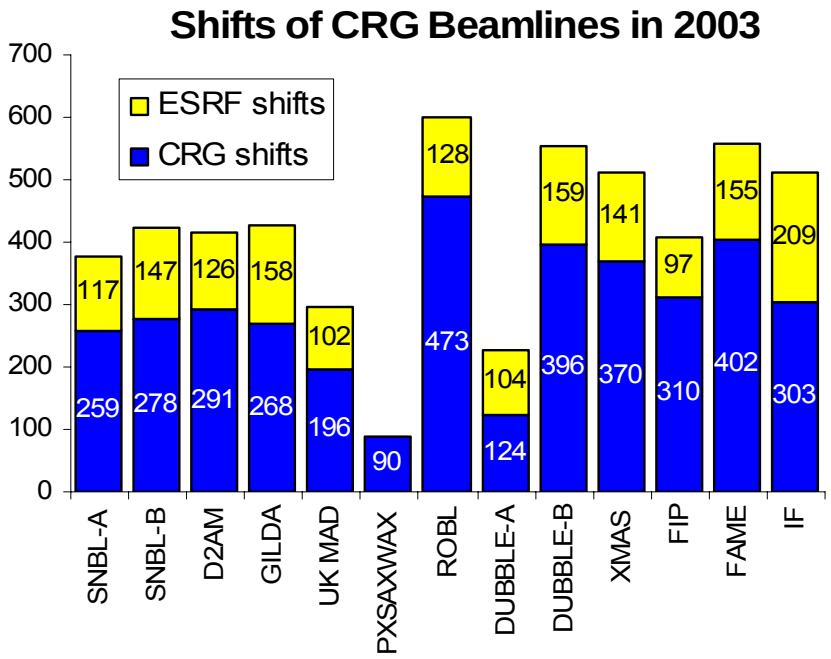

Fig. 4.2. Delivery of shifts for in-house (CRG) and ESRF experiments by the CRG beamlines of the ESRF (Courtesy ESRF User Office).

User Group Institutions

Germany

Advanced Micro Devices (AMD) Saxony, Dresden
Geoforschungszentrum Potsdam, Potsdam
Institut für Ionenstrahlphysik und Materialforschung, FZR, Dresden
Institut für Kernchemie, Universität Mainz, Mainz
Institut für Materialwissenschaft und Technologie der TU Berlin
Institut für Optik und Quantenelektronik, Friedrich-Schiller-Universität Jena, Jena
Institut für Radiochemie, FZR, Dresden

France

CEA Marcoule, Bagnols sur Cèze
CEA Valduc, Is sur Tille
Institut de Physique Nucléaire, Université Paris XI, Orsay
Institut Laue Langevin (ILL), Grenoble
IRES Strasbourg
Laboratoire GERMETRAD-CEA SMAB, Faculté des Sciences et des Techniques, Nantes
Laboratoire Subatech, Nantes

Other European Countries

CENIMAT F.C.T./Universidade Nova de Lisboa, Monte da Caparica, **Portugal**
Departement Interfasechemie, Katholieke Universiteit Leuven, Heverlee, **Belgium**
Department of Mechanical and Materials Engineering, Universidad Politecnica de Valencia, **Spain**
Institute of Inorganic Chemistry, KTH Stockholm, **Sweden**

Institute of Electronic Materials Technology, Warsaw, **Poland**
Institut für Halbleiterphysik, Johannes Kepler Universität, Linz, **Austria**
Institute for Materials Sciences, University of Leoben, **Austria**
Institute of Condensed Matter Physics, Masaryk University, Brno, **Czech Republic**
Institute of Materials Science and Engineering, Technical Univeristy of Szczecin, **Poland**
Institute of Physics and Astronomy, University of Aarhus, Aarhus, **Denmark**
Institute for Terrestrial Ecology, ETH Zuerich, Schlieren, **Switzerland**
Swiss Federal Institute of Environmental Science and Technology, Dübendorf, **Switzerland**
Institut für Werkstoffkunde der TU Wien, **Austria**
Laboratory for Micro- and Nanotechnology, Paul Scherrer Institute, Villigen, **Switzerland**
Nuclear Physics Institute, Rez, **Czech Republic**
Polytechnical University of Catalonia, Barcelona, **Spain**
QuantiSci, Avda Universitat Autonoma, Cerdanyola, **Spain**
Waste Management Laboratory, PSI, Villigen, **Switzerland**

Japan

Faculty of Environmental Engineering, Kitakyushu Univ., **Japan**

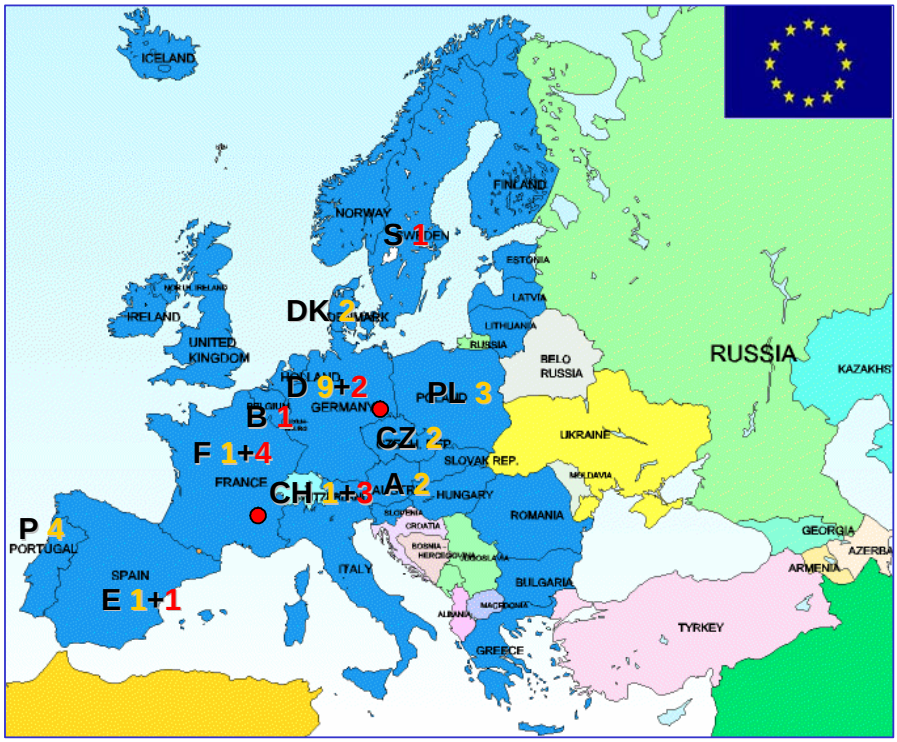

Fig. 4.3. Country specific distribution of the different experiments done at ROBL (in red color for RCH and in yellow for MRH). Only external user groups or FZR collaborations are listed, i.e. no pure FZR in-house experiments.

2.4. Publications

This section lists publications which are based on experiments at the Rossendorf Beamline, independent of whether they have been performed using in-house or ESRF allocated shifts. Only peer-reviewed articles and publications have been taken into consideration. Figure 5.1 gives an overview on the publication activities during the last 6 years, i.e. since the commissioning of the beamline.

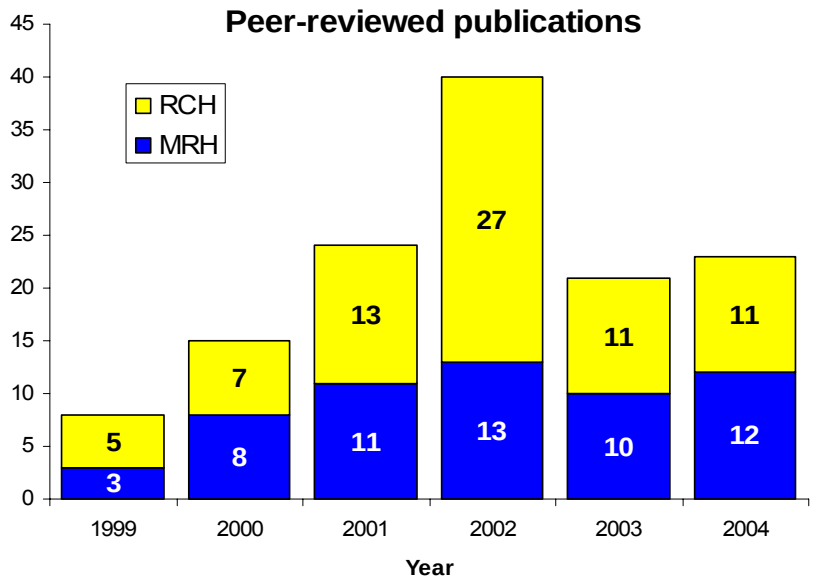

Fig. 5.1. Peer-reviewed publications in Materials Research (MRH) and Radiochemistry (RCH) since 1999, the first year of operation.

2.4.1. Publications in Radiochemistry

Den Auwer, C., Drot, R., Simoni, E., Conradson, S.D., Gailhanou, M., and Mustre de Leon, J.
Grazing incidence XAFS spectroscopy of uranyl sorbed onto TiO_2 rutile surfaces
New Journal of Chemistry **27** (2003) 648-655

Günther, A., Bernhard, G., Geipel, G., Reich, T., Rossberg, A., and Nitsche, H.
Uranium speciation in plants
Radiochimica Acta **91** (2003) 319-328

Hennig, C., Reck, G., Reich, T., Rossberg, A., Kraus, W., and Sieler, J.
EXAFS and XRD investigations of zeunerite and meta-zeunerite
Zeitschrift für Kristallographie **218** (2003) 37-45

Lomenech, C., Simoni, E., Drot, R., Erhardt, J.-J., and Mielczarski, J.
Sorption of unranium(IV) species on zircon: structural investigation of the solid/solution interface
Colloids and Interface Science **261** (2003) 221-232

Martin, P., Ripert, M., Petit, T., Reich, T., Hennig, C., D'Acapito, F., Hazemann, J.L., and Proux, O.
A XAS study of the local environments of cations in (U, Ce)O_2
Journal of Nuclear Materials **312** (2003) 103-110

Merroun, M., Hennig, C., Rossberg, A., Reich, T., and Selenska-Pobell, S.
Characterization of U(VI)-Acidithiobacillus ferrooxidans complexes using EXAFS, transmission electron microscopy, and energy-dispersive X-ray analysis
Radiochimica Acta **91** (2003) 583-591

Moll, H., Geipel, G., Reich, T., Bernhard, G., Fanghanel, T., and Grenthe, I.
Uranyl(VI) complexes with alpha-substituted carboxylic acids in aqueous solution
Radiochimica Acta **91** (2003) 11-20

Moyes, L.N., Jones, M.J., Reed, W.A., Livens, F.R., Charnock, J.M., Mosselmans, J.F.W., Hennig, C., Vaughan, D.J., and Pattrick, R.A.D.
Reactions of neptunium with mackinawite
ESRF Highlights 2002 (2003) 39-41

Roßberg, A., Reich, T., and Bernhard, G.
Complexation of uranium(VI) with protocatechuic acid - application of iterative transformation factor analysis to EXAFS spectroscopy
Analytical and Bioanalytical Chemistry **376** (2003) 631-638

Schmeide, K., Sachs, S., Bubner, M., Reich, T., Heise, K.H., and Bernhard, G.
Interaction of uranium(VI) with various modified and unmodified natural and synthetic humic substances studied by EXAFS and FTIR spectroscopy
Inorganica Chimica Acta **351** (2003) 133-140

Walter, M., Arnold, T., Reich, T., and Bernhard, G.
Sorption of uranium(VI) onto ferric oxides in sulfate-rich acid waters
Environmental Science & Technology **37** (2003) 2898-2904

Chukalina, M., Funke, H., and Dubrovskii, Y.
Wavelet analysis: application to tunnel- and x-ray spectroscopy
Low Temperature Physics **30** (2004) 1235-1243

Chukalina, M., Golosio, B., Simonovici, A., and Funke, H.
A study of the accuracy problem in x-ray fluorescence tomography
Spectrochim. Acta **B 59** (2004) 1755-1758

Koban, A., Geipel, G., Rossberg, A., and Bernhard, G.
Uranyl(VI) complexes with sugar phosphates in aqueous solution
Radiochimica Acta **92** (2004) 903-908

Kretzschmar, R., Pfister, S., Voegelin, A., and Scheinost, A.C.
Zinc speciation in an artificially contaminated soil: Formation of a new mineral phase within 3 years
Geochimica et Cosmochimica Acta **68** (2004) A361-A361

Livens, F.R., Jones, M.J., Hynes, A.J., Charnock, J.M., Mosselmans, J.F.W., Hennig, C., Steele, H., Collison, D., Vaughan, D.J., Pattrick, R.A.D., Reed, W.A., and Moyes, L.N.
X-ray absorption spectroscopy studies of reactions of technetium, uranium and neptunium with mackinawite
Journal of Environmental Radioactivity **74** (2004) 211-219

Maes, A., Geraedts, K., Bruggeman, C., Vancluysen, J., Rossberg, A., and Hennig, C.
Evidence for the interaction of technetium colloids with humic substances by X-ray absorption spectroscopy
Environmental Science & Technology **38** (2004) 2044-2051

Merroun, M., Raff, J., Rossberg, A., Hennig, C., Reich, T., and Selenska-Pobell, S.
Interaction of U(VI) with bacterial strains isolated form uranium mining piles: Spectroscopic and microscopic studies
Geochimica et Cosmochimica Acta **68** (2004) A499-A499

Moll, H., Stumpf, T., Merroun, M., Rossberg, A., Selenska-Pobell, S., and Bernhard, G.
Time-resolved laser fluorescence spectroscopy study on the interaction of curium(III) with Desulfovibrio aspoensis DSM 10631
Environmental Science & Technology **38** (2004) 1455-1459

Scheinost, A.C., Bernhard, G., and Selenska-Pobell, S.
Fate of uranium in the environment
Geochimica et Cosmochimica Acta **68** (2004) A526-A526

Scheinost, A.C., Rossberg, A., Hennig, C., Vantelon, D., Kretzschmar, R., and Johnson, C.A.
Quantitative antimony speciation in Swiss shooting range soils
Geochimica et Cosmochimica Acta **68** (2004) A521-A521

Stumpf, T., Hennig, C., Bauer, A., Denecke, M.A., and Fanghanel, T.
An EXAFS and TRLFS study of the sorption of trivalent actinides onto smectite and kaolinite
Radiochimica Acta **92** (2004) 133-138

Walter, M., Arnold, T., Geipel, G., Scheinost, A.C., and Bernhard, G.
An EXAFS and TRLFS investigation on uranium(VI) sorption to pristine and leached albite surfaces
Journal of Colloid and Interface Science **282** (2005) 293-305

2.4.2. Publications in Materials Research

Berberich, F., Matz, W., Kreißig, U., Schell, N., and Mücklich, A.
Mechanism of degradation of surface hardening at elevated temperature in TiAlV-alloys by in situ synchrotron radiation diffraction
Nuclear Instruments and Methods B **199** (2003) 54-58

Eichhorn, F., Schell, N., Mücklich, A., Metzger, H., Matz, W., and Kögler, R.
Structure of ion beam synthesized SiC nanocrystals in Si
ESRF Highlights 2002 (2003) 30-32

Linss, V., Halm, T., Hoyer, W., Richter, F., and Schell, N.
Analysis of the biaxial strain state of Al-doped c-BN films using diffraction experiments with synchrotron radiation
Vacuum **70X** (2003) 1-9

Martins, Rui M.S., Braz Fernandes, F.M., Silva, Rui J.C., Pereira, L., Marques, A., Gordo, P.R., Maneira, M.J.P., and Schell, N.
DSC and in-situ XRD annealing of shape memory nickel titanium sputtered thin films
Analele Universitatii "Dunarea de Jos" Galati – Fascicula IX Metalurgie si Stiinta Materialelor (May 2003) 26-30

Prokert, F., Schell, N., and Gorbunov, A.
Use of anomalous scattering for synchrotron x-ray reflectivity studies of Fe-Cr and Co-Cu double layers
Nuclear Instruments and Methods B **199** (2003) 123-127

Rinderknecht, J., Prinz, H., Kammler, T., Schell, N., Zschech, E., Wetzig, K., and Gessner, T.
In situ high temperature synchrotron radiation diffraction studies of silicidation processes in nanoscale Ni layers
Microelectronic Engineering **70** (2003) 226-232

Schell, N., Bøttiger, J., Matz, W., and Chevallier, J.
Growth mode and texture development in TiN films during magnetron sputtering – an in situ synchrotron radiation study
Nuclear Instruments and Methods B **199** (2003) 133-138

Schell, N., Jensen, T., Petersen, J.H., Andreasen, K.P., Bøttiger, J., and Chevallier, J.
The nanostructure evolution during and after magnetron deposition of Au films
Thin Solid Films **441** (2003) 96-103

Schell, N., Petersen, J.H., Bøttiger, J., Mücklich, A., Chevallier, J., Andreasen, K.P., and Eichhorn, F.
On the development of texture during growth of magnetron-sputtered CrN
Thin Solid Films **426** (2003) 100-110

Sztucki, M., Metzger, T.H., Milita, S., Berberich, F., Schell, N., Rouvière, J.L., and Patel, J.
Depth resolved investigations of boron implanted silicon
Nuclear Instruments and Methods B **200** (2003) 52-59

Abendroth, B., Gago, R., Eichhorn, F., and Möller, W.
X-ray diffraction study of stress relaxation in cubic boron nitride films grown with simultaneous medium-energy ion bombardment
Applied Physics Letters **85** (2004) 5905-5907

Andreasen, K.P., Jensen, T., Petersen, J.H., Chevallier, J., Bøttiger, J., and Schell, N.
The structure and the corresponding mechanical properties of magnetron sputteed TiN-Cu nanocomposites
Surface and Coating Technology **182** (2004) 268-275

Andreasen, K.P., Schell, N., Jensen, T., Petersen, J.H., Jensen, M.S., Chevallier, J., and Bøttiger, J.
On the development of the <111> fiber texture in nanocrystalline gold during growth and annealing
Materials Research Society Symposium Proceedings **788** (2004) 49-54

Dieter, S., Pyzalla, A., Bauer, A., Schell, N., McCord, J., Seemann, K., Wanderka, N., and Reimers, W.
Correlation between magnetic properties of CoFe single and CoFe/SiO_2 multi-layer thin films and their microstructure, texture and internal stress state
Zeitschrift für Metallkunde **95** (2004) 164-175

Grosse, M., Kalkhof, D., Keller, L., and Schell, N.
Influence parameters of martensitic transformation during low cycle fatigue for steel AISI 321
Physica B **350** (2004) 102-106

Martins, Rui M.S.
Master thesis, *Produção e Caracterização de Películas Finas de Ni-Ti com Memória de Forma*
Universidade Nova de Lisboa – Faculdade de Ciências e Tecnologia (2004)

Martins, Rui M.S., Silva, Rui J.C., Braz Fernandes, F.M., Pereira, L., Gordo Paulo, R., Maneira, Manuel J.P., and Schell, N.
In-situ GIXRD characterization of the crystallization of Ni-Ti sputtered thin films
Materials Science Forum **455-456** (2004) 342-345

Paula, A.S., Canejo, J.P.H.G., Martins R.M.S., and Braz Fernandes, F.M.
Effect of thermal cycling on the transformation temperature ranges of a Ni-Ti shape memory alloy
Materials Science and Engineering A **378** (2004) 92-96

Pełka, J.B., Andrejczuk, A., Reniewicz, H., Schell, N., Krzywiński, J., Sobierajski, R., Wawro, A., Żytkiewicz, Z., Klinger, D., and Juha, L. *
Structure modifications in silicon irradiated by ultra-short pulses of XUV free electron laser
Journal of Alloys and Compounds **382** (2004) 264-270

Rogozin, A., Shevchenko, N., Vinnichenko, M., Prokert, F., Cantelli, V., Kolitsch, A., and Möller, W.
Real-time evolution of the indium tin oxide film properties and structure during annealing in vacuum
Applied Physics Letters **85(2)** (2004) 212-214

Schell, N., Andreasen, K.P., Bøttiger, J., and Chevallier, J.
On the structural evolution of nanocrystalline Cu films during thermal annealing
Thin Solid Films **XX** (2004) *in press, online available*

Schell, N., Jensen, T., Petersen, J.H., Andreasen, K.P., Bøttiger, J., and Chevallier, J.
The nanostructure evolution during and after magnetron deposition of Au films
ESRF Highlights 2003 (2004) 39-40

Turos, A., Gaca, J., Wojcik, M., Nowicki, L., Ratajczak, R., Groetzschel, R., Eichhorn, F., and Schell, N.
Virtues and pitfalls in structural analysis of compound semiconductors by the complementary use of RBS/channeling and high resolution x-ray diffraction
Nuclear Instruments and Methods in Physics Research B **219-220** (2004) 618-625

Thiele, E., Klemm, R., Hollang , L., Holste, C., Schell, N., Natter, H., and Hempelmann, R.
An approach to cyclic plasticity and deformation-induced structure changes of electrodeposited nickel
Materials Science and Engineering A **390** (2005) 42-51

2.5. Experiments

The following tables list all experiments which have been performed at the beamline, separated by end-station (Radiochemistry, Materials Research) and by type of experiment (CRG, ESRF, technical shifts). Experiments with more than 18 shifts indicate that these experiments have been performed during several experimental runs and are part of long-term research programs.

2.5.1. List of Radiochemistry Experiments

In-house Experiments

number	title	proposer	institution	experimenters	shifts
20-01-024 R02	Polarized EXAFS measurements at uranyl sorbed montmorillonite	C. Hennig, T. Reich, A. Rossberg, H. Funke	FZR	T. Reich, A. Scheinost, E. Marosits, A. Rossberg, H. Funke, C. Hennig, J. Drebert	3
20-01-030	EXAFS investigation on uranium uptake by plants	A. Guenther, G. Bernhard, G. Geipel, T. Reich	FZR	H. Moll, M. Walter, A. Rossberg, H. Funke	9
20-01-038	Structural studies of uranyl phosphates including adenosine phosphates using EXAFS	C. Hennig, G. Geipel, G. Bernhard, A. Guenther	FZR	C. Hennig, H. Funke, A. Rossberg	6
20-01-060	EXAFS investigation of uranium complexation by sugar phosphates	A. Guenther, T. Reich, A. Rossberg, A. Koban	FZR	A. Koban, H. Funke, C. Hennig, A. Rossberg, A. Scheinost	39
20-01-065	Interaction between Pseudomonas sp. and uranium using EXAFS	M. Merroun, S. Selenska-Pobell, T. Reich	FZR	M. Merroun, A. Rossberg, H. Funke, C. Hennig, A. Scheinost, H. Moll, M. Walter	32
20-01-069	Uranium binding of sol-gel immobilized cells and S-layers of Bacillus sphaericus JG-A12 and NCTC 9602	J. Raff, S. Selenska-Pobell, H. Funke, T. Reich, C. Hennig, A. Rossberg	FZR	M. Merroun, A. Rossberg, H. Funke, C. Hennig, A. Scheinost, H. Moll, M. Walter	20

number	title	proposer	institution	experimenters	shifts
20-01-611	Interaction of actinides with predominant bacteria isolated at nuclear waste repositories using X-ray absorption spectroscopy	H. Moll, C. Hennig, A. Rossberg, H. Funke, M. Merroun	FZR	A. Koban, H. Moll, M. Walter, H. Funke, C. Hennig, A. Rossberg, A. Scheinost	9
20-01-617	Study of the surface complexes formed between uranium and thorium and iron corrosion products. Effect of hydroxo-apatite on the uptake of uranium	L. Duro, M. Grive, F. Seco, T. Missana	UPC Barcelona	M. Grive, F. Seco, T. Missana, U. Alonso	12
20-01-618	Spectro-electrochemical cell for in situ XAS measurements of uranium solution species	C. Hennig, J. Tutschku, G. Geipel, A. Rossberg, G. Bernhard	FZR	C. Hennig, J. Tutschku, A. Rossberg, A. Scheinost	60
20-01-619	EXAFS study of uranium(VI) complexation with dicarboxylic acids	T. Reich, I. Cuesta Hernandez	Uni Mainz	A. Rossberg, T. Reich, I. Cuesta Hernandez, A. Soldati	6
20-01-621	Uranium(VI) sorption on clinochlore surfaces	M. Walter, T. Arnold, E. Krawczyk-Baersch, C. Hennig, A. Rossberg, H. Funke	FZR	H. Funke, M. Merroun, A. Scheinost, A. Rossberg, C. Hennig	5
20-01-622	Chemical speciation of metals in shooting-range soils	A. Scheinost, C. Hennig, D. Vantelon, I. Xifra	FZR, ETHZ	A. Scheinost, C. Hennig, D. Vantelon	18
20-01-623	Low-temperature phase-transition of $H[UO_2AsO_4]x4H_2O$	C. Hennig	FZR	C. Hennig, H. Funke	18
20-01-624	Speciation of Zn in rhizosphere soil	A. Scheinost, C. Hennig, A. Rossberg, H. Funke, A. Voegelin, S. Pfister	FZR, ETHZ	A. Scheinost, D. Vantelon, I. Xifra, H. Funke, S. Pfister, A. Voeglin, O. Jacquat, C. Hennig	26
20-01-625	Interaction between microorganisms and metals using EXAFS	M. Merroun, S. Selenska-Pobell, J. Raff, C. Hennig	FZR	M. Merroun, A. Scheinost, C. Hennig, A. Rossberg, H. Funke	32

number	title	proposer	institution	experimenters	shifts
20-01-626	Oxidation state and local structure of uranium in soils and sediments	A. Scheinost	FZR	A. Scheinost, H. Funke, C. Hennig, A. Rossberg	56
20-01-629	Polarization dependency of x-ray absorption fine structure on the uranyl unit	C. Hennig	FZR	C. Hennig	9
20-01-630	The structure of organic uranium complexes at low temperature	A. Rossberg, A. Scheinost, G. Geipel	FZR	A. Rossberg, A. Scheinost, H. Funke, C. Hennig	30
20-01-632	Uranium sorption onto natural iron colloids in mine waters	K.-U. Ulrich, A. Scheinost, H. Zaenker	FZR	K.-U. Ulrich, A. Scheinost, H. Funke, A. Rossberg, C. Hennig	30
20-01-637	Feasibility EXAFS experiment for neptunium sorption on kaolinite	T. Reich, S. Amayri, S. Sachs	Uni Mainz	T. Reich, J. Drebert, T. Reich, A. Jermolajev, C. Hennig, A. Scheinost	6
20-01-638	X-ray absorption spectroscopy studies on gold nanoparticles formed by bacteria and their surface layer proteins	M. Merroun, S. Selenska-Pobell, A. Scheinost, C. Hennig	FZR	M. Merroun, A. Rossberg, C. Hennig, H. Funke, A. Scheinost	15
20-01-639	Investigation of U(VI)/U(V) carbonato complexes in aqueous solution by spectro-electrochemistry	C. Hennig, I. Grenthe, G. Palladino, A. Scheinost	FZR/Uni Stockholm	C. Hennig, A. Scheinost, H. Funke, A. Rossberg	9
20-01-640	Study of the influence of humic acid on the U(VI) sorption onto kaolinite	A. Krepelova, S. Sachs, A. Scheinost	FZR	A. Krepelova, C. Hennig, A. Scheinost, H. Funke, A. Rossberg	9
20-01-641	Uranyl(VI) sorption on gibbsite and quartz	T. Arnold, N. Baumann, V. Brendler, A. Scheinost	FZR	C. Hennig, A. Scheinost, H. Funke, A. Rossberg	6
20-01-642	Local structure of U(IV) and U(VI) in natural and synthetic minerals	A. Scheinost, A. Rossberg, C. Hennig, H. Funke, T. Arnold	FZR	A. Scheinost, A. Rossberg, C. Hennig, H. Funke	14

ESRF Experiments

number	title	proposer	institution	experimentator	shifts
HE-1393	Delta-phase stabilization in Pu(x)Am(1-x) alloys studied by EXAFS	B. Ravat, N. Baclet, L. Jolly, C. Vallot	CEA Valduc	B. Ravat, L. Jolly, C. Vallot, L. Gogolusko, E. Aubert, F. Coulon, B. Oudot, H. Funke, C. Hennig	15
CH-1454	EXAFS/XANES studies on the interaction of Tc(IV) with selected chemical components as a reference for Tc(IV)-humic substance interaction	A. Maes, K. Geraedts, C. Bruggeman, L. Van Loon	KU Leuven, PSI	A. Rossberg, A. Maes, K. Geraedts, C. Bruggeman, C. Hennig, H. Funke, A. Scheinost	12
CH-1455	Speciation of Tc(VII), Tc(IV) and Tc(III) by in situ coupled XAS-electrochemistry	F. Poineau, M. Fattahi, B. Grambow	Subatech, Nantes	F. Poineau, P. Frenoy, C. Hennig, J. Tutschku, H. Funke	12
SC-1349	Americium speciation in ferritin protein	C. Barbot, C. Den Auwer, F. Goudard, J. Pieri, E. Simoni, P. Germain	CEA Nantes	C. Den Auwer, C. Hennig, H. Funke, A. Rossberg, A. Scheinost	9
CH-1567	Uranium(VI) complexation with tri-butyl-phosphate (TBP) in room temperature ionic liquid	I. Billard, C. Gaillard	IRES Strasbourg	C. Hennig, H. Funke, A. Rossberg, A. Scheinost	12
ME-815	Study of the surface complexes formed between thorium and iron corrosion products	L. Duro, M. Grive, J. Bruno	ENVIROS Barcelona	L. Duro, M. Grive, C. Hennig, H. Funke, A. Rossberg	6
CH-1671	EXAFS/XANES studies on the speciation of Tc(IV) in the presence of complexing organics and fulvic acids	A. Maes, C. Bruggeman, E. Breynaert	KU Leuven	A. Maes, C. Bruggeman, E. Breynaert, H. Funke, A. Rossberg, C. Hennig	12
ME-817	EXAFS study of uranium(VI) uptake by kaolinite	T. Reich, E. Marosits	Uni Mainz	T. Reich, S. Amayri, J. Drebert, H. Funke, C. Hennig, A. Rossberg, A. Scheinost	12

number	title	proposer	institution	experimentator	Shifts
ME-740	Determination of Th(IV) and U(VI) uptake mechanisms onto hectorite using polarized EXAFS	R. Daehn, A.M. Scheidegger, B. Baeyens	PSI Villigen	R. Dähn,D. Kunz, B. Baeyens, F. Gonzalez, C. Hennig, A. Scheinost	15
CH-1766	Study of complexation behavior of Bispidone derivates towards europium, neptunium and copper	G. Geipel, H. Stephan, T. Suzuki, A. Rossberg	FZR	T. Suzuki, C. Hennig, A. Rossberg, H. Funke, M. Leckelt, A. Scheinost	9
CH-1764	Interaction of iron metalloprotein with actinide (IV): the transferrin and ferritin case	C. DenAuwer, P. Moisy, C. Barbot, F. Goudard	CEA Marcoul	C. DenAuwer, C. Bresson, B. Caniffi, A. Ruas, X. Deschanel, D. Guillaumont, H. Funke, C. Hennig, A. Rossberg, A. Scheinost	12

2.5.2. List of Materials Research Experiments

In-house Experiments

number	title	proposer	institution	experimentator	shifts
20_02_606	Influence of TiN cap layer, dopant and metal film thickness on phase formation processes in nanoscale nickel layers during heat treatment on different silicon substrates	J. Rinder-knecht, T. Kammler, H. Prinz	AMD Saxony Manufactur-ing Dresden, ROBL-CRG	Rinderknecht, Prinz, Schell, Dekadjevi	8
20_02_607	Characterization of InGaAs /GaAs and InGaAs/InP hetero-structures by x-ray scattering	J. Sass, J. Gaca, K. Mazur, M. Wojcik, F. Eichhorn	ITME Warsaw, FWIS, ROBL-CRG	Sass, Mazur, Gaca, Wojcik, Eichhorn, Dekadjevi, Schell, Cantelli	39
20_02_608 ME-584	*In-situ* x-ray diffraction during sputter deposition of TiAlN *In-situ* XRD study of sputtered Ni-Ti SMA thin films	M. Beckers, N. Schell Braz-Fernandes, C. Silva, N. Schell	FWIS, FWII, ROBL-CRG CENIMAT, Campus FCT/UNL, FZR, FWIS	Beckers, Gago, Schell, Martins, Canejo, Schell	54
20_02_609 *long term*	The evolution of texture in thin-film copper during growth and annealing	J. Bøttiger	University of Aarhus, ROBL-CRG	Bøttiger, Pakh Andreasen, Schell, Martins	18

number	title	proposer	institution	experimentator	shifts
20_02_610	X-ray diffraction and reflectivity studies of Si/SiGe based quantum cascade structures	G. Bauer, M. Meduna, N. Schell, D. Dekadjevi	University of Linz, ROBL-CRG	Meduna, Falub, Chen, Dekadjevi, Schell	18
20_02_612	Gracing incidence x-ray techniques applied to nano-structured materials	D. Dekadjevi, N. Schell, H. Prinz, J. Rinderknecht, F. Eichhorn, J.v. Borany	ROBL-CRG, AMD, FWIS	Dekadjevi, Schell, Borany	26
20_02_613	Characterization of structure and morphology of buried layers of transition metal oxides	N. Shevchenko	FWIS, ROBL-CRG	Shevchenko, Scholz, Schell	17
20_02_617	SR-μ-XRD stress measure-ments of dual damascene inlaid copper interconnect structures at temperatures between RT and 500°C	J. Rinder-knecht, H. Prinz	AMD Saxony Manufactur-ing Dresden, ROBL-CRG (CENIMAT)	Rinderknecht, Prinz, Zienert, Schell, (P. Andersan)	6
20_02_618	Influence of substrate temperature at the MBE process on the interface structure of Fe/Cr multilayers	F. Prokert, N. Shevchenko, E. Kravtsov	FWIS, ILL, ROBL-CRG	Prokert, Scholz, Shevchenko, Schell, Cantelli	9
20_02_609 *long term* (in 2004)	The evolution of texture in thin-film silver during growth and annealing	J. Bøttiger	University of Aarhus, ROBL-CRG	Bøttiger, Pakh Andreasen, Schell, Martins	18
20_02_617 *long term* (in 2004)	SR-μ-XRD stress mea-surements of dual damascene inlaid copper interconnect structures at tempera-tures between RT and 500°C	J. Rinder-knecht, H. Prinz	AMD Saxony Manufactur-ing Dresden, ROBL-CRG	Rinderknecht, Prinz, Zienert, Schell	36
20_02_619	Ion-beam synthesis of wide band-gap semi-conductor nano-crystals: structural studies	F. Eichhorn, R. Koegler, H. Weishart	FWIS, FWIM, ROBL-CRG	Eichhorn, Schell	9
20_02_620	*In-situ* XRD during magnetron deposition and subsequent annealing for nc metals and two-component alloys	N. Schell	FWIS, ROBL-CRG	Schell, Martins, Beckers	18
20_02_621	Study of Au-Ge nanoalloy formation by grazing incidence x-ray diffraction	F. Prokert, T. Som	FWIS ROBL-CRG	Prokert, Som, Cantelli	8
20_02_622	Structural studies of semiconductor materials for optoelectronic applications	J. Sass, F. Eichhorn, J. Gaca, K. Mazur, M. Wojcik	ITME Warsaw, FWIS, ROBL-CRG	Sass, Eichhorn, Gaca, Mazur, Wojcik, Cantelli, Schell	35
20_02_623	Investigation of the nanocluster formation and phase transition of nanoparticles embedded in a dielectric matrix	J. v. Borany, V. Cantelli, N. Schell	FWIS, ROBL-CRG	Borany, Cantelli, Schell	9

number	title	proposer	institution	experimentator	shifts
20_02_624	Investigation of structural ordering in thin metal alloy films designed for future magnetic memory materials	J. v. Borany, V. Cantelli, N. Schell	FWIS, ROBL-CRG	Borany, Schell, Cantelli	21
20_02_625	Investigation of the thermal stability of the phases formed during low temperature gas nitriding of austenitic steel	D. Busquets, J. Baranowska, V. Cantelli, N. Schell	U. Politécnica Valencia, TU Szczecin, FWIS, ROBL-CRG	Busquets, Baranowska, Cantelli, Schell, Strauch	9
20_02_626	*In-situ* XRD during thermal cycling of Ni-Ti Shape Memory Alloy	F. Braz-Fernandes, P. Andersan	CENIMAT, Campus FCT/UNL, ROBL-CRG	Andersan, Mahesh, Martins, Cardosa, Schell	9

Technical Shifts

test no.	topic	institute	responsible	experimentator	shifts
03/1 20_02_IH8	DCM commissioning *In-situ* study of the phase stability of carbonitrided austenitic stainless steel samples at heating from RT to 800°C	ROBL-CRG, FWIS	N. Schell	Schell, Cantelli, Prokert, Abd El-Rahman	21
03/2 20_02_IH9	DCM commissioning Ion beam synthesis of 3C-SiC nanocrystals buried in diamond single crystals: structural study	ROBL-CRG, FWIS	N. Schell	Schell, Eichhorn	18
03/3	DCM commissioning	FWIS	N. Schell	Schell, Cantelli	14
04/1 IH-SI-142	Real-time studies of the ITO film structure and resistivity behavior during annealing	FWIS, FWII	V. Cantelli N. Shevchenko	Cantelli, Schell, Shevchenko, Rogozin	18
04/2 IH-SI-166	Investigation of ordering in thin metal (multi)layers designed as future magnetic memory materials / 4 x 10 mA / **20_02_624**	FWIS	V. Cantelli	Cantelli, Martins	21
04/3 IH-SI-176	XRD and GID characterisation of hard covers	FWIS	N. Schell	Schell, Martins	15
04/4 IH-BLC-1736	Monochromator setup and testing	FWR, FWE, FWIS	A. Scheinost	Hennig, Scheinost Strauch, Cantelli	21
04/5 IH-MI-329	XRD, GID and GIXS test measurements	FWIS	N. Schell	Schell, Martins, Cardoso	15

ESRF Experiments

number	title	proposer	institution	experimentator	shifts
ME-474	Crystallisation of Ni-Ti thin film Shape Memory Alloy (SMA)	F.M. Braz Fernandes, R.J. Cordeiro Silva	CENIMAT, Campus FCT/UNL, Monte da Caparica	Braz Fernandes, Cordeiro Silva, Martins, Schell	12
ME-587	Texture and strain measurements of quartzite	K. Walther, P. Mikula	Geo.-for.zent. Potsdam, Nuc. Phys. Inst. (Prague)	Walther, Scheffzük, Schell	9
ME-586	Chalcopyrite thin films on silicon substrates	J. Kräußlich, B. Wunderlich, T. Hahn	FSU Jena	Kräußlich, Wunderlich, Schell	9
ME-584	*In situ* XRD study of sputtered Ni-Ti SMA thin films	F.M. Braz Fernandes, R.J. Cordeiro Silva, N. Schell	CENIMAT, Campus FCT/UNL, Monte da Caparica, ROBL-CRG	Braz Fernandes, Cordeiro Silva, Martins, Schell	18
ME-706	X-ray diffraction studies on stress-released cubic boron nitride thin films	R. Gago, B. Abendroth	FZR, FWII	Gago, Abend-roth, Schell, Cantelli	9
ME-705	*In situ* stress state analysis during thermal cycling of Ni-Ti Shape Memory Alloy	F.M. Braz Fernandes, P. Andersan, J. Canejo, N. Schell	CENIMAT, Monte da Caparica, ROBL-CRG	Braz-Fernandes, Canejo, Andersan, Schell	15
ME-708	Strain and texture investigation across a crack in an experimen-tal deformed granite sample	K. Walther, A. Frischbutter, P. Mikula	Geo.-for.zent. Potsdam, Nuc. Phys. Inst. (Prague)	Walther, Scheffzük, Schell	9
ME-814	*In-situ* XRD study of sputtered Ni-Ti SMA thin films	F.M. Braz Fernandes, R. Martins, R.J.C. Silva, M. Silva	CENIMAT, Campus FCT/UNL, Monte da Caparica	Braz Fernandes, Martins, Cordeiro Silva, Silva, Schell	18
ME-816	Oxide growth on iron single crystals	A. Pyzalla, W. Reimers	TU Wien, TU Berlin	Pyzalla, Da Silva, Skorina, Schell	15
SI-1031	Characterization of Cu(In, Ga)S2 thin films using GID	J. Kräußlich, J. Cieslak, B. Wunderlich	FSU Jena	Kräußlich, Wunderlich, Cantelli	12
SI-1125	Structural investigation of Si/SiGe-based cascade emitters in the far-infrared	G. Bauer, M. Meduna, D. Gruetzmacher N. Schell	University of Linz, ROBL-CRG	Meduna, Gruetzmacher, Schell	15

3. Experimental Reports

Below is a compilation of Experimental Reports, as far as they have been provided by the users until December 2004. The responsibility for the communicated results lies with the users. An updated list of experimental reports can also be downloaded from our web-site, which is accessible through the ESRF at http://www.esrf.fr/UsersAndScience/Experiments/CRG/BM20/ or directly at http://www.fz-rossendorf.de/FWE.

3.1. Experimental Reports Radiochemistry

Due to the inevitable delay between the experimental work and the Experimental Report, this compilation lacks some of the late experiments (20-01-639, 20-01-640, 20-01-642) and a report of work already performed in 2002 has been added (20-01-600).

ROBL-CRG	**Experiment title:** **EXAFS investigation on uranium uptake by plants**	**Experiment number:** **20-01-30**
Beamline: BM 20	**Date of experiment:** from: 09/07/03 to: 12/07/03	**Date of report:** 31/12/04
Shifts: 9	**Local contact(s):** André Roßberg	*Received at ROBL:*

Names and affiliations of applicants (* indicates experimentalists):
A. Günther[1], G. Bernhard[1], G. Geipel[1], T. Reich[2], A. Scheinost*[2], A. Roßberg*[2], C. Hennig*[2], H. Funke*[2], H. Moll*[1], S. Amayri*[1], M. Walter*[1]
[1]Forschungszentrum Rossendorf e.V., Institute for Radiochemistry, P.O. Box 510119, 01314 Dresden, Germany
[2]ESRF-ROBL/CRG, Avenue des Matryrs, B.P. 220, 38043 Grenoble Cedex, France

Report:

Experimental: The goal of this study is the determination of the structural parameters of the uranyl complex species in the liquids and solid components of the plant cells. Lupine plants were grown in uncontaminated soil and then transferred into hydroponic solution. The uranium concentration in the hydroponic solution was $1 \cdot 10^{-2}$ M at pH 3.5. After the harvesting the plants were washed, separated into root, shoot and leaf. The cells of the section samples of the roots and shoots were destroyed in an oscillating mill while being cooled with liquid nitrogen. Afterwards the green mass was centrifuged and the cell liquid separated from the solid cell components.
The U L_{III}-edge spectra were measured in fluorescence mode. The EXAFS spectra were analyzed using the suite of program EXAFSPAK /1/. The theoretical scattering phases and amplitudes were calculated for m-autunite with the scattering code FEFF8 /2/.

Results and discussion: The figure shows the raw U L_{III}-edge k^3-weighted EXAFS spectra and their corresponding Fourier transforms (FT) of the several uranium containing cell components of the plant. The structural parameters are summarized in the table. The EXAFS spectra of the investigated plant samples are different (see figure). The changes in the EXAFS spectra are attributed to structural changes in the equatorial plane of uranium(VI.

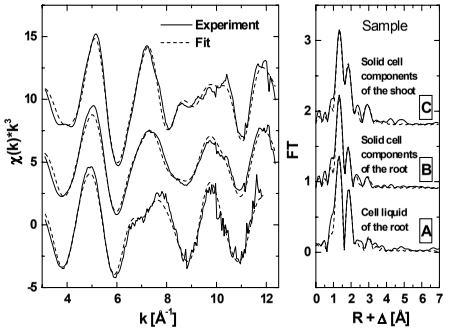

Raw U L_{III}-edge k^3-weighted EXAFS spectra (left) and its corresponding Fourier transform (right) of investigated cell components.

For the cell liquid (A) we obtained similar structural parameters to uranylhydrate (see table), which is the main component in the hydroponic solution. Furthermore, the EXAFS spectrum of the sample (A) shows a U–P interaction at 3.60 Å. For the solid cell components (C) we obtained a relatively short U-O_{eq} bond distance of 2.28 Å. In case of this sample the EXAFS structural parameters agree with those of m-autunite (inorganic uranyl phosphate). Sample (B) shows two structural different types of coordinated O_{eq} atoms. The short U-$O_{eq(1)}$ bond distance of 2.31 Å and the U-P interaction at 3.61 Å indicates a monodentate bind phosphate group. If sample (B) consists of one complex with one type of interacting ligand, than the $O_{eq(2)}$ atoms could arises from the organic rest on the phosphate group.

Tab. 1: EXAFS structural parameters of the uranyl complex species in several cell components of the lupine

Sample	U-O_{ax}		U-$O_{eq(1)}$			U-$O_{eq(2)}$			U-P		
	R[Å]	$\sigma^2 \cdot 10^3$ [Å^2]	N	R[Å]	$\sigma^2 \cdot 10^3$ [Å^2]	N	R[Å]	$\sigma^2 \cdot 10^3$ [Å^2]	N	R[Å]	$\sigma^2 \cdot 10^3$ [Å^2]
A	1.77	0.9	6.0	2.41	8.7	-	-	-	2.4	3.60	4
B	1.78	1.5	3.0	2.31	4.0	2	2.50	10	2.0	3.61	4
C	1.78	1.9	5.4	2.28	5.7	-	-	-	4.6	3.59	4

During the fitting procedure the coordination number of O_{ax} was held constant at N=2, N-coordination number with an uncertainty of 25%, R-radial distance with an uncertainly of±0.02Å, σ^2- Debye-Waller factor

References

/1/ George, G. N., Pickering, I. J.: EXAFSPAK A Suite of Computer Programs for Analysis of X-Ray Absorption Spectra. Stanford Synchrotron Radiation Laboratory, Stanford, CA. USA. (1995)

/2/ Ankudinov, A. L., Ravel, B., Rehr, J.J., Conradson, S. D., real-space multiple scattering calculation and interpretation of x-ray absorption near-edge structure, Phys. Rev. B **58** (1998), 7565-7576

ROBL-CRG	**Experiment title:** **EXAFS investigations of uranium complexation by sugar phosphates**	**Experiment number:** **20-01-60**
Beamline: BM 20	**Date of experiment:** from: 05/04/03 to: 08/04/03 from: 03/08/03 to: 07/08/03 from: 03/10/03 to: 07/10/03	**Date of report:** 31/12/04
Shifts: 39	**Local contact(s):** André Roßberg	*Received at ROBL:*

Names and affiliations of applicants (* indicates experimentalists):
A. Günther[1], G. Bernhard[1], G. Geipel[1], T. Reich[2], A. Scheinost*[2], A. Roßberg*[2], C. Hennig*[2], H. Funke*[2], A. Koban*[1], M. Merroun*[1]
[1]Forschungszentrum Rossendorf e.V., Institute for Radiochemistry, P.O. Box 510119, 01314 Dresden, Germany
[2]ESRF-ROBL/CRG, Avenue des Matryrs, B.P. 220, 38043 Grenoble Cedex, France

Report:

Experimental:

The complex formation in the aqueous systems of uranium(VI) with glucose 1-phosphate, glucose 6-phosphate, fructose 6-phosphate and glycerol 1-phopshate were studied using EXAFS. The measurements were carried out on solutions containing variable uranyl and ligand concentrations and pH (Table 1). The EXAFS spectra were analyzed using the suite of programs EXAFSPAK /1/. The theoretical scattering phase and amplitude functions were calculated using x-ray data from uranyl nitrate trimethylphosphate $UO_2(NO_3)_2(PO_4(CH_3)_3)$ /2/ with the scattering code FEFF8 /3/.

Results and discussion:

The EXAFS structural parameters of the U(VI)/glucose 6-phosphate and U(VI)/fructose 6-phopshate system are summarized in Table 1 /4/.

Uranium L_{III}-edge EXAFS measurements at pH 3.5, 4.0, and 5.5 yielded a shortened $U–O_{eq}$ bond distance (2.30 ± 0.02 to 2.37 ± 0.02 Å), compared to the $UO_2^{2+}(H_2O)_5$ ion (2.40 ± 0.02 Å), due to a monodentate coordination *via* the oxygen atoms of the phosphate group. In the case of monodentate bound phosphate groups, a backscatterer contribution of phosphorus should be visible in the FT at about 3.0 Å. Due to the fact, that the single scattering U–P path and the three-fold U–O–P multiple scattering path nearly mutually extinguish themselves through destructive interference the small amplitudes of the U–P and the U–O–P backscatterer contribution are underneath the noise level and were not fitted. The possibility of the presence of phosphate groups, which do not coordinate in a monodentate fashion to the U(VI) ion, is supported by the fact that the significant peak at 2.3 Å in the FT cannot be reproduced by only coordinated water molecules and monodentate coordinated phosphate groups. We have modeled this backscatterer contribution with oxygen atoms ($O_{eq(2)}$). Usually it is expected that this peak is caused by carbon atoms. In consideration of the possible arrangements of U(VI) at the functional groups of these molecules it seems improbably to be carbon. However, the origin of this scattering contribution is not yet understood and is currently under investigation.

Tab.1: EXAFS structural parameters for UO_2^{2+} complexes with glucose 6-phosphate(G6P) and fructose 6-phosphate (F6P)

Sample	$U-O_{ax}$		$U-O_{eq(1)}$			$U-O_{eq(2)}$		
	R[Å]	$\sigma^2\cdot10^3$ [Å^2]	N	R[Å]	$\sigma^2\cdot10^3$ [Å^2]	N	R[Å]	$\sigma^2\cdot10^3$ [Å^2]
10^{-3} M U(VI),10^{-2} M G6P, pH=3.5	1.768(2)	0.7(2)	7(1)	2.34(1)	19(3)	1.4(3)	2.84(2)	4*
10^{-3}M U(VI), 5x10^{-2} M G6P, pH=4.0	1.773(3)	1.2(2)	5.2(9)	2.33(1)	12(2)	1.0(6)	2.90(2)	1(3)
10^{-3} M U(VI), 5x10^{-2} M G6P, pH=5.5	1.771(3)	1.0(2)	5.9(8)	2.31(1)	13(1)	0.9(3)	2.90(2)	4*
10^{-3} M U(VI), 5x10^{-3} M F6P, pH=3.5	1.776(3)	0.9(1)	5.7(9)	2.37(1)	16(2)	1.3(3)	2.87(1)	4*
10^{-3} M U(VI), 5x10^{-2} M F6P, pH=4.0	1.773(3)	1.4(2)	5.2(8)	2.32(1)	12(2)	1.6(3)	2.88(2)	4*
5x10^{-3} M U(VI), 5x10^{-2} M F6P, pH=5.5	1.773(2)	1.3(1)	4.8(5)	2.30(1)	20(4)	1.3(2)	2.88(1)	4*

During the fitting procedure the coordination number of O_{ax} was held constant at N=2. Standard deviations of the variable parameters are given in parenthesis. (N-coordination number with an uncertainty of 25%, R-radial distance with an uncertainly of ±0.02Å, σ^2- Debye-Waller factor, * parameter fixed during the fitting procedure)

References

/1/ George, G. N., Pickering, I. J.: EXAFSPAK A Suite of Computer Programs for Analysis of X-Ray Absorption Spectra. Stanford Synchrotron Radiation Laboratory, Stanford, CA. USA. (1995)

/2/ Agostini, G., Giacometti, G., Clemente, D. A., Vincentini, M.: Inorg. Chim. Acta **62**, 237 (1982).

/3/ Ankudinov, A. L., Ravel, B., Rehr, J. J., Conradson, S. D.: Real-space multiple scattering calculation and interpretation of x-ray absorption near-edge structure, Phys. Rev. B **58** (1998), 7565-7576

/4/ Koban, A., Geipel, G., Roßberg, A., Bernhard, G.: Radiochim. Acta **92**, 1-6 (2004)

ROBL-CRG	**Experiment title:** **Interaction between *Pseudomonas* sp. and uranium using EXAFS**	**Experiment number**: **20-01-65**
Beamline: BM 20	**Date of experiment**: 12.3.-13.3.03; 12.6.-14.6.03; 13.7.-15.7.03; 2.10.-3.10.03; 30.6.-4.7.04; 23.-24.09.04	**Date of report**: 20.11.04
Shifts: 32	**Local contact(s)**: Dr. Christoph Hennig	*Received at ROBL:*
Names and affiliations of applicants (* indicates experimentalists): M. Merroun*, M. Heilig, A. Scheinost*, A. Rossberg*, C. Hennig*, H. Funke*, S. Selenska-Pobell		

Report: Uranium is a long-living radionuclide that represents ecological and human health hazards. The mining and processing of uranium during the last decades for nuclear fuel and nuclear weapon production resulted in generation of significant amounts of radioactive wastes. It is critical that the uranium in these wastes has to be effectively immobilized and removed away in order to prevent ground water contamination. Microbial biosorption of U(VI) was proposed as one of the methods for uranium immobilization. In this paper, we investigate the coordination chemistry of uranium bound to different bacteria isolated from uranium mining wastes using Extended X-ray Absorption Fine Structure (EXAFS) spectroscopy.

Experimental: Bacterial cells grown to the late exponential phase were harvested by centrifugation (11000 rpm for 20 min at 4°C) and washed three times with 0.1 M $NaClO_4$ to remove the disturbing ingredients of the growth medium. The washed cells were resuspended and shacked for 48 h in 35 ml 10^{-3} M $UO_2(NO_3)_2$ x 6 H_2O resolved in 0.1 M $NaClO_4$, at two pH values of 2 and 4.5. After the uranyl contact, the cells were harvested and washed with 0.1 M $NaClO_4$. The pellet samples were dried in a vacuum incubator at 30°C for 24 h and powdered.

Results: The X-ray absorption near edge structure (XANES) spectra (data not shown) of uranium complexes formed by different bacteria studied in this work contain an XANES peak at 17188 eV which has previously been attributed to uranium in the 6+ oxidation state. In addition, the intensity maximum for the absorption edge occurs at the position characteristic of U(VI). Both observation indicate that uranium is present in the samples as U(VI).

The k^3-weighted χ spectra determined from EXAFS analyses of the uranium species formed at pH 2 and 4.5 are presented in Figure 1 along with the best fits obtained from the fitting procedure. The FT of the EXAFS spectra of the samples studied in this section at pH 2 and 4.5 show five significant peaks. The first two peaks arise from the scattering contribution of the axial oxygen atoms (O_{ax}) at 1.3 Å and the equatorial oxygen atoms (O_{eq}) at 1.8 Å. The U-O_{eq} bond distance is within the range of previously reported values for the oxygen atom of the phosphate bound to uranyl. The third and the fourth FT peak, which appear at 2.3 and 3 Å, are a result of the back-scattering from oxygen and phosphorous atoms, respectively. This U-P distance is consistent with monodentate coordination of phosphate to the uranyl equatorial plane as was found in m-autunite.
Interestingly, in the case of pH 4.5, a fifth shell was modelled to a contribution from U-U at distance of 5.20 Å, this bond distance is present in m-autunite EXAFS spectrum indicating that at this pH value the uranium is precipitated by bacterial cells as a m-autunite like phase (inorganic uranyl phosphate phase). However, at pH 2, this peak is absent but we can found another peak which could be probably fitted to a contribution of U-C at distance of 3.72 Å. This C atom most probably originates from the organic phosphate molecules of the cell surface which are implicated in the binding of uranium.

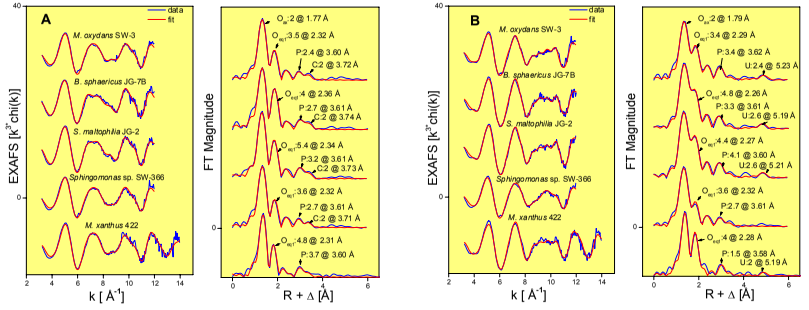

Fig. 1: U L_{III}-edge EXAFS spectra and their corresponding FT of the U complexes formed by the uranium minig waste isolates at pH 2 (A) and 4.5 (B).

Acknowledgments:
This work was supported by a grant 03I4004B from the Bundesministerium für Bildung und Forschung, Germany.

ROBL-CRG	**Experiment title:** **Uranium binding of sol-gel immobilized cells and S-layers of *B. sphaericus* JG-A12 and NCTC 9602**	**Experiment number**: **20-01-69**
Beamline: BM 20	**Date of experiment**: 13.3.-15.03.03; 13.07.03; 7.2.-10.2.04; 4.7.-5.7.04	**Date of report**: 15.11.04
Shifts: 20	**Local contact(s)**: Dr. Christoph Hennig	*Received at ROBL:*
Names and affiliations of applicants (* indicates experimentalists): M. Merroun*, K. Brottka, A. Scheinost*, A. Rossberg*, C. Hennig*, H. Funke*, S. Selenska-Pobell		

Report: Water pollution due to toxic heavy metals remains a serious environmental and public problem. Strict environmental regulations on the discharge of heavy metals require a development of various efficient technologies for their removal. Therefore numerous approaches have been studied for the development of cheaper and effective metal sorbents, such as microbial cells. However, microbial biomass in its native form is not suitable for large-scale process utilization. It is be necessary to immobilize the biomass. As a current trend in the field of bio-engineered materials, sol-gel technology opens new vistas in immobilization of biocomponents. Using an aqueous sol-gel process for embedding microbial biomass in silica gel, it is possible to construct a filter matrix with a homogeneous structure and completely immobilized biocomponents called biological ceramics (biocers). Because of the ability of the strain *Psuedomonas stutzeri* DSM 5190 to bind selectively U and other heavy metals, it was chosen for construction of novel biocers. In this work we study the structural parameters of the U complexes formed by cells, xerogel and biocers using EXAFS spectroscopy.

Experimental: Sol-gel ceramics were prepared by dispersing *Pseudomonas* cells in a aqueous silica nanosol, gelling and drying. 100 mg biocer consists of 81.8 mg SiO_2 and 18.2 mg cells. Before the experiments, the pH of the biocer was adjusted to pH 4.5. For uranium sorption, all components were shaken for 48h in 30 ml 0.9 mM uranium nitrate pH 4.5 at 30°C. After incubation, samples were washed with 0.9% $NaClO_4$. The particles were dried in a vacuum incubator at 30°C and powdered.

Results: Uranium L_{III}-edge EXAFS spectra of the uranyl treated xerogel, cells of *P. stutzeri* DSM 5190 and of the biocer particles are shown in Figure 1 together with the corresponding Fourier Transforms (FT).

In all samples uranium is surrounded by two O_{ax} atoms at 1.77 ± 0.02 Å. Backscattering from oxygen atoms lying in the equatorial plane of UO_2^{2+} appears as a single broad peak at about 1.8 Å. For the xerogel and biocer samples, the best fits occur with the inclusion of a second equatorial oxygen shell. The two O_{eq} shells are observed to have radial distances of 2.26 and 2.40 ± 0.02 Å.

The FTs of the uranium complexes formed by xerogel contain a peak at about 2.3 Å and was originated from aproximately 1 atom of silicon at a distance of 3.1 Å. Similar results have been reported for uranyl samples prepared on silica gel at pH 6.14/1/**.** The atomic distance of 3.1 Å for U-Si and the coordination number for Si ca. 1 would imply an adsorption to the surface via complexation with two oxygens bound to the same silicon atom; a bidentate complexation to a single silica center. Monodentate complexation with the surface would be expected to give a coordination number for Si of ca. 1 at a longer distance of 3.80 Å/1/**.**

The broad FT path peak between 2.7 and 3.9 Å in the biocer sample which is found also in the uranium- *P. stutzeri* DSM 5190 spectrum could arise from a phosphorus and the twofold degenerated 3-legged MS path U-O_{eq1}-P.

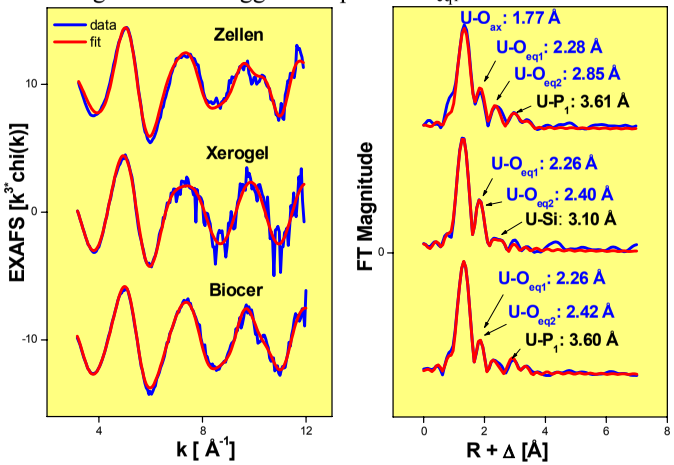

Fig. 1: U L_{III}-edge EXAFS spectra and their corresponding FT of the U complexes formed by the cells of *P. stutzeri*, the xerogel and by the biocer.

Summary: EXAFS spectra indicate that in the case of the cells of *P. stutzeri* DSM 5190, phosphates are the main functional groups implicated in the complexation of uranium in a monodentate binding mode. The sorption of U(VI) by the biocers occurs mainly via phosphate groups. The SiO_2-matrix alone binds U(VI) via silicate groups.

Acknowledgments:
This work was supported by a grant 03I4004B from the Bundesministerium für Bildung und Forschung, Germany.

References:

/1/ Bargar, J. R., et al. Geochim. Cosmochim. Acta **64**, 2737 (2000).

ROBL-CRG	**Experiment title:** **Interaction of actinides with predominant bacteria isolated at nuclear waste repositories using X-ray absorption spectroscopy**	**Experiment number:** **20-01-611**
Beamline: BM 20	**Date of experiment:** From: 03.04.2003 to: 05.04.2003 12.07.2003 to: 13.07.2003	**Date of report:** 18.10.2004
Shifts: 9	**Local contact(s):** Ch. Hennig	*Received at ROBL:*
Names and affiliations of applicants (* indicates experimentalists): H. Moll*, Ch. Hennig*, M. Merroun*, H. Funke*, A. Rossberg*, G. Bernhard, S. Selenska-Pobell		

Report: It is important to increase the knowledge about the role of microorganisms in the migration behavior of actinides. This subject has not yet been studied in detail at the Hard Rock Laboratory in Äspö, Sweden. At this part of the project the research will be focused on the recovered bacterial strain *Desulfovibrio äspöensis* which is indigenous at the Äspö site /1/. In the report published in 2002 we could show that *D. äspöensis* bacteria are able to reduce U(VI) to U(IV). The reason to continue this study was to extend the amount of reduced uranium (app. 20% U(IV) detected in 2002) due to the activity of the cells.

Experimental. After culturing *D. äspöensis* in optimized growth medium, the bacterial cells were obtained by centrifugation. They were washed and re-suspended in a solution of 0.9% NaCl. Four samples were prepared. After shaking the samples for 48 or 168 h under nitrogen atmosphere, the biomass was separated by centrifugation, washed with 0.9% NaCl solution, and sealed in polyethylene cuvettes. The amount of accumulated uranium ranged between 1.37 and 37.35 mgU/$g_{\text{dry weight}}$.

Results. Unfortunately the XANES spectra of all samples showed that the main part of the uranium occurred as U(VI). The amount of U(IV) was always below 5%. This study shows again the difficulties to detect U(IV) formed by microorganisms in the presence of large amounts of U(VI). Our investigations indicated that *D. äspöensis* interacts with U in a complex mechanism consisting of biosorption, bioreduction and bioaccumulation. It seems that in the test samples the biosorption of U(VI) on the cell envelope is the dominating process. The following enzymatic reduction of U(VI) to U(IV) is somehow inhibited. One reason for the difficulties in detecting U(IV) in these samples could be a re-oxidation of U(IV) to U(VI).

In the following we are describing the structure of uranyl biosorbed on the cell envelope of the Gram-negative bacterium *Desulfovibrio äspöensis*. The figure shows a typical uranium L_{III}-edge EXAFS spectrum and the corresponding Fourier transform of the uranium species formed by *D. äspöensis* at pH 5.

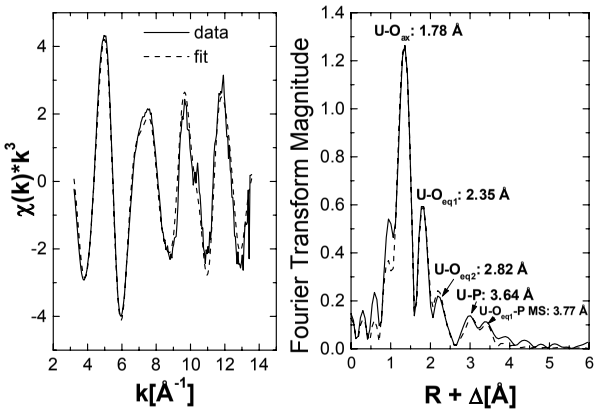

The EXAFS data evaluation yielded an relatively short U-O_{eq1} distance of 2.35 Å. This indicates an intensive interaction of U(VI) with the surface of the bacteria. The U-P distance of 3.64 Å points to a coordination of U(VI) in a mainly monodentate mode to phosphate groups of the cell envelope. Organic phosphato-groups can originate, e.g., from the lipopolysaccharide (LPS) layer and from phosphoryl residues of the polar head of phospholipids in the outer membrane of the cell envelope /2/. We have noticed the close agreement of the structural parameters determined for U in this study with those recently reported for other Gram-negative bacteria, e.g., *Acidithiobacillus ferrooxidans* /3, 4/.

Acknowledgements. This work is supported by the BMWi (no. 02E9491).

Reference

/1/ M. Motamedi, et al.: Int. Syst. Bacteriol. **48**, 311 (1998).
/2/ T. J. Beverige, et al.: Appl. Environ. Microbiol. **42**, 325 (1981).
/3/ M. Merroun, et al.: Radiochim. Acta **91**, 583 (2003).
/4/ M. Merroun, et al.: FZR Annual Report 2002, FZR-373 p. 33 (2003).

ROBL-CRG	**Experiment title:** Study of the surface complexes formed between uranium and thorium and iron corrosion products. Effect of hydroxoapatite on the uptake of uranium	**Experiment number**: **20-01-617**
Beamline: BM20	**Date of experiment**: from: 15/03/03 to: 19/03/03	**Date of report**: June , 2003
Shifts:12	**Local contact(s):** Christoph Hennig	*Received at ROBL:*

Names and affiliations of applicants (* indicates experimentalists):
Lara Duro, Mireia Grivé*, Ferran Seco*, Tiziana Missana, Ursula Alonso

Report:

INTRODUCTION

One of the objectives in these series of experiments is the study of the effect of phosphate or carbonate on the sorption of uranium (VI) onto ferrihydrite and on the type of the surface complexes formed when working in presence of each ligand. On the other hand, the study of the surface complex responsible of the schoepite dissolution under carbonate atmosphere has been studied.

EXPERIMENTAL

Uranium (VI) sorbed onto HFO in phosphate aqueous solution and anoxic conditions

The sorbed uranium onto ferrihydrite samples were prepared at room temperature by equilibrating a weighed amount of powdered ferrihydrite with an uranyl solution containing a well known phosphate concentration ([P]=$5\cdot10^{-4}$ mol·dm^{-3}). This sorption experiments were carried out under $N_{2(g)}$ atmosphere in order to avoid the intrusion of CO_2(g) in the experiment and using a batch procedure. After 6 hours of equilibration, samples were filtered and washed through 0.02 μm pore size filters. The pH of the solution was adjusted to 4.0 by means of diluted $HClO_4$ the final uranium concentration was measured by ICP-MS.

Uranium (VI) sorbed onto HFO in carbonate aqueous solution

The sorbed uranium onto ferrihydrite samples were prepared at room temperature by equilibrating a weighed amount of powdered ferrihydrite with a known uranyl solution ([U]i = $8\cdot10^{-7}$ M). pH of the sample was adjusted to pH=8.26 by additions of $NaHCO_3$ $5\cdot10^{-3}$M. These sorption experiments were carried out under atmospheric conditions and after one day of equilibration samples were filtered and washed through 0.02 μm pore size filters. The final uranium concentration was measured by ICP-MS.

RESULTS

All the EXAFS spectra were collected in fluorescence mode at room temperature and the data analysis was performed using the EXAFSPAK software. Theoretical scattering amplitudes and phases for each adsorber and backscattered pair, U-O (axial and equatorial) and U-Fe, were calculated with the program FEFF8 (Zabinsky et al (1995)). The contribution of a multiple scattering (MS) interaction within the uranyl unit to EXAFS signal was taken into account. A single value of the shift in threshold energy, ΔE_0, was allowed to vary for all coordination shells of a given sample.

According to the results shown in table 1(a) and 1(b), five Oeq are coordinated to the uranyl group at 2.38 Å when phosphate is present and at 2.35 Å when carbonate is present. The large Debye-Waller factor observed for this shell indicates a rather broad distribution of U-Oeq distances,which is higher when phosphate is present in the experiment.

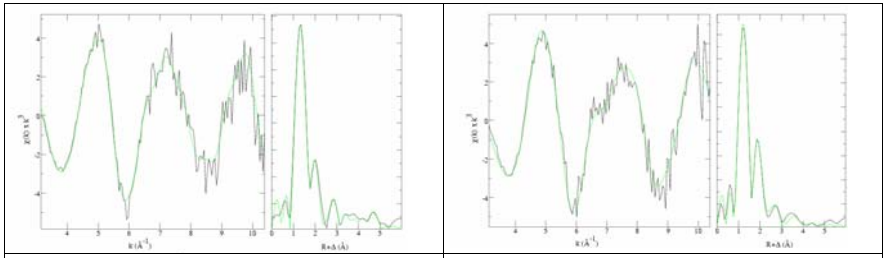

(a) **(b)**

Figure 1: Experimental (solid black line) and fitted (green line) uranium L_{III}-ed k3-weighted EXAFS spectra and their Fourier Transforms: (a) Uranium sorbed onto ferrihydrite with phosphate in the media under anoxic conditions (b) Uranium sorbed onto ferrihydrite with $NaHCO_3$ in the media under atmospheric conditions

Table 1. EXAFS structural parameters

Sample	Shell	R [Å] [a]	N	σ^2 [Å^2]	ΔE_0 [eV]
(a) Uranium sorbed onto HFO with phosphate in the media under anoxic conditions	O_{ax}	1.80	2	0.0008	-3.0
	O_{eq}	2.38	4.5	0.0118	
	Fe	3.44	1.8	0.0091	
	P	3.80	0.6	0.0065	
	U	4.91	1.7	0.0080	
(b) Uranium sorbed onto HFO in carbonate media	O_{ax}	1.74	2.1	0.0014	-10.8
	O_{eq}	2.35	4.4	0.0094	
	C	2.92	2.2	0.0027	
	Fe	3.41	0.7	0.0091	
	U	3.92	0.8	0.0080	

The U-C distance of 2.92 Å (fig 1(b) and table 1(b)) is the distance observed for a bidentate coordination of the CO_3^{2-} group to UO_2^{2+}(Bargar et al., 2000). This interaction may indicate the formation of a ternary complex such as (>FeO_2)$UO_2CO_3^{2-}$.

On the other hand, the distance observed for U-P of 3.80 Å (figure 1(a) and table 1(a)) is a typical distance for bidentate coordination observed when the coordination number for U-Oeq is around six. In our case, the coordination shell corresponding to the U-Oeq is lower (around five), being the typical U-P distance at this coordination number around 3.55 Å. One possible explanation could be that we had a combination of monodentate and bidentate coordination, i.e. a combination of distances U-P of 3.55 Å corresponding to a bidentate phosphate with five Oeq with distances around 3.95 Å corresponding to monodentate phosphate coordination.

Concerning the U-Fe shell, we can see that in the case to have a phosphate media, U has two neighbors Fe atoms at 3.44 Å under the presence of phosphate, while in carbonate media this coordination number decreases to 1 Fe atom at 3.41 Å (table 1(a) and 1(b)). These 0.03 Å of difference can be either a consequence of the error in bond lengths (R±0.02 Å) or a reflect of the different distances between the U-Oeq shell, which is 0.03 Å higher in the case of having phosphate in the media.

Finally, we can see that the distance in the U-U shell is much higher (about 1 Å) when having phosphate than carbonate media. This could be explained because of the larger size of phosphate in front of carbonate. The first ligand, due to steric impediments, makes more difficult the adsorption of additional uranyl units.

REFERENCES

Bargar, J., R., Reitmeyer, R., Lenhart, J.J. and Davis, J.A. (2000). Geochim. Cosmochim. Acta, 64, 16, pp. 2737-2749.

ROBL-CRG	**Experiment title:** **Spectro-electrochemical cell for in situ XAS measurements of uranium solution species**	**Experiment number**: **20-01-618**
Beamline: BM 20	**Date of experiment**: between: 19. 02. 2003 and 25.04. 2004	**Date of report**: 24. 10. 2004
Shifts: 60	**Local contact(s)**: Christoph Hennig	*Received at ROBL:* 24. 10. 2004

Names and affiliations of applicants (* indicates experimentalists):
C. Hennig*, J. Tutschu*, A. Rossberg*, A. Scheinost*, H. Funke*
Forschungszentrum Rossendorf e.V., Institute of Radiochemistry,
D-01314 Dresden, Germany

Report:

While in-situ investigations by combining electrochemical cells with XAS are not new, the prevention of any gas-releasing electrode reaction due to the special safety regulations for actinides required a new electrochemical approach. We used an Ag metal electrode as anode, where Ag^+ is released and precipitates as AgCl. The solved Ag^+ ions are in equilibrium with solid AgCl and the equilibrium potential of the electrode is then given by the solubility constant of the precipitate. In order to avoid a high polarization of the cell, no diaphragm was used. The cell itself consists of a double confinement (Figure 1) following the safety regulations for the use of radioactive samples at the ESRF.

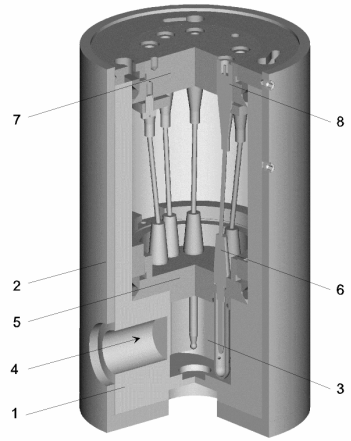

Figure 1. Drawing of the spectro-electrochemical cell.

1 – Cell body of chemically resistant material
2 – Stainless steel housing
3 – Space for the sample solution
4 – X-ray window
5 – Inner cover plate (first compartement)
6 – Electrode
7 – Outer cover plate (second compartement)
8 – Electrical connector

The cell body and the X-ray windows are machined from one piece of chemically resistant material, which is closed by air-tight cover plates. Two X-ray windows are 10 to 20 mm apart from each other to allow sufficient X-ray transmission. The cover plates are screwed gas tight using rubber gaskets. Each cover plate contains up to 6 gas-tight connectors for cables and electrodes. The liquid volume of 10 ml can be agitated by an adjustable magnetic stirrer combined with a specific shaped environment in order to guarantee an nearly laminar liquid flow in the cell. A thermocouple was used for temperature control during the reduction process in the solution. As reference was used the Ag/AgCl potential. As working electrode (cathode) we employed a Pt gauze. The reduction of 0.01 M U(VI) to U(IV) at the cathode is related with a transfer of two electrons. As compensating reaction at the anode 0.02 M Cl^- are needed enabling the precipitation of AgCl. Due to the element-selectivity of X-ray absorption spectroscopy, the dissolved Ag does not disturb the measurements. Additionally in the cell are situated a pH-electrode and a redox electrode. The redox reaction is performed at a constant electrochemical potential for several hours.

Prior preparation of the XANES experiment, independent UV-Vis measurements of the solutions are performed in order to verify that uranium was completely reduced (not shown here). In order to validate the complete reduction of U(VI) to U(IV) at the synchrotron, U L_3 edge XANES spectra are measured (Figure 2, left side). One XANES spectra was obtained each 30 minutes without interrupting the redox procedure. A quantitative analysis of the uranium redox species are performed by iterative transformation factor analysis of the XANES spectra (Figure 2, right side).

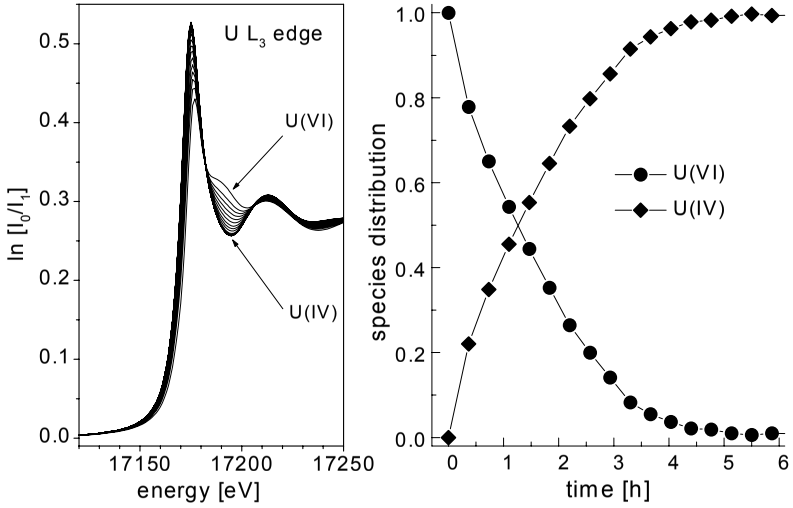

Figure 2. *In situ* XANES measurmenents and species distribution in the solution. Left side: U L_3 edge XANES spectra obtained during the reduction of 0.01M U(VI) in 0.2 M formic acid. The reduction was performed at a constant potential of –350 mV vs. Ag/AgCl. Right side: Distibution of U(VI):U(IV) species extracted by factor analysis.

ESRF	**Experiment title:** EXAFS study of uranium(VI) complexation with dicarboxylic acids	**Experiment number:** 20-01-619
Beamline: BM20	**Date of experiment:** from: 23/04/2003 to: 25/04/2003	**Date of report:** 06/10/2003
Shifts: 6	**Local contact(s):** André ROSSBERG	*Received at ESRF:*

Names and affiliations of applicants (* indicates experimentalists):

Jakob DREBERT, Inés CUESTA HERNANDEZ*, Tobias REICH*, Analia SOLDATI*

Institute of Nuclear Chemistry, Johannes Gutenberg-Universität Mainz

Fritz-Strassmann-Weg 2, 55128 Mainz, Germany

Report:

A recent spectrophotometric study by Havel et al. [1] describes for the first time the formation of two binuclear uranium(VI) complexes with oxalic acid in aqueous solution. Previous studies reported polynuclear species only in solids [2] but not in solutions [3]. The aim of our study was to apply EXAFS spectroscopy to detect and possibly determine the structure of the species $[(UO_2)_2(C_2O_4)_3]^{2-}$ and $[(UO_2)_2(C_2O_4)_5]^{6-}$, which were derived from UV-vis spectroscopy, conductometry, and vapor pressure osmometry [1].

For the EXAFS measurement, nine samples with 10 mM uranium(VI) and an ionic strength of 1 M $NaClO_4$ were prepared at pH 3.0 under ambient conditions. The concentration of oxalic acid in the solutions varied between 0 and 60 mM. According to the equilibrium model of Havel et al. [1], $[(UO_2)_2(C_2O_4)_5]^{6-}$ is the dominating species in solution at an oxalic acid concentration greater than 25 mM (see Fig. 1). Multiple sweeps of the uranium L_3-edge EXAFS spectra were recorded in transmission mode using Ar filled gas ionization chambers. The stability of the solution samples was confirmed by pH measurements and UV-vis spectroscopy (350 – 550 nm) before and after the EXAFS experiments.

The eigenanalysis of the uranium L_3-edge k^3-weighted EXAFS spectra showed that the sample series contained two uranium(VI) species (spectral components) of different molecular structure. Therefore, the experimental spectra shown in Fig. 2 could be reproduced using the first two factors of the eigenanalysis. The relative concentration of these two species was determined by iterative target testing as described in [4] and is shown in Fig. 3. Without oxalic acid present, the 10 mM uranium(VI) solution at pH 3.0 contains only the uranium aquo ion. Its concentration decreases and the relative amount of the second uranium species increases as the oxalic acid concentration increases (see Fig. 3). The EXAFS spectra of the two uranium species and the best theoretical fit to the data are shown in Fig. 4. The corresponding EXAFS structural parameters are summarized in Table 1. The first species, which dominates at low oxalic acid concentrations, shows the characteristic U-O bond distances of the uranium(VI) aquo ion, i.e., 1.76±0.02 and 2.40±0.02 Å. The second species, which dominates the speciation at higher oxalic acid concentrations, is a mononuclear uranium(VI) complex with oxalate ligands. The EXAFS spectrum of the oxalate complex did not show any evidence of an U-U interaction at approximately 3.9 Å, which would be expected if binuclear uranium species were formed. The U-O and U-C bond distances of the aqueous uranium(VI) oxalate complex agree well with recent quantum chemical calculations by Vallet et al. [5] for oxalate ligands forming five-membered chelate rings.

In summary, our uranium L_3-edge EXAFS study did not show any indication of binuclear uranium(VI) species and, therefore, does not support the equilibrium model of Havel et al. shown in Fig. 1. Our data support the equilibrium models of Ferri et al. [3] and the previous work of Havel [6] that include only mononuclear species, i.e., $[UO_2C_2O_4]_{(aq.)}$, $[UO_2(C_2O_4)_2]^{2-}$, and $[UO_2(C_2O_4)_3]^{4-}$.

Acknowledgement A. Soldati was supported by a fellowship of DFG Graduiertenkolleg GRK 826/1. We thank C. Hennig, A. Rossberg, and A. Scheinost for their support during the EXAFS measurement.

References

[1] Havel J., Soto-Guerrero J., Lubal P. Polyhedron 21 (2002) 1411
[2] Tschernajev I.I. (Ed.) Complex Compounds of Uranium, Nauka, Moscow, 1964 (in Russian)
[3] Ferri D., Iuliano M., Manfredi C., et al. J. Chem. Soc., Dalton Trans. (2000) 3460
[4] Rossberg A., Reich T., Bernhard G. Analyt. Bioanalyt. Chem. 376 (2003) 631
[5] Vallet V., Moll H., Wahlgren U., Szabo Z., Grenthe I. Inorg. Chem. 42 (2003) 1982
[6] Havel J. Collect. Czech. Chem.. Commun. 34 (1969) 2348

Table 1 EXAFS structural parameters for the two spectral components

Species	Shell	N	R (Å)	σ^2(Å^2)	ΔE_0 (eV)
Oxalate complex	Oax	2.1	1.78	0.0021	-8.7
	Oeq	5.2	2.38	0.0063	
	C	5.2*	3.26	0.0078	
	C (MS)	10.4*	3.38	0.0022	
	O (MS)	5.2*	4.44	0.0041	
Aquo ion	Oax	2.2	1.76	0.0021	-9.1
	Oeq	5.6	2.40	0.0079	

* Parameter linked to Oeq during the fit.

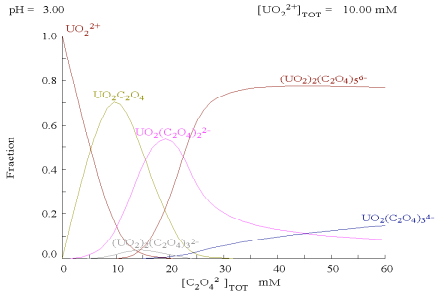

Fig. 1 Distribution diagram for solutions of $[UO_2^{2+}]_{total}$=10 mM, pH 3, I=3 M $NaClO_4$, and $[C_2O_4^{2-}]_{total}$ varying from 0 to 60 mM at 25 °C. According to ref. [1].

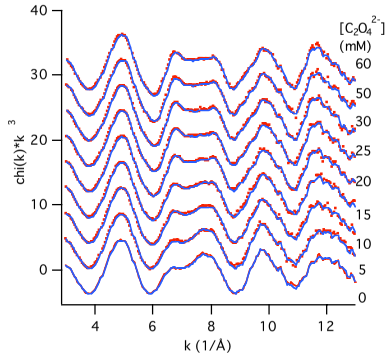

Fig. 2 Raw U L_3-edge k^3-weighted EXAFS spectra (dots) and their abstract reproductions (solid line).

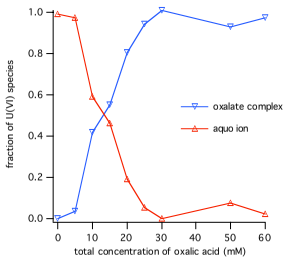

Fig. 3 The real concentration distribution of the U(VI) species as a function of pH.

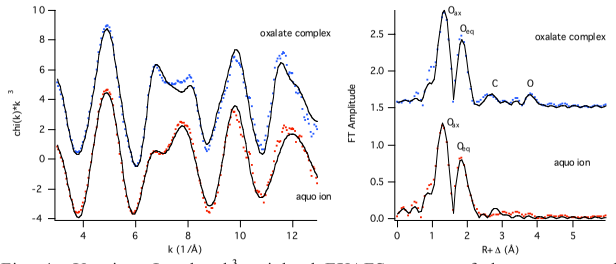

Fig. 4 Uranium L_3-edge k^3-weighted EXAFS spectra of the two spectral components (left) and their corresponding Fourier transforms (right). Solid line – best theoretical fit to the data (dots).

FZR ROBL-CRG	**Experiment title:** **Uranium (VI) sorption on clinochlore surfaces**	**Experiment number:** **20-01-621**
Beamline: BM 20	**Date of experiment:** from: 14.06. to: 16.06.2003	**Date of report:** 15.11.04
Shifts: 5	**Local contact(s):** H. Funke	*Received at ROBL:* 16.11.04

Names and affiliations of applicants (* indicates experimentalists):

M. Walter, T. Arnold, G. Bernhard, H. Funke*, C. Hennig*, A. Scheinost*, H. Moll*, A. Rossberg*, M. Merroun*

Forschungszentrum Rossendorf e.V., Institut für Radiochemie, P.O. Box 510119, D-01314 Dresden

Report:

Pyrophyllite, $Al_2[(OH)_2/Si_4O_{10}]$, is a 2:1 sheet silicate mineral with marginal substitution of both cationic positions. It can be used as a reference compound for iron–rich chlorites, where the uranium(VI) sorption occur as well on chlorite as on secondary formed ferric iron oxides /1/.

Experimental

Two different grain sizes (2–6.3 µm: 9.3 m^2/g, <2µm: 15.7m^2/g) of pyrophyllite were used for sorption experiments to study U(VI) surface species at low and intermediate surface coverage. Briefly, 200 mg of pyrophyllite were dispersed in 500 ml 0.01 M $NaClO_4$ solution. Before U(VI) adding, the suspensions were equilibrated for 4 weeks to adjust the pH value to 5.8 and 6.9, respectively. The initial U(VI) concentrations were set to $2 \cdot 10^{-6}$ and $1 \cdot 10^{-5}$. After a reaction period of approx. 40 hours, the suspensions were centrifuged and the sorption samples were prepared as wet pastes in Teflon sample holders for XAS measurements.

The X-ray absorption measurements were performed at the ROBL-CRG in fluorescence mode using a 4-element germanium solid-state detector. In addition to the XAS measurements, time–resolved laser–induced fluorescence spectra (TRLFS) were recorded to obtain information about the formed uranium(VI) surface species. For further details see reference /2, 3/.

Results

The time–resolved fluorescence spectra indicate the presence of three U(VI) surface species, which are characterized by different lifetimes and nearly identical fluorescence spectra /2, 3/.

The EXAFS spectra were fitted with two axial oxygen's O_{ax} at 1.78 Å and 4–5 equatorial oxygen's O_{eq} at a distance of 2.36 Å. In combination with the large disorder of the O_{eq} shell such short U–O_{eq} distances are typical for inner sphere surface complex formation.

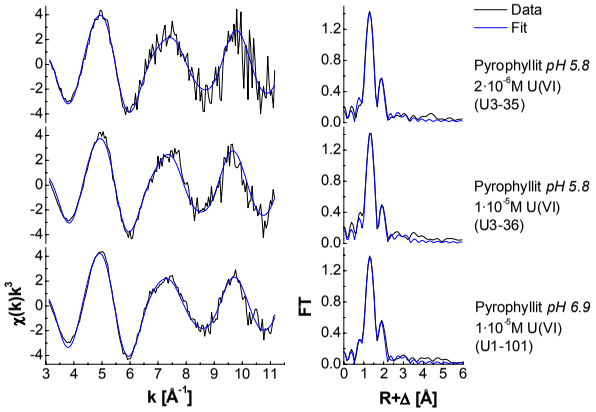

The uranium(VI) sorption on pyrophyllite occurs – even at low surface coverage – by the formation of three surface species. Consequently, the measured EXAFS spectra contain the averaged structural information. This may preclude the identification of the detailed surface complex structure by EXAFS spectroscopy.

U(VI) - sample	Shell	N	R (Å)	σ^2 (Å^2)	ΔE_0
Pyrophyllit *pH 5.8*	O_{ax}	2.0[a]	1.77	0.0020	0 eV
$2 \cdot 10^{-6}$ M U(VI)	O_{eq}	4.4	2.36	0.015	
(U3-35)					
Pyrophyllit *pH 5.8*	O_{ax}	2[a]	1.79	0.0017	3 eV
$1 \cdot 10^{-5}$ M U(VI)	O_{eq}	4.0	2.38	0.017	
(U3-36)					
Pyrophyllit *pH 6.9*	O_{ax}	2.3	1.78	0.0033	1 eV
$1 \cdot 10^{-5}$ M U(VI)	O_{eq}	5.1	2.36	0.016	
(U1-101)					

[a] Parameter was fixed during the fit, ΔN = 25 %, ΔR = 0.02 Å

References:

/1/ Arnold, T., et al., Chem. Geol. **151**, 129-141 (1998)
/2/ Walter M., et al., Report FZR-400, p.35 (2003)
/3/ Walter M., Dissertation, TU Dresden (2004)

ROBL-CRG	**Experiment title:** **Chemical speciation of metals in shooting-range soils**	**Experiment number:** **20-01-622**
Beamline: BM 20	**Date of experiment:** 25.4.-29.4.03 27.01.-29.01.04	**Date of report:** 05.12.2004
Shifts: 18	**Local contact(s):** A. Scheinost	*Received at ROBL:*

Names and affiliations of applicants (* indicates experimentalists):

A. Scheinost, FZR*
Ch. Hennig, FZR*
D. Vantelon, ETH Zurich*
A. Rossberg, FZR*
H. Funke, FZR*

Report:

For many decades, lead bullets deposited in shooting-range soils have been considered a low toxic risk because of low solubility of metallic lead. More recently, however, it has been found that these bullets rapidly corrode and sometimes completely dissolve in soils within a few years. While the fate of Pb was investigated by other studies (*1-3*), the intention of this study was to elucidate the fate of Sb by determining the Sb speciation in shooting range soils.

Nine soil samples were collected at six shooting ranges in Switzerland, representing a wide range of geochemical conditions including pH, organic and inorganic carbon content and mineralogy, and representing a range of Sb (and Pb) pollution levels. Antimony K-edge EXAFS spectra were collected at the Rossendorf Beamline (BM20) at the ESRF in fluorescence mode. Sample cooling to 20 K using a He cryostat greatly improved spectra quality due to reduction of the thermal contributions to the Debye-Waller factors, and was applied to all samples. Quantitative speciation was performed by applying iterative target transformation factor analysis (ITFA) to the set of k^3-weighted chi spectra (*4, 5*).

The EXAFS spectra are shown in Figure 1. All nine spectra could be reconstructed using two spectral components, suggesting that all samples contained only two Sb species. Using Iterative Target Test Factor Analysis, the spectra of the two species and the relative amount of the two species in each sample were determined. Using shell fitting, species 1 was identified as metallic Sb, while species 2 was identified either as Sb(V) sorbed to an Fe or Mn (hydr) oxide, or as Sb(V) antimonate (table 1). The speciation, i.e. the distribution among the two species was variable and did not follow a clear geochemical pattern.

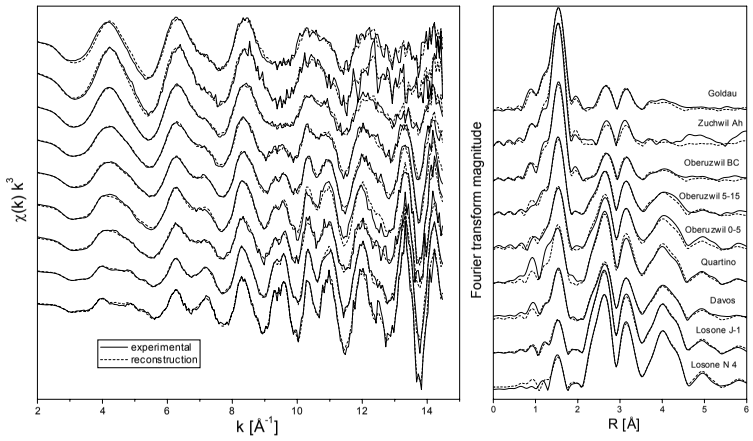

Fig. 1. Antimony K-edge EXAFS spectra of soil samples from 6 different shooting ranges (full lines), and their reconstruction with 2 principal components (dotted lines).

Table 1. Local structure of species 1 and 2 and of selected references.

	Coordination shell			Further shells				
Sample	CN[1] and element	R [Å][2]	σ^2 [Å^2][3]	CN and element	R [Å]	σ^2 [Å^2]	ΔE_0 [eV][4]	χ^2_{res} %[5]
Species 1	2.1 Sb	2.90	0.0013	2.1 Sb 6.7 Sb 6.1 Sb	3.35 4.30 4.51	0.0027 0.0045 0.0039	6.6	7.5
Species 2	5.3 O	1.98	0.0033	1.1 Fe 1.4 Sb	3.10 3.35	0.0026 0.0053	8.1	3.3
Sb metal	2.2 Sb	2.91	0.0013	1.8 Sb 6.9 Sb 6.3 Sb	3.34 4.29 4.49	0.0021 0.0047 0.0056	9.5	13.0
Sb(V) sorbed goethite	6.1 O	1.99	0.0042	1.0 Fe	3.08	0.0030	7.7	9.2
Sb(V) antimo-nate	6.1 O	1.98	0.0043	2.4 Fe 2.9 Sb 2.3 Sb	3.08 3.37 3.62	0.0080 0.0070 0.0070	5.6	7.4

REFERENCES

1. L. Knechtenhofer, Diploma Thesis, Swiss Federal Institute of Technology (ETH) (2002).
2. L. A. Knechtenhofer, I. O. Xifra, A. C. Scheinost, H. Flühler, R. Kretzschmar, *Journal of Plant Nutrition and Soil Science* 166, 84-92 (2003).
3. D. Vantelon *et al.*, *Geochimica et Cosmochimica Acta* 66, A799-A799 (Aug, 2002).
4. A. C. Scheinost, A. Rossberg, M. Marcus, S. Pfister, R. Kretzschmar, *Physica Scripta*, in press (2004).
5. A. Rossberg, T. Reich, G. Bernhard, *Analytical and Bioanalytical Chemistry* 376, 631-638 (2003).

[1] Coordination number
[2] Radial distance
[3] Debye-Waller factor
[4] Phase shift
[5] Fit error

ROBL-CRG	**Experiment title:** **Low-temperature phase-transition of $H[UO_2AsO_4]\cdot 4H_2O$**	**Experiment number:** **20-01-623**
Beamline: BM 20	**Date of experiment:** from: 30. 4. 2003 to: 6. 5. 2003	**Date of report:** 24. 10. 2004
Shifts: 18	**Local contact(s):** Christoph Hennig	*Received at ROBL:* 24. 10. 2004

Names and affiliations of applicants (* indicates experimentalists):
Christoph Hennig*, Harald Funke*
Forschungszentrum Rossendorf e.V., Institute of Radiochemistry,
D-01314 Dresden, Germany

Report:

The EXAFS Debye-Waller factor is different from that determined with XRD. The Debye-Waller factor of EXAFS is a mean square relative displacement (MSRD) between absorbing and backscattering atom, whereas XRD experiments provide the mean square absolute displacements (MSD). The EXAFS Debye-Waller factor σ comprises two components σ_{stat} and σ_{vib} due to static structural disorder and thermal vibrations, respectively. Assuming disorder effects with symmetric pair distribution function for static disorder and harmonic vibrations for thermal disorder, the Debye-Waller factor is given by $\sigma^2 = \sigma_{stat}^2 + \sigma_{vibv}^2$. These two factors can be separated by temperature dependent measurement of $\sigma(T)$. For small disorder effects with $\Delta r < 0.1$ Å the terms can be combined to one single term corresponding to the average distance whereas for $\Delta r > 0.1$ Å the EXAFS equation must be averaged over a pair distribution function g(r) including asymmetric correlation functions or/and anharmonic vibrations as described as example by the cumulant approach. EXAFS is sensitive only to relative motion along the bond direction. At T = 297 K the U-O_{eq} distances in $H[UO_2AsO_4]\cdot 4H_2O$ are equal due to the space group symmetry P4/nnc. After the low-temperature phase transition P4/nnc → P$\bar{1}$ the atomic positions O_{eq} will become symmetry independent [1,2]. Hence, the U-O_{eq} distance becomes different and it is expected that σ_{stat} increases which should affect the function $\sigma(T)$ [3].
EXAFS measurements were performed in transmission mode at the U L_{III} edge and the As K edge in the temperature range of 20 K - 297 K using a He cryostate. The solid powder samples were prepared as pellets and fixed into a teflon sample holder. EXAFS signals have been extracted and Fourier transformed in the *k*-range of 3.2 - 15.7 $Å^{-1}$ (Fig. 1). Backscattering shells were separated by Fourier filtering. Subsequent data analysis was performed by fixing the coordination number according the crystallographic values. Distances R, Debye-Waller-Factors σ^2, and energy shifts ΔE were used as free fit parameters.
We observed a strong temperature dependence of the U-As scattering pair $R_{(U\text{-}As)}$ = 3.69 Å (Fig. 2). The temperature dependence of the scattering pair U-O_{eq} is less pronounced. However, we observed no P4/nnc → P$\bar{1}$ phase transition. In principle, the metal - oxygen bond is sensitive for phase transitions: Sani et al [4] observed a phase transition in $La_{1.48}Nd_{0.4}Sr_{0.12}CuO_4$ using the σ^2 of the Cu-O scattering pair. In contrast to the σ^2(U-O_{eq}), σ^2(U-O_{ax}) is almost constant over the whole temperature range. It indicates that this covalent bonding is not significant influenced by thermal vibrations.

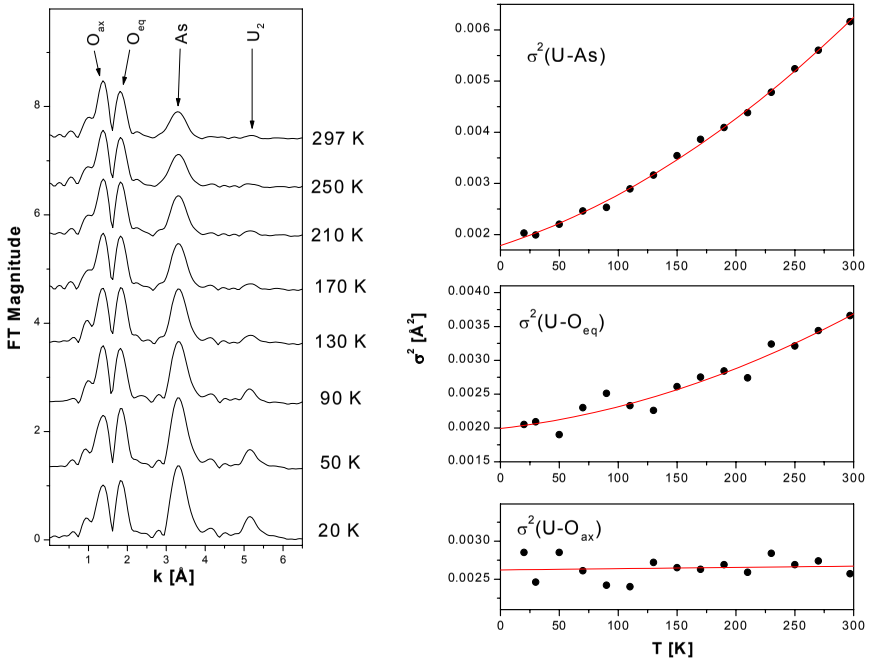

Figure 1: Left: Fourier transform of the U L_{III}-edge k^3-weighted EXAFS data of k = 3.2 - 15.7 $Å^{-1}$. Right: Temperature dependence of EXAFS Debye-Waller factor for the first three backscattering shells.

References

[1] Fitch, A.N. et al. Acta Cryst. C **39** (1983) 159.
[2] Fitch, A.N. et al. Acta Cryst. B **39** (1982) 2546.
[3] Hennig, C. et al. J. Synchr. Rad. **8** (2001) 695.
[4] Sani, N.L. et al. Phys. Rev. B64 (2001) 132510.

FZR ROBL-CRG	**Experiment title:** **Speciation of Zn in rhizosphere soil**	**Experiment number**: **20-01-624**
Beamline: BM 20	**Date of experiment**: from 14.05.03 to 18.05.03 from 07.07.04 to 12.07.04	**Date of report**: 11.10.2004
Shifts: 26	**Local contact(s)**: H. Funke, A. Scheinost	*Received at ROBL:*

Names and affiliations of applicants (* indicates experimentalists):

*A. Scheinost, *C. Hennig, *A. Rossberg, *H. Funke
Institute of Radiochemistry, FZR, Dresden, Germany

*A. Voegelin, *S. Pfister
Institute of Terrestrial Ecology, ETH Zurich, Switzerland

Report:

Zinc is an essential nutrient for plants, but may also be phytotoxic at elevated concentrations, depending on its chemical speciation. In soils, Zn bearing contaminants dissolve and Zn either adsorbs to the soil matrix or precipitates in new mineral phases. Soil contamination with sphalerite (ZnS) may results from mining and smelting activities or from the application of dredged sediments. Zincite (ZnO) is emitted from brass foundries. In this study, we investigate the transformation of ZnS and ZnO in 4 soils with differing properties (Table 1). The soils were spiked with ZnS or ZnO to achieve a Zn concentration of 2000 ppm and incubated for 2 years (moisture ~ 50% field capacity). Samples for solid phase and solution characterization were collected after 1 and 2 years. Zn K-edge spectra (Figure 1) were evaluated by linear combination fits. The results (Table 1) indicate that ZnS dissolves more slowly in the acidic soils. The oxidation of sulfide produces acidity, which is not buffered in the acidic soils, potentially inhibiting further sulfide oxidation and ZnS dissolution. The reason for the slow ZnS dissolution in the calcareous Hu soil is not yet clear. The ZnO dissolved much faster than ZnS and with an opposite pH dependence. Almost all ZnO was dissolved in the acidic soils U1 and Rie, whereas ~20% are still present in the soils ZB and Hu. The Fourier transforms point to the incorporation of Zn into HIM in the acidic soils. In the soils ZB and Hu, the second shell peak points to the incorporation of Zn into a brucite-like structure similar to Zn-Talc. We currently analyze soil solutions collected after 1 and 2 years for major and trace elements, anions, and organic carbon. Combining solid phase and solution speciation data will allow for a more detailed understanding of the factors affecting ZnS and ZnO dissolution in different soils.

Table 1: Soil properties and results from linear combination fits

				dissolution in 2 years	
Soil	pH	Clay	Composition	ZnS (%)	ZnO (%)
U1	5.0	47%	kaolinite, HIM	20%	95%
Rie	4.2	16%	mixed clay mineralogy	55%	100%
Hu	7.7	n.d.	~1.5% $CaCO_3$	60%	82%
ZB	6.5	16%	mixed clay mineralogy	83%	82%

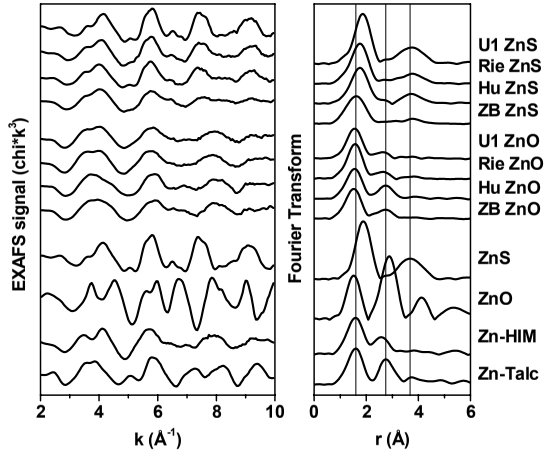

Figure 1: Zn K-edge spectra for soils incubated for 2 years with either ZnS or ZnO, for ZnS and ZnO, and for Zn in Al-hydroxy interlayered montmorillonite (HIM) and Zn-Talc ($Zn_3Si_4O_{10}(OH)_2$).

ROBL-CRG	**Experiment title:** **Interaction between microorganisms and metals using bacteria**	**Experiment number:** **20-01-625**
Beamline: BM 20	**Date of experiment:** from: 10.06.03 to: 12.06.03; from 9.11.03 to:11.11.03; 29.04-3.5.04; 5.7-6.7.04; 24.-26.09.04	**Date of report:** 20.11.04
Shifts: 32	**Local contact(s):** Dr. Andreas Scheinost	*Received at ROBL:*
Names and affiliations of applicants (* indicates experimentalists): M. Merroun*, K. Pollmann, J. Raff, A. Scheinost*, A. Rossberg*, C. Hennig*, H. Funke*, S. Selenska-Pobell		

Report: Metallic nanostructures are promising candidates for the development of sensors, catalysts and nanoscopic electrical connections. Palladium is one of the most widely used metals in transition metal catalyzed organic synthesis, as it is capable of catalyzing a wide variety of commercially important reactions. It has also been used as catalyst for removing nitrate ion from drinking water, for hydrogenation and for combustion reactions. In this work the formation of Pd nanoclusters at the cells and S-layer of *B. sphaericus* JG-A12 was studied using EXAFS spectroscopy.

Experimental: *B. sphaericus* cells were grown in a batch culture to mid exponential phase and harvested by centrifugation at 10.000 rpm for 30 min. Afterwords, the cells were washed in MOPS/NaOH buffer pH 7.0 several times. To palladise *B. sphaericus* JG-A12 cells, 50 ml of 2 Mm Pd(II) solution (Na_2PdCl_4) was poured into 55 ml serum bottles and degassed under nitrogen for 15 min. The reduction of Pd was induced by the use of H_2 gas.

Results: Palladium K-edge EXAFS spectra of the Pd deposition on the cells and the S-layer protein sheets of *B. sphaericus* JG-A12 in presence and absence of H_2 and their corresponding Fourier transforms (FT) are shown in Fig. 1.

In the presence of H_2, and using Pd-Pd shell parameters of a Pd foil as a reference, all peaks of the FT spectra of the cells and S-layer/Pd composites were attributed to four Pd-Pd shells with distances of 2.75, 3.88, 4.77 and 5.42 Å. A better estimate of the average cluster size is obtained from the number of the first neighbours (5-6.3) which is considerably lower than the coordination number of 12 of an infinite lattice.

According to Mojet B.L. /1/ and Kodre et al. /2/ the range coordination number between 5 and 6.3 of the first shell found in this work is reached in a cluster with a diameter range smaller than 10Å, formed at a layer of nearest neighbors around a central atom.

In the absence of H_2, The FT spectra of the two Pd treated samples show both Pd-O and Pd-C contributions at distances of 2.02 and 2.90 Å, indicating the implication of carboxyl groups in the complexation of Pd. These results are confirmed by the use of other techniques such as Infrared spectroscopy.

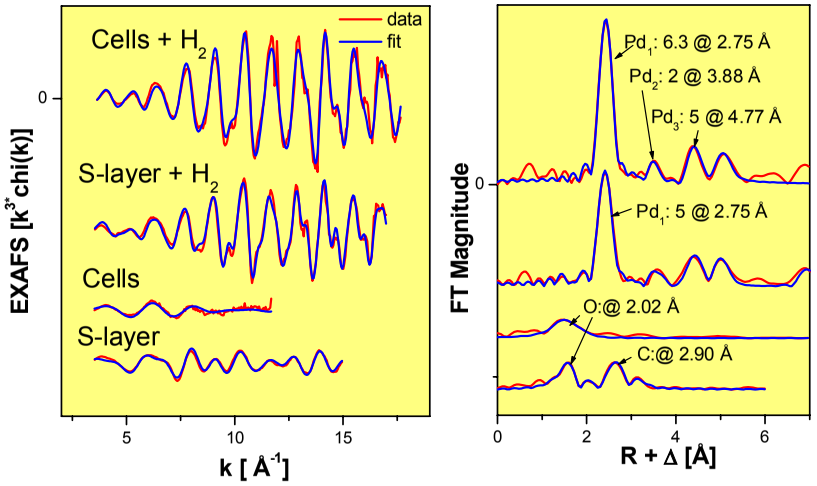

Fig. 1: Pd K-edge EXAFS spectra and their corresponding FT of the Pd nanoclusters and Pd complexes formed at the cells and S-layer of *B. sphaericus* JG-A12.

The cells and S-layer sheets of *B. sphaericus* JG-A12 are able to reduce Pd and to form Pd nanoclusters with a size smaller than 1 nm in the presence of molecular H_2 as electron donor. However, in the absence of this reducing agent, the Pd is bound to the carboxyl groups of these two biocomponents.

References:

/1/Mojet, B.L . PhD Thesis 1997.
/2/ Kodre et al. J. 1999. Synchrotron Rad. 6:458-459.

Acknowledgments:

This study was supported by EU grant GRD1-2001-40424. I. Mikheenko form the School of Biosciences, Univeristy of Birmingham, UK, is thanked for the palladisation of the *B. sphaericus* JG-A12 cells .

FZR ROBL-CRG	**Experiment title:** **Oxidation state and local structure of uranium in soils and sediments**	**Experiment number**: **20-01-626**
Beamline: BM 20	**Date of experiment**: 1.8.-3.8.03; 27.09.-2.10.03; 29.01.-31.01.04; 28.07.-2.08.04; 03.-06.09.04; 22.-23.09.04; 02.-03.10.04	**Date of report**: 05.12.2004
Shifts: 56	**Local contact(s)**: A. Scheinost, A. Rossberg	*Received at ROBL:*

Names and affiliations of applicants (* indicates experimentalists):

A. Scheinost, FZR*
Ch. Hennig, FZR*
A. Rossberg, FZR*
H. Funke, FZR*

Report:

Forty years of uranium mining in the German state of Saxony have left a legacy of uranium-contaminated pits, waste piles, mine tailings and surrounding soils. Since 1963, and more extensively since 1989, contaminated sites were covered in order to protect people and environment in this densely populated area. By both the mining and the clean-up activities, the natural geochemical cycle of uranium is greatly perturbed. Tetravalent uranium is enriched in the geological deposits because of its low solubility and mobility. During the ore extraction, it is converted to its highly mobile hexavalent state, which presents an immediate risk for the environment. After covering by soil materials, microbial and surface-catalytic reduction and precipitation may transform uranium back to immobile tetravalent or hexavalent mineral species. The mechanisms and kinetics of this last step, which takes place since the remediation, are largely unknown, but are essential to predict the long-term risk of these covered deposits.

Five sediment samples were collected from covered mine tailings in the Freital area, representing different U extraction procedures (sulfuric acid or carbonate), covering material (municipal and mine waste, pH, redox and elemental composition. In addition, two contaminated surface soil samples were collected. Uranium L_{III}-edge EXAFS spectra were measured at the Rossendorf Beamline (BM20) at the ESRF in fluorescence mode. In this project, great experimental difficulties had to be overcome, related to the relatively low U concentrations (200-500 mg/kg) and the high Sr and Rb concentrations leading to strongly overlapping fluorescence lines. Finally, having available a new 13-element detector with digital electronics for both high energy resolution and high count rate, EXAFS spectra of reasonable quality could be collected (Fig. 1).

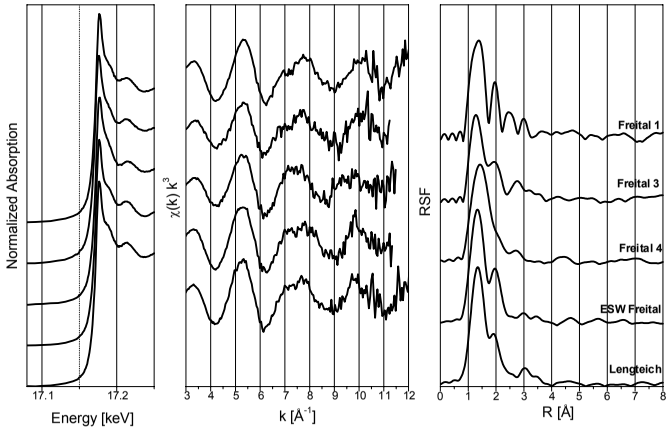

Fig. 1. U L_{III}-edge EXAFS spectra of 3 sediment (Freital 1-4) and 2 soil samples.

All XANES, EXAFS and Fourier Transform spectra are dominated by features indicative of the uranyl unit, i.e. indicate the predominance of U(VI). Selective chemical extractions and principal component analysis indicated the presence of several species. Hence, a linear combination fit was performed, using k^3-weighted EXAFS spectra of samples and 15 references (see experimental report 20-01-642). The results suggest that both U(VI) silicates (soddyite, boltwoodite) and alkaline U(VI) hydroxides and sulfates (zippeite, billietite) prevail. Only one sample showed a small amount of U(IV) in pitchblende, which may be due to incomplete U extraction or secondary precipitation. In contrast, soil samples collected near the impact zone of DU tank penetrators (samples Iraq) contain U(VI) and U(IV) minerals in more equal quantities. Considering the different "equilibration" periods of both types of samples (< 10 years for Iraq samples, 30-50 years for U mining samples), both types of samples suggest formation of U(VI) minerals in surface and subsurface (>50 m) environments after contamination.

Table 1. Linear combination fit results.

	Soddyite	Boltwood.	Zippeite	Billietite	Bayleyite	Uraninite	Sum	χres
ESW	43		57				100	0.60
Lengteich	35		71				105	0.63
Freital 1	57		37				94	0.65
Freital 3	35		39			13	87	0.51
Freital 4	40			63			102	0.26
Iraq 5.6		42				67	109	0.24
Iraq 6.1.1				54		61	116	0.26
Iraq 7.3					32	51	84	0.25

ROBL-CRG	**Experiment title:** **Polarization dependency of x-ray absorption fine structure on the uranyl unit**	**Experiment number**: **20-01-629**
Beamline: BM 20	**Date of experiment**: between: 24. 09. 2003 and 27. 09. 2003	**Date of report**: 24. 10. 2004
Shifts: 9	**Local contact(s)**: Christoph Hennig	*Received at ROBL:* 24. 10. 2004

Names and affiliations of applicants (* indicates experimentalists):
Christoph Hennig*
Forschungszentrum Rossendorf, Inst. of Radiochemistry, D-01314 Dresden

Report:

In anisotropic materials the amplitude of the EXAFS spectrum and thus the coordination number *N* depends on the angle θ between the polarization vector $\vec{\varepsilon}$ and the vector $\vec{r}$ connecting the absorbing and backscattering atoms /1/. As result, the real or crystallographic coordination number N_{cryst} is detected as a function of θ and appears as effective coordination number N_{eff}. For a single-scattering process and in plane–wave approximation the angular dependence can be written for both L_1 and *K* edges as:

$$N_{eff}(\theta) = \sum_{n=1}^{N} 3\left|\vec{\varepsilon}\cdot\vec{r}\right|^2 \qquad (1)$$

The curved-wave approximation of the photoelectron scattering includes a second order term /2/, which is negligible. In most cases $\vec{r}$ is unknown. In order to relate $\vec{\varepsilon}$ and $\vec{r}$ to morphological parameters of the sample, θ is divided into two angles, where α is the angle between $\vec{\varepsilon}$ and a morphological plane of the sample and β is the angle between $\vec{r}$ and the normal vector $\vec{n}$ of the morphological plane /3/:

$$\left|\vec{\varepsilon}\cdot\vec{r}\right|^2 = \cos^2\theta = \cos^2\beta\sin^2\alpha + (\sin^2\beta\cos^2\alpha)/2 \qquad (2)$$

The effective coordination number N_{eff} is then related to the real crystallographic coordination N_{cryst} by:

$$N_{eff}(\theta) = N_{cryst}\,3\left(\cos^2\beta\sin^2\alpha + (\sin^2\beta\cos^2\alpha)/2\right) \qquad (3)$$

A special case happens if $|\vec{n}\cdot\vec{r}|^2 = 1/3$, as discussed by Pettifer et al. as “magic angle theorem” /4/. In that situation the value N_{eff} is independent of β for an angle of α = 35.3°, and inversely, N_{eff} is independent of α at β = 54.7° /4,5/.

We investigated the polarization effect on the coordination number using a single crystal of $Ca[UO_2PO_4]_2{\cdot}6H_2O$ measured in transmissen mode and ambient temperature. In order to tilt the sample along α, an uniaxial goniometer was used. EXAFS measuremets were taken at α = 0°, 15°, 35° 55° and 75°. For the first fit the spectrum collected at the magic angle (35°) was chosen. The coordination numbers were fixed to the crystallographic values ($N_{eff} = N_{cryst}$) and S_0^2 was fixed to 1. Free fit parameters were the distances U-O_{ax} and U-O_{eq}, the associated Debye-Waller factors σ^2 and ΔE. For all other angles N_{eff} was fitted, while σ^2 were fixed at the values determined for the magic angle. The fit results for the coordination numbers N_{eff} in comparison to the theoretical values according equation (3) are shown in the Figure.

The polarization dependence of U L_1 edge EXAFS spectra is relatively simple because the photoelectron is excited from a ground state *s* (*l* = 0) to one excited state (l = 1). By contrast, the polarization dependence is more complicated at the L_2 and L_3 edges were the photoelectron is excited from p ground state into final states s (l = 0) and d (l = 2). The EXAFS expression of L_2 and L_3 edges comprises here pure s, pure d and coupled s-d states. Defining *c* as the ratio between the radial dipol matrix elements M_{01} and M_{21} coupling the initial *2p* wave function with the *l = 0* and *l = 2* final states, the coordination number can be expressed as a sum of three effective partial coordination numbers /3/:

$$N_{eff}^{d}(\theta) = 0.5\left[\frac{2}{2+c^2}\right]\sum_{i=1}^{N}(1+3\left|\vec{\varepsilon}\cdot\vec{r}\right|^2) \qquad (4)$$

$$N_{eff}^{s} = 0.5\left[\frac{c^2}{2+c^2}\right] \qquad (5)$$

$$N_{eff}^{sd}(\theta) = \left[\frac{2c}{2+c^2}\right]\sum_{i=1}^{N}(1-3\left|\vec{\varepsilon}\cdot\vec{r}\right|^2) \qquad (6)$$

The value *c* is relatively independent of *k* and has been approximated to 0.2 for elements with *Z* > 20. Using *c* = 0.2 in eq. 1-3 and neglecting the N_{eff}^{s} term the expression can be approximated according /3/ by:

$$N_{eff}(\theta) = \sum_{i=1}^{N}(0.7 + 0.9\left|\vec{\varepsilon}\cdot\vec{r}\right|^2) \qquad (7)$$

The Figure shows the fit results for the coordination numbers N_{eff} in comparison to the theoretical values according eq. 4. In this figure is clearly visible, that the polarization dependency at the L_3 edge is less pronounced than that at the L_1 edge. The dominant contribution at the L_3 edge, N_{eff}^{d}, running with $1+3\cos^2\theta$, has a similar angle dependence as N_{eff} at the L_1 edge but its influence is attenuated by the N_{eff}^{sd} cross term running with $1-3\cos^2\theta$ in the opposite direction. In consequence, for studies of polarization dependence one should favour measurements at the U L_1 edge. Otherwise, the use of the L_3 edge seems to be more preferable for diluted samples due to the higher signal intensity.

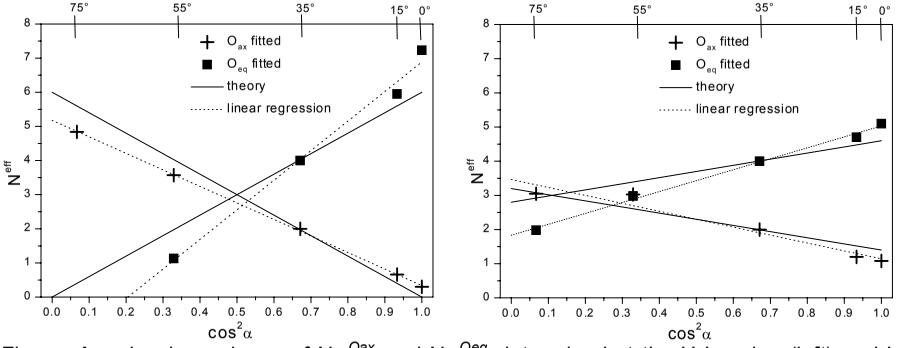

Figure: Angular dependence of N_{eff}^{Oax} and N_{eff}^{Oeq} determined at the U L_1-edge (left) and L_3-edge (right) and in comparison with the theory.

/1/ Stöhr, J. et al., Phys. Rev. B **27** 5146 (1983), /2/ Benfatto, M., et al., Phys.Rev. B **39** 1936 (1989), /3/ Citrin, P.H., Phys. Rev. B **31** 700 (1985), /4/ Pettifer, R.F., et al. Phys. Rev. B **42** 37 (1990), /5/ Manceau, A., et al. Phys. Chem. Min. 347 (1998)

ROBL-CRG	**Experiment title:** **The structure of organic uranium complexes at low temperature**	**Experiment number**: **20-01-630**
Beamline: BM 20	**Date of experiment**: from 31.01. to: 03.02.04 25.04. 29.04.04 08.06. 10.06.04 02.08. 04.08.04	**Date of report**: 22.11.04
Shifts: 30	**Local contact(s)**: André Rossberg	*Received at ROBL:*

Names and affiliations of applicants (* indicates experimentalists):
A. Rossberg[1], A. Scheinost[1], G. Geipel[2]
[1]ESRF-ROBL/CRG, Avenue des Martyrs, B.P. 220, 38043 Grenoble Cedex, France
[2]Forschungszentrum Rossendorf e.V., Institute for Radiochemistry, P.O. Box 510119, 01314 Dresden, Germany

Report

One possibility to improve the EXAFS spectral data quality is to cool the samples to low temperatures to decrease the thermal disorder. We compare measurements of aqueous U(VI)/salicylic acid (SAL) complexes recorded at room temperature and at 20K.

Results and discussion

The k^3-weighted U L_{III}-edge EXAFS spectra of the pH-series with the initial concentration of [U(VI)] = 10 mM and [SAL] = 50 mM, were recorded at room temperature (RT) and at 20K in fluorescent mode (Fig. 1). In addition the precipitates at pH 4 and 8 of the aqueous solutions were measured at room temperature in transmission mode (Fig. 2). For RT and 20K all spectra can be reproduced by three structural different complex species (Fig. 1). According to speciation calculation, at low pH only the carboxylic group interacts with U(VI) by forming the complex UO_2HSAL^+. At higher pH the deprotonation of the OH group leads to $UO_2SAL(aq)$ and $UO_2SAL_2^{2-}$ where U(VI) is coordinated by forming a 6-membered ring with the deprotonated OH group and the carboxylic group. At 20K the spectrum at pH 4 agrees with the spectrum of the precipitated solid complex (Fig. 2).

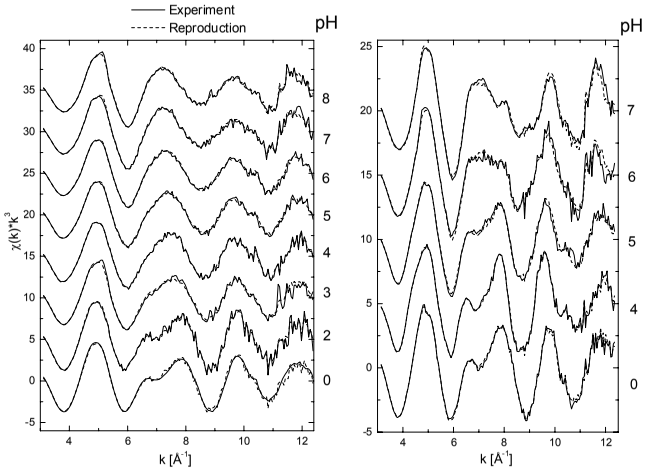

Fig. 1: U L_{III}-edge EXAFS spectra of U(VI)/SAL complexes at different pH and their reproduction by three spectral components. Left – RT, Right – 20K.

From this we conclude that the cooling by "shock freezing" of liquid samples, using liquid nitrogen, is not fast enough to avoid the precipitation of the solid U(VI)/SAL complexes. The spectrum of the aqueous U(VI)/acetic acid complex $UO_2(AC)_3^-$ at pH 4.5 agrees with the spectrum of the solid U(VI)/SAL complex at pH 4 at RT and 20 K. In $UO_2(AC)_3^-$ three carboxylic groups coordinate U(VI) bidentately. At pH 8, schoepite precipitates (Fig. 2).

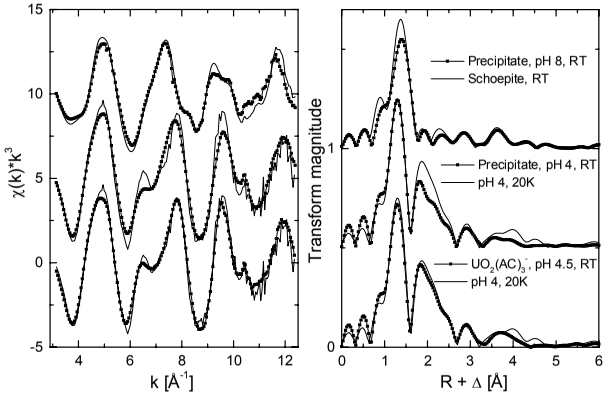

Fig. 2: Comparison of EXAFS spectra of precipitates in U(VI)/SAL at pH 4 with the $UO_2(AC)_3^-$ complex at pH 4.5. Upper spectrum – precipitated schoepite at pH 8.

ROBL-CRG	**Experiment title:** **Uranium sorption onto natural iron colloids in mine waters**	**Experiment number:** **20-01-632**
Beamline: BM 20	**Date of experiment:** from: 04/02 to 07/02/2004	**Date of report:** 02.11.2004
Shifts: 9	**Local contact(s):** Dr. Andreas Scheinost	*Received at ROBL:*

Names and affiliations of applicants (* indicates experimentalists):

Dr. Kai-Uwe Ulrich[1]*
Dr. Andreas Scheinost[2]*
Dr. André Rossberg[2]*
Dr. Harald Zänker[1]

[1] Forschungszentrum Rossendorf e.V., Institute of Radiochemistry, B.P. 510119, D-01314 Dresden, Germany
[2] ROBL-CRG at the ESRF, B.P. 220, F-38043 Grenoble Cedex, France

Report:

We simulated flooding of an abandoned uranium mine by mixing acid mine water with near-neutral groundwater up to pH 5.5 and by oxygenation. More than 95% of U adsorbed onto the freshly generated colloids (c(U)=20.6 mg/g) that consisted of ferrihydrite besides Al, S, Si, C, and trace elements. This XAS investigation is aimed at characterizing the bonding structure of uranyl on the colloidal bulk. The measurement took place at 30K in a He purged cryostat, while one sample was additionally measured at 293K. The data were recorded at the Fe-K edge in transmission mode and at the U-L_{III} edge in fluorescence mode. EXAFSPAK codes served for energy calibration and deadtime correction of the 4 element Ge detector. The codes WINXAS 3.0, Feff 7.02, and Monte Carlo simulation [1] were used for EXAFS fitting and refinement.

Results. In contrast to the U-L_{III} edge, where the temperature of measurement did not visibly affect the EXAFS, the $\chi(k)$ function gained from the Fe-K edge has more noise at k>5 $Å^{-1}$ in case of measurement at 293 K. Nevertheless, the spectra and structural parameters were in accordance with a reference sample of ferrihydrite and some earlier results [2]. Preliminary fit data of the EXAFS spectra (Tab. 1) supported a mononuclear inner-sphere ternary complex of U(VI) bidentately bridged to one FeO_6 octahedron and bidentately linked with one silicate or (bi)carbonate anion. But since further sorption experiments showed the existence of a light backscatterer in absence of both anions (see following Experimental Report), a new structural model was derived from Monte-Carlo fitting in which the bidentately bridged UO_2^{2+} ion is oriented in a way that yields a distance of ~2.88 Å to the O atom of an adjacent, edge-shared FeO_6 octahedron (Fig. 1). This model is highly consistent owing to a second Fe shell at ~4.35 Å.

Tab. 1: Structural data of the mine water colloid sample MW-2 (30 K). The FT peak at ~2.3 Å fitted by backscattering atom Si, C, or O. Error: $\Sigma(\chi_{fit}(k)k^3 - \chi_{data}(k)k^3)^2/(P-F)$ P: number of data points, F: number of free variables. * Parameter fixed during fit.

X =	ΔE_0 (eV)	Error	Shell	U-O_{ax}	U-O_{eq1}	U-O_{eq2}	U-X	U-Fe1	U-O-MS	U-Fe2
Si	5.4	0.25	N	2*	2.1	4.1	0.7	0.9	2*	-
			R [Å]	1.79	2.25	2.39	2.73	3.44	3.58	-
			σ^2 [$Å^2$]	0.0013	0.005*	0.005*	0.002 8	0.0086	0.0026	-
C	6.4	0.25	N	2*	1.9	3.1	1.7	0.9	2*	0.6
			R [Å]	1.80	2.29	2.42	2.90	3.44	3.60	4.33
			σ^2 [$Å^2$]	0.0018	0.004*	0.005*	0.003 6	0.009*	0.0036	0.002 9
O	6.2	0.23	N	2*	2.3	3.0	0.9	1.1	2*	1.0
			R [Å]	1.80	2.29	2.42	2.85	3.44	3.60	4.33
			σ^2 [$Å^2$]	0.0018	0.005*	0.005*	0.002 0	0.010	0.0036	0.006*

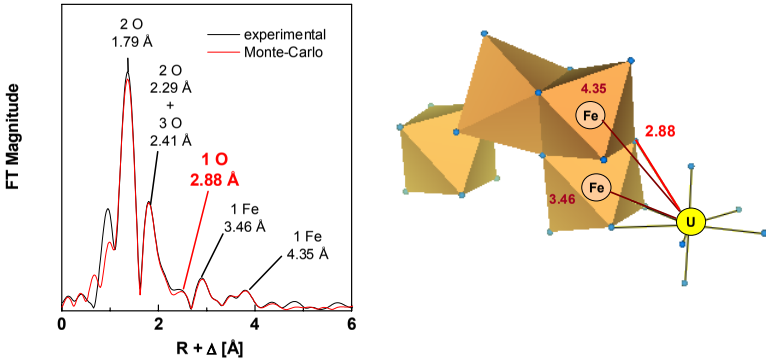

Fig. 1: Experimental FT data of the mine water colloid sample MW-2 (30 K) and calculated Monte-Carlo fit (left side) based on the structural model shown on the right.

References

[1] Rossberg A., Scheinost A., Linking Monte-Carlo Simulation and Target Transformation Factor Analysis: A novel tool for the EXAFS analysis of mixtures, Physica Scripta, Vol. 00, 1-3 (2004), in press.
[2] Hennig C., et al., Annual Report 1998, Institute of Radiochemistry, FZR-247: 56 (1999).

ROBL-CRG	**Experiment title:** **Uranium sorption onto natural iron colloids in mine waters**	**Experiment number**: **20-01-632**
Beamline: BM 20	**Date of experiment**: from: 10/06 to 15/06 and 01/09 to 03/09/04	**Date of report**: 03.11.2004
Shifts: 21	**Local contact(s)**: Dr. Harald Funke	*Received at ROBL:*

Names and affiliations of applicants (* indicates experimentalists):

Dr. Kai-Uwe Ulrich[1]*
Dr. Andreas Scheinost[2]*
Dr. A. Rossberg[2]*
Dr. Harald Zänker[1]

[1] Forschungszentrum Rossendorf e.V., Institute of Radiochemistry, B.P. 510119, D-01314 Dresden, Germany
[2] ROBL-CRG at the ESRF, B.P. 220, F-38043 Grenoble Cedex, France

Report:
Preliminary EXAFS data on colloids generated by simulated flooding of an U mine under oxic conditions indicated that U(VI) was bidentately bound as mononuclear inner-sphere complex on ferrihydrite (p. ??, this report). But a light backscatterer responsible for a small peak at ~2.4 Å in the FT remained to be explained. Based on the chemical composition of the floodwater, ternary complex structures with silicate, sulfate, nitrate, or carbonate were models to be tested. We conducted sorption experiments starting from solution of either 1 mM $Fe(NO_3)_3$ x 9 H_2O or $FeCl_3$ x 6 H_2O and c(U) = 1.2 E-05 or 1.0 E-04 M, titrated by adding NaOH up to pH 5.5 to precipitate ferrihydrite at I=1.5 E-02 M in absence and in presence of $Si(OH)_4^-$, SO_4^{2-}, or atmospheric CO_2, and $NaNO_3$ or NaCl as background electrolyte. EXAFS spectroscopy was performed on wet pastes frozen and stored in liquid N_2. Measurement took place in a He cryostat (~30K) at the U-L_{III} edge either in transmission or in fluorescence mode. Energy calibration was based on the absorption of an Y foil. The EXAFSPAK codes served for dead-time correction of the 13 element Ge detector and processing of the raw data.

Results. The FT's of all spectra exhibited the shells of U-O_{ax} (N=2, R=1.78-1.80 Å, σ^2=0.002 Å), U-O_{eq1} (N=1.8-2.4, R=2.2-2.3 Å, σ^2=0.003-0.006 Å), U-O_{eq2} (N=2.8-4.1, R=2.39-2.41 Å, σ^2=0.003-0.008 Å), and U-Fe_1 (N=0.7-1.1, R=3.38-3.41 Å, σ^2=0.003-0.007 Å). Samples made from c(U)=1.2 E-05 M showed a second U-Fe shell (N=0.5-1.0, R=4.28-4.33 Å, σ^2=0.005-0.009 Å), while those prepared from c(U)=1.0 E-04 M showed an U-U shell (N=0.7-1.0, R=3.82, σ^2=0.004-0.006 Å) indicative for surface precipitation of polymeric U species like schoepite. All FT's included the shell U-X at ~2.4 Å (uncorrected for phase shift) with a similar height reflecting that neither Si nor S, N, or C were the responsible backscatterers in the samples prepared in absence of these atoms. Thus another backscattering atom, obviously oxygen, must be taken into consideration (see previous Experimental Report).

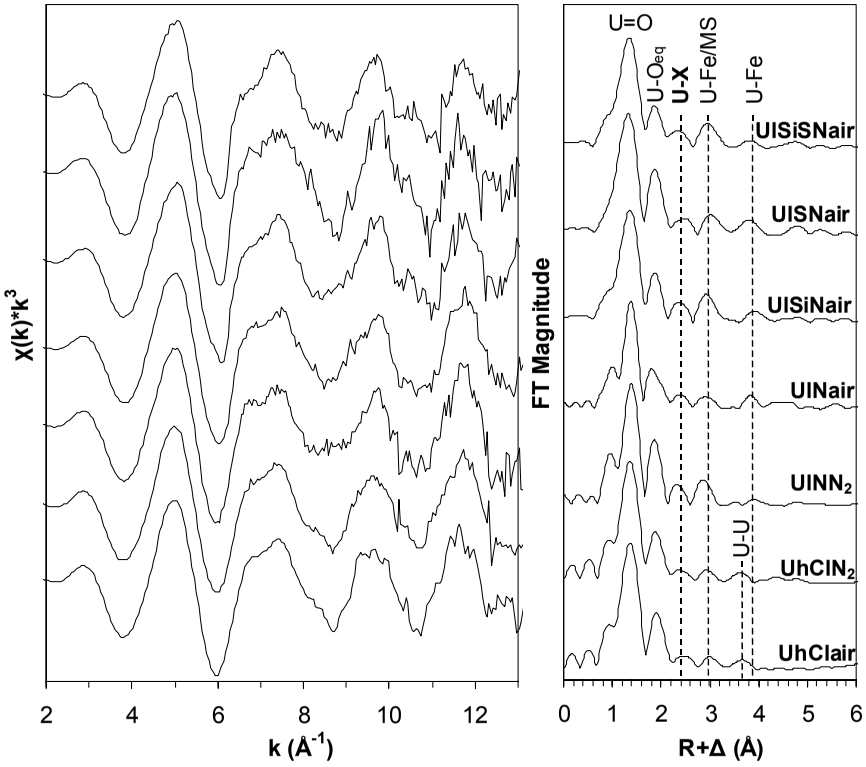

Fig. 1: U-L_{III} EXAFS spectra and corresponding FT's (uncorrected for phase shift) of ferrihydrite prepared in presence of UO_2^{2+} (**Ul**: 1.2 E-05 M, **Uh**: 1.0 E-04 M), **Si**$(OH)_4^-$, **S**O_4^{2-}, **N**O_3^-, **Cl**$^-$, and ambient atmosphere of **air** or **N_2** (CO_2 excluded).

ROBL-CRG	**Experiment title:** **Feasibility EXAFS experiment for neptunium sorption on kaolinite**	**Experiment number:** **20-01-637**
Beamline: BM20	**Date of experiment:** from: 03/10/2004 to: 05/10/2004	**Date of report:** 07/12/2004
Shifts: 6	**Local contact(s):** Christoph HENNIG	*Received at ESRF:*

Names and affiliations of applicants (* indicates experimentalists):

Samer AMAYRI, Jakob DREBERT*, Aleksandr JERMOLAJEV*, Tatiana REICH*, Tobias REICH*, Susanne SACHS§, Christoph HENNIG§*, Andreas SCHEINOST§*
Institute of Nuclear Chemistry, Johannes Gutenberg-Universität Mainz
Fritz-Strassmann-Weg 2, 55128 Mainz, Germany
§ Institute of Radiochemistry, Forschungszentrum Rossendorf e.V., P.O. Box 510119, 01314 Dresden, Germany

Report:

This feasibility study is the basis for future EXAFS measurements to investigate the sorption of neptunium on kaolinite KGa-1b (Source Clays Repository). Several collaborating groups selected this kaolinite as reference clay for a broad range of investigations dealing with the interaction of actinides in the system clay, humic acid, and aquifer. During recent EXAFS measurements of uranium(VI) sorption onto kaolinite KGa-1b (see report ME-817), we found that this kaolinite contains traces of zirconium. The energy of the Zr K edge equals 17998 eV. Therefore, we expect a distortion of the Np L_3-edge (17610 eV) EXAFS signal at this energy or at k approximately equal to 9.8 $Å^{-1}$. This experiment aimed at exploring the possibilities for avoiding severe distortions in the Np EXAFS signal without limiting the k range to 9.8 $Å^{-1}$.

Two samples 1 and 2 with different amounts of neptunium(V) sorbed were prepared from a 1.8 mM Np(V) stock solution of Np-237. This stock solution had been purified from traces of Pu-239 and Pa-233. 200 mg kaolinite KGa-1b were suspended in 50 mL de-ionized water. The ionic strength was adjusted to 0.1 M $NaClO_4$ and the pH to 9.0. The system was open to air. After shaking these mixtures for 72 hours, aliquots of the Np(V) stock solution were added with immediate readjustment of the pH. The total neptunium concentration for samples 1 and 2 was $8•10^{-6}$ and $2•10^{-5}$ mol/L, respectively. After a contact time of 72 hours, the solid and liquid phases were separated by centrifugation at 5000 rpm for seven minutes. The neptunium uptake of samples 1 and 2 as measured by γ-spectroscopy was 300 and 510 ppm, respectively. The solid residue was loaded without drying into the EXAFS sample holder. The neptunium EXAFS spectra were measured in fluorescence mode using the new 13-element Ge solid-state detector of the ROBL radiochemistry hutch.

The following measurements were performed on these samples:

1) The Np $Lα_1$ radiation at 13.9 keV was recorded as a function of photon energy across the Np L_3-edge EXAFS region using the single-channel analyzers (SCA's). The signal was corrected for detector dead time using the measured total count rates (ICR`s).

2) The same as in 1) but with a specially designed rubidium nitrate fluorescence filter placed between sample and Ge solid-state detector to reduce the contribution of the Zr Kα fluorescence at 15.8 keV to the ICR`s.

3) The EXAFS spectrum was measured at the Np L_2 edge (21600 eV) by setting the SCA's at 17.8 keV to record the Np $Lβ_1$ radiation.

The measurements showed that the rubidium filter is able to significantly reduce the contribution of the Zr Kα fluorescence to the ICR. However, the absorption of the Zr Kα fluorescence by the rubidium atoms increased the intensity of the Rb Kα fluorescence at 13.4 keV. Unfortunately, the Np $Lα_1$ radiation at 13.9 keV could not be separated from the Rb Kα fluorescence at 13.4 keV. Since both the Np and Rb X-ray emission lines were recorded in the SCA`s, the $RbNO_3$ filter enhanced the distortion of the Np L_3-edge fluorescence signal. Therefore, the rubidium filter cannot be used to reduce the effect of the zirconium trace on the Np L_3-edge EXAFS signal above 9.8 $Å^{-1}$.

Figure 1 shows the Np EXAFS spectra and the corresponding Fourier transforms of sample 1 (300 ppm Np) measured at the L_3 and L_2 edges. Seven sweeps at the Np L_2 edge and six sweeps at the L_3 edge were averaged. The useful k range at the L_3 edge was limited to k_{max} equal 9.4 $Å^{-1}$ due to the Zr K absorption edge. The Np L_2-edge EXAFS signal could be recorded with good statistics up to k_{max} equal 11.4 $Å^{-1}$. Therefore, it is preferable to record the Np EXAFS signal of the kaolinite samples at the Np L_2 edge.

Table 1 summarizes the EXAFS structural parameters of sample 1 derived from the Np L_3- and L_2-edge k^3-weighted EXAFS spectra. The detected neptunium coordination shells and bond distances are consistent with the formation of a Np(V) carbonato species at the kaolinite surface due to precipitation. A similar result was obtained for sample 2 (510 ppm, not shown here).

In conclusion, these test experiments showed that it is possible to study the sorption of neptunium onto kaolinite KGa-1b successfully using Np L_2-edge EXAFS spectroscopy. With the new 13-element Ge detector, it is possible to study sorption samples with less than 300 ppm neptunium in the future by collecting more than seven sweeps per sample.

Table 1 EXAFS structural parameters for 300 ppm Np(V) sorbed onto kaolinite at pH 9.0 under ambient conditions. Multiple-scattering paths are not listed. Coordination numbers were held constant during the final fit according to the result of previous fits.

Shell	Np L_2 edge		Np L_3 edge	
	R (Å)	$σ^2$ ($Å^2$)	R (Å)	$σ^2$ ($Å^2$)
2 x Oax	1.85	0.0021	1.84	0.0010
4 x Oeq	2.55	0.0051	2.55	0.0054
2 x C	2.94	0.0060	2.95	0.0027
2 x Odist	4.24	0.0040	4.25	0.0044
1 x Np	4.86	0.0023	4.89	0.0050

Figure 1 Np L-edge k^3-weighted EXAFS spectra (left) and corresponding Fourier transforms (right) of 300 ppm Np(V) sorbed onto kaolinite at pH 9.0 under ambient conditions. Solid line - raw data, dots - best theoretical fit to the data. Top – Np L_3-edge data, bottom – L_2-edge data.

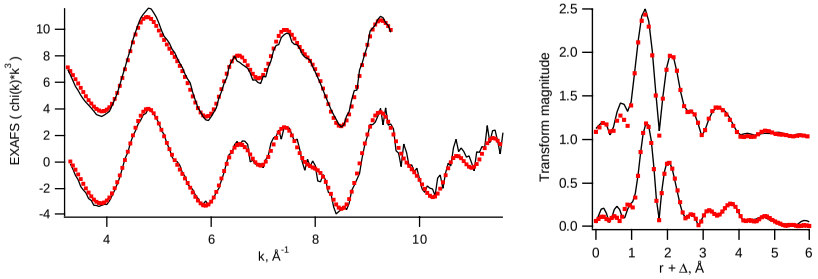

ROBL-CRG	**Experiment title:** **X-ray absorption spectroscopy studies on gold nanoparticles formed by bacteria and their surface layer proteins**	**Experiment number**: **20-01-638**
Beamline: BM 20	**Date of experiment**: from: 26.09.04 to: 28.09.04	**Date of report**: 08.11.04
Shifts: 15	**Local contact(s)**: Dr. André Rossberg	*Received at ROBL:*
Names and affiliations of applicants (* indicates experimentalists): M. Merroun*, A. Scheinost*, A. Rossberg*, C. Hennig*, H. Funke*, S. Selenska-Pobell		

Report: The area of nanotechnology, which spans the synthesis of nanoscale matter, understanding /utilizing their exotic physicochemical and optoelectronic properties, and organization of nanoscale structures into predefined superstructures, promises to play an increasingly important role in many key technologies of the new millenium. As far as the synthesis of nanoparticles is concerned, there is an ever-growing need to develop clean, non-toxic, and environmentally friendly ("green chemistry") synthetic procedures. Consequently, researchers in the field of nanoparticle preparation have been looking at biological systems for insipration. In this work, we studied the formation of gold nanoparticles by cells and S-layer protein of *B. sphaericus* JG-A12 using X-ray absorption spectroscopy.

Experimental: The samples were prepared as follows: *B. sphaericus* cells were grown in a batch culture to mid exponential phase and harvested by centrifugation at 10.000 rpm for 30 min. The preparation of S-layer protein was perfomed as described in /1/. To metallize *B. sphaericus* JG-A12 cells and S-layer, 40 ml of Gold(III) solution ($HAuCl_4$. $3H_2O$) were poured into 55 ml serum bottles, degassed under nitrogen for 15 min. In both cases, cells and S-layer, the reduction of Au(III) was induced by addition H_2.

Results: Gold K-edge EXAFS spectra of the Au complexes and Au clusters formed by cells and S-layer of *B. sphaericus* JG-A12 in the absence and presence of H_2 as well as Au reference compounds (au foil, Au oxide, Au sulfide, Au chloride) and their corresponding Fourier transforms (FT) are shown in Fig. 1.

XANES spectroscopy and Factor Analysis /1/ demonstrated that in presence of H_2 the cells and S-layer of this bacterium are able to reduce 67% and 37% of Au(III) to Au(0), respectively. Using Au-Au shell parameters of Au foil all the peaks were attributed to 4 Au-Au shells with distances of 2.87, 4.06, 4.98 and 5.68 Å. The size of the Au clusters formed by the 2 biocomponents are smaller than those present in the gold foil since the coordination number of the first shell in the samples (N=6-7) is smaller than in the Au foil (N=12). The formation of gold nanoparticles by the cells and S-layer is confirmed by the UV-vis spectroscopy data which demonstrate the presence of absorption band at 540 nm which arises due to excitation of surface plasmon vibrations in the gold nanoparticles and is responsible for their lovely ruby-red colour. The estimation of the cluster size is now in progress.

In addition to these Au-Au shells, an Au-O/N/C contribution at 2.01 Å was detected in the EXAFS spectra which corresponds probably to the Au bound to the functional groups of the cells and S-layer.

In the absence of reducing agent, the Factor Analysis demonstrated that there are a mixture of about 35% Au(0) and 65% Au(III) in the cell sample and only 10% A(0) in the S-layer sample which could probably due to the effect of Au photoreduction since the S-layer of *B. sphaericus* JG-A12 doesn't contain sulfur residues which could reduce Au in absence of H_2.

The EXAFS spectra of Au/cell sample contain in addition of the Au-Au shells which arise from the Au clusters, also contributions from backscattering of light atoms such as oxyge, nitrogen or carbon at bond distances of 2.01 Å and 2.29 Å. Theses atoms belong to functional residues of the biocomponents which are implicated in the binding of gold.

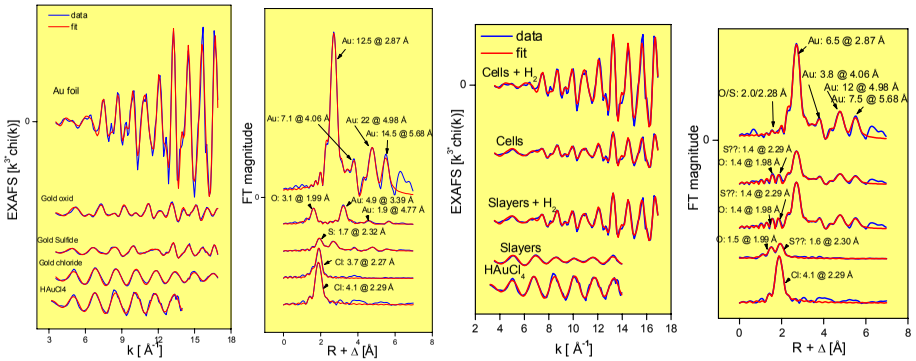

Fig. 1. Pd K-edge EXAFS spectra and their corresponding FT of the Au complexes and nanoclusters formed by cells and S-layer of *B. sphaericus* JG-A12 and some gold reference compounds.

Acknowledgements. This work is supported by SMWK Grant N° 7531.50-03.0370-1/5.

References:

/1/ Raff, J. Ph. D. Thesis, TU Leipzig (2002)
/2/ Rossberg, A. Ph. D. Thesis, TU Dresden (2002)

ROBL-CRG	**Experiment title:** **Local structure of U(IV) and U(VI) in natural and synthetic minerals**	**Experiment number**: **20-01-642**
Beamline: BM 20	**Date of experiment**: 03.-05.11.04; 24.-25.11.04; 4.-7.12.04	**Date of report**: 05.12.2004
Shifts: 17	**Local contact(s)**: A. Scheinost, A. Rossberg	*Received at ROBL:*

Names and affiliations of applicants (* indicates experimentalists):

Andreas SCHEINOST*, FZR
Renaud VOCHTEN, University of Antwerp, Belgium
Thuro ARNOLD, FZR
Harald FUNKE*, FZR
Christoph HENNIG*, FZR
Andre ROSSBERG*, FZR

Report:

Reliable metal speciation in environmental samples depends heavily on complete spectral data bases for statistical analyses like principal component analysis and linear combination fits (*1, 2*). This is particularly important for uranium speciation (see Experimental Report 20-01-626), since hundreds of uranium minerals are known (> 5 % of all known minerals contain U as essential constituent) (*3*). Recent investigations demonstrated that uranyl minerals are difficult to distinguish by EXAFS spectroscopy, since they commonly form layered structures (silicates, vanadates, carbonates, hydroxides, phosphates, etc.) (*4, 5*). However, these studies were based on a relatively limited number of mineral samples, were performed at room temperature, and preferential orientation (texture effects) cannot be completely excluded. Hence, we intend to follow up this study using a large range of mineral samples, to measure the samples at both room temperature and 20 K, and to avoid texture effects by using a magic angle sample orientation. Prof. Vochten from Antwerp University has provided a large number of samples he has collected or synthesized in order to investigate their structure by XRD and their solubility by thermodynamic equilibrium methods. This collection, which he made available to us, is ideally suited to further investigate the EXAFS limitations and to build a spectral data base for EXAFS speciation of U in environmental samples.

The table below shows the 25 minerals and solids, for which EXAFS spectra have been collected so far at room temperature (RT) or 30 K. Figure 1 demonstrates the excellent data quality routinely achieved, using as example the subset of uranium oxides, hydroxides and sulfates measured at RT. Measurement of the complete Vochten collection (ca. 80 samples) will be accomplished in upcoming runs.

In addition to EXAFS spectroscopy, samples will be characterized by powder x-ray diffraction, IR and time-resolved laser fluorescence spectroscopies.

Table. Uranium reference minerals.

No	mineral	group	formula	RT	30K
Fz 9	meta-zeunerite	arsenate	$Cu[UO_2,AsO_4]_2\ 8H_2O$	x	x
Vo 29	kahlerite	arsenate	$Fe[UO_2AsO_4]_2\ 12H_2O$	x	x
Fz 1	andersonite	carbonate	$Na_2Ca[UO_2(CO_3)_3]\ 6H_2O$	x	x
Fz 2	Ba uranyl carbonate	carbonate	$Ba[(UO_2)(PO_4)]_2\ xH_2O$	x	
Fz 3	bayleyite	carbonate	$Mg_2UO_2(CO_3)_3\ 18H_2O$	x	x
Fz 13	swarzite	carbonate	$CaMg(UO_2)(CO_3)_3\ 12\ H_2O$	x	x
Fz 8	liebigite	carbonate	$Ca_2UO_2(CO_3)_3\ 10H_2O$		x
Fz 12	Sr uranyl carbonate	carbonate	$Sr_2UO_2(CO_3)_3\ 6H_2O$		x
Fz 4	becquerelite	hydroxide	$Ca(UO_2)_6O_4(OH)_6\ 8H_2O$	x	x
Fz 7	compreignasite	hydroxide	$K_2(UO_2)_6O_4(OH)_6\ 8H_2O$	x	x
Vo 12	billietite	hydroxide	$Ba(UO_2)_6O_4(OH)_6\ 4H_2O$	x	x
Vo 40	zippeite	hydroxide	$K(UO_2)_2(SO_4)(OH)_3\ H_2O$	x	x
Vo 72	zippeite	hydroxide	$K(UO_2)_2(SO_4)(OH)_3\ H_2O$	x	x
Fz 11	schoepite	oxide	$UO_3\ 2H_2O$	x	x
Vo 6	woelsendorfite	oxide	$Pb\ U_2O_7\ 2H_2O$	x	x
Vo 4	pitchblende	uraninite	U_3O_8	x	x
Fz 6	Ca uranyl phosphate	phosphate	$Ca[(UO_2)(PO_4)]_2$	x	
Vo 8	chernikovite	phosphate	$(H_3O)_2(UO_2)_2(PO_4)_2\ 6H_2O$	x	x
Vo 21	autunite	phosphate	$Ca(UO_2)_2(PO_4)_2\ 10\text{-}12\ H_2O$	x	x
Vo 32	parsonsite	phosphate	$Pb_2(UO_2)(PO_4)_2\ 0.5H_2O$	x	x
Vo 43	soddyite	silicate	$Na_2(UO_2)_2SiO_4F_2$	x	x
Vo 45	boltwoodite K	silicate	$K(H_3O)(UO_2)(SiO_4)\ nH_2O$	x	x
Vo 50	weeksite Na	silicate	$K_2(UO_2)_2(Si_2O_5)_3\ 4H_2O$	x	x
Fz 5	boltwoodite	silicate	$K(H_3O)(UO_2)(SiO_4)\ nH_2O$		x
Vo 41	carnotite	vanadate	$K_2(UO_2)_2(V_2O_8)_2\ 1\text{-}3H_2O$	x	x

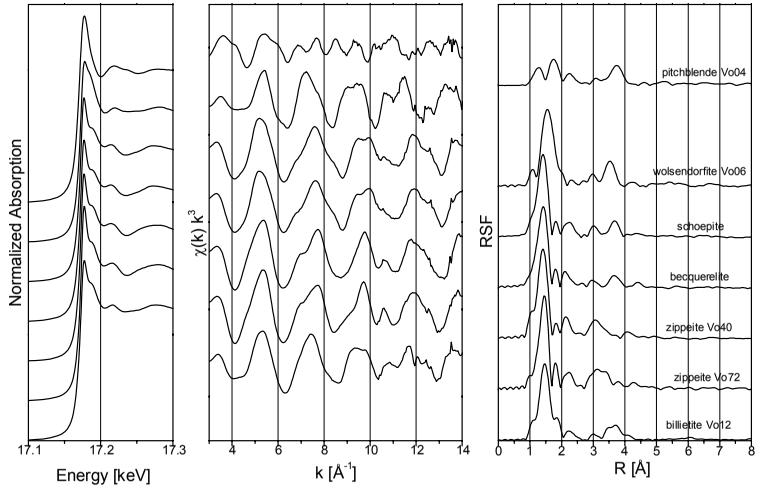

Fig. 1. U L_{III}-edge EXAFS spectra of uranium oxides, hydroxides and sulfates.

1. D. R. Roberts, A. C. Scheinost, D. L. Sparks, in *Geochemical and Hydrological Reactivity of Heavy Metals in Soils* H. M. Selim, W. L. Kingery, Eds. (CRC Press, Boca Raton, 2003) pp. 187-227.
2. A. C. Scheinost, R. Kretzschmar, S. Pfister, D. R. Roberts, *Environmental Science & Technology* **36**, 5021-5028 (2002).
3. P. C. Burns, R. Finch, Eds., *Uranium: Mineralogy, Geochemistry and the Environment*, vol. 38 (Mineralogical Society of America, Washington DC, 1999).
4. J. G. Catalano, S. M. Heald, J. M. Zachara, G. E. Brown, Jr., *Environmental Science & Technology* (2004).
5. J. G. Catalano, G. E. Brown, *American Mineralogist* **89**, 1004-1021 (Jul, 2004).

ESRF	**Experiment title:** δ-phase stabilization in $Pu_{(x)}Am_{(1-x)}$ alloys as studied by EXAFS	**Experiment number:** HE-1393
Beamline: BM 20	**Date of experiment:** from: 30.01.2003 to: 04.02.2003	**Date of report:** 19.11.2004
Shifts: 15	**Local contact(s):** C. Hennig	*Received at ESRF:*

Names and affiliations of applicants (* indicates experimentalists):
*B. RAVAT, *L. JOLLY, *C. VALOT, N. BACLET
CEA-Centre de Valduc

Report:

The plutonium δ-phase (face-centered cubic) can be stabilized at room temperature with so-called deltagen elements such as Ga, Al, Am, Ce… While PuGa and PuAl alloys have been extensively studied, few works have been devoted to PuCe and PuAm alloys. A Ph.D. (initiated in 10/98) was devoted to a better understanding of the δ-phase stabilization in especially binary $Pu_{(x)}Am_{(1-x)}$ alloys [1]. Electronic and crystalline structure appeared to be strongly related in these alloys. Electronic effects have been suggested through a positive deviation from the Vegard's law, as shown by XRD [2]. A strong localization of the 5f electrons of Pu atoms has been indicated by electrical and magnetic measurements for an Am content of about 25 at% [1]. However, the techniques used until now gave only an overall information, whereas, as EXAFS measurements in $Pu_{(x)}Ga_{(1-x)}$ alloys revealed, important phenomena can happen at a short range order [3,4].

Experiment

EXAFS measurements have been performed at the LIII-edges of Pu (18057 eV) and Am (18504 eV) in the transmission mode on four alloys: $Pu_{0.95}Am_{0.05}$, $Pu_{0.85}Am_{0.15}$, $Pu_{0.75}Am_{0.25}$ and $Pu_{0.57}Am_{0.43}$. EXAFS spectra have been recorded at 20 K using the cryostat from the BM20 line.

Results and discussion

Preliminary theoretical study

The LIII-edge of Am being close to Pu one, the EXAFS spectrum of the Pu interferes with the Am one. Therefore, using FEFF calculation, the theoretical FT of the Pu, Am and PuAm alloy EXAFS spectra have been compared. The results (Fig.1) show that the Am-Pu contribution is not influenced by the Pu signal. The addition of the Pu signal does not modify the peak position of the Am-Pu contribution. A study of the Am-Pu distances is then possible by filtering this contribution in experimental spectra.

Experimental study

The results (Fig. 2) highlight an increase in both Am-Pu and Pu-Pu distances with the Am content and the Am-Pu distances are always larger than the Pu-Pu ones with an expansion of 0.03Å. Moreover, an increase in cell parameter with Am content has been equally observed by XRD, technique which is sensitive to long range order. The values obtained by XRD tend towards the Pu-Pu distances for the lowest Am content and towards the Am-Pu ones for the highest Am content. This can first be attributed to a steric effect, the Am atomic volume being more important than the Pu one.

However, as the Am content increases, Pu atoms are replaced by Am atoms whose atomic volume is larger. Consequently, the resulting lattice expansion induces a decrease in the overlapping of the 5f wave function of the plutonium. This phenomenon leads to an increase in the 5f electrons localization and thus an increase in the atomic volume. So, the increase in the Am-Pu and Pu-Pu distances are the result of both steric and electronic effects.
It is noticeable that Pu atoms seem to reach their 5f electrons maximum localization degree in this kind of alloys, as it was suggested by the susceptibility result [1], since a slight decrease in the slope can be observed from an Am content of 25%. This effect, only observed for the Pu-Pu distances, shows that, from this Am content, only the steric effect remains. Finally, the great difference between the Am-Pu and Pu-Pu distances for an Am content of 43% seems to highlight that the distances for both pairs will be never equal whatever Am content. This involves that the 5f e^- localization degree of Pu could not reach the 5f electron localization degree of Am in this alloy.

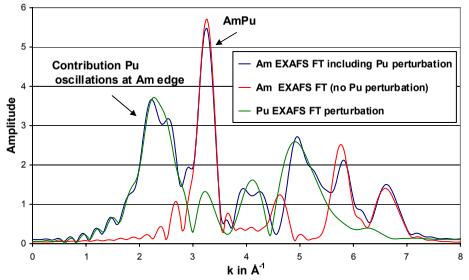

Fig. 1: Theoretical EXAFS FT calculation using FEFF7.

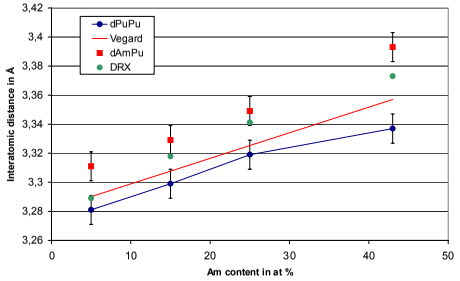

Fig. 2: Interatomic distances for the Am-Pu and Pu-Pu pairs.

Acknowledgement
Financial support for access to the actinide User Laboratory at ITU-Karlsruhe within the frame of the European Community-Access to Research Infrastructures action of the Improving Human Potential Programme (IHP), contract HPRI-CT-2001-00118, is acknowledged.

[1] M. Dormeval, "Structure électronique d'alliages Pu-Ce(-Ga) et Pu-Am(-Ga) stabilisés en phase δ", thèse de l'Université de Bourgogne, septembre 2001.
[2] M. Dormeval, N. Baclet, "Plutonium Futures - the Science", July 2000, Santa-Fe, New Mexico.
[3] Ph. Faure, B. Deslandes, D. Bazin, C. Tailland, J.M. Fournier, J. Alloys and Comp., 244, p131 (1996).
[4] S. D. Conradson,"Where is the Gallium?", Los Alamos Science Number 26, 2000.

ESRF	**Experiment title:** EXAFS/XANES studies on the interaction of Tc(IV) with selected chemical components as a reference for Tc(IV)-humic substance interaction	**Experiment number**: CH 1454
Beamline: BM-20	**Date of experiment**: from: 18/05/2003 to: 21/05/2003	**Date of report**: 29/08/2003
Shifts: 9	**Local contact(s)**: André Rossberg	*Received at ESRF:*

Names and affiliations of applicants (* indicates experimentalists):

André Maes*, Christophe Bruggeman*, Kathleen Geraedts*
K.U.Leuven, Laboratorium voor Colloïdchemie, Kasteelpark Arenberg 23,
B-3001 Leuven, Belgium

Luc Van Loon
Paul Scherrer Institute, Laboratory for Waste Management, OHLB/409a,
CH-5232 Villigen PSI, Switserland

Report:

Introduction

The redox-sensitive fission product technetium-99 (Tc) is of great interest in nuclear waste disposal studies because of its potential for contaminating the geosphere due to its very long half-life (2.13×10^5 year) and high mobility under oxidising conditions, where technetium forms pertechnetate (TcO_4^-) [1]. Under suitable reducing conditions, e.g. in the presence of an iron(II) containing solid phase which can act as an electrondonor, the solubility can be limited by the reduction of pertechnetate followed by the formation of a surface precipitate [2]. However, by association with mobile humic substances (HS), the solubility of reduced Tc species may be drastically enhanced [3].

A first XANES measuring campaign (performed at ESRF, March 2001, CH-1050) demonstrated for the first time that pertechnetate was reduced to Tc(IV) and Tc(IV)-HS species were formed in Gorleben sand/Gorleben groundwater (rich in humic acids) reducing systems. These results were published in Radiochimica Acta [4].

A second EXAFS/XANES campaign (performed at ESRF, July 2002, SI-790) was then performed on samples in which TcO_4^- was reduced by various solid phases (pyrite, magnetite, Gorleben sand, Boom Clay), both in absence and presence of humic acids (HA). These experiments were set up in order to elucidate the chemical environment of Tc in these systems on atomic scale. The data from these experiments showed very interesting and surprising results, because all spectra could be fitted with a hydrated amorphous Tc(IV) oxide phase, independent of the reducing surface used and of the eventual presence of HA. These results could only mean that Tc(IV) oxide colloids were formed and precipitated upon reduction of TcO_4^-, and that these colloids could also interact with the organic colloidal material from Gorleben and Boom Clay HA. This latter observation was confirmed by batch sorption experiments with Tc and Boom Clay suspensions from which an interaction constant could be derived describing the interaction of a neutral Tc(IV) species and dissolved HA [5]. A paper containing the results from the above described EXAFS/XANES data was sent to Environmental Science & Technology for reviewing [6].

It was the intention from the EXAFS measurements given in the present report to further clarify the nature and kind of Tc(IV)-humic substance species, in terms of complexation or colloid-colloid interaction.

Sample preparation

To investigate the universality of the observed interaction between Tc(IV) colloids and HA for other organic molecules, batch systems were set up at KULeuven in which TcO_4^- was chemically reduced to Tc(IV) and to which 9 reference organic compounds varying in size from small to large (citric acid, hydroxybenzoic acid, pyrogallol, glutaminate, isosaccharinic acid, aurintricarboxylic acid, calconcarboxylic acid, Laurentian fulvic acid, Fluka humic acid) and Boom Clay HA were added. The systems were allowed to equilibrate over a certain time period before preconcentration of the samples, after which aliquots were transferred into the measuring vials.

The allocated shifts were used to measure the XANES/EXAFS spectra of the abovementioned samples in fluoresence (and where possible transmission) detection mode.

Results

The results from this campaign are still being investigated, but the following preliminary conclusions were already drawn :

1) the technique used to reduce TcO_4^- still yielded the same colloidal Tc(IV) spectra in presence of large humic acid molecules (Fluka HA and Boom Clay HA) as observed before, however different spectra were now obtained in the presence of small dissolved organic molecules ;
2) as described in literature [7,8], Tc(IV) species probably formed chelates with most smaller organic molecules by means of a ligand exchange between the hydrolysed Tc(IV) molecules and functional groups present on the organics. Since for all samples a different spectrum was obtained, this reflects the different nature of chelates formed dependent on the availability and geometry of the ligands on the different organic molecules. If the obtained EXAFS spectra can be interpreted correctly, they form the first direct spectroscopic proof for this range of Tc(IV) complexes ;
3) in view of the foregoing results, it is now assumed as a working hypothesis that Tc(IV) can interact with different organic molecules in two ways : the first is by colloidal association between anorganic Tc(IV) and large organic matter (HA) molecules, the second is by making complexes with smaller organic ligands. However, the exact contribution of each interaction mechanism in intermediate HS molecules such as Laurentian FA and in natural waters containing a wide range of organic matter (mixture of HA, FA and low molecular weight organic acids), remains unknown due to the lack of sufficient knowledge concerning the mechanisms and associated constants.

References

[1] Lieser K.H., Bauscher Ch., Radiochimica Acta, 42 (1988) 205.
[2] Cui D., Eriksen T.E., Environ.Sci.Technol., 30 (1996) 2263.
[3] Sekine T., Watanabe K., Kim J.I., Radiochimica Acta, 63 (1993) 87.
[4] Geraedts K., Maes A., Bruggeman C., Van Loon L., Rossberg A., Reich T., Radiochimica Acta 90 (2002) 879.
[5] Maes A., Bruggeman C., Geraedts K., Vancluysen J., Environ.Sci.Technol., 37 (2003) 747.
[6] Maes A., Geraedts K., Bruggeman C., Vancluysen J., Rossberg A., Hennig C., paper sent for reviewing to Environ. Sci. Technol. (2003)
[7] Kennedy C.M., Pinkerton T.C., Int.J.Radiat. Appl.Instrum. Part A, 39 (1988) 1167.
[8] Noll B., Seifert S., Münze R., Int.J.Radiat. Appl. Isot., 34 (1983) 581.

ESRF	**Experiment title:** EXAFS study of uranium(VI) uptake by kaolinite	**Experiment number:** CH-1455
Beamline: BM 20	**Date of experiment:** from: 02/07/2003 to: 04/07/2003 from: 30/07/2003 to: 01/08/2003	**Date of report:** 22/11/2004
Shifts: 12	**Local contact(s):** Christoph HENNIG	*Received at ESRF:* *22/11/2004*

Names and affiliations of applicants (* indicates experimentalists):

Frederec POINEAU*, Massoud FATTAHI*

Laboratoire de Physique subatomique et des technologies associées

Unité Mixte de Recherche 6457

Ecole des Mines de Nantes,
IN2P3/CNRS,
Université de Nantes

Report

Introduction

Previous study of the chemistry of Technetium in sulfato-chloride media showed that the electroreduction of TcO_4^- in 3M NaClor in 0.1 M H_2SO_4 media with a pH range 0 to 2.5 lead to the formation of $Tc_nO_y^{(4n-2y)+}$ [1]. However, the formation of this specie is not well understood. Recent studies on Tc(IV) have shown that $Tc_nO_y^{(4n-2y)+}$, $Tc^{IV}(\mu\text{-}O)_2Tc^{IV}$ structure, is a precursor for precipitation of TcO_2. Kinetic studies have shown that the condensation of $Tc^{IV}Cl_5(H_2O)^-$ in chloride media leads to a dimer.

Experimental

EXAFS measurements were carried out on the Rossendorf Beamline under dedicated ring conditions (6.0 GeV, 200 mA). The monochromator equipped with a water-cooled Si(111) double-crystal was used in channel-cut mode. Tc K-edge spectra were collected in transmission mode using argon-filled ionization chambers. An Mo metal foil (first inflection point at 19837 eV) was used for energy calibration. The EXAFS threshold energy, $E_{k=0}$, was defined as 21064 eV. The experiments were performed in an electrochemical cell [2] and cuvettes with a diameter of 8 mm. The polymerization step was investigated with [Tc] = 8.8 mM, [Cl^-] = 3 M and pH = 0.3.

Results and Discussion

This experiment was focused on the initial polymerization step. Figure 1 shows the Tc K-edge EXAFS of the sample in oxidation state IV. The first shell comprises one oxygen atom in a distance of 1.94 Å and five chlorine atoms at 2.35 Å. A single Tc atom in a distance of 3.67 Å is clealy visible in the Fourier Transform. The resulting stucture is the dimer with a linear structure Tc^{IV}-O-Tc^{IV} This complex compound with the formula $Tc_2OCl_{10}^{4-}$ is stable at pH = 0.3 and undergoes further polymerization to $Tc_nO_y^{(4n-2y)+}$ at pH =1.5 [3].

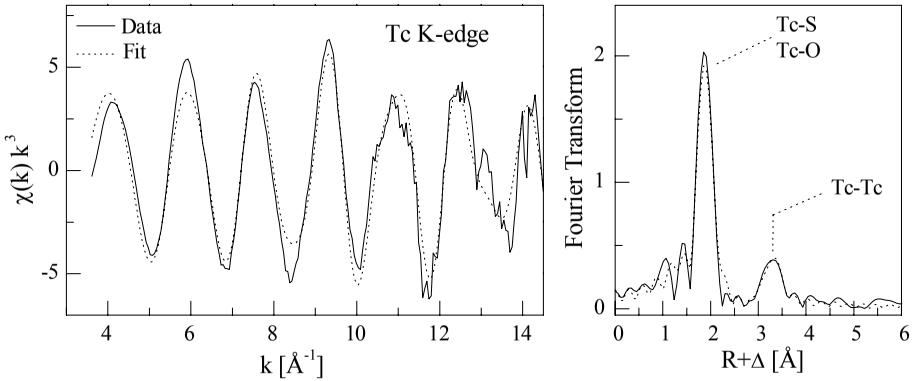

Figure 1 : *Tc K-edge k^3 weighted EXAFS data (left) and corresponding Fourier transforms (right) taken over k = 3.5-14.6 $Å^{-1}$ for $Tc_2OCl_{10}^{4-}$, [Tc] = 8.8 mM, [Cl^-] = 3 M and pH = 0.3.*

References

[1] Vichot, L., Thesis on Speciation of technetium in chloro-sulfate media. Paris, 2001
[2] Hennig, C. et al., this Report.
[3] Poineau, F., Thesis on Speciation of Tc(IV) in aquo-chloro media. Nantes, 2004

ESRF	**Experiment title:** Americium speciation in Ferritin protein	**Experiment number:** SC-1349
Beamline:	**Date of experiment:** from: 05/11/04 to: 08/11/04	**Date of report:** 24/02/04
Shifts: 9	**Local contact(s):** Dr. Harald FUNKE	*Received at ESRF:*

Names and affiliations of applicants (* indicates experimentalists):

C. Barbot : GERMETRAD SMAB, Univ. Nantes, 2 rue Houssinière 44322 Nantes Cedex 3

F. Goudard, J.-P. Durand, J. Pieri : idem

P. Germain : IRSN rue Max-Pol Fouchet 50130 Cherbourg-Octeville

***C. Den Auwer** : CEA Marcoule DEN/DRCP/SCPS 30207 Bagnols sur Cèze Cedex

E. Simoni : IPN Orsay Univ. Paris XI 91405 Orsay Cedex

Preliminary report:

The ferritin protein is an iron storage macromolecule of many species as mammals, marine organisms or plants. It is composed of 24 bundles (Figure 1) linked together by symmetry axis of order 2, 3 and 4, thus forming an inner cavity of 7-8 nm. Although some EXAFS studies have been devoted to the characterization of the inner iron oxyhydroxide core [Wald95], very little is known about its contamination processes by exogeneous metal cations. This project aims to better understand the interaction of an actinide contaminant with this protein. Kinetic studies of ^{241}Am incorporation have shown that ferritin was the first protein to be contaminated and the last to decorporate this radionuclide [Goud94].

Technical difficulties in the laboratory regarding the preparation of suitable starting ^{241}Am reactant obliged us to study another actinide of first interest : ^{237}Np. Note that ^{241}Am is one of the most active radionuclide used in our researches and preparation of adequate starting solutions is always a challenge. Np(IV) starting solution was prepared in nitroso triacetic acid in order to avoid the formation of hydroxydes at working pH = 5.

In order to better understand the interactions between the cation and the protein, two amino acids / cation adducts have been first investigated. The proteic part of the ferritin is mostly composed of carboxylate groups (aspartate, glutamate), although other amino acids may participate to the metal binding (histidine, tyrosine). Therefore the coordination of Np(IV) with aspartate and histidine is a good representative of most of the possible interactions with the proteic part. In case of interaction with the oxyhydroxy iron part, heavy iron backscatter signal is expected. Figure 2 shows that the two EXAFS spectra of aspartate/Np(IV) and histidine/Np(IV) are similar. They have been fitted with comparable structural parameters : 3 O(water) @ 2.31 Å and 5 O(asp) @ 2.35 Å. Note that the total coordination number of neptunium has been fixed to 8 (average coordination number for Np(IV)) and the relative values of water *versus* aspartate has an error estimated at ± 1. In this model, the aspartate carboxylate group is monodentate (a bidentate model gives a significantly lower fit agreement). Structural data on Np(IV)/carboxylates are scarce. In the structure of tetrakis(Formato-O,O')-neptunium(IV) [Hau76] the coordination number is 8 in a distorted cubic polyhedron. The 4 Np-O first neigbour are located at 2.43 Å while the additional 4 Np-C neigbhours are at 2.50 Å. In another system (uranyl/carboxylic acids), Moll *et al.* have found that water molecules bind at a shorter

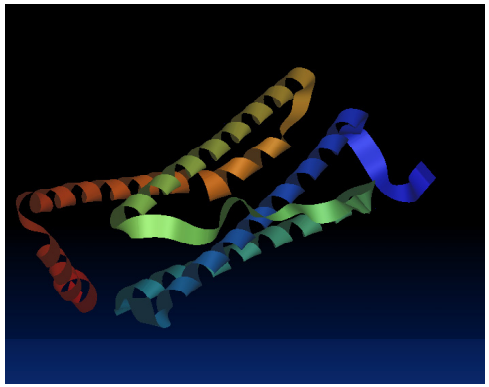

Figure 1 : L-type bundle of spleen horse ferritin (from PDB, ref 1IER).

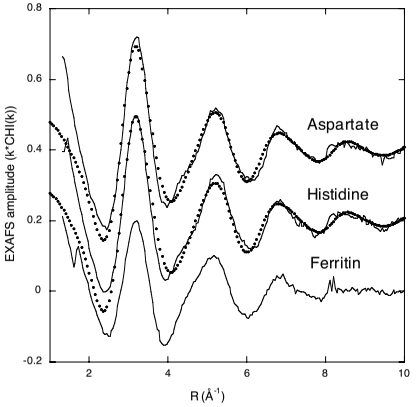

Figure 2 : Raw EXAFS spectra of solutinos of aspartate/Np(IV), histidine/Np(IV) and ferritin/Np(IV).

distance than carboxylates. Complementary IR and RAMAN studies are under investigations to confirm these results. The similarity of the aspartate and histidine spectra shows that the imidazol group does not bind Np(IV) in these conditions and a similar carboxylate coordination is observed.

In the case of ferritin intricate structure, data analysis is complicated by the diversity of the possible coordination sites as well as the lower signal to noise ratio due to the low protein/Np concentration (10^{-4}M). A qualitative analysis of the EXAFS Fourier transform shows that Np(IV) does not bind to the oxyhydroxy iron core but to the proteic part of the protein. Metal coordination sites have been already reported for this protein [Harr96]. At this point of the data analysis we have observed that carboxylate groups participate to the coordination polyhedron. However significant deviation has been found in comparison with the aspartate system. It is believed that other amino acids as tyrosine or histidine also take part to the coordination. In order to perform a quantitative analysis of the neptunium coordination sphere, computer simulations of the possible chelation sites are under investigation.

[Goud94] : F. Goudard, F. Paquet, J-P. Durand, M. C. Milcent, P. Germain, J. Pieri, Biochem. Mol. Bio. Int. (1994), 33, 841.
[Harr96] : P. M. Harrison, P. Arosio, Biochim. Biophys. Acta (1996), 1275, 161.
[Hau76] : J. Hauck, Inorg. Nuclear. Chem. Lett. (1976), 12, 617.
[Moll03] : H. Moll, G. Geipel, T. Reich, G. Bernhard, T. Fanghänel, I. Grenthe, Radiochim. Acta (2003), 91, 11.
[Wald95] : G. S. Waldo, E. Wright, Z. Whang, J-F. Briat, E. C. Theil, D. E. Sayers, Plant. Physiol. (1995), 109, 797.

ROBL-CRG	**Experiment title:** Uranium (VI) complexation with tri-butyl-phosphate (TBP) in room temperature ionic liquid	**Experiment number**: CH-1567
Beamline: BM 20	**Date of experiment**: from: 28/11/2003 to: 02/12/2003	**Date of report**: 27/10/2004
Shifts: 12	**Local contact(s)**: Christoph Hennig	*Received at ROBL:*

Names and affiliations of applicants (* indicates experimentalists):
Isabelle Billard, Clotilde Gaillard*, Soufiane Mekki*

Institut de Recherches Subatomiques
Chimie Nucléaire
23 rue du Loess
67037 Strasbourg cedex 2

Report:

The aim of this work is to study the extraction mechanism of uranyl by TBP in C_4mimTf_2N. In kerosene, it is well known that this extraction is made through the formation of a neutral complex $UO_2(NO_3)_2(TBP)_2$. In imidazolium based-RTILs, the studies made until now on cation transfert from acidic aqueous solution into the RTIL containing a neutral extractant agent (like crown-ether) [1] suggest that the extraction may not be achieved through the formation of a neutral complex, but by a cation exchange process between a cationic complex and the imidazolium cation.

We have analysed solutions in which uranyl ions are readily dissolved and solutions obtained from liquid-liquid extraction, in order to compare the coordination sphere of uranyl extracted in TBP/C_4mimTf_2N and the coordination sphere of uranyl dissolved in the same solution. The influence of the anion on the nature of the complexes formed was checked by analyzing TPB/C_4mimTf_2N solutions in which uranyl salts are dissolved (uranyle nitrate and triflate). The effect of the solvent on the structure of the complexes formed was checked by using C_4mimTf_2N and a conventional aliphatic solvent, dodecane.

Figure 1 displays the exeprimental spectra of 3 samples. $(UO_2)(NO_3)_2(TBP)_2$ is the our reference compound, known to be the neutral extracted species by the TBP/dodecane system (pink line). This is confirmed by our experiment, the two EXAFS and corresponding FT are identical. The green line represents the spectrum of a sample obtained by liquid liquid extraction of uranyl by the system TBP/C_4mimTf_2N. Differences are observed on the FT spectra, in particular in the 2-2.25 Å region which corresponds to the equatorial oxygens from the phosphate and nitrate groups. In $(UO_2)(NO_3)_2(TBP)_2$, uranium is surrounded by 2 O coming from the phosphate groups at 2.36 Å and 4 O from the nitrate groups at 2.49 Å. In the complex extracted by the system TBP/C_4mimTf_2N, uranium is found surrounded by ~2 O at 2.37 Å and ~2 O at 2.51 Å. We can therefore conclude that the species extracted in this case are cationic, i.e. containing only one nitrate group per uranyl.

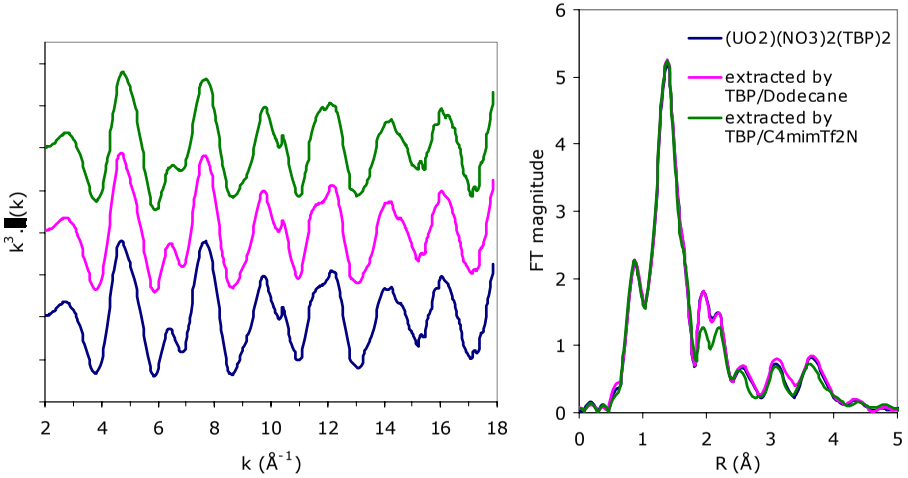

Figure 1 : EXAFS and corresponding Fourier Transform of analyzed samples

[1] M.P. Jensen, J.A. Dzielawa, P. Rickert, M.L Dietz, J. Am. Chem. Soc., 2002, 124, 10664.

ROBL-CRG	**Study of the surface complexes formed between thorium and iron corrosion products.**	**Experiment number**: ME-815
Beamline: BM 20	**Date of experiment**: from: 25/02/04 to:27/02/04	**Date of report**: March , 2004
Shifts: 6	**Local contact(s)**: Christoph Hennig	*Received at ROBL:*
Names and affiliations of applicants (* indicates experimentalists):Mireia Grivé*, Lara Duro, Ferran Seco, Frederic Clarens*, Isabelle Bonhour*, Joan de Pablo, Jordi Bruno		

INTRODUCTION: The objective of this work is the spectroscopic study of surface interaction mechanisms between a tetravalent actinide, Th, and the products of corrosion of the steel canister used in a HLNW repository. The selection of Th as metal to study is straigthfoward. Under the reducing environment expected to develop in the vicinity of the spent nuclear fuel stored in the repository, the most stable redox states for the long-lived actinides is the tetravalent state (Th(IV), U(IV) and Pu(IV) mainly). The elucidation of the structure of the surface species formed between the surface of the corrosion products and these metals will help in the understanding of their sorption mechanims, what can lead to a better and more proper assessment of the concentrations of these metals likely to occur when in contact with the mineral. This can have important implications in risk assessment given that normally the sorption processes are conceptualised as distribution coefficients in the mentioned risk assessments, what poses important limitations to the confidence-building process necessary to ensure in this type of safety exercises.

EXPERIMENTAL: sorption experiments onto ferrihydrite (THF) and magnetite (THM) samples have been conducted at pH 3-4 and initial concentrations below the solubility of the most amorphous Th oxides reported. In order to maximize the surface coating of the solid, several enrichment cycles have been followed. Surface coating has been conducted from supersaturation and from undersaturation

experiments. EXAFS spectra of standard $ThO_2 \cdot xH_2O$(s) (THREF) pellet and an aqueous reference sample at pH=3 (THAQ2) have been also recorded .

RESULTS:

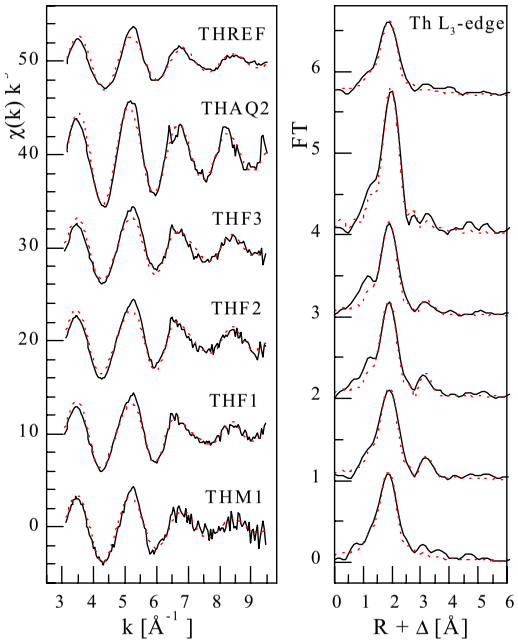

Preliminary data analysis was performed using the EXAFSPAK software. Theoretical scattering amplitudes and phases for each adsorber and backscattered pair were calculated with the program FEFF8. In general, the Th-O distance (around 2.4 Å) seems to be much shorter in the sorption samples than in the aqueous sample while in this later case the coordination number of the oxygen shells is higher. In some cases a shell at ~3.9Å showing Th-Th interactions is obtained. The ~3.5 Å shell seems to correspond to the interaction Th-Fe, which has not been previously reported as far the authors are aware.

ESRF	**Experiment title:** EXAFS/XANES studies on the speciation of Tc(IV) in the presence of complexing organics and fulvic acids	**Experiment number:** CH 1671
Beamline: BM20	**Date of experiment:** from: 27/02/04 to: 02/03/04	**Date of report:** 31/08/04
Shifts: 12	**Local contact(s):** Dr. Harald FUNKE	*Received at ESRF:*

Names and affiliations of applicants (* indicates experimentalists):

Prof.Dr. André MAES
Ir. Eric BREYNAERT
Ir. Christophe BRUGGEMAN

Laboratory for Colloïd Chemistry
Departement of Interphase Chemistry – K.U.Leuven
Kasteelpark Arenberg 23
B-3001 Leuven - BELGIUM

Introduction

The redox-sensitive fission product technetium-99 (Tc) is of great interest in nuclear waste disposal studies because of its potential for contaminating the geosphere due to its very long half-life (2.13×10^5 year) and high mobility under oxidising conditions, where technetium forms pertechnetate (TcO_4^-) [1]. Under suitable reducing conditions, e.g. in the presence of an iron(II) containing solid phase which can act as an electrondonor, the solubility can be limited by the reduction of pertechnetate followed by the formation of a surface precipitate [2]. However, upon association with mobile humic substances (HS), the solubility of reduced Tc species may be drastically enhanced [3].

A first XANES measuring campaign (performed at ESRF, March 2001, CH-1050) demonstrated for the first time that pertechnetate was reduced to Tc(IV) and Tc(IV)-HS species were formed in Gorleben sand/Gorleben groundwater (rich in humic acids) reducing systems. These results were published in Radiochimica Acta [4].

A second EXAFS/XANES campaign (performed at ESRF, July 2002, SI-790) was then performed on samples in which TcO_4^- was reduced by various solid phases (pyrite, magnetite, Gorleben sand, Boom Clay), both in absence and presence of humic acids (HA). These experiments were set up in order to elucidate the chemical environment of Tc in these systems on atomic scale. The data from these experiments showed very interesting and surprising results, because all spectra could be fitted with a hydrated amorphous Tc(IV) oxide phase, independent of the reducing surface used and of the eventual presence of HA. These results could only mean that Tc(IV) oxide colloids were formed and precipitated upon reduction of TcO_4^-, and that these colloids could also interact with the organic colloidal material from Gorleben and Boom Clay HA. This latter observation was confirmed by batch sorption experiments with Tc and Boom Clay suspensions from which an interaction constant could be derived describing the interaction of a neutral Tc(IV) species and dissolved HA [5]. The results from the above described EXAFS/XANES data were incorporated in an article published in Environmental Science & Technology [6].

The aim of a third EXAFS/XANES campaign was to investigate the universality of the observed interaction between Tc(IV) colloids and HA for other organic molecules. Therefore batch systems were set up at KULeuven in which TcO_4^- was chemically reduced to Tc(IV) in presence of 9 reference organic compounds varying in size from small to large (citric acid, hydroxybenzoic acid, pyrogallol, glutaminate, isosaccharinic acid, aurintricarboxylic acid, calconcarboxylic acid, Laurentian fulvic acid, Fluka humic acid) and of Boom Clay HA. These samples still yielded the same colloidal Tc(IV) spectra in presence of large humic acid molecules (Fluka HA and Boom Clay HA) as observed before, however different spectra were now obtained in the presence of small dissolved organic molecules. At that time no performant modeling capabilities were accessible, due to which only single scattering analysis of the data was possible. Based on only SS analysis it was not possible to elucidate an exact structure for the complexes formed.

In order to further elucidate the behaviour of Tc(IV) in the presence of organic matter (colloïd association and/or complexation), a new, fourth, EXAFS/XANES campaign was set up in which the experience of the third campaign was used to specifically investigate Tc(IV) complexation in function of the pH with complexing agents resulting in strong complexes.

Experimental setup

TcO_4^- was chemically reduced to Tc(IV) and contacted with sufficient amounts of 1) small reference organic molecules (salicylic acid, protocatechuic acid, pyrogallol, gallic acid as natural decay products of lignin or polyphenol [11] and representative for the main complexing functional group geometries on FA and HA) and 2) fulvic acids. The systems were buffered in order to obtain a series covering both acidic and basic pH (2-10) so as to obtain a range of competition between H^+ and Tc(IV) for the complexing sites. TcO_4^- reduction and subsequent association with the organic molecules was monitored as a function of time by Gel Permeation Chromatography, UV-VIS to determine the speciation of Tc(IV)/organic complexes. All samples were then preconcentrated and transferred into heat-sealed poly-ethylene microtubes as a slurry. A total of 20 samples were prepared to be measured at the ESRF.

Results

Although the research on the results of this fourth campaign and its precessor is not yet finished completely, some main conclusions could already be drawn:

1) The technique used for the preparation of the samples produced relatively pure samples with technetium concentrations high enough for XAS-measurements in fluorescence mode and in some cases also transmission mode. The complete XAS campaign resulted in spectra for 10 samples. Due to the installation of a new monochromator crystal in the beamline optics (BM20), the raw spectra contain more glitches as compaired to the previous campaigns. Although data extraction was more difficult, good EXAFS spectra were obtained.

2) As described in literature [7, 8] and observed in the results of the previous session, Tc(IV) species formed chelates with most smaller organic molecules by means of a ligand exchange between the hydrolysed Tc(IV) molecules and functional groups present on the organics. For all samples the presence of an organic Tc-complex could be identified by SS analysis of the spectra (exafspak/feff8.28)[9].

3) The structure extracted from the spectra of a pertechnetate standard solution was nearly identical to the optimized structure obtained from DFT[1]-calculations (ub3lyp/lanl2dz) (Table 2 ; Fig 1) which was in accordance with the results of Gancheff *et al.* [10] and [11].

Table 1: Parameters for the TcO_4^- structure obtained from EXAFS analysis and DFT.

	DFT (ub3lyp/lanl2dz)		EXAFS^{++}	
	d(Tc-O) (Å)	N	R (Å)	σ^2
SS: Tc-O	1.75561	4.01961	1.72546	0.00164
MS: Tc-O-O		12.0588	3.19108	0.00577

$^{++}$ E_0=2.91059, Scale=0.94658, Expected resolution=0.116355 Å. All parameters were floated during the fit, except for the coordination number $N_{MS} = 3 * N_{SS}$ and E_0 which was forced to be identical for all paths.

4) In the pH range from 4 to 9 the protocatechuic and pyrogallol-complexes were identified as similar monomeric di-phenol complexes, in contrast with the dimeric structure of the citric acid Tc(IV) complex measured in the third campaign. Both phenolic complexes were modeled by DFT-calculations (ub3lyp/lanl2dz) to obtain a more detailed structure of the complexes. The interatomic distances obtained from the model and from the EXAFS spectra coincided within 0.1Å, the expected error on both techniques. Based on FEFF-calculations (feff 8.2) on the modeled structures a MS path, between 2 carbon atoms of the rigid aromatic

[1] Density Functional Theory

structure could be identified in the spectra. Other less rigid MS paths from the FEFF- calculations could not be identified up until now.

Table 2: Atomic coordinates for the structure Fig 1.

#	Elem	X	Y	Z
1	Tc	0.000000	0.000000	0.000000
2	O	1.013600	1.013600	1.013600
3	O	-1.013600	-1.013600	1.013600
4	O	1.013600	-1.013600	-1.013600
5	O	-1.013600	1.013600	-1.013600

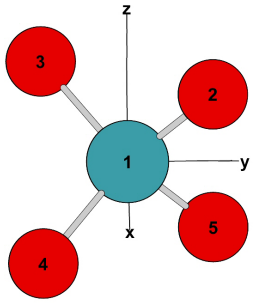

Fig 1: DFT (ub3lyp/lanl2dz) optimized structure of TcO_4^-

References

1. Lieser, K.H. and C. Bauscher, *Technetium in the Hydrosphere and in the Geosphere .1. Chemistry of Technetium and Iron in Natural-Waters and Influence of the Redox Potential on the Sorption of Technetium.* Radiochimica Acta, 1987. **42**(4): p. 205-213.
2. Cui, D.Q. and T.E. Eriksen, *Reduction of pertechnetate in solution by heterogeneous electron transfer from Fe(II)-containing geological material.* Environmental Science & Technology, 1996. **30**(7): p. 2263-2269.
3. Sekine, T., A. Watanabe, K. Yoshihara, and J.I. Kim, *Complexation of Technetium with Humic-Acid.* Radiochimica Acta, 1993. **63**: p. 87-90.
4. Geraedts, K., C. Bruggeman, A. Maes, L.R. Van Loon, A. Rossberg, and T. Reich, *Evidence for the existence of Tc(IV) - humic substance species by X-ray absorption near-edge spectroscopy.* Radiochimica Acta, 2002. **90**(12): p. 879-884.
5. Maes, A., C. Bruggeman, K. Geraedts, and J. Vancluysen, *Quantification of the interaction of Tc with dissolved boom clay humic substances.* Environmental Science & Technology, 2003. **37**(4): p. 747-753.
6. Maes, A., K. Geraedts, C. Bruggeman, J. Vancluysen, A. Roßberg, and H. Hennig, *Evidence for the Formation of Technetium Colloids in Humic Substances by X-Ray Absorption Spectroscopy.* Environmental Science & Technology, 2004. **38**(7): p. 2044-2051.
7. Noll, B., S. Seifert, and R. Munze, *Preparation and Characterization of Technetium(Iv)-Complexes with Diethylenetriaminepentaacetic Acid and Ethylenediaminetetraacetic Acid as Ligands.* International Journal of Applied Radiation and Isotopes, 1983. **34**(3): p. 581-584.
8. Kennedy, C.M. and T.C. Pinkerton, *Technetium Carboxylate Complexes .2. Structural and Chemical Studies.* Applied Radiation and Isotopes, 1988. **39**(11): p. 1167-1177.
9. Ankudinov, A.L., B. Ravel, J.J. Rehr, and S.D. Conradson, *Real Space Multiple Scattering Calculation of XANES.* Phys. Rev. B, 1998. **58**: p. 7565.
10. Gancheff, J., C. Kremer, E. Kremer, and O.N. Ventura, *Density functional study of technetium and rhenium compounds.* Journal of Molecular Structure-Theochem, 2002. **580**: p. 107-116.
11. Krebs, B. and K.D. Hasse, *Refinements of Crystal-Structures of Ktco-4, Kreo-4 and Oso-4 - Bond Lengths in Tetrahedral Oxo-Anions and Oxides of Do Transition-Metals.* Acta Crystallographica Section B-Structural Science, 1976. **32**: p. 1334-1337.

ESRF	**Experiment title:** EXAFS study of uranium(VI) uptake by kaolinite	**Experiment number:** ME-817
Beamline: BM 20	**Date of experiment:** from: 13/03/2004 to: 17/03/2004	**Date of report:** 31/08/2004
Shifts: 12	**Local contact(s):** Harald FUNKE	*Received at ESRF:*

Names and affiliations of applicants (* indicates experimentalists):

Samer AMAYRI*, Jakob DREBERT*, Tobias REICH*

Institute of Nuclear Chemistry

Johannes Gutenberg-Universität Mainz
Fritz-Strassmann-Weg 2
55128 Mainz
Germany

Report:

We studied the uptake of uranium(VI) by kaolinite in batch experiments and by EXAFS spectroscopy. These experiments were performed as a function of pH, uranium concentration in solution, and partial CO_2 pressure.

Experimental For batch experiments, kaolinite KGa-1b (Source Clays Repository) was contacted with 10^{-6} and 10^{-5} M U(VI) solutions, respectively, for 60 h following a 72 h pre-equilibration. The ratio kaolinite to solution was 4 g/L. The ionic strength was 0.1 M $NaClO_4$. The pH was varied between 3.0 and 10.0. The sorption was studied under inert gas conditions in a glove box and at $p(CO_2) = 10^{-3.5}$ atm. To study the influence of the chemical parameters mentioned above on the structure of the surface complexes, we prepared the following samples for EXAFS measurements. 1) Influence of pH: $[U(VI)] = 1 \cdot 10^{-5}$ M, pH = 5, 6, 7, 8.5. 2) Influence of uranium concentration: pH = 7, $[U(VI)] = 5 \cdot 10^{-6}$, $1 \cdot 10^{-5}$, $2 \cdot 10^{-5}$ M. 3) Influence of CO_2: pH = 8.5, $[U(VI)] = 1 \cdot 10^{-5}$ M, with and without ambient CO_2. The solid and liquid phases were separated by centrifugation at 10000 rpm. The amount of uranium taken up by the kaolinite was measured by ICP-MS and INAA.

Results Figure 1 shows the results of the batch experiments. The uptake of uranium(VI) from 10^{-6} M solution increases with pH up to pH 6.0. In the presence of CO_2, the uptake decreases above pH 8 [1]. No decrease in uptake was observed in the absence of CO_2 (Fig. 1). When the total uranium concentration is increased from 10^{-6} M to 10^{-5} M, the sorption pH edge shifts by one pH unit to higher pH. In addition, the decrease of uranium uptake at $p(CO_2) = 10^{-3.5}$ atm due to competition between the formation of surface complexes and uranium(VI) carbonato complexes in solution occurs already below pH 8 (Fig. 1). Table 1 summarizes the analytical results for samples 1 – 8 that were studied as wet pastes by uranium L_3-edge EXAFS spectroscopy in fluorescence mode at room temperature. The influence of pH and initial uranium concentration in solution in the presence of CO_2 was studied using samples 1 – 4 and 5 – 7, respectively. The effect of CO_2 was investigated by comparing samples 4 and 8. Table 2 shows the results of the EXAFS analysis. As expected for the UO_2^{2+} moiety, two axial oxygen atoms at a distance of 1.79 ± 0.02 Å surround uranium in all samples. In the equatorial plane of UO_2^{2+}, an average of five oxygen atoms were found. The U-O_{eq} bond distance varies as a function of pH (see samples 1 – 4 in Table 2). At pH 5.0 the average U-O_{eq} bond distance equals 2.32 ± 0.02 Å. With increasing pH and presence of CO_2, this bond gets longer, i.e., 2.38 ± 0.02 Å at pH 8.4. When CO_2 is excluded from the system at pH 8.5 (sample 8), the U-O_{eq} bond distance is 2.32 ± 0.02 Å, i.e., identical to the value measured at pH 5. These results show that the presence or absence of CO_2 in the system has not only a strong influence on the amount of uranium(VI) sorbed onto kaolinite (Fig. 1), but also on the structure of the surface complexes. The U-O_{eq} bond distance in all samples is significantly shorter than 2.41 Å of the uranium(VI) aquo ion. This shortening of the U-O_{eq} bond indicates the formation of inner-sphere surface complexes. This conclusion is supported by the detection of an additional Al/Si backscattering atom at an average distance of 2.7 Å. Following the discussion of a recent EXAFS study on uranium(VI) sorption on montmorillonite [2], this relatively short U-Al/Si distance can be rationalized by coordination of the uranium atom to the [SiO_4] tetrahedrons of the kaolinite. In addition, we did not observe any evidence of U-U interaction up to initial concentrations of $2 \cdot 10^{-5}$ M U(VI).

In summary, uranium(VI) forms mononuclear, inner-sphere complexes with [SiO_4] tetrahedrons of kaolinite in the pH range of 5.0 – 8.5. At pH 8.5, the presence of carbonate leads to a longer U-O_{eq} bond distance of 2.38 Å compared to the corresponding distance of 2.32 Å in the absence of CO_2. This is the first spectroscopic indication of the possible formation of ternary surface complexes in the system uranium(VI)/ kaolinite/carbonate.

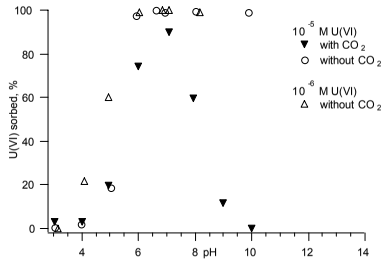

Fig. 1 U(VI) uptake by kaolinite

Table 1 Analytical results for EXAFS samples

Sample	[U(VI)]	pH_{final}	% sorbed
1	$1 \cdot 10^{-5}$	5.0	17
2	$1 \cdot 10^{-5}$	5.9	79
3	$1 \cdot 10^{-5}$	6.9	91
4	$1 \cdot 10^{-5}$	8.4	12
5	$5 \cdot 10^{-6}$	6.7	98
6	$1 \cdot 10^{-5}$	6.7	98
7	$2 \cdot 10^{-5}$	6.8	98
8	$1 \cdot 10^{-5}$	8.5	99

Samples 1 – 7 were prepared at atmospheric levels of CO_2. Sample 8 was prepared CO_2 free.

Table 2 Results of the analysis of the U L_3-edge k^3-weighted EXAFS spectra in the k range of 3.1 – 12.4 $Å^{-1}$

Sample	2 x O_{ax}		5 x O_{eq}		1 x Si	
	R(Å)	σ^2(Å^2)	R(Å)	σ^2(Å^2)	R(Å)	σ^2(Å^2)
1	1.78	0.002	2.32	0.012	2.71	0.008
2	1.78	0.001	2.33	0.011	2.69	0.008
3	1.78	0.001	2.35	0.011	2.72	0.006
4	1.80	0.001	2.38	0.010	2.71	0.004
5	1.79	0.002	2.35	0.011	2.74	0.006
6	1.79	0.001	2.35	0.011	2.74	0.008
7	1.79	0.001	2.35	0.014	2.88	0.004
8	1.79	0.001	2.32	0.013	2.71	0.008

References

[1] K. Sekine, T.E. Payne, T.D. Waite, J.A. Davis; International Alligator Rivers analogue project (18): Experimental study of the uranium adsorption on kaolinite – pH dependence in air-equilibrated system; JAERI-memo 03-036 (1991) 1-14.

[2] C. Hennig, T. Reich, R. Dähn, A.M. Scheidegger; Structures of uranium sorption complexes at montmorillonite edge sites; Radiochim. Acta 90 (2002) 653-657.

ESRF	**Experiment title:** Determination of Th(IV) uptake mechanisms onto hectorite using polarized EXAFS	**Experiment number:** ME-740
Beamline: BM20	**Date of experiment:** from: 12.05.2004 to: 17.05.2004	**Date of report:** 13.10.2004
Shifts: 15	**Local contact(s):** C. Hennig	*Received at ESRF:*

Names and affiliations of applicants (* indicates experimentalists):

R. Daehn*, B. Baeyens*, D. Kunz*, F. Gonzalez*

Laboratory for Waste Management, Paul Scherrer Institute, 5232 Villigen, Switzerland.

Report: Aims of the experiment and scientific background

The underlying goal of the experimental efforts at the Laboratory for Waste Management at the Paul Scherrer Institute is to understand the processes controlling the uptake (sorption) and release (desorption) of safety relevant radionuclides in (underground) nuclear waste repositories. The flow of ground water through a repository can potentially result in the release of radionuclides from waste matrices. The released radionuclides can then be transported through engineered barrier systems (cement and clay barriers) and the surrounding geosphere (often clay rich settings) and potentially harm environmental quality. The release of radionuclides can be considerably retarded due to interactions with clay minerals. Thus, a detailed molecular level understanding of sorption mechanisms of radionuclides in clay systems is of fundamental importance for safety assessment for nuclear waste repositories. Smectitic clay minerals are abundant in the environment and major components of sedimentary rock formations considered as waste sites. From a chemical view point, radionuclides and other metal ions can sorb on edge sites and/or interlayer sites of smectites. The planar sites result from isomorphic substitution in the octahedral and tetrahedral sheets, and edge sites are due to broken Al/Mg-OH and Si-OH bonds at the sites of the clay mineral.

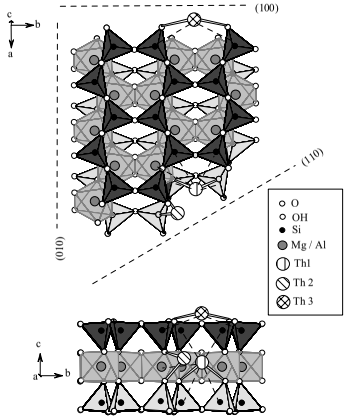

Fig. 1: Three possible Th surface complexes (Th1-Th3) bounded to the montmorillonite surface.

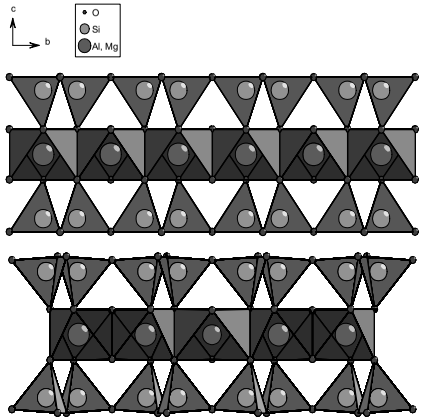

Fig. 2: Representation of the hectorite (top) and montmorillonite (bottom) structure.

Using a combination of powder EXAFS and P-EXAFS we recently investigated the uptake of Ni(II) and Th(IV) onto montmorillonite (1-3). The Ni study showed a strong P-EXAFS dependency and the formation of a Ni-phyllosilicate-like phase at elevated pH and Ni concentrations (1). At near neutral pH and low Ni concentrations the formation of Ni inner-sphere mononuclear surface complexes located at the edges of montmorillonite platelets was observed using P-EXAFS (2). In the Th/montmorillonite system, however, the P-EXAFS dependency was only negligible (3). It was speculated in the Th/montmorillonite study that the absence of a P-EXAFS dependence is caused by the formation of a wide variety of Th surface complexes which are bound to the montmorillonite surface in different configurations and bond angles (e.g. Th1-Th3, Fig. 1). Instead of this hypothesis it could be argued that the absence of a P-EXAFS dependency in the Th/montmorillonite uptake system is caused by the corrugated clay structure of montmorillonite. This corrugated montmorillonite structure is caused by unoccupied octahedral positions (Fig. 2). To investigate whether the corrugated clay structure is responsible for the absence of a P-EXAFS dependence the uptake of Th onto hectorite was examined in this study. Trioctahedral clays like hectorite are lacking vacancies in the octahedral sheets and are consequently highly ordered and uncorrugated clays with a flat basal plane (Fig. 2) (4), and can therefore be considered as "model" clays for uptake experiments.

Experiments + Results

The samples were prepared by adding Th to a montmorillonite suspension (pH 3, 0.3 M $NaClO_4$). After 7 days of reaction time the suspensions were filtrated and highly oriented self supporting clay films were prepared. Th L_{III}-edge fluorescence P-EXAFS spectra were recorded for incident beam angles of α = 10, 35, and 80 degrees (α = the angle between the electric field vector and the plane of the self-supporting film) using a 13-element solid state detector. The k^3-weighted P-EXAFS spectra of Th treated self-supporting clay films for a Th loading of 25 µmol/g and 3 µmol/g are shown in Fig. 3 and 4. The figures illustrate that the P-EXAFS spectra of the clay films have no significant polarization dependence although the self-supporting clay films were well orientated. In P-EXAFS measurements backscattering pairs in the in-plane direction are strongly attenuated when the X-ray polarization vector is parallel to film plane. Therefore, the lack of a P-EXAFS dependency indicates that Th is not sorbed to the hectorite in the continuity of the octahedral sheet in a single surface complex. A mixture of surface complexes which all have bonds to Si that form different angles would severely decrease the P-EXAFS angular dependence. It is therefore possible that there is a series of similar complexes in which Th polyhedra bridge to the hectorite surface in such a manner that the average angle of Th-O and Th-Si pairs with respect to the c* direction (β) is ~54.7°. At this particular β-angle polarized and powder EXAFS spectra are identical and would eliminate any angular dependence in P-EXAFS measurements. We could therefore demonstrate that the uptake of Th onto montmorillonite and hectorite is similar and in particular that the uptake of Th is not affected by the corrugated montmorillonite structure.

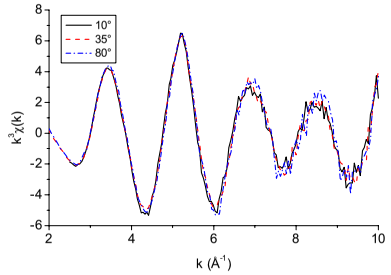

Fig. 3: k^3-weighed Th L_{III}-edge EXAFS spectra at beam angles of 10, 35 and 80 degrees for 25 µmol/g Th sorbed onto hectorite.

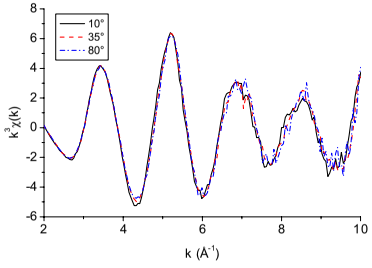

Fig. 4: k^3-weighed Th L_{III}-edge EXAFS spectra at beam angles of 10, 35 and 80 degrees for 3 µmol/g Th sorbed onto hectorite.

1. Dähn, R., et al., *Geochim. Cosmochim. Acta* 66, 2335 (2002).
2. Dähn, R., et al., *Geochim. Cosmochim. Acta* 67, 1 (2003).
3. Dähn, R., et al., *J. Colloid Interface Sci.* 249, 8 (2002).
4. Güven, N., "Smectites.", *in* "Hydrous phyllosilicates (exclusive micas)" Vol. 19, 1988.

ROBL-CRG	**Experiment title:** **Study of complexation behavior of Bispidone derivates towards europium, neptunium and copper**	**Experiment number:** **CH-1766**
Beamline: BM 20	**Date of experiment:** from: 29/09/04 to: 02/10/04	**Date of report:** 03/12/04
Shifts: 12	**Local contact(s):** André Roßberg	*Received at ROBL:*

Names and affiliations of applicants (* indicates experimentalists):
G. Geipel[1], H. Stephan*[1], T. Suzuki[1], A. Rossberg*[2], C. Hennig*[2], H. Funke*[2], M. Leckelt*[1], A. Scheinost*[2]
[1]Forschungszentrum Rossendorf e.V., Institute for Radiochemistry, P.O. Box 510119, 01314 Dresden, Germany
[2]ESRF-ROBL/CRG, Avenue des Martyrs, B.P. 220, 38043 Grenoble Cedex, France

Report:
High complex stabilities towards Eu^3 and Cu^2 have been found particularly in the case of the hexadentate ligand N2Py4 (Fig. 1a). Preliminary studies performed with lipophilic derivates of N2Py4 point to a preferred extraction of actinides over lanthanides.

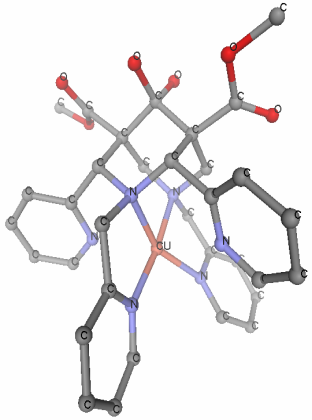

Fig. 1: a) Copper complex of the hexadentate bisbidone ligand (N2Py4) with amine and pyridine nitrogen as donor atoms.

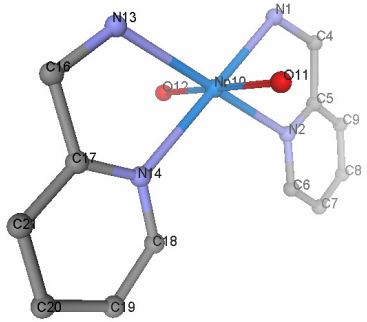

b) Structural model for calculation of theoretical EXAFS phase and amplitude functions for Np L_{III}-edge.

Thus, these compounds seems to be very promising in view of the separation of lanthanides from actinides. Up to now there is no structural information available on such complexes in solution. The study was done in view of the need of selective actinide complexants.

Results
The aqueous solutions were measured in fluorescence mode at the Np L_{III}-edge. At pH 2 and pH 4 the Np(V):N2Py4 ratio was 1:2, while for the sample at pH 3 the ratio was 1:1. Figure 2 shows the Np L_{III}-edge EXAFS spectra with their best theoretical fit.

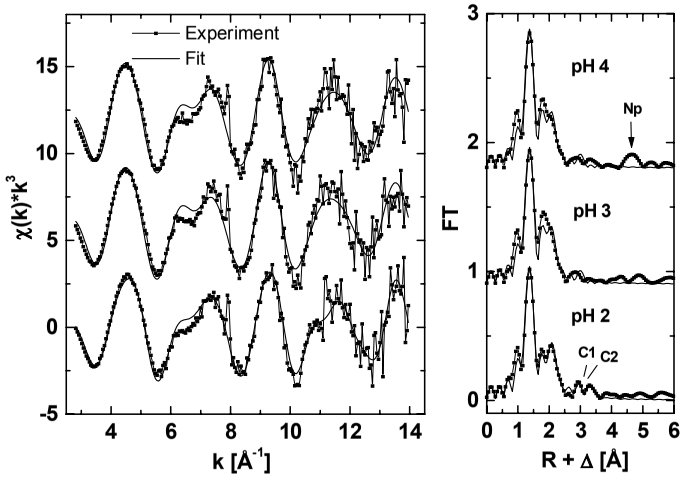

Fig. 2: Np L_{III}-edge EXAFS spectra of aqueous Np(V)/N2Py4 complexes at different pH.

For pH 2, 3, and 4 the radial Np-O_{axial} distance is 1.83±0.02 Å. Considering only N atoms in the equatorial coordination plane of Np(V), one derives a coordination number (CN) of 4-5 at pH 3 and pH 4. At pH 2, the CN is 3. At pH 2, two carbon atoms at radial Np-C distances of 3.49±0.02 Å and 3.69±0.02 Å were fitted. These C atoms indicate a coordination of Np according to Fig. 1b (C4, C5 and C16, C17). At pH 4, a Np-Np interaction at 4.86±0.02 Å indicates formation of polynuclear solution species (Fig. 2).

3.2. Experimental Reports Materials Research

ROBL-CRG	**Experiment title:** **Influence of TiN cap layer, dopant and metal film thickness on phase formation processes in nanoscale Nickel layers during heat treatment on different silicon substrates**	**Experiment number:** **20_02_606**
Beamline: BM 20	**Date of experiment:** from: 09.02.2003 to: 11.02.2003	**Date of report:** 16.04.2003
Shifts: 8	**Local contact(s):** Dr. Norbert Schell	*Received at ESRF:* *17.04.03*

Names and affiliations of applicants (* indicates experimentalists):

Jochen Rinderknecht*, AMD Saxony LLC & Co. KG, Dresden, Germany
Dr. Thorsten Kammler, AMD Saxony LLC & Co. KG, Dresden, Germany
Dr. Hartmut Prinz*, AMD Saxony LLC & Co. KG, Dresden, Germany

Report:

Work and results were presented as a poster at the conference "Materials for Advanced Metalization 2003" (MAM2003), at La Londe les Maures, France, in March 2003.

***In press* for Microelectronic Engineering 2003**

In situ High Temperature Synchrotron-Radiation Diffraction Studies of Silicidation Processes in Nanoscale Ni Layers

Abstract

The formation of nickel silicides has been studied by X-ray diffraction experiments using synchrotron radiation with an energy of 8.048 keV. A gracing incidence setup was chosen with a fixed angle of incidence of 0.5 degree to perform the large angle XRD detector scans. For thermal treatment, an annealing chamber was used to investigate the phase formation and transition processes under quasi-static conditions at elevated temperatures in the range of RT to 650°C. Samples with different dopants, different metal layer thicknesses as well as samples with and without a 150 Å TiN capping layer on single-crystal and polycrystalline (001) silicon substrates have been examined. The results showed that the n-type dopants had no significant impact on the silicidation processes, whereas boron decreases the range of thermal stability of the low resistivity phase NiSi. The capping layer shifts the formation and transition temperatures to higher values.

Summary:

The temperature range for the existence of the target phase NiSi is between 300°C and 500-525°C for doped samples. The n-type doping species, i.e. As^+ or P^+, does not have a significant impact on the formation and transition temperatures. This result confirms previous investigations [1]. The p-type dopant B^+ increases the formation temperature of NiSi and, therefore, it decreases the stability range of the low-resistivity NiSi phase. Further backend-of-line processing has to consider the limited high-temperature stability of this phase, especially on polycrystalline substrates, for which the formation temperature of $NiSi_2$ is generally lower than for single-crystal substrates. Higher temperatures cause an epitaxial growth of the high-resistivity $NiSi_2$ phase on single-crystal substrates, as confirmed by TEM. In general, the doping stabilizes the NiSi phase, especially in the high temperature regime. The TiN capping layer shifts the formation temperatures to higher values on both types of substrates for Ni_2Si and for NiSi. The doping and the deposition of a capping layer increases the formation and transition temperatures of the disilicide phase $NiSi_2$ (compare figures 1 and 2).

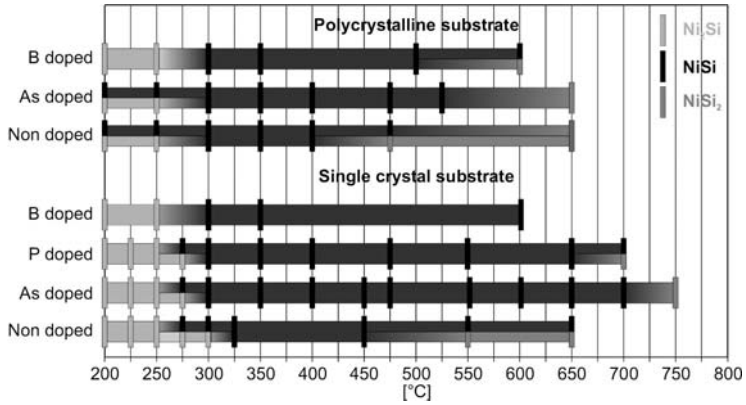

Fig. 1: Summary of 60 SR-XRD results of 100 Å nickel samples with several dopants. High bars are actual measuring temperatures.

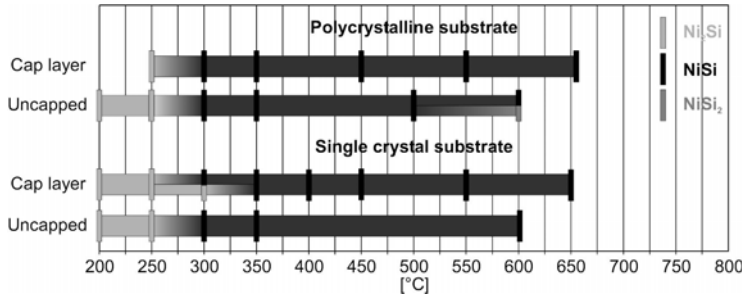

Fig. 2: Summary of 32 SR-XRD results of B^+ nickel samples without a capping layer. High bars are actual measuring temperatures.

[1] J. Rinderknecht, H. Prinz, T. Kammler, F. Berberich, E. Zschech, *In situ high-temperature synchrotron-radiation diffraction studies of Ni and Co-Ni silicidation processes*, Microelectronic Engineering **64** (2002) 143-149.

FZR ROBL-CRG	**Experiment title:** **Characterization of $In_xGa_{1-x}As$/GaAs and $In_xGa_{1-x}As$/InP heterostructures by x-ray scattering (improvement of the analyzer resolution)**	**Experiment number:** **20_02_607**
Beamline: BM 20	**Date of experiment:** from: 13.02.03 to: 18.02.03 (**A**) and from: 08.10.03 to: 12.10.03 (**B**) and from: 03.12.03 to: 09.12.03 (**C**)	**Date of report:** 28.11.2003 **A**
Shifts: 15 + 12 + 18	**Local contact(s):** Dr. Norbert Schell (schell@esrf.fr)	*Received at ROBL:* *10.12.03*

Names and affiliations of applicants (* indicates experimentalists):

J. Sass*, K. Mazur* Institute of Electronic Materials Technology; Wolczynska 133, 01 919 Warsaw, Poland

F. Eichhorn* Forschungszentrum Rossendorf, Institute of Ion Beam Physics and Materials Research, P.O.B. 510119, 01314 Dresden, Germany

Report: A

The investigation of ***stress relaxation in $In_{0.1}Ga_{0.9}As$/GaAs epi-layers on GaAs(001)*** with thicknesses above the critical one may be performed with the asymmetric reflection 224. Preliminary studies of (224) RSMs showed that a slit system in the beam path in front of the detector realizes only a poor resolution in the diffracted beam: a clear analyser / detector streak is seen in Fig. 1 (left-hand side). It disturbes seriously the intensity distribution to be analysed.

In order to improve the resolution, a ***channel-cut analyser*** (CCA) optical module was installeded at the ROBL material research goniometer. It was designed and manufactured by the Department Z-2 of the Institute of Electronic Materials Technology Warsaw. It consits of a two-bounce Ge channel-cut crystal with (022) reflection in a two-circle goniometer with remote control for its adjustment. The optimum radiation wavelength is $\lambda = 0.154$ nm (E = 8.048 keV); nevertheless, the accessible energy ranges from 6.2 keV to 13.7 keV, corresponding to the K-absorption edges for Z = 25 (Mn) to 35 (Br) or the L-absorption edges for Z = 57 (La) to 77 (Ir). The CCA may be used for measurements of diffraction in the reciprocal space (in one and two dimensions) and of reflectivity under very high resolution conditions.

The right part of Fig. 1 shows the (224) RSM of a 400 nm thick $In_{0.08}Ga_{0.92}As$ layer on GaAs(001) collected with the CCA optical module. The analyser streak disappeared completely. Finally, we found ***for epi-layers with different thicknesses that a lattice coherency between the substrate and layer exist up to the layer thickness up to 85 nm***.

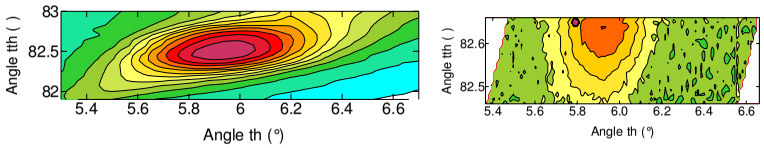

Fig. 1: (224) reciprocal map (in angular coordinates) of a 400 nm thick $In_{0.08}Ga_{0.92}As$ layer on GaAs(001) measured with a detector slit width of 0.13 mm (left-hand side) and with the channel-cut analyser (right-hand side), respectively.

The CCA optical module was tested for various x-ray scattering techniques as shown in Fig. 2.

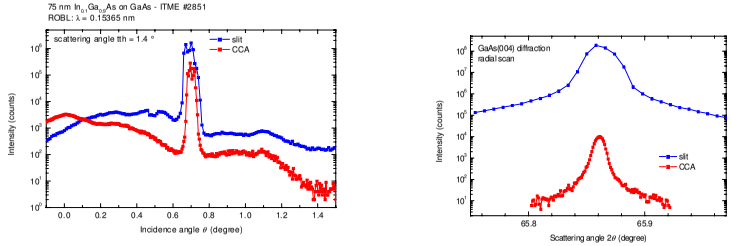

Fig. 2: Comparison of data measured with detector slit (blue) and CCA (red) for diffuse scattering in the specular reflection range (left-hand side) and for a GaAs(004) diffraction peak (right-hand side), respectively.

From a detailed characterization of the CCA optical module for improved resolution in the diffracted beam we conclude:

– the ***maximum angular resolution of 0.0046° = 17“*** is achieved for a symmetric diffraction (this value is near to the calculated / ideal resolution of 12“)

– using the CCA the ***intensity is reduced by a factor ≈10 … 1000*** (this is not at all a severe drawback for the study of specular reflection or diffraction from single crystalline semiconductor material)

– the ***highest improvement of resolution was found for symmetric diffraction*** and the lowest for asymmetric diffraction with flat incidence: the reason may be the modification of the angular width of the acceptance and diffraction ranges for asymmetric beam pathes according to the dynamic theory of diffraction.

ROBL-CRG	**Experiment title:** **Characterization of $In_xGa_{1-x}As/GaAs$ and $In_xGa_{1-x}As/InP$ heterostructures by x-ray scattering**	**Experiment number:** **20_02_607**
Beamline: BM 20	**Date of experiment:** from: 13.02.03 to: 18.02.03 (**A**) and from: 08.10.03 to: 12.10.03 (**B**) and from: 03.12.03 to: 09.12.03 (**C**)	**Date of report:** 27.11.2003 **B** *Received at ROBL:* *01.12.03*
Shifts: 15 + 12 + 18	**Local contact(s):** Dr. Norbert Schell (schell@esrf.fr)	

Names and affiliations of applicants (* indicates experimentalists):

J. Gaca*, M. Wójcik* Institute of Electronic Materials Technology; Wolczynska 133, 01 919 Warsaw, Poland

N. Schell* ROBL-CRG at ESRF

Report: B

The aim of our experiment was to investigate: a) the ***profile of the chemical composition*** in the growth direction for ***laser heterostructures with a very thin highly strained d ≈ 10 nm InGaAs active layer***. To this end the diffraction profiles in the vicinity of the (004) InP substrate reflection have been measured using synchrotron radiation (λ = 0.15396 nm). Fig. 1 gives an example of such a profile.

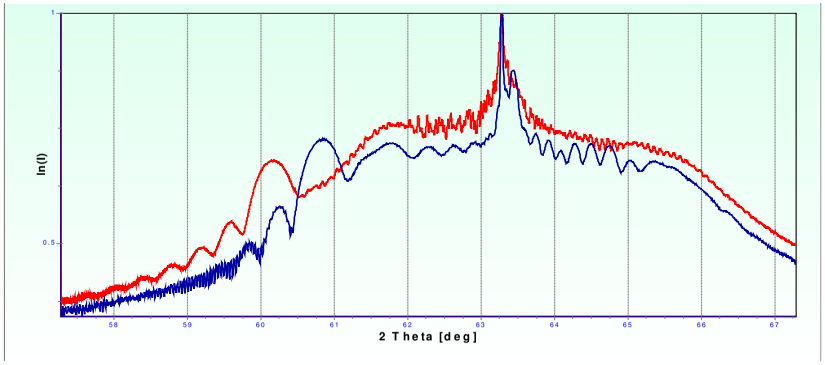

Fig. 1: X-ray diffraction radial scans in the vinicity of the (004) InP substrate reflection performed for: laser structure grown directly on the InP substrate (blue) and on the Bragg mirror 19 x $In_{0.53}Ga_{0.47}As/InP$ (red).

b) We also performed investigations of the ***chemical composition profile for ultra thin $In_xGa_{(1-x)}As$ layers*** deposited on GaAs [001] substrate. Meassured diffraction profiles were analysed by means of numerical methods. Fig. 2 shows an example.

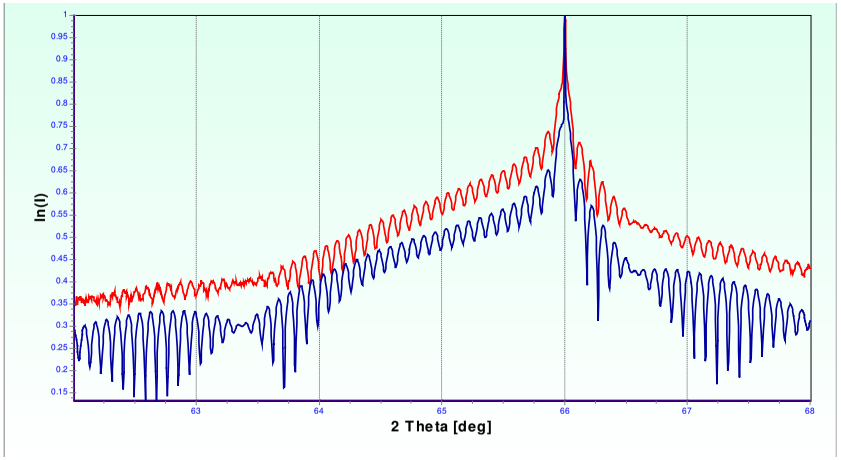

Fig. 2: The experimental (red) and simulated (blue) diffraction profiles for ultra thin d < 6 nm $In_xGa_{(1-x)}As$ layer grown with x = 0.1 covered with a 110 nm GaAs cup layer.

c) The last task was to investigate the ***chemical composition profiles for the ultra thin layers $In_xGa_{(1-x)}As$ and superlattices $In_xGa_{(1-x)}As/InP$*** grown on InP substrate. The analysis was carried out by means of computer simulation. Fig. 3 shows an example.

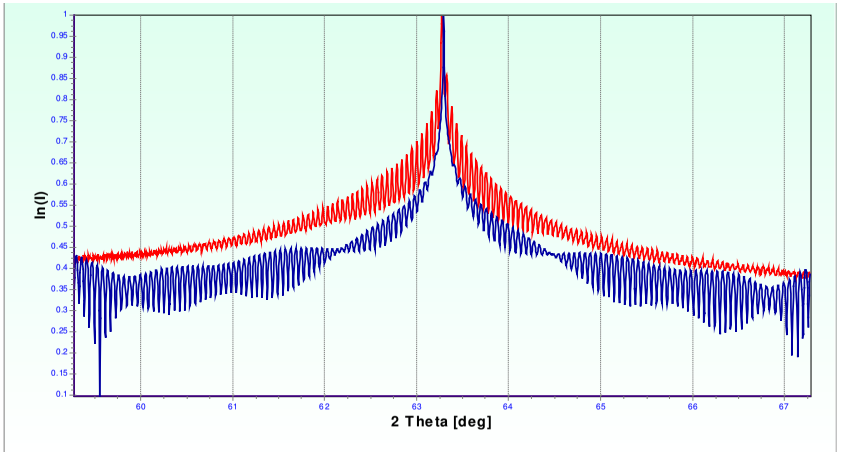

Fig. 3: The experimental (red) and simulated (blue) diffraction profiles for 4 $In_xGa_{(1-x)}As/InP$ layers with varied thickness grown on InP [001] substrate.

ROBL-CRG	**Experiment title:** ***In situ* x-ray diffraction during sputter deposition of $Ti_{1-x}Al_xN$**	**Experiment number:** **20_02_608**
Beamline: BM 20	**Date of experiment:** from: 05.03.2003 to: 11.03.2003	**Date of report:** 18.11.2003
Shifts: 18	**Local contact(s):** Dr. Norbert Schell	*Received at ROBL:* *18.11.03*
Names and affiliations of applicants (* indicates experimentalists): *M. Beckers, Forschungszentrum Rossendorf, Germany *N. Schell, ROBL-CRG, Germany		

Report:

The **growth of $Ti_{1-x}Al_xN$** thin films on oxidized silicon wafers, deposited by **reactive magnetron co-sputtering** from metallic **Al and Ti targets**, has been studied ***in situ***. The film thickness was measured with specular x-ray reflectivity. Using Bragg-Brentano geometry as well as grazing incidence in-plane wide angle scattering, the thickness dependent in-plane and off-plane texture of $Ti_{1-x}Al_xN$ was investigated. Additional examinations on texture development were carried out using a Bruker AXS SMART two-dimensional detector. Additionally, post-deposition laboratory work like transmission electron microscopy and evaluation of pole figures on laboratory x-ray instruments complemented the *in-situ* measurements. By this laboratory work the data recorded during the experiment could be accredited to **tilted off-plane** and presumably **in-plane texture** of the $Ti_{1-x}Al_xN$ thin films.

EXPERIMENTAL

The **deposition chamber** (together with scattering geometry and quality of data, like intensity, resolution, background, which can be obtained with the set-up) is described in previous reports. Both magnetrons with sources of 1 inch target diameter are **tilted 30 degrees** away from the substrate normal at a distance of 100 mm. The magnetron with ***Ti target*** was run at a conctant ***DC power of 80 W***, while the one with ***Al target*** was varied between ***30 and 50 W***. The substrates were 1.5 x 1.5 cm^2 oxidized Si(001) wafers. The base pressure before deposition was appr. $5x10^{-6}$ mbar. The working pressure was varied between $3x10^{-3}$ and $5.5x10^{-3}$ mbar with a fixed reactive sputter gas ***mixture of Ar and N_2 at a ratio of 4:1***. The substrate ***temperature*** was varied between 200 °C and 350 °C by a resistivity heater. A constant substrate ***bias voltage of -30 V*** was applied.

The chamber was mounted onto the goniometer in the MRH. The incident x-rays were monochromatized to 12.8 keV (λ = **0.969 Å**). To study the growth of the films ***in situ***, four scattering geometries were used:

1. Vertical Bragg-Brentano large-angle scattering (**XRD**) revealing the texture. In addition, from the positions of Bragg peaks, information on out-of-plane lattice strain as well as grain sizes and microstrain (lattice defects) can be obtained.
2. Grazing incidence grazing exit in-plane large-angle scattering (**GIXS**). With an incident angle of 0.2°, the calculated x-ray penetration depth was about 200 Å, assuming a mass density of 4.3 g/cm^3. Crystallographic planes perpendicular to the surface are identified and, from the positions and widths of the Bragg peaks, in-plane lattice parameters (strain), grain sizes and microstrain can be gained.
3. Low-angle **specular reflectivity (XRR)** with information on film thickness and surface roughness.
4. Grazing incidence off-plane large-angle scattering (**GID**) to improve off-plane surface sensivity.
5. Real-time Debye-Scherrer recordings with the two-dimensional SMART detector in Braggg-Brentano geometry.

For the latter one the deposition was continious while for the first 5 samples it had been sequential.

Cross-section micrographs were obtained with a Philips CM300 **transmission electron microscope** after grinding the samples mechanically and then doing a final ion erosion step. The stochiometry was obtained by RBS (He^+, E_{He}=1.7 *k*eV, standard fitting routine SIMNRA).

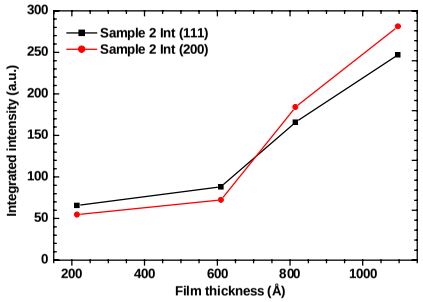

Fig. 1 (left): Integrated **GIXS** intensities per deposition step.

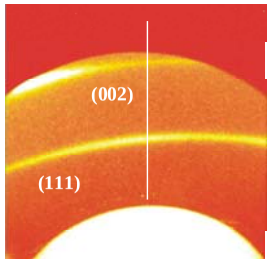

Fig. 2 (right): SMART picture. *(as data examples)*

SUMMARY:

A total of **seven $Ti_{1-x}Al_xN$** films were deposited with the experimental paramters given above. *In-situ* XRD scans showed very low peak intensity for low gas pressure also for 3000 Å thick films, while there was a **steep intensity rise in GIXS** which always probes the last deposition step each time. The typical **crossover** from (002) to (111) orientation perpendicular to the sample surface **could not be observed**. Increasing the total gas pressure led to higher, but still relatively low XRD intensities. SMART measurements showed **tilted (111) and (200) crystallographic planes** leading to low vertical off-plane intensities.

RBS showed the samples were **substochiometric in nitrogen** for lower gas pressure. Cross-sectional TEM at specific film thicknesses revealed increased texture from the substrate interface towards the sample surface, with off-plane (220) texture – not accessable in XRD geometry due to windows restriction – and correlated in-plane (111) and (200) orientation, explaining the increasing GIXS intensities. Pole figures also proved **off-plane (220) fiber texture** but (besides in-plane texture) directed along the incoming Ti particle flux. Ongoing research must clarify this behaviour previously not observed.

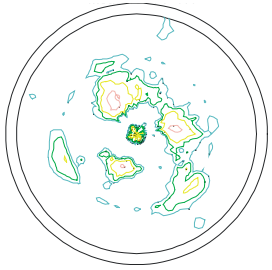

Fig. 3: (111) pole figure showing in plane textured (220) crystallites at χ = 45°.

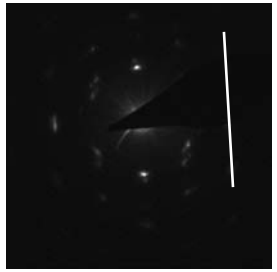

Fig. 4: TEM SAED picture showing pronounced in-plane (111) texture.

ROBL-CRG	**Experiment title:** ***In-situ* x-ray diffraction during sputter deposition of $Ti_{1-x}Al_xN$ – Part II**	**Experiment number:** **20_02_608**
Beamline: BM 20	**Date of experiment:** from: 12.11.2003 to: 18.11.2003	**Date of report:** 17.11.2004
Shifts: 18	**Local contact(s):** Dr. Norbert Schell	*Received at ROBL:* *17.11.04*

Names and affiliations of applicants (* indicates experimentalists):

*M. Beckers, Forschungszentrum Rossendorf, Germany

*N. Schell, R.M.S. Martins, ROBL-CRG, France

Report:

The **growth of** magnetron-sputtered **$Ti_{1-x}Al_xN$** thin films on amorphous substrates has been monitored by ***in-situ*** XRD. The **texture** development of these films shows a **strong dependence on deposition rate**, while **low values of the Al concentration x** and the deposition **temperature play a negligible role**. **Suppresing the ion current** to the substrate by a positive bias voltage can completely **reverse the final texture** even for low deposition rates, showing the importance of ion-substrate interaction, in accordance with [1].

EXPERIMENTAL

The $Ti_{1-x}Al_xN$ films have been grown in the ROBL deposition chamber, the characteristics of which are described in detail elsewhere [2]. As substrates, Si(100) wafers with a 1400 Å amorphous oxide capping layer of size 15 x 15 mm have been used. The base pressure before deposition was appr. 1 x 10^{-4} Pa. Ar and N_2 were applied as sputter gases with a gas flow of 2.82 sccm, leading to a constant working pressure of 0.35 Pa. During the reactive co-sputtering process the Ti and Al targets of 99.999 % purity were run at a constant DC power of 80 W, and 0/5 W, respectively. For a reactive gas mixture of Ar/N_2 = 2/0.6 this resulted in a growth rate of ~1 Å/s, and halved down to 0.5 Å/s for a mixture of Ar/N_2 = 2/1. The substrate temperature was varied between 150°C and 300°C. A bias voltage of -30 V and +10 V was applied.

The growth process has been studied *in-situ* by threee different scattering techniques. First, specular relectivity (XRR) for growth rate calculation. Second and third , large angle off-plane scattering in Bragg-Brentano geometry (XRD) and Grazing Incidence Grazing exit large angle in-plane Scattering (GIXS). The integrated peak intensities reveal information about the texture and crystallinity, and the exact positions of the Bragg peaks yield information about the lattice constants, off-plane and in-plane, repectively.

For all samples, the energy of the incident x-rays was monochromatized to 12.917 keV (λ = 0.961 Å).

	Power Ti (W)	Power Al (W)	Temperature (°C)	Gas ratio Ar/N	Bias (V)
G3_05	80	0	300	2/1	- 30
G2_01	80	5	300	2/1	- 30
G2_02	80	5	300	2/1	- 30
G2_03	80	5	150	4/1.2	- 30
G4_04	80	5	300	2/1	+ 10

Deposition parameters for the various samples investigated.

RESULTS

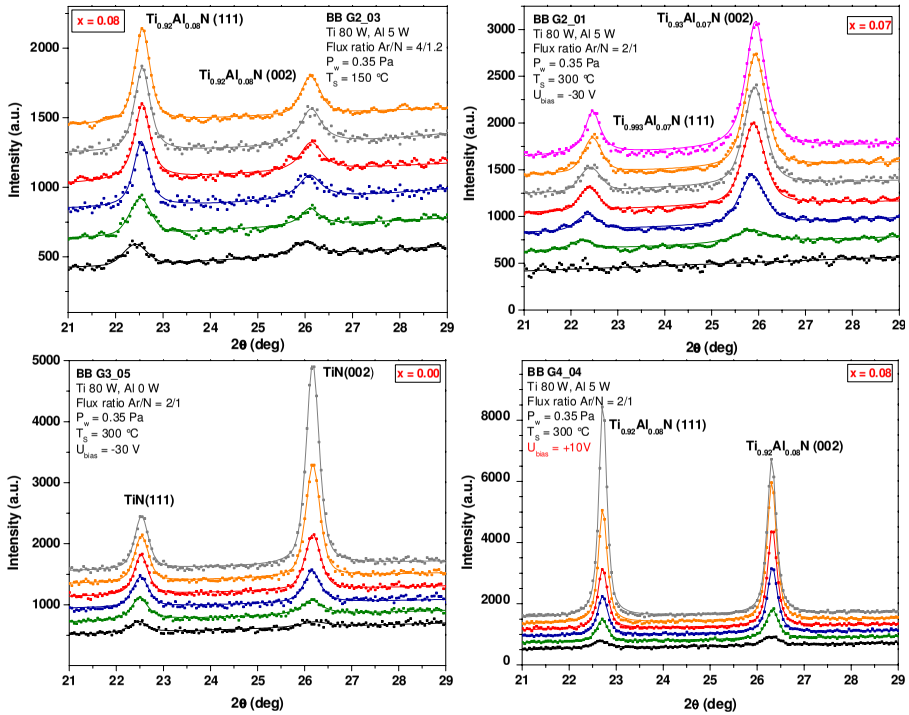

Fig 1: The dotted curves show the observed Bragg-Brentano intensities with increasing sample thickness (final thickness around 200–300 nm), the superposed straight lines show the fits obtained using a Pseudo-Voigt function for each single peak. The GIXS data show corresponding behaviour (*not shown*).

A deposition at 150°C and a growth rate of 1 Å/s results in a typical (111) preferred off-plane orientation for higher thicknesses (Fig. 1 *top left*). An increase of nitrogen partial pressure leads to stronger target poisening which in consequence leads to a lower deposition rate of 0.5 Å/s. This strongly effects the preferred off-plane orientation, which stays (002) even at higher thicknesses, practiacally regardless of substrate temperature (Fig. 1 *top right*). This behaviour cannot be attributed to the small amount of Al, since pure TiN shows exactly the same behaviour (Fig. 1 *bottom left*).

Because a reduced depositon rate also changes the ion/neutral-flux-ratio on the substrate, we suggest that the change in preferred orientation is not due to strain surface-energy competition but due to the increased ion bombardement during growth [3], and in fact suppressing the ion current by applying a positve bias reverses the texture into a competitive growth, where (111) orientation gets the upper hand at higher thicknesses (Fig. 1 *bottom right*).

[1] D. Gall, S. Kodambaka, M.A. Wall, I. Petrov, and J.E. Greene, J. Appl. Phys. **93** (2003) 9086
[2] W. Matz, N. Schell, W. Neumann, J. Bøttiger, and J. Chevallier, Rev. Sci. Instrum. **72** (2001) 3344
[3] M. Beckers, N. Schell, R.M.S. Martins, A. Mücklich, and W. Möller, *submitted* for publication

ROBL-CRG	**Experiment title:** ***In-situ* XRD study of sputtered Ni-Ti SMA (Shape Memory Alloy) thin films**	**Experiment number:** **20_02_608** **ME-584**
Beamline: BM 20	**Date of experiment:** from: 25.06.2003 to: 01.07.2003	**Date of report:** 19.08.2003
Shifts: 18	**Local contact(s):** Dr. Norbert Schell	*Received at ROBL:* *20.08.03*

Names and affiliations of applicants (* indicates experimentalists):

Norbert Schell[1]*, Rui M. S. Martins[2]*, João Canejo[2]*

[1] Institute of Ion Beam Physics and Materials Research,
Forschungszentrum Rossendorf, P.O. Box 510119, 01314 Dresden, GERMANY

[2] CENIMAT – Centro de Investigação de Materiais,
Campus da FCT/UN L, 2829-516 Monte de Caparica, PORTUGAL

Report:

Ni-Ti thin films present great advantages for the fabrication of microactuators. Current intensive research demonstrates that unique fine microstructures are responsible for the superior shape-memory characteristics observed in thin films as compared with bulk materials [1]. The phase transformation and precipitation, which are responsible for the shape memory effect, have been widely studied in bulk and thin films. However, *in-situ* studies have been limited to the aging/annealing treatments after deposition. *In-situ* study of the sputter deposition of Ni-Ti thin films has not yet been reported. At ROBL, *in-situ* studies of the crystallization kinetics [2] have now been followed by ***in-situ* analysis of the sputter deposition of NiTi thin films**.

EXPERIMENTAL

A sputter deposition chamber for the *in-situ* study of film growth by synchrotron x-ray diffraction and reflectivity was used [3]. The two magnetrons are placed at a distance of 100 mm from the substrates and tilted 30 degrees away from the substrate normal. To avoid cross contamination of the targets, chimneys (1 inch long) are mounted on the magnetrons. Air–pressure-controlled shutters are placed in front of the chimneys. Further experimental parameters were: base pressure appr. 2×10^{-6} mbar, target material Ni-Ti (49 at% Ni – 51 at%Ti), sputter gas Ar (99.9996%) at a pressure of 3.5×10^{-3} mbar. The magnetron (only one at the time) was run at a dc power of 40 W, resulting in a deposition rate of approximately 1.2 Å/s.

The deposition chamber was mounted on the six-circle goniometer in MRH. The incident x-rays were monochromatized to 18.367 keV (λ = 0.675 Å). To study the growth of NiTi films *in-situ*, two different scattering geometries were used:

1. Vertical Bragg-Brentano large angle scattering (XRD).
2. Low-angle specular reflectivity with information on film thickness and surface roughness.

Sample	*Substrate*	*Bias (V)*
1	SiO_2 / Si(100)	0
2	SiO_2 / Si(100)	-45
3	Si(100)	0
4	Si(100)	-45
5	SiO_2 / Si(100)	0
6	Poly Si (CVD 675ºC) / Si(100)	0

Table 1: Parameters used for sputtering deposition.

RESULTS

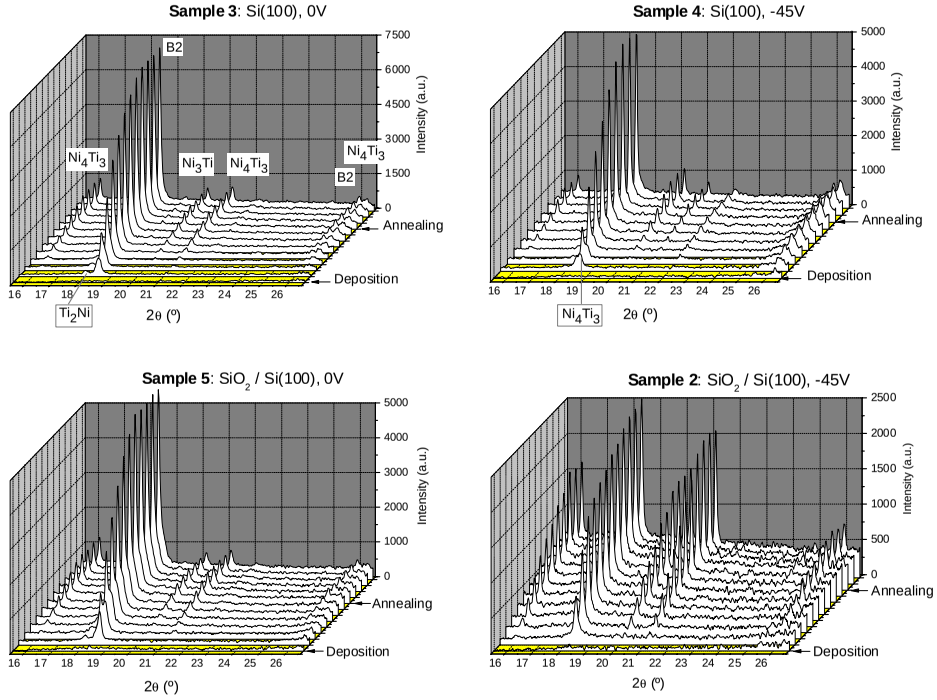

Fig. 1: *In-situ* XRD study during sputter deposition at 470ºC (steps of ≈ 110 nm) and during annealing (steps of ≈ 15 min).

The experimental results show that:

- when a **bias** is applied, a much more significant **change of the peak intensities of the precipitates** Ni_3Ti and Ni_4Ti_3 is present for the deposition on SiO_2/Si(100), compared to the one on Si(100) (Fig 1);
- there is a significant **reduction of the B2(110) peak area when a bias (-45 V) is applied** to the substrate (Fig. 2);
- after deposition, **during the annealing** (at 470ºC) that follows, the intensity of the **B2(110) peak does not increase** (Fig. 2); for sample 2 this stabilization is already reached *during* deposition.

Further exploitation of these results is in course.

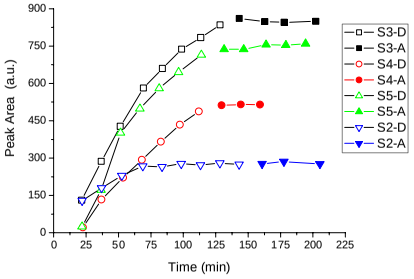

Fig. 2: Area of B2(110) *in-situ* Bragg-Brentano diffraction peaks, recorded during (*D*) and after (*A*) deposition at 470ºC *versus* time.

REFERENCES

[1] A. Ishida and V. Martynov, MRS Bulletin, February 2002, p. 111.

[2] "*In-situ* GIXRD characterization of the crystallization of Ni-Ti sputtered thin films"; R.M.S. Martins, R.J.C. Silva, F.M.Braz Fernandes, L. Pereira, P.R. Gordo, M.J.P. Maneira, N. Schell; presented at "Materiais 2003" (*submitted for publication* in Materials Science Forum).

[3] W. Matz, N. Schell, W. Neumann, J. Bottiger, and J. Chevallier, Rev. Sci. Instrum. **72** (2001), p. 3344.

ROBL-CRG	**Experiment title:** The evolution of texture in thin-film copper during growth and annealing	**Experiment number:** 20_02_609
Beamline: BM 20	**Date of experiment:** from: 09.04.2003 to: 15.04.2003	**Date of report:** 29.08.2003
Shifts: 18	**Local contact(s):** Dr. Norbert Schell	*Received at ROBL:* *29.08.03*
Names and affiliations of applicants (* indicates experimentalists): * J. Bøttiger, University of Aarhus, Denmark		

Report:

By ***in-situ*** XRD, the ***grain size***, ***texture*** and ***lattice constant*** of magnetron-sputtered, nanocrystalline (nc) Cu films were monitored ***during thermal annealing***. The grain growth and the texture development were found to be sensitively dependent on the negative bias voltage on the substrate, which, in turn, controlled the microstructure. Furthermore, the ***activation energy for grain growth*** was determined.

EXPERIMENTAL

The nc Cu thin films (see Table below) were synthesized by d.c. magnetron sputtering in a growth chamber esp. designed for *in-situ* x-ray measurements [1]. The relevant parameters had been: base pressure $\approx 9\times10^{-5}$ Pa; Ar (purity 99.9996%) was used as sputter gas at a pressure of 0.5 Pa and a flow rate of 4 sccm; the substrates, mounted on a resistive heater, were Si(001) wafers (15×15 mm^2) with a 100 nm amorphous SiO_2 layer on top. The films were deposited at room temperature under varying bias voltage (-70 V, -150 V, -250 V). The x-ray wavelength had been $\lambda = 0.960$ Å (12.915 keV).

During film deposition and subsequent annealing, Bragg-Brentano θ-2θ scans were carried out repeatedly (only planes parallel to the film surface probed). The integrated peak intensities reveal information about the texture and crystallinity, and the exact positions of the Bragg peak yield information about the out-of-plane lattice distance. From the shape and width of the diffraction peaks, out-of-plane average grain sizes and microstrain (rms strain) can be obtained. The diffraction peaks were fitted using a pseudo-Voigt peak profile, from which Gaussian β_G and Lorentzian β_L constituents to the total integral breadth were calculated according to a method described by de Keijser *et al.* [2]. The Bragg-Brentano peak profiles were found to be close to purely Lorentzian, i.e. the microstrain was negligible (for this reason, the peak broadening was assumed to be originating solely from finite grain sizes).

To investigate the ***(111) fiber texture*** development of the film during annealing, **χ scans** were carried out repeatedly keeping θ-2θ fixed in the Bragg position Cu(111), the diffraction intensity was measured as a function of the sample tilt χ (tilt axis lying at the intersection of the scattering plane and the film surface). The χ-FWHM intensity of the peaks of the χ scans was used as a quantitative measure of the texture.

Sample	Power (W)	Bias (V)	Deposition time (min)	Thickness (nm)
1	30	-75	10	100
2	30	-75	10	110
3	30	-150	10	105
4	40	-250	10	130
5	40	-250	10	130

RESULTS

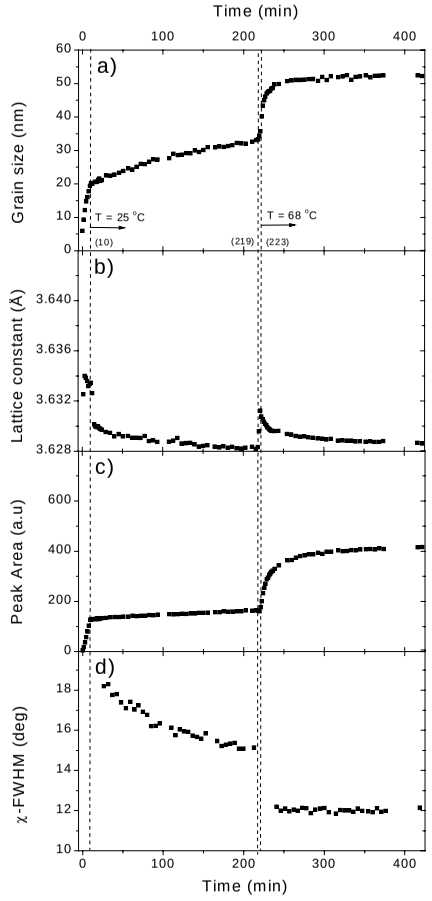

Fig. 1: Structural parameters of Sample #1 (bias –75 V), ***versus* time** after start of growth (the film was kept at 25 °C for 219 min.; after 223 min. the film was kept at 68 °C). (a) grain size, (b) lattice constant, (c) peak area, (d) χ-FWHM.

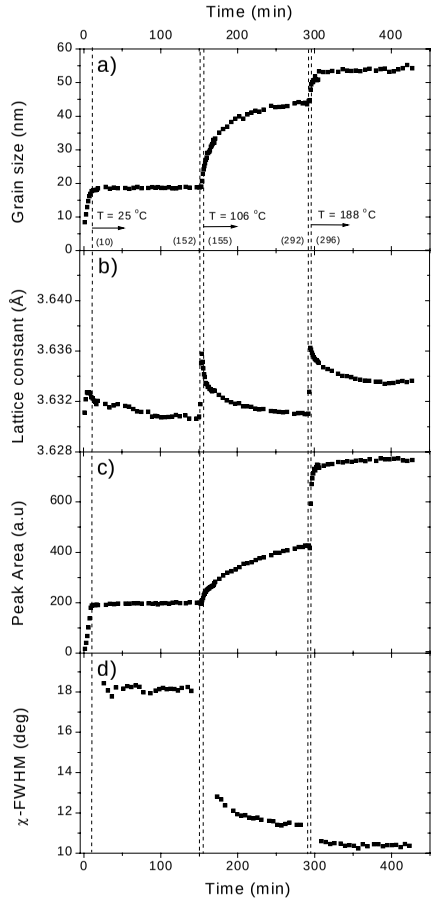

Fig. 2:. Structural parameters of Sample #3 (bias –150 V), *versus* time after start of growth (the film was kept at 25 °C for 152 min.; between 155 and 292 min. the film was kept at 106 °C and after 296 min. at 188 °C).

Activation energies for the grain growth were obtained by analysing the curves of grain size, *D*, *versus* annealing time, *t*. Values in the range 0.90 ± 0.08 (bias –75 V) to 0.82 ± 0.07 eV (bias –150 V) were found.

Grain growth and texture changes decreased monotonically with increasing bias voltage (significant grain growth at RT in films deposited with –75 V bias voltage, fig. 1, very little / no grain growth in films with –150 V and –250 V bias, fig. 2).

This behaviour (corroborated by *ex-situ* XRD and TEM) is ascribed to ***differences in the nanostructure*** [3].

[1] W. Matz, N. Schell, W. Neumann, J. Bøttiger, and J. Chevallier, Rev. Sci. Instrum. **72** (2001) 3344.
[2] Th. De Keijser, J.I. Langford, E.J. Mittemeijer, and A.B.P. Vogels, J. Appl. Cryst. **15** (1982) 308.
[3] N. Schell, K.P. Andreasen, J. Bøttiger, and J. Chevallier, *submitted* for publication.

FZ4R ROBL-CRG	**Experiment title:** **The evolution of texture in thin-film silver during growth and annealing – Part II**	**Experiment number:** **20_02_609**
Beamline: BM 20	**Date of experiment:** from: 18.02.2004 to: 24.02.2004	**Date of report:** 06.11.2004
Shifts: 18	**Local contact(s):** Dr. Norbert Schell	*Received at ROBL:* *07.11.04*
Names and affiliations of applicants (* indicates experimentalists): * J. Bøttiger, University of Aarhus, Denmark		

Report:

The nanostructural evolution during heat treatments of DC magnetron-sputtered Ag films, deposited at room temperature at different substrate bias voltages, was experimentally studied. The thermal stability of the nanostructure was sensitively dependent on the substrate bias voltage. ***Increasing the bias voltage resulted in significantly lower rates of grain growth,*** which we ascribe mainly to the formation of Ar bubbles. Furthermore, ***the grain size in the as-deposited films decreased with increasing bias voltage while the width of the one-dimensional pole figures*** (measured *ex situ*) increased.

EXPERIMENTAL

The nanocrystalline (nc) Ag thin films were synthesized by DC magnetron sputtering in the ROBL *in-situ* growth chamber [1]. The relevant parameters had been: base pressure ≈7×10^{-5} Pa; Ar (purity 99.9996%) was used as sputter gas at a pressure of 0.5 Pa and a flow rate of 4 sccm; the substrates, mounted on a resistive heater, were Si(001) wafers (14×14 mm^2) with a 100 nm amorphous SiO_2 layer on top. The films were deposited at RT under different bias voltages (-50 V, -150 V, -250 V). The x-ray wavelength had been $\lambda = 0.950$ Å (13.051 keV).

During film deposition and subsequent annealing, Bragg-Brentano θ-2θ scans were carried out repeatedly (only planes parallel to the film surface probed). The integrated peak intensities reveal information about the texture and crystallinity, and the exact positions of the Bragg peak yield information about the out-of-plane lattice distance. From the shape and width of the diffraction peaks, out-of-plane average grain sizes and microstrain (rms strain) can be obtained. The diffraction peaks were fitted using a pseudo-Voigt peak profile, from which Gaussian β_G and Lorentzian β_L constituents to the total integral breadth were calculated according to a method described by de Keijser *et al*. [2]. The Bragg-Brentano peak profiles were found to be close to purely Lorentzian, i.e. the microstrain was negligible.

RESULTS

The table gives results obtained from *in-situ* Bragg-Brentano x-ray diffractograms shown in Fig. 1 of three Ag films. Tabulated are the integrated intensities $I_{(111)}$, the ratio $I_{(111)}/I_{(002)}$, and the (111) grain size for the as-deposited films and after 80 min. annealing at 81°C (for comparison, $I_{(111)}/I_{(002)} = 2.5$ for a Ag powder).

Bias (V)	$I_{(111)}$ as deposited	$I_{(111)}$ annealed at 81°C	$I_{(111)}/I_{(002)}$ as deposited	$I_{(111)}/I_{(002)}$ annealed at 81°C	Grain size (nm) as deposited	Grain size (nm) Annealed at 81°C
-50	5500	9000	12.6	16.4	35	44
-150	3200	3700	9.9	9.7	18	22
-250	3300	3500	14.2	13.6	15	16

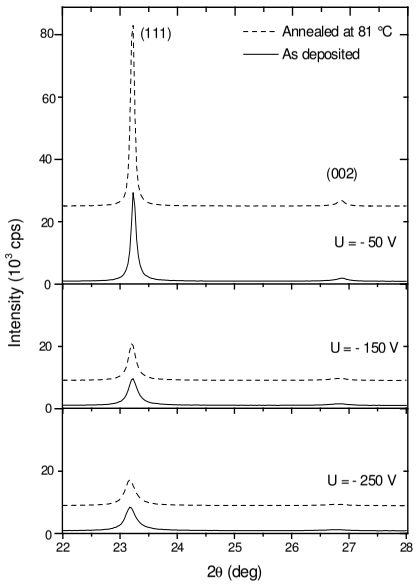

Fig. 1: *In-situ* Bragg-Brentano x-ray diffractograms obtained for three Ag films deposited with various bias voltages, recorded in the as-deposited state (RT) and after 80 min annealing at 81°C, resp. Top: -50 V; middle: -150 V; bottom: -250 V. The film thicknesses are 114, 96 and 93 nm, resp.

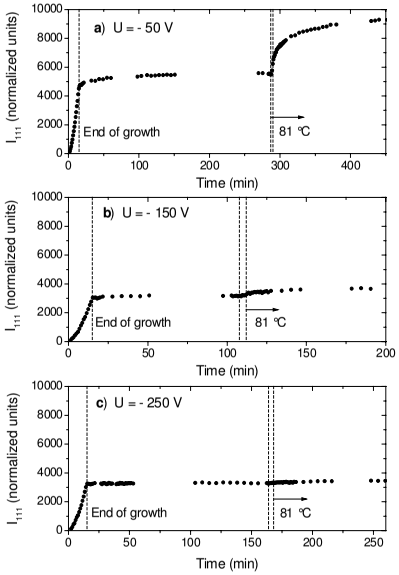

Fig. 2:. Integrated intensities of Bragg-Brentano Ag(111) diffraction peaks recorded as a function of time after start of film growth. Three films deposited at different bias voltages: (a) -50 V, (b) -150 V and (c) -250 V are shown. The film thicknesses are 114, 96 and 93 nm, resp. After a growth period of 15 min, the films were kept some hours at RT before the temperature was raised to 81°C.

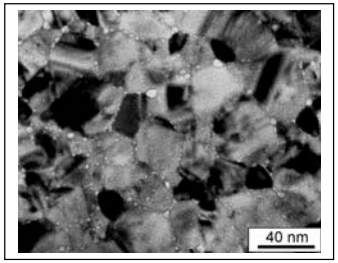

Fig. 3:. Plan-view, bright-field under-focused image of a film as deposited with -250 V bias. ***Ar bubbles*** are observed as small bright spots. Some decorate the grain boundaries while others are found in the interior of the grains. A few Ar bubbles were also observed in the films grown with -150 V bias, while in -50 V biased films no bubbles were detected. Ar bubbles were not observed in previously studied Cu films [3]. Finally, focused, plan-view bright-field micrographs (not shown) from all films revealed ***twinning***.

Grain growth and texture changes decreased with increasing bias voltage. For ***Cu*** [3] this was explained by ***decreasing defect concentrations*** (larger bias results in more energetic ion bombardments of the growing film, which, in turn, make the surface atoms more mobile, whereby the defect concentration in the form of vacancies decreases). As a result, the driving force for grain growth due to recrystallization also decreases. In the case of ***Ag***, however, the build-up of Ar atoms, which formed ***Ar bubbles***, is ***dominating*** the reduction of the grain growth (some of the Ar bubbles were spread over the interior of the grains, slowing down the recrystallization process, while others decorated the grain boundaries, reducing the grain boundary mobility due to pinning).

[1] W. Matz, N. Schell, W. Neumann, J. Bøttiger, and J. Chevallier, Rev. Sci. Instrum. **72** (2001) 3344.
[2] Th. De Keijser, J.I. Langford, E.J. Mittemeijer, and A.B.P. Vogels, J. Appl. Cryst. **15** (1982) 308.
[3] N. Schell, K. Pagh Andreasen, J. Bøttiger, and J. Chevallier, Thin Solid Films *in press* (2004).

ROBL-CRG	**Experiment title:** X-ray diffraction and reflectivity studies of Si/SiGe based quantum cascade structures	**Experiment number:** 20_02_610
Beamline: BM 20	**Date of experiment:** from: 18.06.2003 to: 24.06.2003	**Date of report:** 20.08.2003
Shifts: 18	**Local contact(s):** Dr. David Dekadjevi (e-mail: dekadjevi@esrf.fr)	*Received at ROBL:* *20.08.03*

Names and affiliations of applicants (* indicates experimentalists):

G. Bauer, M. Meduna*, G. Chen*, *Institute of Semiconductor Physics, J. Kepler University, Linz, Austria*

C.V. Falub*, *Laboratory for Micro- and Nanotechnology, Paul Scherrer Institute, Villigen, Switzerland*

D. Dekadjevi*, N. Schell*, *ROBL beamline at ESRF, Grenoble, France*

Report:

High Ge composition $Si/Si_{1-x}Ge_x$ (x=80%) superlattices are important for design flexibility of SiGe based quantum cascade lasers. In this experiment, we focused on the **annealing behavior of strain compensated $Si/Si_{1-x}Ge_x$ multiple quantum well (MQW) structures with high Ge composition (x=80%), grown on $Si_{0.5}Ge_{0.5}$ pseudo-substrates**. These structures have been investigated by **x-ray small angle scattering** and high resolution x-ray diffraction (**XRD**) in a coplanar setup. XRD is sensitive mainly to the strain and x-ray small angle scattering, e.g. x-ray reflectivity (XRR) is only sensitive to the morphology of interfaces. Such superlattices which are originally designed for their photoluminescence and tunneling properties remain enormously highly strained, and are in a metastable regime. Thus, a study on the temperature dependence of the Ge inter-diffusion is desirable and XRR measurements are very suitable for the investigation of inter-diffusion.

The investigated samples contained MBE-grown (300°C) MQW's with 30 periods of $Si_{0.2}Ge_{0.8}$ (83.3Å)/Si (50Å) grown on a $Si_{0.5}Ge_{0.5}$ graded relaxed pseudo-substrate. The superlattices were strain symmetrized by the system of layers graded up to $Si_{0.2}Ge_{0.8}$ situated below the MQW and above the MQW in reversed order, in order to avoid the formation of misfit dislocations in the MQW. We have performed a series of XRR and XRD measurement for the samples *in-situ* annealed at different temperatures, in order to obtain the evolution of interfaces during annealing and to find a temperature limit, at which the strain and inter-diffusion start to affect the structure.

X-ray reflectivity and diffraction reciprocal space maps (**RSM**) have been obtained at room temperature and during annealing for temperatures ranging from 600°C up to 830°C for different annealing periods, using a wavelength λ=1.5405 Å. We have used a small furnace with a Be dome available at ROBL, to perform the *in-situ* annealing study. A **position sensitive detector** was used, in order to record the scattering signal intensity. We have found, that significant changes in reflectivity RSMs start to appear around a temperature of 790°C. At lower temperatures (<700°C), we did not observe any change in the reflectivity for 4 hours. However, the change in scattered intensity in RSM was so fast while the temperature was reaching 830°C, that only two maps could be measured. Fig. 1 shows a whole set of reflectivity RSMs corresponding to different annealing temperatures and time, i.e., room temperature (a), 800°C (b), 830°C (c), and 830°C for 35 minutes (d), where the MQW structure disappeared. In fig. 2, a series of specular reflectivity curves, obtained as cuts from RSMs, are plotted for temperatures 790°C (a) and 830°C (b). The notable difference in the velocity of structure evolution under the above two annealing temperatures could be seen clearly. At 790°C the structure disappeared after 330 min annealing, while at 830°C the structure disappeared after 35 min. We have also performed a series of XRD RSMs at different temperatures. The evolution of diffraction signals around (224) reciprocal space point is depicted in the fig. 3. It is evident that significant changes in the diffraction RSMs already start to appear at temperature 735°C. This means that the **changes in the strain status precede the inter-diffusion processes**, considering the fact that, the structure has almost disappeared in diffraction after 2 hours at 780°C, while in XRR the signal from the periodical structure is still observable.

As a **conclusion**, the results of our experiment exhibit that the ***critical temperature for Ge inter-diffusion in $Si_{0.2}Ge_{0.8}$ is likely around 790°C*** although the strain status of the MQW already starts to change at 735°C.

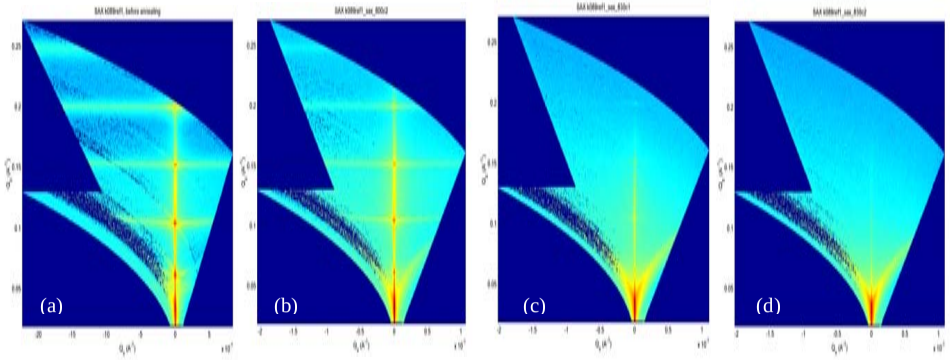

Fig. 1: Series of examples of XRR reciprocal space maps at room temperature (a), 800°C (b), 830°C (c) and 830°C after 35 min (c). The measurement interval between (b) and (c) was about 50 min.

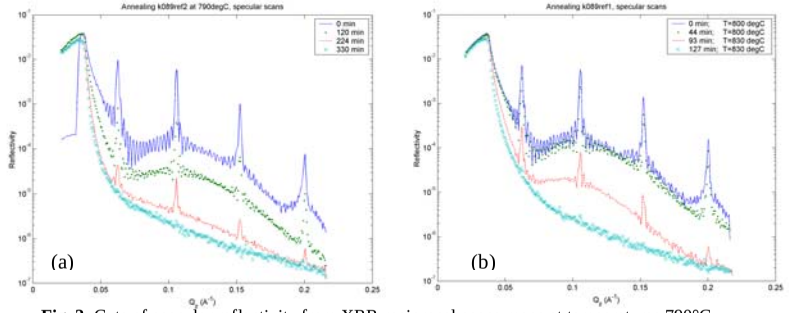

Fig. 2: Cuts of specular reflectivity from XRR reciprocal space maps at temperatures 790°C, 800°C and 830°C.

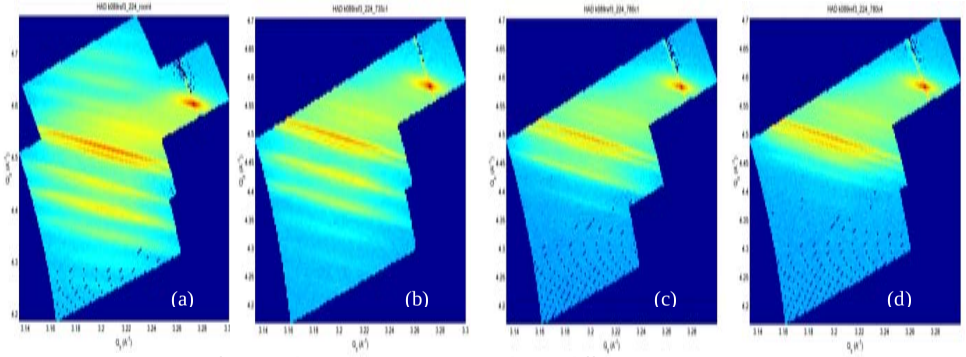

Fig. 3: Series of reciprocal space maps in asymmetrical (224) diffraction at room temperature (a), 735°C (b), 780°C (c) and 780°C after 125 min (d). The time interval between (b) and (c) was about 75 min.

ROBL-CRG	**Experiment title:** **Gracing incidence x-ray techniques applied to nanostructured materials**	**Experiment number:** **20_02_612**
Beamline: BM 20	**Date of experiment:** from: 16.04.2003 to: 22.04.2003 **and** from: 26.07.2003 to: 28.07.2003	**Date of report:** 18.08.2003
Shifts: 18 + 8	**Local contact(s):** Dr. Norbert Schell	*Received at ROBL:* *20.08.03*
Names and affiliations of applicants (* indicates experimentalists): Dr. D. Dekadjevi* FZR, FWIS Dr. J. v. Borany* FZR, FWIS Dr. N. Schell* FZR, ROBL-CRG		

Report:

In this experiment, the suitability of ROBL for Grazing Incidence Small Angle X-ray Scattering (**GISAXS**) has been investigated. The primary beam (λ = 0.12 nm) was defined as 100 µm*100 µm. No anti-scatter slits were needed and the beam was kept within He tubes. The result obtained on **mesoporous silicon layers** with the use of the scintillator detector is shown in fig. 1.

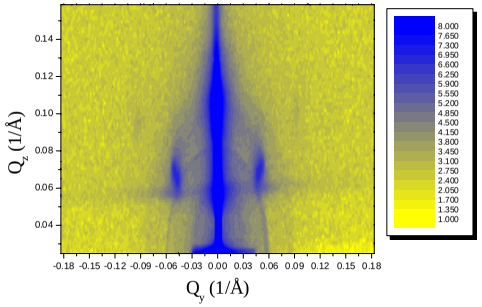

***Fig. 1**: GISAXS pattern of mesoporous Si.*

The pattern is showing a periodic structure in and out of Q_z. Such pattern was compared with results obtained at Brookenhaven National Laboratory and is in good agreement. For the future, the use of a PSD or a 2D CCD is needed to decrease counting time.

As a further step, we have used this technique as well as **Grazing incidence x-ray diffraction and reflectivity** to gain information on the **formation of Ge nanocrystals**. Ge was implanted in a 100 nm SiO_2 film grown on Si(100). The evolution of the diffraction, reflectivity as well as the small angle scattering spectra was observed during an *in-situ* experiment. The sample was **annealed** in different stages under high vacuum (10^{-6} mbar):

(i) **Reflectivity** has shown important changes of the electron density profile. In particular the change of Kiessig fringes amplitude could be related to a **narrowing of the Ge concentration profile within the SiO_2 layer**. In fig. 2, the electron density profile is plotted for the sample at the end of the thermal treatment and is found to be in good agreement with the Ge concentration obtained from RBS technique.

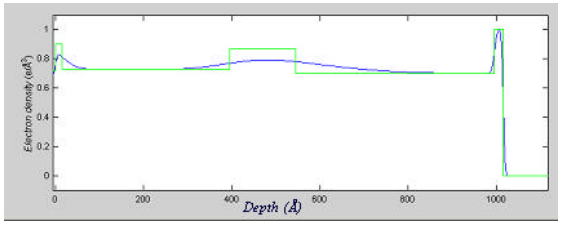

***Fig. 2**: Electron density profile obtained from reflectivitiy at the end of thermal treatment.*

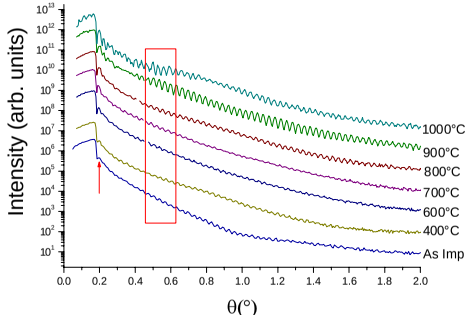

***Fig. 3**: Reflectivity curves obtained as function of the annealing temperature. Note the increase of the Kiessig fringes indicated by the red rectangle. The arrow mark a typical rise of intensity observed by reflectivity on implanted materials.*

(ii) **GISAXS** spectra have shown no evolution during thermal threatment. The presence of Ge nanocrytslals is, however, shown by GIXRD and TEM. Such unsensitivity is understood from a **very wide distribution function of nanocrystal size and intercluster distances shown by TEM analysis**. Note that similar experiments were performed on an annealed sample in N_2 and have shown typical GISAXS patterns.

(iii) **GIXRD** has shown a constant evolution of the angular intensity distribution from 700°C to 1000°C confirming the **nanocrystal formation** (fig. 4).

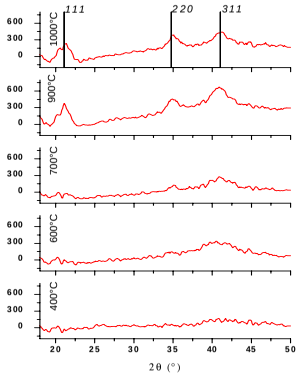

***Fig. 4**: Plot of the intensity at a given annealing temperature minus the intensity of the as implanted sample. From 700°C, a crystalline transformation is clearly observed.*

Further experiments have been performed at constant temperature and as function of time. Some difficulty arose from a very weak signal at high temperature. Such phenomenon could be related to a **liquid phase formation of Ge** as well as thermal vibration of the lattice. For these experiments, a PSD would be needed as well as a fast cooling system in order to enhance the statistics or freeze the system.

ROBL-CRG	**Experiment title:** (Part I) **Gracing incidence X-ray techniques applied to nanostructured materials**	**Experiment number:** **20_02_612**
Beamline: BM 20	**Date of experiment:** from: 16.04.2003 to: 22.04.2003 and from: 26.07.2003 to: 28.07.2003	**Date of report:** 18.08.2003
Shifts: 18 + 8	**Local contact(s):** Dr. Norbert Schell	*Received at ROBL:* *20.08.03*
Names and affiliations of applicants (* indicates experimentalists): Dr. D. Dekadjevi* FZR, FWIS Dr. J.v. Borany* FZR, FWIS Dr. N. Schell* FZR, ROBL-CRG		

Report

Grazing incidence X-ray diffraction (GIXRD), grazing incidence small angle X-ray scattering (GISAXS) and reflectivity (XRR) have been applied to gain information on the formation of Ge nanocrystals in SiO_2 films. Ge was implanted in 100 nm SiO_2 grown on Si(100) with a peak concentration in the centre of the oxide of ~ 20 at.%. The cluster evolution was observed during an *in-situ* experiment where the diffraction, reflectivity and small angle scattering spectra were recorded after different annealing treatments (400-1000°C for 10 min) under high vacuum conditions (10^{-6} mbar).

(i) **Reflectivity data** (**Fig. 1**) analysis reveal important changes of the electron density profile. In particular, the change of Kiessig fringes amplitude could be related to a narrowing of the Ge concentration profile which is due to Ostwald ripening. In **Fig. 2**, the electron density profile is plotted for the sample at the end of the annealing procedure and is found to be in good agreement with the Ge concentration profile derived from RBS (**Fig. 3**).

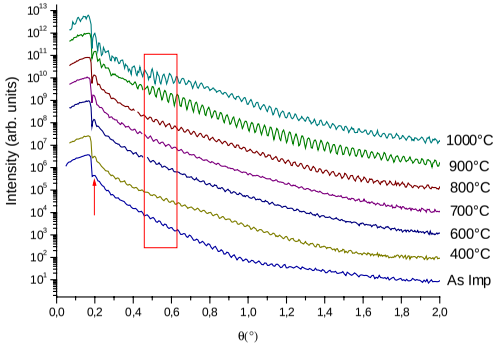

Fig. 1: Reflectivity curves obtained as function of the annealing tempera ture. Note the increase of the Kiessig fringes indicated by the red rectangle. The arrow marks a typical rise of in tensity observed by reflectivity on im planted Ge material.

(ii) **GISAXS spectra** have shown no evolution during thermal treatment. The presence of Ge nanocrystals is, however, confirmed by GIXRD and TEM (**Fig. 4**). Such unsensitivity is understood from a very wide distribution function of nanocrystal sizes and intercluster distances shown by TEM analysis (**Fig. 4**).

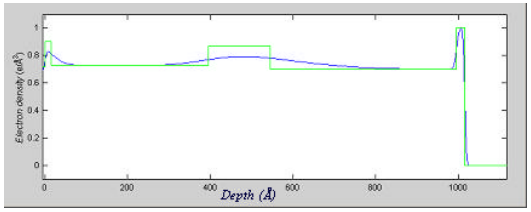

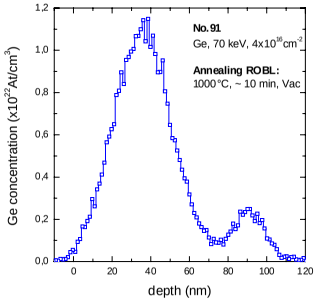

Fig. 2 (left): Electron density profiles obtained from reflectivity at the end of thermal treatment.
Fig. 3 (right): Ge distribution after 1000°C annealing as calculated from RBS spectra.

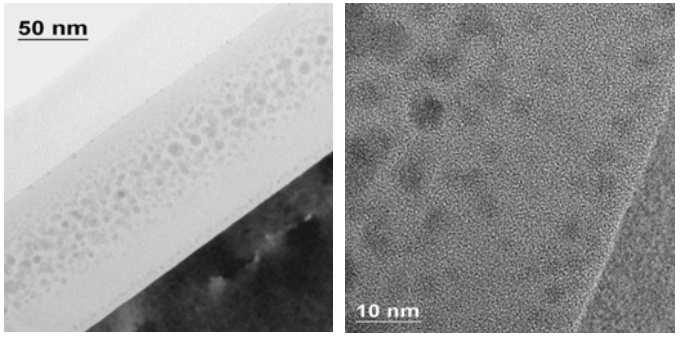

Fig. 4: XTEM micrographs of the sample after annealing at 1000°C, 10 min, vac. The broad cluster size and cluster distance distribution is clearly shown (left). The right micrograph shows the shallow nanocluster band near the Si/SiO_2 interface.

(iii) **GIXRD** (**Fig. 5**) has shown a constant evolution of the angular intensity distribution from 700°C to 1000°C confirming the nanocrystal formation.

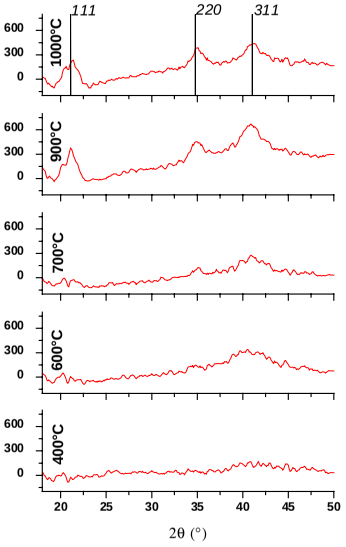

Fig. 5: Plot of GIXRD spectra (0.25° incidence) for various annealing temperatures. The plotted intensity is the measured difference to the as-implanted sample. During measurement the sample temperature was kept at a constant level of 400°C to freeze the present nanocluster distribution.

From 700°C, a crystalline transformation is clearly observed. The mean nanocrystal size increases from < 2 nm (at 700°C) to about 4 nm (at 1000°C). The latter value is in agreement with TEM (Fig. 4) where the cluster size is derived to 5-7 nm (center) and 2-3 nm (borders). The (111) lattice distance (0.332 nm) is slightly above the tabulated value (0.325 nm).

A further experiment has been performed at high temperature XRD as a function of time. Some difficulties arose from disappearing XRD signals above 700°C. Such phenomenon could be related to a liquid phase formation of Ge, as the (reduced) melting temperature of a nanostructure is a strong function of its dimension.

ROBL-CRG	**Experiment title:** **Characterization of structure and morphology of buried layers of transition metal oxides**	**Experiment number:** **20_02_613**
Beamline: BM 20	**Date of experiment:** from: 23.07.2003 to: 26.07.2003 and from: 22.11.2003 to: 24.11.2003	**Date of report:** 15.01.2004
Shifts: 9 + 8	**Local contact(s):** Dr. Norbert Schell	*Received at ROBL:* *15.01.04*

Names and affiliations of applicants (* indicates experimentalists):

N. Shevchenko *, FZ Rossendorf, IIM, Dresden, Germany

F. Prokert *, FZ Rossendorf, IIM, Dresden, Germany

A. Scholz *, FZ Rossendorf, IIM, Dresden, Germany

Y. Bohne, Institut für Oberflächenmodifizierung, Leipzig, Germany

B. Rauschenbach, Institut für Oberflächenmodifizierung, Leipzig, Germany

Report:

Thin buried layers of molybdenum oxide have received great attention due to their possible use as protective layers, insulators, optical coatings or sensors [1, 2]. However, up to now, the structural phase formations in such buried implanted layers were not investigated by *in-situ* XRD analysis during implantation and annealing, thus yielding no direct information on the kinetics.

The polycrystalline molybdenum samples were implanted with oxygen ions at an energy of 1.5 MeV up to a fluence of 1.6×10^{18} O^+-ions/cm^2 without additional heating. The pressure in the implantation chamber was $\leq 10^{-6}$ mbar. A rise in the target temperature of ~300°C was observed during the implantation process due to ion beam heating.

The first part of the ROBL experiment was aimed at the *ex-situ* XRD characterization of structure and morphology of the thin oxide layers by the high intense synchrotron radiation. In the second part the structure changes in the buried molybdenum oxide layer were studied by *in-situ* XRD *during* annealing.

The XRD patterns of the *as-implanted* Mo samples show that ***by high dose implantation the MoO_2 precipitates have been formed in the molybdenum substrate***. The structure evolution of MoO_2 phase during annealing was studied by *in-situ* XRD analysis in Bragg-Brentano geometry. Up to 500°C the pattern remains unchanged, but with increase of the temperature the intensity of the MoO_2 peaks grows. This indicates the ***formation and growth of the crystallites***. ***After annealing at 600°C (1 h) the MoO_2 crystallite size is about 8 nm*** as calculated by the Scherrer formula.

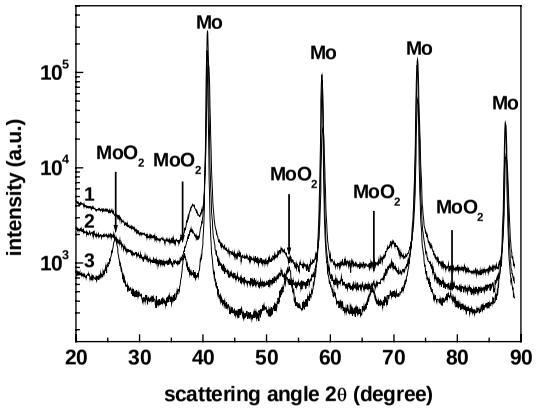

Fig. 1: Synchrotron radiation XRD pattern of the O^+-implanted and post-annealed Mo sample recorded at the incidence angles of 0.5° (1), 1° (2), 4° (3) and wavelength of 0.154 nm.

The *ex situ* recorded XRD patterns (Fig. 1), taken under different grazing incidence, reveal the generation of a ***buried layer and MoO_2 phase formation after implantation and annealing***. In the scans taken at 0.5 and 1° incidence angle the penetrating radiation reaches only the near surface region and MoO_2 was not detected, but for incidence angle of 4° the x-rays penetrate deeper (1/e-depth ~500 nm) and the occurring strong reflections come from a buried MoO_2 layer.

The evaluation of the *in-situ* annealing measurements is not yet completed.

References

[1] C. Hammerl, B. Rauschenbach, Nucl. Instr. and Meth. B **178** (2001) 220.

[2] C. Hammerl, B. Renner, B. Rauschenbach, *et al.*, Nucl. Instr. and Meth. B **148** (1999) 851.

ROBL-CRG	**Experiment title:** **SR-μ-XRD stress measurements of dual damascene inlaid copper interconnect structures at temperatures between RT and 500°C**	**Experiment number:** **20_02_617**
Beamline: BM 20	**Date of experiment:** from: 23.06.2004 to: 29.06.2004 and from: 17.11.2004 to: 23.11.2004	**Date of report:** 19.11.2004
Shifts: 36	**Local contact(s):** Dr. Norbert Schell	*Received at ESRF:* *19.11.04*
Names and affiliations of applicants (* indicates experimentalists): Jochen Rinderknecht*, AMD Saxony LLC. & Co. KG Dr. Hartmut Prinz*, AMD Saxony LLC. & Co. KG Inka Zienert*, AMD Saxony LLC. & Co. KG		

REPORT

Introduction

The stress state of dual damascene copper interconnect structures in low-k materials was measured by XRD at temperatures between RT and 400°C. Stress in the interconnect structure on micro-devices is a very important issue for their long term reliability. With smaller dimensions and implementation of many materials with different mechanical and thermo-mechanical properties, interpolation and simulation of the final stress state is becoming more unreliable and experimental characterisation is, therefore, desperately needed.

Experimental

A small heating stage (DHS900, Anton Paar) fixed to the ROBL six-circle diffractometer allowed a wide range in Chi (±40) and Phi (±60) to be measured. Exact sample positioning, which is necessary for very small structured samples, was enabled with a ***newly installed microscope video camera system*** on the diffractometer. The beam energy was fixed to copper $K_{\alpha 1}$ (λ = 1.541 Å) and the ***beam size reduced down to 300 x 300 μm***.

It is of high importance for stress measurements to choose a high angle reflection because the difference in the angle caused by the elastic deformation of the lattice is higher for larger angles and, thus, the precision of the measurement is much better. In our experiment the Cu(311) reflection at $2\theta = 89.943°$ was chosen. The use of an ***area detector*** (SMART 1000, Bruker AXS) enabled a simultaneous measurement in a 10°-χ range and thus further reduced time for data taking and additionally increased accuracy. The large χ-range is of special importance for Cu structures: These samples show a pronounced texture and thus, together with the low divergence of the synchrotron beam, diffracted intensity is only observed at certain χ and φ angles. As the texture may slightly change from sample to sample, measurements with point detectors will often miss the signal and get very complicated and time consuming to take.

After alignment, the samples were measured at room temperature and subsequently heated up to 400°C in 50°C steps. At each temperature, 12 frames with 4 different χ angles and 3 different φ angles were taken. Finally, the stress tensor is calculated by fitting the deformation of the diffraction cone for different directions with the fundamental stress equation.

Results

Three samples with different low-k (organo silicate) inter-layer dielectric (ILD) materials were measured up to 400°C with two different line widths (0.18 μm and 1.8 μm, respectively) on each sample. S_{11} represents the stress along the line, S_{22} is the stress across the line and S_{33} stands for out-of-plane stress. At room temperature all samples showed tensile stress.

The room temperature stress values depend to a certain degree on the structure geometry: For small lines the tensile stress along the lines is higher, than across (Fig. 1). With increasing temperature the stress is decreasing until it finally gets compressive. The measurements showed, that the slope of the stress-temperature-curve is not only depending on the ILD material, but also different across and along the line for small structures. This means, that also the stress along the line is higher in small structures at RT, the zero stress state is reached at the same temperature for both directions. Above 250ºC the stress along the line again shows larger, now compressive values.

Large line widths show nearly the same values along and across a line for the whole temperature range (Fig. 2). This effect can be essential for structure design, as large stress gradients can build up at the interfaces between structures with different widths and might lead to device failure. The out-of-plane stress S_{33} exhibits the largest variations with temperature. It shows very similar values and slope compared to S_{11} and S_{22} up to 200°C, but sometimes shows a non-systematical variation for higher temperatures (Fig. 1). Local degradation effects like adhesion failure or Cu extrusion cause this variation. The upper interface of the line is covered with SiN/SiO_2 and is much weaker than the Cu/Ta interface at the bottom and the side-walls of the line. Improvement of this interface is an essential step to increase the Cu interconnects` reliability.

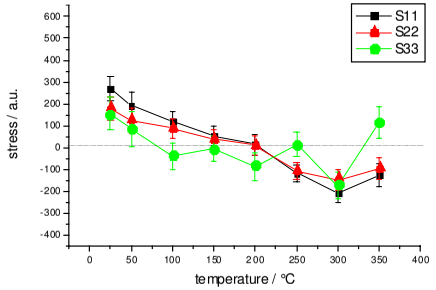

Fig. 1: Stress-temperature curve of an array with ***0.18 μm*** lines in low-*k* Cu inlaid interconnect technology.

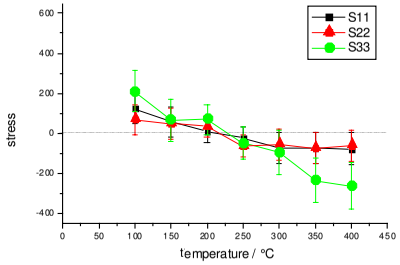

Fig. 2: Stress-temperature curve of an array with ***1.8 μm*** lines in low-*k* Cu inlaid interconnect technology.

The measurements gave very important information on the mechanical properties of the device system and processes of stress relaxation or sample degradation at elevated temperatures.

ROBL-CRG	**Experiment title:** **Influence of substrate temperature at the MBE process on the interface structure of Fe/Cr multilayers**	**Experiment number:** **20_02_618**
Beamline: BM 20	**Date of experiment:** from: 19.11.2003 to: 22.11.2003	**Date of report:** 08.01.2004
Shifts: 9	**Local contact(s):** Dr. Norbert Schell	*Received at ROBL:* *09.01.04*

Names and affiliations of applicants (* indicates experimentalists):

F. Prokert *, FZ Rossendorf, IIM, Dresden, Germany

N. Shevchenko *, FZ Rossendorf, IIM, Dresden, Germany

A. Scholz *, FZ Rossendorf, IIM, Dresden, Germany

E.A. Kravtsov, Russian Academy of Science, IMP, Ekaterinburg, Russia

M.A. Milyaev, Russian Academy of Science, IMP, Ekaterinburg, Russia

Report:

This study is a part of measurements on a series of this type of multilayers (MLs). The MLs were grown on (1 0 -1 2) Al_2O_3 substrates, covered by 7 nm – Cr buffer layer, at different substrate temperatures in the range 20–480°C. Preceding investigations [1] have shown that the interface rms-roughness in these Fe/Cr-MLs strongly depends on the substrate temperature.

The present measurments are a continuation of the experiment number 20_02_059 and were aimed to study the interface structure of Fe/Cr MLs by x-ray ***reflectometry*** (XRR) and ***diffuse scattering*** using the *contrast enhancement* between Fe and Cr at energies above and below of the K-edge of these elements. The Fe/Cr MLs , UU9_3, UU9_1 and UU9_4, having the double layer structure 8 x [^{57}Fe(2 nm)/Cr(1 nm)], were prepared by MBE on oriented sapphire at the substrate temperatures of 20°C, 100°C, 200°C and 280°C, respectively.

Besides the measurements of the specular scattering also the diffuse scattering was studied by rocking and offset scans. Fig. 1 shows the plotted intensity of such scans taken at an energy below the Fe K-edge (7.10 keV).

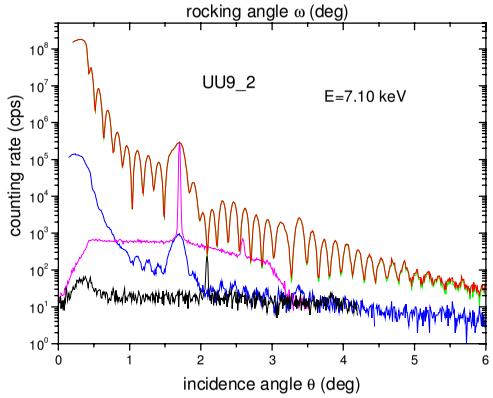

Fig. 1: Specular, longitudinal and transverse scans from the Fe/Cr ML UU9_2 measured below the Fe K-edge at 7.10 keV. The intensity of the transverse scan is plotted *versus* the rocking angle.

For the model-based fitting of the specular reflectivity and the simulation of the diffuse scattering the new REFS program (Bede Scientific; V.4.00) was used. The consistency of the results, demanded for the four energies, could be remarkably improved by revised fit data, obtained by the new genetic fit algorithm [2].

At present the evaluation of the measurements is not completed. First results show that ***the interface width*** $\sigma^{rms}_{Fe} > \sigma^{rms}_{Cr}$ ***and that the roughness structure weakly depends on the substrate temperature***. In the series, ***the MBE layer growth yields a laterally short correlated roughness which is vertically only partly correlated*** ($\sigma^{rms}_{corr}/\sigma^{rm} < 50$ %).

References

[1] V.V. Ustinov *et al.*, J. of Magnetism and Magnetic Materials **240** (2002) 511

[2] M. Wormington, Ch. Panaccione, K.M. Matney, and D.K. Bowen, Phil. Trans. R. Soc. London A **357** (1999) 2827

ROBL-CRG	**Experiment title:** **Ion-beam synthesis of wide band-gap semiconductor nanocrystals: structural studies** ***SiC nanocrystals in a diamond matrix***	**Experiment number:** **20_02_619**
Beamline: BM 20	**Date of experiment:** from: 14.04.2004 to: 17.04.2004	**Date of report:** 19.11.2004 *Received at ROBL:* *19.11.04*
Shifts: 9	**Local contact(s):** Dr. Norbert Schell	

Names and affiliations of applicants (* indicates experimentalists):

F. Eichhorn[1,*], H. Weishart[1], V. Heera[1], N. Schell[1,2,*]

[1] Forschungszentrum Rossendorf, Institute of Ion Beam Physics and Materials Research
P.O.B. 510119, 01314 Dresden, Germany

[2] ROBL-CRG at ESRF, B.P. 220, 38043 Grenoble cedex, France

Report:

Wide band gap semiconductors like silicon carbide and diamond are very promising for the production of high frequency opto- and microelectronic devices able to work under extreme environmental conditions like high temperature, radiation or aggressive media. While heavy p-type doping of SiC is still difficult to achieve, n-type doping can easily be done [1]. On the other hand, a sufficient n-type doping of diamond has not been achieved up to now [2]. Fabrication of heterostructures of n-type SiC and p-type diamond is considered as a new approach to wide band gap semiconductor devices. Recent studies have demonstrated that SiC-nanocrystals in diamond [3] and diamond-nanocrystals in SiC [4] can be formed by ion beam synthesis (IBS).

Ion beam synthesis (IBS) is an excellent method for growing new phases within any substrate. Its advantages over other growth techniques are the possibility to synthesize phases beyond the thermodynamic equilibrium and to grow nanocrystals in contact with the surrounding host matrix. The crystal lattice damage inherent to this method can be largely reduced by performing ion implantation at elevated temperatures. Here, 150 keV Si ions were implanted into diamond to form 3C-SiC nanocrystals. The implantation temperatures were 900°C and 1100°C, respectively.

Grazing incidence grazing exit diffraction technique was used to study the depth distribution of the nanocrystals as well as their amount, size, strain and the orientation relationship to the matrix. The 3C-SiC nanocrystals with a diameter of 8 nm are buried and epitaxially oriented in the diamond matrix: the cubic crystallographic axes coincide. For the implantation temperature of 1100°C the amount of SiC is five times higher than the one at the lower temperature. Immediately at the surface a layer of epitaxially oriented large crystals is detected: they may be strained crystals of graphite or lonsdaleite, a hexagonal diamond phase. Details are given in Figs 1 and 2.

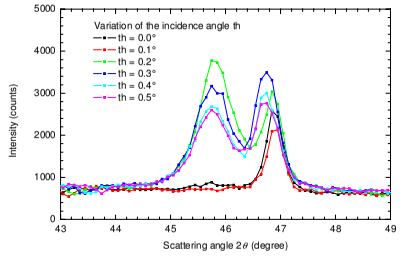

Fig. 1: Grazing incidence grazing exit x-ray diffraction patterns for different penetration depths controlled by the incidence angle. 3C-SiC nanocrystals form the peak at 2θ=45.8°: they are arranged in a buried layer. The peak at 2θ=46.9° may be connected with a graphite or lonsdaleite (hexagonal diamond) carbon phase.

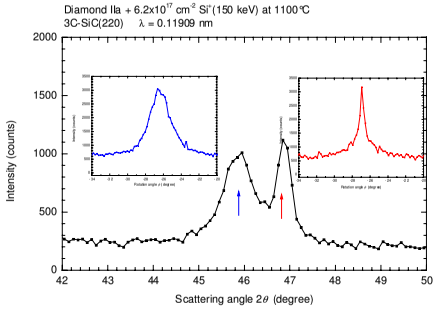

Fig. 2: Details of a diffraction pattern: the insets show the rocking curves at the positions of the 3C-SiC and carbon phase peak, respectively. The SiC nanocrystals form a broad intensity distribution, whereas the laterally large carbon matrix gives a much smaller peak.

[1] M.V. Rao *et al.*, Nucl. Instrum. Methods **B127**, 655 (1997)
[2] R. Kalish, Diamond Relat. Mater. **10**, 1749 (2001)
[3] H. Weishart *et al.*, J. Appl. Phys. **94**, 1195 (2003)
[4] H. Weishart *et al.*, Diamond Rel. Mater. **13**, 627 (2004)

ROBL-CRG	**Experiment title:** ***In-situ* XRD during magnetron deposition and subsequent annealing for nc metals and two-component alloys**	**Experiment number:** **20_02_620**
Beamline: BM 20	**Date of experiment:** from: 16.06.2004 to: 22.06.2004	**Date of report:** 17.11.2004
Shifts: 18	**Local contact(s):** Dr. Norbert Schell	*Received at ROBL:* *18.11.04*
Names and affiliations of applicants (* indicates experimentalists): * N. Schell, R.M.S. Martins, ROBL-CRG, France * M. Beckers, Forschungszentrum Rossendorf, Germany		

Report:

We studied the **growth of** magnetron-sputtered **$Ti_{1-x}Al_xN$** thin films on amorphous substrates. In expansion of previous results concerning the influence of deposition rate on texture, here the Al concentration x was tuned from 0 to 0.73 while keeping all other parameters (especially the deposition rate) constant. For **x < 0.1** the **texture is not affected** by Al incorporation. For **0.15 < x < 0.48** a complete **reversal of preferred orientation from (002) to (111)** can be induced. Increasing x towards the AlN segregation threshold at **x = 0.60** leads to extremely hard **nano-composite TiAlN/AlN**, and pushing x further to **0.73** leads to stressed **AlN** with an a-axis off-plane **(1000) preferred orientation.**

EXPERIMENTAL

All samples were deposited in the ROBL growth chamber [1]. Si(100) wafers with a 1400 Å amorphous oxide capping layer of size 15 x 15 mm have been used as substrates. By applying a liquid notrogen trap, the base pressure was reduced to appr. 1 x 10^{-4} Pa. A constant working pressure of 0.35 Pa was achieved by a sputter gas inlet of 2.82 sccm in the ***ratio Ar/N_2 = 2/1***. The summed DC power of the Ti and Al targets (99.999 % purity) was kept constant at 80 W during all depositions, resulting in a growth rate of ~0.38 ± 0.02 Å/s. The ***substrate temperature was kept at 300°C***. A substrate ***bias voltage of -30 V*** was applied.

Three different scattering techniques have been used to characterize the growth process. First, specular reflectivity (XRR) for growth rate calculation. Second and third, large angle off-plane scattering in Bragg-Brentano geometry (XRD) and Grazing Incidence grazing exit large angle in-plane X-ray Scattering (GIXS). The fitted integrated peak intensities reveal information about texture and crystallinity, and the exact positions of the Bragg peaks yield information about lattice constants, off-plane and in-plane, repectively. The energy of the incident x-rays was monochromatized to 12.917 keV (λ = 0.961 Å).

	Power Ti (W)	Power Al (W)	Stoichiometry
G3_05	80	0	TiN
G4_01	67	13	$Ti_{0.77}Al_{0.23}N$
G3_03	48	32	$Ti_{0.43}Al_{0.57}N$
G4_03	46	34	$Ti_{0.37}Al_{0.63}N$
G3_06	44	36	$Ti_{0.33}Al_{0.67}N$
G3_04	38	42	$Ti_{0.27}Al_{0.73}N$

Deposition parameters for the various samples investigated.

RESULTS

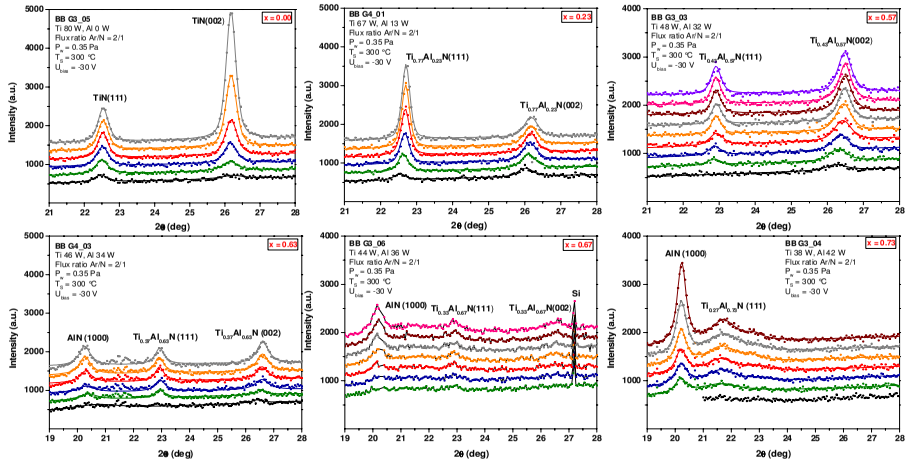

Fig. 1: The dotted curves show the observed Bragg-Brentano intensities with increasing sample thickness (final thickness around 200–300 nm) for various Al concentration x. The superposed straight lines show the fits obtained using a Pseudo-Voigt function for each single peak. The GIXS data show corresponding behaviour.

A deposition at a growth rate of 0.38 Å/s results in a (002) dominated preferred off-plane orientation even for higher thicknesses. Increasing x up to ~0.10 does not change this behaviour (Fig. 1, *top left*), which has been addressed to the high ion/neutral flux ratio to the substrate [2].

Contrary to expectatins, for 0.1 < x < 0.48 the samples show the typical cross-over behaviour from rather (002) oriented nucleation to a (111) preferred orientation at higher thicknesses (Fig. 1, *top middle*). This change of texture is attributed to the higher adatom mobility of Al (compared to Ti) giving rise to a higher concentration of Al in (111) grains, as can be seen from calculated lattice constants.

For x values near the segregation threshold of x ~ 0.6 this higher Al concentration leads to "disturbing" AlN precipitation mainly on (111) grains. Therefore, the (111) preferred orientation is reversed again to (002) (Fig. 1, *top right and bottom left*). For higher x values (yet still close to the segregation threshold), the crystal size dramatically decreases (Fig. 1, *bottom middle*). Due to the nanocrystalline structure of the $Ti_{1-x}Al_xN$ grains, each separated by a thin amorphous AlN matrix, increased hardnesses up to 35 GPa have been found.

For x values reasonably above the segregation threshold, the hexagonal wurtzite $Al_{1-y}T_{1-y}N$ phase prevails. In contrast to pure AlN films which tend to grow with (0002) off-plane texture, here (1000) off-plane texture has been observed (Fig. 1, *bottom right*). This has been reported to be the energetically favoured orientation for highly stressed films [3]. Since the hexagonal $Al_{1-y}T_yN$ grains are still sorrounded by kind of "misfitting" fcc $Ti_{1-x}Al_xN$ grains we assume high stresses to be the origin of the observed (1000) orientation.

[1] W. Matz, N. Schell, W. Neumann, J. Bøttiger, and J. Chevallier, Rev. Sci. Instrum. **72** (2001) 3344
[2] M. Beckers, N. Schell, R.M.S. Martins, A. Mücklich, and W. Möller, *submitted* for publication
[3] M.M.M. Bilek, D.R. McKenzie, and W. Moeller, Surf. Coat. Technol. **186** (2004) 21

ROBL-CRG	**Experiment title:** **Study of Au-Ge nanoalloy formation by grazing incidence x-ray diffraction**	**Experiment number:** **20_02_621**
Beamline: BM 20	**Date of experiment:** from: 04.05.2004 to: 07.05.2004	**Date of report:** 18.05.2004
Shifts: 8	**Local contact(s):** Dr. Valentina Cantelli	*Received at ROBL:* *03.06.04*
Names and affiliations of applicants (* indicates experimentalists): Dr. F. Prokert *, FZ Rossendorf, IIM, Dresden, Germany Dr. T. Som, Institute of Physics, Sachivalaya Marg, Bhubaneswar 751005, India		

Report:

The samples were Au/Ge nonoisland thin films deposited on native oxide covered Si(100). Au and Ge both are having nominally 1 nm thickness. The samples were all irradiated by 1.5 MeV Au^{2+} ions at RT. The fluences used were: 1x 10^{13} ions/cm^2 (sample #N6), 1x 10^{14} ions/cm^2 (#N7), and 5x 10^{14} ions/cm^2 (#N8). The aim of the experiment was to proof the expections of a formation of $Au_{0.6}Ge_{0.4}$ phase due to ion beam mixing of the Au and Ge nonoislands.

At first the samples were studied by grazing incidence specular and off-specular diffuse scattering. The measured reflectivity is shown in Fig. 1. The decrease of the critical angle ω_c with increased irradiation (L→M→H) is illustrated by the insert. The reflectivity was fitted by a two layer Au(x)Ge(1-x) 'alloy' model with x=0.016 (on top) and x=0.847 at the Si substrate. The density as well as the alloy composition x were free parameters. With the highest irradiation a change from two periods to a single one occurs, expressing a transition to a single layer, having x=0.56, an increased thickness but nearly unchanged area density (see Table 1). The value of the fitted composition parameter x=0.56 is a crucial indication for an alloying to $Au_{0.6}Ge_{0.4}$.

Fig. 1: Specular reflectivity of the irradiated Si/Au(x)Ge(1-x) samples. The measured (bold) and simulated (dotted) curves of the samples (H-#N8, M-#N7,and L-#N6) are shifted for clarity. A normalized linear plot is inserted.

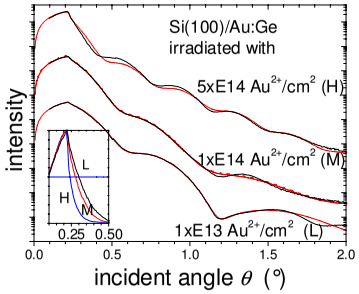

Table 1: Evaluation of XRR data: Estimation of density and calculation of Au(x)Ge(1-x) area density (t_L - cumulative AuGe layer thickness, ρ_m^{exp} – exp. density, ρ_m^{th}- theoret. density, m –*mass*, a – area).

sample	ω_c (deg.)	ρ_m^{exp} (g/cm^3)	$\rho_m^{exp}/\rho_m^{th}{}_{AuGe}$ (%)	t_L layer tickness (nm)	$t_L\rho_m^{exp}=m_{AuGe}/a$ (g/cm^2)
#N6 (L)	0.300	5.717	44	Σ : 8.41	4.81 x10^{-6}
#N7 (M)	0.275	4.804	37	Σ : 8.70	4.18 x10^{-6}
#N8 (H)	0.242	3.720	29	12.1	4.50 x10^{-6}

From the evaluation of the transverse diffuse scattering follows: The roughness correlation length is extremely short in all samples (ξ : 5 -15 nm). This may be expected for a nano-alloyed Au(x)Ge(1-x) layer. The sample with the highest irradiation dose shows a higher fractal exponent of 2.75 compared to 2.4 for the other ones. This could be due to the strongest intermixing or proceeding *alloying to A* $u_{0.6}Ge_{0.4}$.

The XRD measurements were done in grazing incidence (α_i =0.2°) – grazing exit (α_f =0.6°) technique to be highly surface sensitive. The substrate orientation was carefully controlled to eliminate contributions from the Si(100) substrate. The evaluation of the film in-plane detector scans was hampered by the very low intensity in the Debye rings, broadened by the nono-sized crystallites. Nevertheless, some basic facts are firm: The Au phase is clearly detectable in the sample #N6 and #N7 and not observable in sample #N8. Furthermore, in the EVA plots of #N8 the smoothed measured data are apparently correlated with the peak pattern of the Germanium Gold, $Au_{0.60}Ge_{0.40}$ (PDF No 18-551*). Both facts give a serious hint for such a phase formation after the strong ion beam mixing – but the XRD could not give a doubtless clear detection of this phase.*

ROBL-CRG	**Experiment title:** **Structural studies of semiconductor materials for optoelectronic applications**	**Experiment number:** **20_02_622**
Beamline: BM 20	**Date of experiment:** from: 20.07.04 to: 27.07.04 and from: 27.10.04 to: 29.10.04 and from: 17.12.04 to: 20.12.04	**Date of report:** 19.11.2004
Shifts: 20 + 6 + 9	**Local contact(s):** Dr. Norbert Schell and Valentina Cantelli	*Received at ROBL:* *19.11.03*

Names and affiliations of applicants (* indicates experimentalists):

J. Gaca*, K. Mazur*, J. Sass*, A. Turos, M. Wojcik*

Institute of Electronic Materials Technology, Wolczynska 133, 01 919 Warsaw, Poland

F. Eichhorn*, N. Schell*

Institute of Ion Beam Physics and Materials Research, Forschungszentrum Rossendorf, P.O. Box 51 01 19, 01314 Dresden, Germany

Report

Chemical and crystalline orders in heterostructutes containing $In_xGa_{(1-x)}As$ with high In concentrations

1. Introduction

The study of epitaxial layer composition can easily be performed using high resolution x-ray diffraction (***HRXRD***). Usually such an analysis is carried out in the symmetrical 004 reflection by means of θ/2θ scans. This method provides reliable results as long as the layer thickness remains below the critical one. For ***$In_xGa_{1-x}As/GaAs$ (001) heterostructures*** with x = 0.13 the lattice misfit amounts to 9.3 x 10^{-3} and the critical thickness to t_{cMB} = 15 nm. The reflections from such a thin layer are rather broad and of low intensity. To resolve this problem a method has been developed allowing the determination of In concentrations in strained layers, i.e. without the stress relaxation with thickness above t_{cMB}. ***Epitaxial layers in the thickness range of 30-100 nm were studied***.

2. Experimental

The average degree of relaxation of the heterostructure In_xGa_{1-x} As/GaAs (001) was studied. The investigated samples were grown on 001 oriented GaAs substrates by metalorganic chemical vapour deposition (MOCVD) at the Institute of Electronic Materials Technology (Warsaw). The growth temperature was fixed to ~700^0C with a growth rate of ~0.4 nm/s. For layers exceeding 80 nm a decrease of the angular distance Δθ between the layer and substrate reflections was observed. The difference in Δθ can be attributed either to the variation of layer composition or to the variation of strain. To resolve this ambiguity the ***reciprocal space mapping with asymmetric reflection*** was performed. It is known that the asymmetric reflection geometry modifies both diffractivity and peak width (FWHM). Compared to the symmetric case the diffractivity is larger and the FWHM broader when the ϕ_- (grazing incidence) geometry is used. The broadening of the peak diminishes the accuracy of the determination of the average lattice relaxation R. The ϕ_+ (steep incidence) set-up provides narrow peak widths. Furthermore, for the $\bar{2}\bar{2}4$ reflection and ***$\lambda = 0.154$ nm*** the layer truncation rod is directed almost parallel to the Ewald sphere. As a consequence the ***ϕ_+ geometry provides sufficient scattering intensity for thin layer experiments***.

3. Results and discussion

Fig. 1 shows reciprocal space maps (RSMs) around the $\bar{2}\bar{2}4$ and $\bar{2}24$ reciprocal lattice points (RLP) in the ϕ_+ geometry for the $In_{0.13}Ga_{0.87}As/GaAs$ heterostructure with 58 nm thick epilayer in two perpendicular <110> azimuths. $Q_{[001]}$ is the component of the diffraction vector along the layer normal, and $q_{<110>} = Q_{<110>} - h^{220}$ (where $Q_{<110>}$) is the component of the diffraction vector in the layer plane, h^{220} is the reciprocal lattice vector in the layer plane. From mutual positions of substrate and layer reflections one can deduce that:

- the ***lattice coherence between the substrate and the layer is preserved***, and
- the ***lattice of the strained epilayer exhibits tetragonal symmetry***.

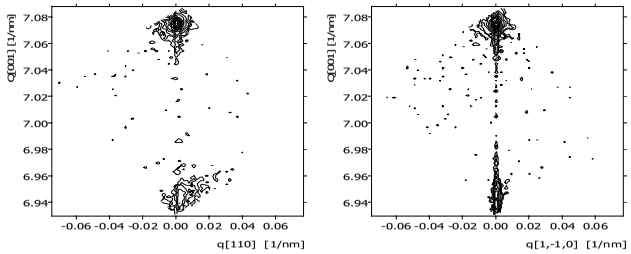

Fig. 1: Reciprocal space map of the $In_{0.13}Ga_{0.87}As/GaAs$ heterostructure: *right* at $\bar{2}24$ with t = 58 nm, *left* at $\bar{2}\bar{2}4$ with t = 58 nm.

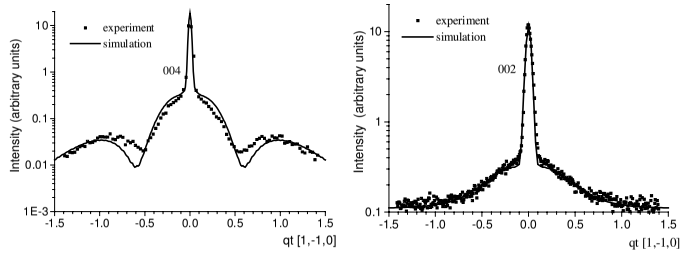

Fig. 2: Transverse scans of the $In_{0.13}Ga_{0.87}As/GaAs$ heterostructure (azimuth $[1\bar{1}0]$). Experimental curve simulated with dislocation density *left* at 004 reflection (ρ t = 0.08, t = 58 nm) and *right* at 002 reflection (ρ t = 0.08, t = 58 nm).

Fig. 2 shows two scans for this same epilayer in directions perpendicular to the diffraction vector for the symmetric 004 and 002 Bragg reflections and the corresponding results of numerical simulations (based on the model of Kaganer *et al.* for the ideal case of randomly distributed uncorrelated dislocations).

A ***bimodal line shape*** was observed with the resolution limited specular component and diffuse scattering. The peak intensity of the latter is about ten times weaker than the specular component. The specular component which comes from the interface area between the misfit dislocations is inversely proportional to the scattering vector. With increasing dislocation density the intensity of the specular component decreases exponentially and can only be observed if the mean distance between dislocations, ρ^{-1}, exceeds the layer thickness. The non-uniformity of strain concentrated around misfit dislocations located at the interface produces diffuse scattering. From numerical simulations of the transverse scans through the symmetric 002 and 004 Bragg reflections the ***density of misfit dislocations at the interface was evaluated to be about*** $\rho = 1.38 \cdot 10^{-3}$ nm^{-3} which is well above the resolution limit of x-ray topography. Since the mean distance between the misfit dislocations $\rho^{-1} > t$ exceeds the layer thickness t, strain relaxation processes are not observed. (The beginning of lattice relaxation is concomitant with an exponential decrease of the specular component in the transverse scans and occurs in the case of a strong disorder $\rho t >> 1$.)

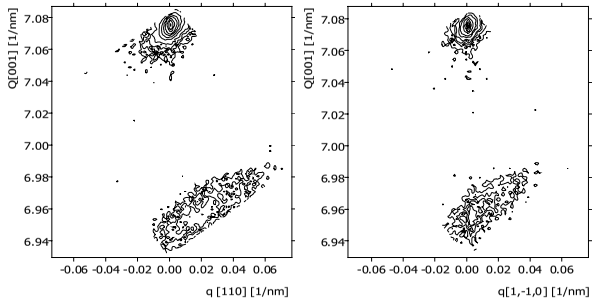

Fig. 3: RSM of $In_{0.13}Ga_{0.87}As/GaAs$ heterostructure: *left* in $\bar{2}\,\bar{2}\,4$, *right* in $\bar{2}\,2\,4$.

Reciprocal space maps for $In_{0.13}Ga_{0.87}As/GaAs$ heterostructure with 80 nm epilayer around the $\bar{2}\,\bar{2}\,4$ and $\bar{2}\,2\,4$ RLP in the ϕ_+ geometry in two perpendicular <110> azimuths are shown in Fig. 3.

Fig. 4 shows 004 transverse scans across the layer RLP for the same sample. As can be seen in the latter case the diffuse intensity is dominating. Since only dislocations perpendicular to the incidence plane contribute to the diffuse scattering, its intensity is proportional to their density. Thus, the shift of the layer RLP depends on the misfit dislocation density and is given by:

$$q_x = h^{220} \cdot b_r \cdot \rho_{110}$$

$$q_y = h^{220} \cdot b_r \cdot \rho_{1\bar{1}0}$$

The z-component of the shift is given by:

$$q_z = \nu / (1-\nu) \cdot h^{004} \cdot b_r \cdot (\rho_{110} + \rho_{1\bar{1}0})$$

where b_r - misfit releasing component of Burgers vector, ρ_{hhl} – density of misfit dislocation, ν - layer Poisson ratio. The different shifts of the layer RLP in the 110 and $1\bar{1}0$ directions shown in Fig. 3 indicate ***orthorhombic layer distortion*** as explained below.

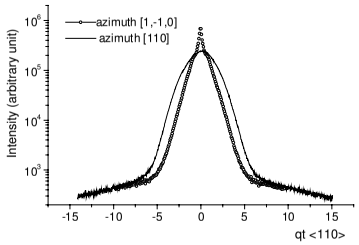

Fig. 4: Transverse scans of the $In_{0.13}Ga_{0.87}As/GaAs$ heterostructure with t = 80 nm in 004.

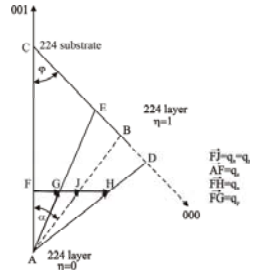

Fig. 5: Relaxation triangle (q_x,q_y, q_z – components of shift vector, AB – tetragonal distortion of epilayer; AD, AE – orthorhombic distortion of epilayer; $\rho_x + \rho_y$ = const).

The ***mechanism of orthorhombic stress relaxation*** is presented in Fig. 5. The relaxation triangles ADC and AEC correspond to two different <110> azimuth directions. From Fig. 5 and the above equations one can notice that the isotropic stress relaxation (tetragonal layer distortion) takes place when the misfit dislocation density $\rho_{110} = \rho_{1\bar{1}0}$. The construction of the relaxation triangle was based on the angle φ between [001] and [224] directions (for the cubic symmetry $\varphi = 35.26^o$) and angle α calculated from the relation $tg(\alpha) = tg(\varphi)c_{11} / 2c_{12}$, where c_{ij} – epilayer elastic constants. For the studied $In_{0.13}Ga_{0.87}As/GaAs$ heterostructure $\alpha = 35.53^o$. The RLP of the unstrained layer is indicated by B (isotropic case) or E and D (orthorhombic distortion) and that of the strained ones for symmetric and asymmetric cases by A. In the relaxed state the epilayer RLP is located on the relaxation line AB (tetragonal distortion) or either AD or AE (orthorhombic distortion).

From the mutual positions of the substrate and the layer reflections (Fig. 3) one can deduce that ***anisotropic stress relaxation takes place in two different azimuthal directions for the 80 nm thick layer***. Moreover, only the diffuse component with a Gaussian distribution was observed (Fig. 4). The coherent component is strongly damped because of the overlapping of the deformation fields of neighboring dislocations. The average degree of relaxation, η, is defined as:

$$\eta = [(q_x + q_y) \; h_{sub}^{004}] / 2h_{sub}^{220} \cdot \Delta h_r^{004}$$

where $\Delta h_r^{004} = h_{subs}^{004} - h_{lay,r}^{004}$, $h_{lay,r}^{004}$ - reciprocal lattice vector of the layer in the unstrained state. In the case of the studied $In_{0.13}Ga_{0.87}As/GaAs$ heterostructure $\eta = 0.27$. To improve the accuracy of the x-ray measurements they were subsequently repeated several times. It was found that the reliable value of the peak shift in the (224) reciprocal space map amounts to $q_x + q_y \cong 0.005$ [1/nm]. Consequently, the equation above yields the ***relaxation threshold*** $\eta_{thr} = 0.05$.

The RSMs in Fig. 1 show that the ***heterostructure with 58 nm thick epilayer is pseudomorph to the substrate***. ***In contrast, the 80 nm thick epilayer*** (Fig. 3.) ***exhibits advanced relaxation in the [110] direction***. One can assume that relaxation for $In_{0.13}Ga_{0.87}As/GaAs(001)$ with lattice misfit $\Delta a/a = 9.3 \cdot 10^{-3}$ and critical thickness $t_{c\,MB} = 15$ nm starts at a layer thickness of about $t \cong 70$ nm, i.e. at about 4.5 t_{cMB}. This means that measurement of the layer composition for the lattice misfit $\Delta a/a = 9.3 \cdot 10^{-3}$ with an accuracy of 1% is feasible well above the critical thickness t_{cMB} The results are consistent with the upper limit of the layer thickness of 5 $t_{c,MB}$ for $In_xGa_{1-x}As/InP$ heterostructure in the mismatch range $\Delta a/a = 10^{-4} - 10^{-2}$ and for 10% relaxation state.

The ***above results allowed*** to curb the range of thickness variation for quantum wells used to ***fabricate a photodiode for 2 μm, based on InP and containing a thin, pseudomorphic, strained $In_{0.83}Ga_{0.17}As$ absorbing layer***. To avoid the creation of misfit dislocations in the absorbing layer, which is mismatched to the substrate, the layer thickness cannot exceed the critical thickness, which is lower than 20 nm. When it is embedded between two layers with a wider band gap, it should be treated as a quantum well (QW). The absorption region consists of one or two quantum wells formed by the layer system $InP/In_{0.53}Ga_{0.47}As/In_xGa_{1-x}As/In_{0.53}Ga_{0.47}As/InP$ ($0.65 \leq x \leq 0.82$) and is placed inside the depletion region of a p-i-n junction based on InP. The heterostructures have been grown by LP MOCVD under various conditions.

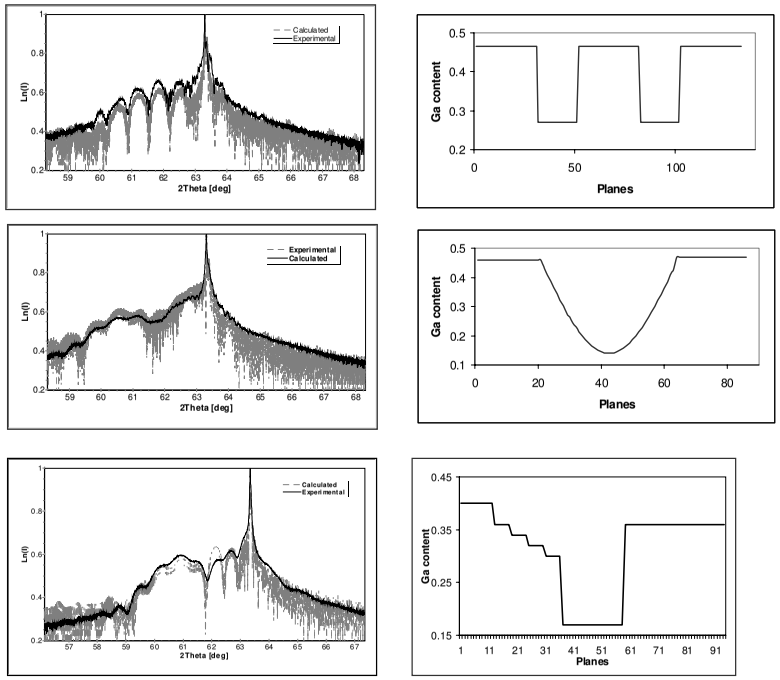

Fig. 6: Experimental and simulated x-ray diffraction profiles (*left*) and calculated average composition of every atomic plane (*right*)

Top: for a double QW structure with $In_{0.73}Ga_{0.27}As$ wells and $In_{0.53}Ga_{0.47}As$ barriers
Middle: for a single QW structure with smoothly graded wells
Bottom: for a single QW structure with abruptly graded wells.

Simulations based on dynamic diffraction theory in crystals have been applied to calculate diffraction profiles. The comparison of XRXRD experimental profiles with theoretical ones in Fig. 6 enabled us to investigate the distances between atomic planes and chemical composition profiles. Very good agreement for an abrupt single and double QW structure consisting of $In_{0.73}Ga_{0.27}As$ and $In_{0.53}Ga_{0.47}As$ layers is seen in Fig. 6(top) and (bottom). On the other hand Fig. 6(middle) presents experimental and theoretical profiles for a single QW structure with a non-rectangular Ga profile in the active layer.

ROBL-CRG	**Experiment title:** **Investigation of the nanocluster formation and phase transition of nanoparticles embedded in a dielectric matrix**	**Experiment number:** **20_02_623**
Beamline: BM 20	**Date of experiment:** from: 07.04.2004 to: 10.04.2004	**Date of report:** 01.09.2004
Shifts: 9	**Local contact(s):** Dr. Norbert Schell	*Received at ROBL:* *01.09.04*

Names and affiliations of applicants (* indicates experimentalists):

Dr. J. von Borany* FZR, FWIS
Dr. N. Schell* FZR, FWIS, ROBL-CRG
V. Cantelli* FZR, FWIS, ROBL-CRG

REPORT

1 µm SiO_2 films on Si(001) were implanted with $^{74}Ge^+$- or $^{59}Co^+$-ions (45-350 keV, $7.8x10^{16}$ cm^{-2}), respectively, leading to a box-like Ge- or Co-profile (C_{max} = 3±1 at.%) in the SiO_2 from the surface until a depth of approx. 300 nm. The evolution of Co and Ge nanocrystals in the SiO_2 matrix during annealing processes (400-1080°C, < $5x10^{-5}$ mbar) has been investigated by *in-situ* Grazing Incidence X-ray Diffraction (GID) (Be dome, α_I = 0.5°; λ = 1.54 Å) and transmission electron microscopy (TEM) studies. Remarkable differences have been found for Ge and Co nanocrystals (-clusters).

Ge nanocrystals: Starting with an as-implanted sample (G6), the Ge(111) reflex first appears after annealing at about 900°C, see **Fig. 1b**. The FWHM of the GID peak successively reduces with increasing annealing temperature as a proof of the Ge-NC growth from 3.5 nm (Ts = 950°C) to about 6 nm (Ts = 1085°C). Due to Ge NC melting (bulk value 938°C, but lower for nanoparticles) the diffraction pattern can be detected only if the GID-scans are performed at 300°C, compare **Fig. 1 a,b**.

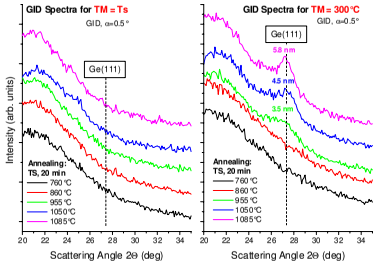

Fig. 1 a,b: Gid-scans for Ge implanted SiO_2 films (G6) after annealing at Ts for 20 min, measured at Ts (left) or 300°C (right).

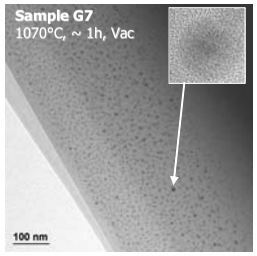

Fig. 2: TEM micrograph, showing the Ge NC distribution after 1070°C, ~ 1h annealing in vacuum. **Inset:** HRTEM image of the single marked cluster.

In general, annealing at temperatures at around 1000°C leads to the formation of an ensemble of small Ge nanocrystals (d ~ 5 nm). If the GID measurement is performed on an annealed sample (G7: Ts = 1070°C, 1h → TEM-micrograph in **Fig. 2**) at different temperatures T_M a change of the mean NC size (derived from Debye-Scherrer formulae) from 4 nm (T_M = RT) to 5.5 nm (T_M = 800°C) is observed (**Fig. 3**). This is related to a size-dependent melting temperature which successively excludes the contribution of very small clusters with raising T_M. Above 900°C the Ge reflexes disappear, but, as expected, reducing T_M < 900°C the Ge related peaks appear again.

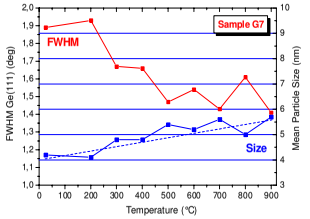

Fig. 3: FWHM of Ge(111) and NC size as a function of the GID-scan temperature T_M, measured after an annealing at 1070°C, 1 h.

As confirmed by TEM and RBS (not shown here), the cluster size depth distribution differs from the Ge concentration profile. This could be explained by a near-surface consumption of Ge to form amorphous GeO_x. Therefore, the cluster size near the surface (~ 100 nm depth) is often smaller in comparison to larger depth. The necessary oxygen originates from moisture penetrating into the damaged oxide after ion implantation before the annealing treatment.

Co nanorystals: After annealing at 750°C for 2 min a homogenous distribution of small (d ~ 4nm) amorphous Co clusters exists (**Fig. 4a**) in a depth of about 50 to 350 nm. Increasing the annealing temperature to 850°C a significant rearrangement has been obtained. Now the sample shows a bimodal cluster distribution with nearly spherical large Co NC [HREM: 0.206 nm → Co(111)] of 20-40 nm diameter in a near-surface region (0-50 nm) and a region of smaller clusters (mean size ~ 7nm) in a depth between 200-400nm (**Fig. 4b**). The existence of a large number of tiny clusters around a large one (see **Fig. 4b, inset**) reveals that the conventional Ostwald ripening process does not drive the formation of the large clusters (alone).

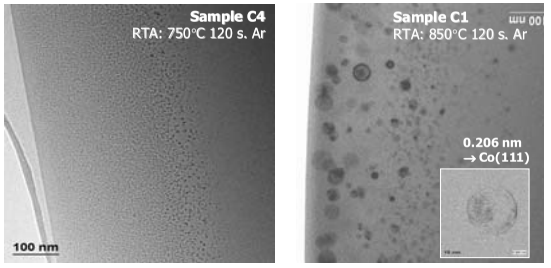

Fig. 4 a,b: TEM images of Co implanted SiO_2 films after annealing at 750°C (left) or 850°C (right) for 2 min in Ar atmosphere showing different cluster distributions.

By GID (**Fig. 5**) the first Co NC reflexes [Co(111) and Co(200)] appear after 750°C, 30 min annealing. The NC size grows with increasing annealing temperature or time, but, due to the limited Co content, the mean cluster size saturates at approx. 25 nm (**Fig. 6**). The spectra does not differ for measuring at T_M = Ts or at 300°C (except the peak shift due to lattice expansion). Thus, the influence of melting can be neglected in the investigated temperature range even for small NC.

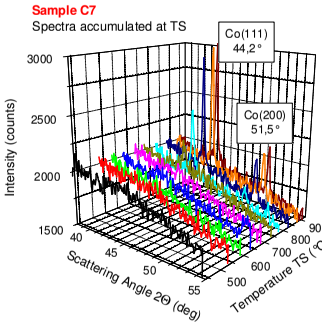

Fig. 5: *In-situ* GID scans of the as-implanted Co sample for T_M = Ts.

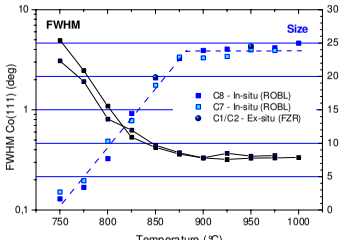

Fig. 6: Mean NC size derived from Co (111) and Co(200) reflexes for GID-scans at different T_M for an annealed sample at 1070°C, 1h.

The TEM investigations were performed by Dr. A. Mücklich at FZR / Institute of Ion Beam Physics and Materials Research which is gratefully acknowledged.

ROBL-CRG	**Experiment title:** Investigation of structural ordering in thin metal alloy films designed for future magnetic memory materials	**Experiment number:** 20_02_624
Beamline: BM 20	**Date of experiment:** from: 10.04.2004 to: 13.04.2004	**Date of report:** 24.06.2004
Shifts: 9	**Local contact(s):** Mrs. Valentina Cantelli	*Received at ROBL:* 29.06.04

Names and affiliations of applicants (* indicates experimentalists):

V. Cantelli* FZR, FWIS, ROBL-CRG
Dr. J. von Borany* FZR, FWIS
Dr. N. Schell* FZR, FWIS, ROBL-CRG

REPORT

50 nm AuCu films on 1µm SiO_2/Si prepared by dual source evaporation (Au: e-beam, Cu: resistive heating) have been investigated. The measurements use different diffraction techniques (GID with θ = 1°, Bragg-Brentano [BB], Rocking curves [RC]) and reflectivity scans. The characterization of as-deposited and annealed-samples was performed *ex-situ*, whereas the temperature dependence of the structural reordering has been investigated *in-situ* using the Be-dome annealing chamber.

The **as-deposited** films exhibit mainly the chemical disordered AuCu fcc phase (Fig. 1). The fcc structure of the polycrystalline films is confirmed by cross-sectional TEM and the corresponding electron diffraction (ED) pattern, Fig. 2

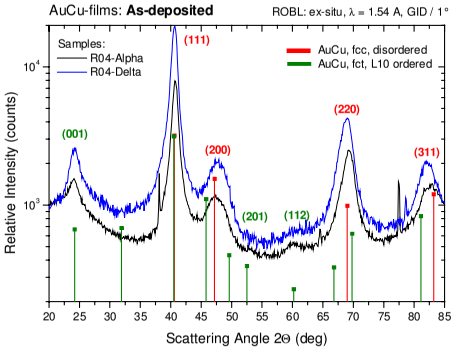

Fig. 1: GID scan for 1° incident angle of two as-deposited AuCu films. Beside the dominant AuCu fcc phase a minor contribution from the L10 phase is observed.

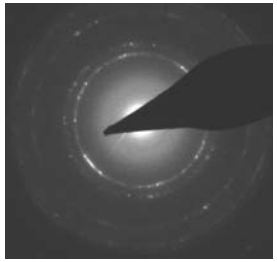

Fig. 2: ED pattern (region 1µm diameter). This pattern confirms the polycrystalline structure with slightly non-random orientation distribution. Fom the first three rings lattice distances of 0.220; 0.189 and 0.135 nm can be derived which are very close to the expected fcc values.

After **annealing** (450°C, 10 min, $2x10^{-7}$ mbar) the AuCu film has been transformed completely towards the chemically ordered L10 structure (fct), Fig. 3. A comparison of GID, BB and RC data exhibit a significant textured film morphology with (111) planes parallel to the surface which is confirmed by high-resolution TEM and electron diffraction (Fig. 4).

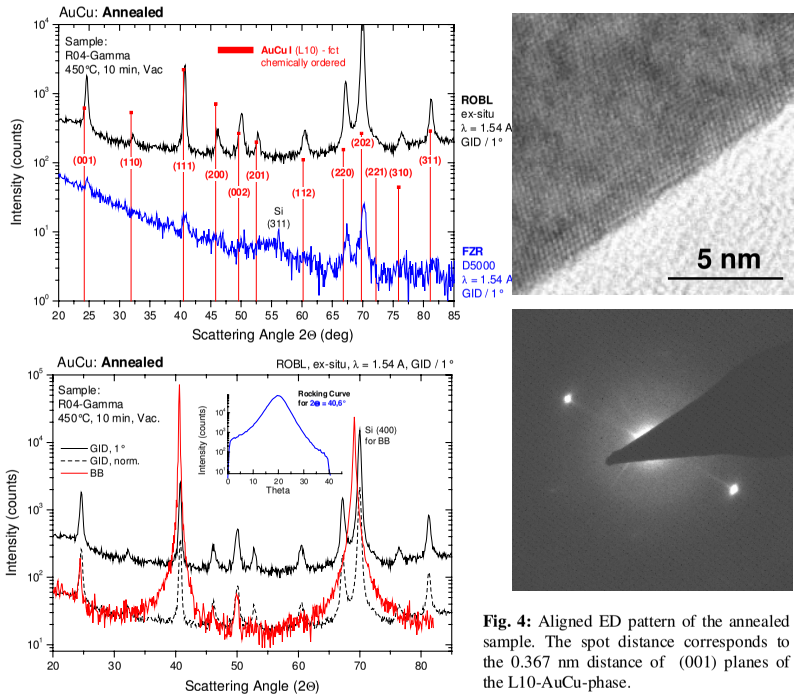

Fig. 3: Top: GID scans of the annealed AuCu film (450°C, 10 min) showing the formation of the L10 structure. For comparison the spectrum collected with standard equipment (D5000) is shown, which clearly demonstrates the advantages of the ROBL investigation. Down: Comparison of diffraction scans in GID and BB geometry and the corresponding θ-scan for the (111) reflex at 2θ=40.6°.

Fig. 4: Aligned ED pattern of the annealed sample. The spot distance corresponds to the 0.367 nm distance of (001) planes of the L10-AuCu-phase.

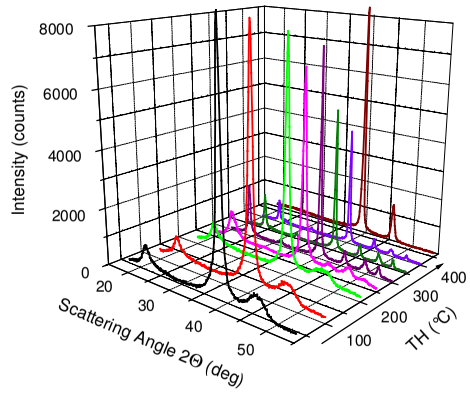

Fig. 5: GID-scan between RT and 450°C. The changes between 25-30° and 45-55° indicate the different phase transformations.

A set of *in-situ* GID scans as a function of the temperature is shown in Fig. 5. The phase transitions fcc→L10 (fct, ordered) at ~230°C, and L10↔AuCu, fcc (disordered) at ~390°C correspond very well with the expected T-values from the AuCu phase diagram. After cooling the film remains in the thermodynamically stable L10 configuration.

The AuCu films stand as model system for magnetic thin films like FePd, FePt, CoPt etc. where the L10 phase is correlated with a large magnetic anisotropy. Future experiments will be directed to sputtered FePt and MnNi films.

ROBL-CRG	**Experiment title:** **Investigation of the thermal stability of the phases formed during low temperature nitriding of austenitic steel**	**Experiment number:** **20_02_625**
Beamline: BM 20	**Date of experiment:** from: 17.04.2004 to: 20.04.2004	**Date of report:** 12.07.2004
Shifts: 9	**Local contact(s):** Mrs. Valentina Cantelli	*Received at ROBL:* *16.07.04*

Names and affiliations of applicants (* indicates experimentalists):

V. Cantelli* FZR, FWIS, ROBL-CRG

J. Baranowska* Institute of Materials Science and Engineering, Technical Univeristy of Szczecin, Poland

D. Busquets Mataix* Department of Mechanical and Materials Engineering, Universidad Politecnica de Valencia, Spain

REPORT

The investigation was carried out on samples made of the austenitic steel AISI 316. Samples before nitriding were electrochemically polished and activated. The activation was carried out using cathode sputtering in nitrogen plasma and later the samples were gas nitrided. The parameters of the treatment are presented in Table 1.

Sample	Activation treatment	Gas nitriding
1	Cathode sputtering, nitrogen, 10 min, current density 1.7 mA/cm^2, 340°C	Ammonia, 475°C, 3 hours
2	Cathode sputtering, nitrogen, 10 min, current density 1.7 mA/cm^2, 460°C	

Table 1. Treatment parameters.

After these treatments, the nitrided layers containing "expanded austenite" were obtained. The phase which was found in both samples belongs to the magnetic one [1] and show a slight shift in the peak position in these two samples.

During the experiments two types of measurement were made:

1. to establish the exact positions of the peaks for both stadiums of the phase, measurements using Ga energy were carried out (E = 9.25173 keV, corresponding to λ = 1.3400 Å); 2-theta range: 30-106°; incident angle: 10°. The measurement results are presented in Figure 1 and the measured positions of the peaks in Table 2.
2. To evaluate the thermal stability of magnetic expanded austenite, *in-situ* studies were performed. Samples were heated using the ROBL high vacuum heating stage according to the following procedure: sample 1 - 358°C, 516°C, 595°C with annealing at each temperature approx. 115 min; sample 2 - 385°C, 434°C, 513°C with annealing 50 min. Results of measurements are presented in Figures 2 and 3 for sample 1 and 2, respectively. The source energy was E = 8.08478 keV corresponding to λ = 1.5335Å. 2-theta range: 30-70°; incident angle: 10°. During the annealing the measurements were continued in the 2-theta range: 32-59° in order to control the behaviour of the phases with the time of the annealing.

Sample	1	2	3	4	5	6	7
1	33.9	38.7	56.9	67.2	71.1	83.5	90.8-103.4
2	34.9	39.5	58.2	69.4	73.38	86.7	92.2-out of range
austenite	37.676	48.805	63.698	76.452	80.514	96.522	108.6
Δd [%] sample 1	-10.8	-12.6	-10.8	-11.8	-11.1	-12	
Δd [%] sample 2	-6.8	-9.1	-7.7	-7.8	-7.3	-7.7	

Table 2. Positions of the peaks evaluated form diffraction patterns as in Figure 1.

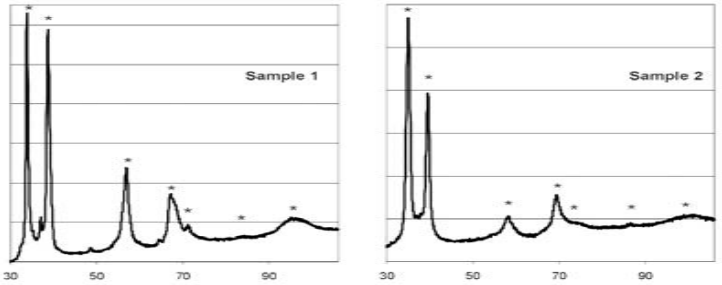

Fig 1. Diffraction patterns for samples 1 and 2: the "expanded austenite" peaks are marked with an asterisk.

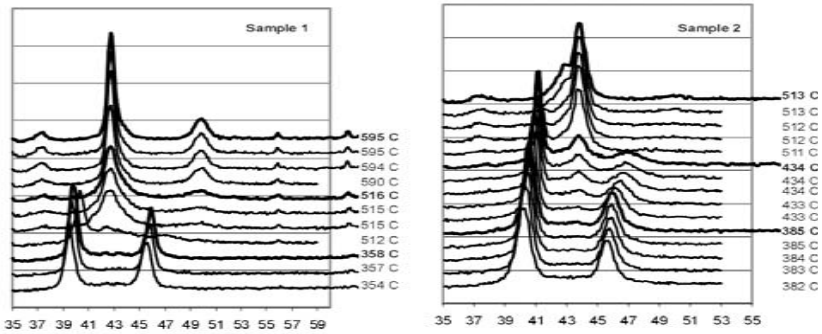

Fig. 2. Diffraction patterns obtained for samples 1 and 2 during heating in vacuum

For both samples there is no observed increase of lattice parameters as a result of thermal expansion. On the contrary, the observed shift indicates the contraction of the lattice. The observed change of d value measured according to the shift of the two first peaks of expanded austenite is equal to 0.2 Å for both samples. Only for sample 2 at temperature 434°C the second peak shift corresponds to the value 0.4 Å. This contraction is probably related to the gradual removing of nitrogen from the structure due to the elevated temperature and vacuum. For sample 1 the sudden decomposition of "expanded austenite" into austenite is observed at temperature 512°C. This decomposition is also observed in sample 2 after approx. 30 min annealing at temperature 434°C. Above 512°C in both samples the presence of CrN is observed.

[1] Baranowska J., *Characteristic of the nitrided layers on the stainless steel at low temperature*, Surf. Coat. Techn. **180-181** (2004) 145-149.

ROBL-CRG	**Experiment title:** ***In-situ* XRD during thermal cycling of Ni-Ti Shape Memory Alloy**	**Experiment number:** **20_02_626**
Beamline: BM20	**Date of experiment:** from: 18.09.2004 to: 21.09.2004	**Date of report:** 08.11.2004
Shifts: 9	**Local contact(s):** Dr. Norbert Schell	*Received at ESRF:* *08.11.04*

Names and affiliations of applicants (* indicates experimentalists):

Francisco Manuel Braz Fernandes, Andersan dos Santos Paula*, Karimbi Koosapa Mahesh*:
CENIMAT – Centro de Investigação de Materiais – FCT / UNL, Campus da Caparica, 2829-516 Monte de Caparica, PORTUGAL
Rui Miguel dos Santos Martins*, Ana Margarida Andrade Cardoso*, Norbert Schell*:
FZR, ROBL-CRG at ESRF, B.P. 220, 38043, Grenoble, FRANCE

Report

Aim

The aim of the experiment was to analyse the structural evolution during *in-situ* annealing of Nickel-Titanium (Ni-Ti) SMA subjected to thermal/mechanical treatments.

Experimental Methodology

The material in study was Ti-rich (Ti 51 at%) NiTi SMA extracted from a 2 mm thick plate, in strain annealed conditions and supplied by Memory-Metalle GmbH, Germany. The samples were analyzed in the following conditions: (i) as-received (AR), (ii) heat treated at 500ºC (HT), (iii) heat treated at 500ºC followed by 10% thickness reduction by cold rolling (HT + CW10%) and (iv) heat treated at 500ºC followed by 40% thickness reduction by cold rolling (HT + CW40%). The heat treatment (HT) was performed by holding the specimen at 500ºC for 30 minutes and subsequently quenching in water at room temperature. The samples were subjected to chemical etching (10% vol HF + 45% vol HNO_3 + 45% vol H_2O) in order to remove the oxide layer as well as the layer deformed during the cutting operation.

XRD analysis was performed at ROBL/BM20 of ESRF for the *in-situ* high temperature $\theta/2\theta$ scans and texture analysis. *In-situ* XRD analysis during annealing has been carried out using x-rays of wavelength 1.54 Å and a vacuum furnace with a hemispherical Be-dome evacuated to a pressure less than $2x10^{-6}$ mbar. The furnace was installed on the ϕ circle (azimuthal orientation) of the six-circle goniometer. The pole figures have been determined for $-85° < \phi < +5°$ and $0° < \chi < +54°$. The rolling direction (RD) is aligned with $\phi = -55°$. The structural evolution during annealing up to 800ºC was observed by *in-situ* XRD.

Results

All the samples are in the martensitic state, at room temperature before *in-situ* high temperature analysis (scan 1 in Fig. 1a-d). The structural evolution while heating (Fig. 1 for the scans up to 400ºC, where the recrystallisation is completed, and Fig. 2 for the full range of temperatures) and cooling (Fig. 3) was followed by *in-situ* XRD. For the HT+CW10% and HT+CW40% samples, overlapping of the martensite peaks are observed. The XRD scans in $\theta/2\theta$ mode (Figs 1 and 2) show a clear variation in peaks corresponding to the structural evolution. In Figs 1c-d, for HT+CW10% and HT+CW40%, it is seen that the full transformation to austenite occurs only when the sample is heated above 100ºC. The recrystallisation temperature is close to 350ºC, which is in agreement with other results [1-4]. At higher temperatures (above 600ºC) a significant structural evolution takes place, illustrated by the increased austenitic peak intensity in both HT and HT+CW40% samples (Figs 2b and c), and the growth of Ti_2Ni precipitates. The structural evolution during cooling (Fig. 3) shows B2→B19' in the AR sample (after heating up to 800ºC) and B2→R→B19' in the HT+CW10% sample (after heating up to 400ºC). These results are in agreement with previous results [3-6], where the R-Phase formation is gradually suppressed with increasing annealing temperatures, leading to one step transformation as it is detected by DSC analysis.

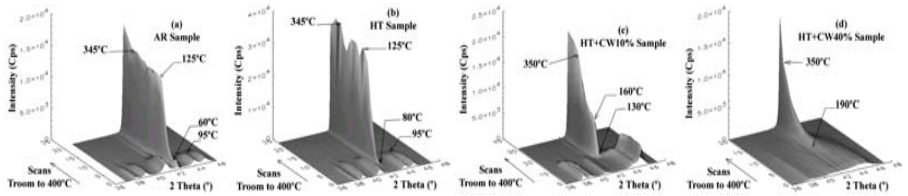

Fig. 1: *XRD spectra during the in-situ high temperature analysis for AR, HT, HT+CW10% and HT+CW40% samples while heating up to 400ºC.*

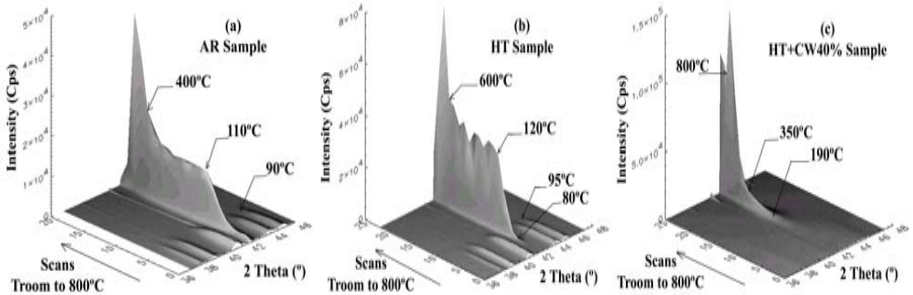

Fig. 2: *XRD spectra evolution during the in-situ high temperature analysis for AR, HT and HT+CW40% samples while heating up to 800ºC.*

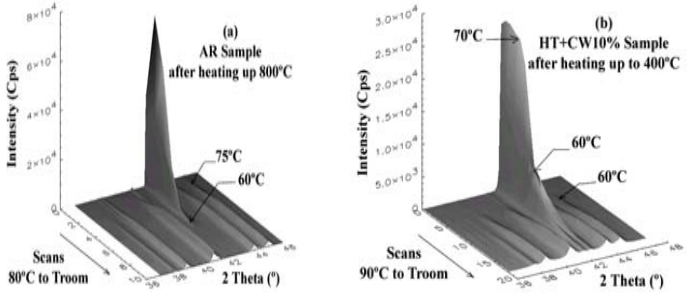

Fig. 3: *XRD spectra evolution during the in-situ high temperature analysis for AR and HT+CW10% samples after heating up to 800ºC and 400ºC, respectivily.*

The texture evolution during the *in-situ* high temperature XRD analysis of the HT and HT+CW40% samples is shown in Figs 4 and 5, respectively.

Annealing up to 350ºC (Figs 4a-c), gives no significant modifications in the {111}<110> austenite texture components of AR and HT samples; recrystallisation in HT+CW40% sample is completed at 350ºC (Fig. 1d) [2-4]. Between 400º and 500ºC (Figs 4d-f and 5a), there are texture evolutions in the direction of {110}<110> austenite texture components [2-4, 7-9]. Above 600ºC, anomalous grain growth of austenite is starting to occur.

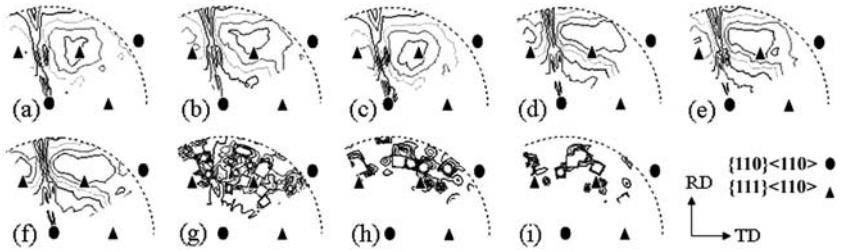

Fig. 4: *Austenite (110) Pole Figures – HT sample – (a) 250ºC, (b) 300ºC, (c) 350ºC, (d) 400ºC, (e) 450ºC, (f) 500ºC, (g) 600ºC, (h) 700ºC and (i) 800ºC during the in-situ high temperature XRD.*

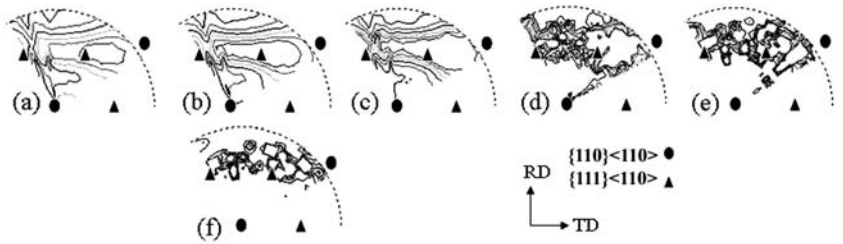

Fig. 5: *Austenite (110) Pole Figures – HT+CW40% sample – (a) 400ºC, (b) 450ºC, (c) 500ºC, (d) 600ºC, (e) 700ºC and (f) 800ºC during the in-situ high temperature XRD.*

Conclusions:

(1) The thermal / mechanical treatments significantly affect the structural evolution in the Ti-rich NiTi SMA.
(2) High annealing temperature develops {110}<110> austenite texture component in Ti-rich NiTi SMA.
(3) Above 500ºC, precipitation of Ti_2Ni takes place, and above 600ºC a tendency for anomalous grain growth appears.

References:

[1] E. Hornbogen: Mater. Sci. Forum **455-456** (2004) 335.
[2] A.S. Paula, J.P.H.G. Canejo, N. Schell and F.M. Braz Fernandes: poster presented at SRMS-4 (2004) (paper submitted to *NIM B*).
[3] F.M. Braz Fernandes, A.S. Paula, J. Canejo, K.K. Mahesh, R.J.C. Silva, R.M.S. Martins, A.M.A. Cardoso and N. Schell: oral communication presented at SMST2004 (2004) (paper submitted to the Proceedings of the Conference).
[4] A.S. Paula, K.K. Mahesh, F.M. Braz Fernandes, R.M.S. Martins, A.M.A. Cardoso and N. Schell: accepted as oral communication at ICOTOM14, Leuven - Belgium (July, 11 to 15, 2005) (paper submitted to the Proceedings of the Conference).
[5] A.S. Paula, J.P.H.G. Canejo, R.M.S. Martins and F.M. Braz Fernandes: Mat. Sci. and Eng. A **378** (2004) 92.
[6] F.M. Braz Fernandes, A.S. Paula, J. Canejo, K.K. Mahesh and R.J.C. Silva: poster presented at SMST2004 (2004) (paper submitted to the Proceedings of the Conference).
[7] T. Bhattacharya and R.V. Kohn: Acta Mater. **44-2** (1996) 529.
[8] L. Zhao, Ph.D. thesis, University of Twente, Enschede, The Netherlands (1997).
[9] Y.C. Shu and K. Bhattacharya: Acta Mater. **46-15** (1998) 5457.

ROBL-CRG	**Experiment title:** ***In-situ* study of the phase stability of carbonitrided austenitic stainless steel samples at heating from RT to 800°C**	**Experiment number:** **20_02_IH8**
Beamline: BM 20	**Date of experiment:** from: 06.09.2003 to: 09.09.2003	**Date of report:** 24.09.2003
Shifts: 9	**Local contact(s):** Dr. Norbert Schell	*Received at ROBL:* *03.10.03*
Names and affiliations of applicants (* indicates experimentalists): F. Prokert *, A. Abd-El-Rahman *, and E. Richter, FZ Rossendorf, IIM, Dresden, Germany		

Report:

The investigated samples were prepared from polished ***ASI 304 stainless steel sheets*** (Fe; 12-20% Cr; 8-11% Ni; 1% Mn; 0.08% Si; 0.04% P; 0.08% C; 0.03%S).

Sample #1 was carbonitrided using plasma immersion ion implantation (PIII) at the following conditions: RF power 350 W, bias potential –30 kV, frequency 550 Hz, base pressure 10^{-5} mbar, gas composition 70% N_2 / 30% C_2H_2 at total gas pressure $6x10^{-3}$ mbar, plasma time 2.5 h at a sample temperature of 355°C.

Sample #2 was prepared by a low pressure RF plasma carbonitriding technique [1] at 450 W. The base pressure was fixed at $1.3x10^{-2}$ mbar. Nitrogen and acetylene were introduced at a working pressure of $8.4x10^{-2}$ mbar with the gas composition 25% N_2 / 75% C_2H_2 .

For comparison, an ***untreated sample*** was additionally measured at room temperature (RT).

The *in-situ* diffraction measurements were done in ***Bragg-Brentano geometry*** with a wave length λ = 1.5335 Å using the ROBL high vacuum heating stage, equipped with a BN sample holder. The x-ray penetration into the samples depends in this technique on the incidence angle. The 1/e-penetration depth is about 250 nm for the starting value of 2θ = 20° and reaches ~1 µm at 2θ = 85°. The thickness of the studied carbonitrided layers was larger than 5µm. Therefore, *diffracted intensity does not come from the ASI 304 bulk material*.

The scans have been evaluated by the standard Bruker-AXS EVA code. During heating the lattice constants of the samples change with increasing temperature. From the mean value of the thermal expansion coefficient of austenitic steel $\alpha_{ASS} = (17\pm8) \times 10^{-6}\ K^{-1}$ [2] one estimates for heating of the bulk from RT to 800°C a change of the lattice parameter of ~1.4±0.5%. At heating this effect covers e.g. in austenite the decrease of the lattice expansion caused by the diminishment of the part of nitrogen or carbon solved in the lattice.

The XRD pattern of the untreated sample shows residuals of the bcc phase of the ferritic iron (PDF No. 6-696, S.G.: 229, a_0 = 2.8664 x 10^{-1} nm [3]) and mainly the cubic phases of chromium iron nickel 304 stainless steel austenite ($Cr_{0.19}Fe_{0.7}Ni_{0.11}$, PDF No. 33-397, S.G.: 225, a_0 = 3.5911 x 10^{-1} nm / Iron austenite, (Fe,C), PDF No. 31-0619, S.G.: 225, a_0 = 3.600 x 10^{-1} nm [3]). Compared to the PDF data, the lattice of the ferrite lattice is expanded by $\Delta a/a_0 = (a-a_0)/a_0 \approx 0.62\%$. The measured patterns are shown in Figs 1 (sample #1) and 2 (sample #2 and untreated ASI 304). The results of the phase analysis are compiled in Tables 1 and 2.

Table 1: Layer composition of ***sample #1*** (ASS 304 carbonitrided by PIII).

Temperature (°C)	Roaldite (Fe_4N) $\Delta a/a_0$	Carlsbergite (CrN) $\Delta a/a_0$	Austenite (γ-Fe) $\Delta a/a_0$	Cohenite (Fe_3C) $\Delta a/a_0$
RT_init (23)	X	0.42%	1.87	X (weak)
300	X	0.2%	2%	X
400	X	0.4%	2%	X
500	X	0.2%	1.7%	X
610	disappeared	X and -0.8%	0.8%	X
700	----------	0.6%	0.8%	X
800	----------	0.8%	1.3%	disappeared
RT_fin (30)	----------	0.4%	Ferrite (α-Fe) 0.2%	----------

Table 2: Layer composition of ***sample #2*** (ASS 304 carbonitrided by RF plasma).

Temperature (°C)	Roaldite (Fe_4N) $\Delta a/a_0$	Carlsbergite (CrN) $\Delta a/a_0$	Austenite (γ-Fe) $\Delta a/a_0$	Cohenite (Fe_3C) $\Delta a/a_0$
RT_init (23)	-------	0.2 %	1.3%	X
300	-------	0.4%	1.9%	X
400	-------	0.4%	1.9%	X
500	--------	0.4%	1.5%	X
610	--------	0.2%	0.8%	X
700	--------	0.4%	0.8%	disappeared
800	--------	0.8%	1.25%	----------
RT_fin (30)	---------	0.4%	Ferrite (α-Fe) 0.2%	----------

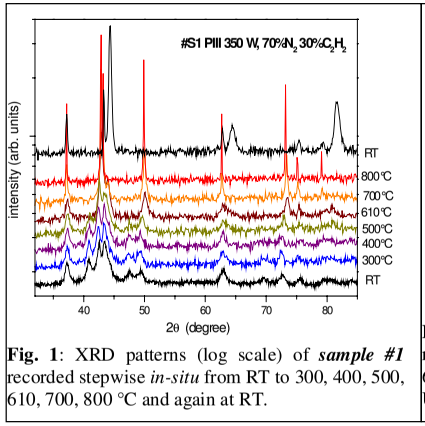

Fig. 1: XRD patterns (log scale) of ***sample #1*** recorded stepwise *in-situ* from RT to 300, 400, 500, 610, 700, 800 °C and again at RT.

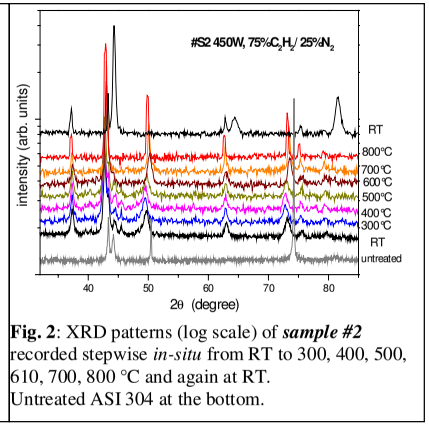

Fig. 2: XRD patterns (log scale) of ***sample #2*** recorded stepwise *in-situ* from RT to 300, 400, 500, 610, 700, 800 °C and again at RT. Untreated ASI 304 at the bottom.

It is found that **at high nitrogen content the phases generated at the corbonitriding of ASI 304 are stable up to 500°C. For high carbon content, the stability range of the phase composition is more extended**. Similar to the findings for pure nitrided ASI 304 [4], it is found here that the iron nitride phase (Roaldite (Fe_4N), PDF No. 06-0627; S.G. Pm3m, 221; a_0 = 3.795 x 10^{-1} nm [3]) disappears at about 500°C. Finally, at RT **after the heating process, in both cases the austenite was transformed into ferrite**.

[1] F.M. El-Hossary, N.Z. Negm, S.M. Khalil, A.M. Abd El-Rahman, Thin Solid Films **405** (2002) 179

[2] S.D. Choi *et al.*, J. Mat. Sci. Lett. **21** (2002) 353-355 http://www.aerofit.com/sma/tinel.htm http://www.sma-inc.com/NiTiProperties.html

[3] PDF ICDD Powder Diffraction File, Internat. Centre for Diffraction Data, Newton Square, Pennsylvania, U.S.A.; www.icdd.com

[4] F.M. El-Hossary and N.Z. Negm, Appl. Surface Science **181** (2001) 185-190

ROBL-CRG	**Experiment title:** **Ion beam synthesis of 3C-SiC nano-crystals buried in diamond single crystals: structural study**	**Experiment number:** **20_02_IH9**
Beamline: BM 20	**Date of experiment:** from: 20.09.2003 to: 21.09.2003	**Date of report:** 21.11.2003
Shifts: 4	**Local contact(s):** Dr. Norbert Schell (schell@esrf.fr)	*Received at ROBL:* *25.11.03*

Names and affiliations of applicants (* indicates experimentalists):

F. Eichhorn*, H. Weishart, V. Heera

Forschungszentrum Rossendorf
Institute of Ion Beam Physics and Materials Research
P.O.B. 510119, 01314 Dresden, Germany

Report:

Their outstanding properties, such as wide band gap, high thermal conductivity and saturated drift velocity, make silicon carbide and diamond useful semiconductors for applications under harsh conditions. A combination of both materials on a microscopic scale may be a promising way to novel devices.

Ion beam synthesis (IBS) is an excellent method for generating precipitates inside any matrix without thermodynamic constraints. Implantation temperature, ion dose and dose rate are crucial parameters for this IBS process. Here we studied the synthesis of nanocrystalline 3C-SiC inside diamond by high-fluence Si implantation at two different temperatures.

Type II a diamond crystals with 001 surfaces were implanted with 5.7 x 10^{17} cm^{-2} Si ions with an energy of 150 keV at 900 °C and 1000 °C, respectively. According to TRIM Si ions penetrate 110 nm (projected range) into diamond with a fluctuation (straggling) of ±21 nm. For characterizing the structure of both the 3C-SiC crystallites and the diamond matrix specular x-ray reflectivity and grazing incidence grazing exit diffraction of x-rays with a wavelength of 0.11864 nm were used.

Fig. 1 shows the specular reflectivity of the samples including virgin material. According to the shift of the critical angle of the external total reflection the surface layers have a mass density which is reduced by 7 % and 13 % in relation to bulk diamond for the implantation temperature of 1000 °C and 900 °C, respectively. The material implanted at 900 °C has a pronounced layer structure with thicknesses of 10, 56 and 159 nm.

Under grazing incidence grazing exit diffraction condition the penetration of x-rays is controlled by the beam incidence angle according to Fig. 2. Fig. 3 shows the high intense diamond (220) and the 3C-SiC(220) diffraction with varying intensity as the incidence angle increases. 3C-SiC crystallites were only found if x-rays penetrate more than 100 nm into diamond. They have the same crystallographic orientation as the diamond matrix as proved in Fig. 4.

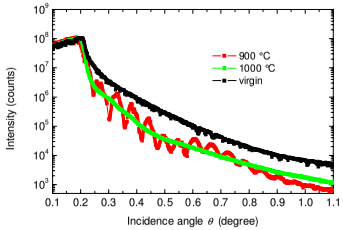

Fig. 1: Specular reflectivity.

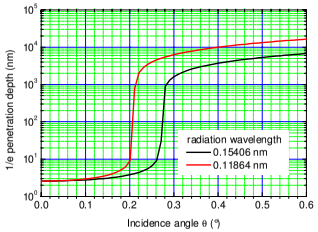

Fig. 2: 1/e penetration depth of x-rays in diamond.

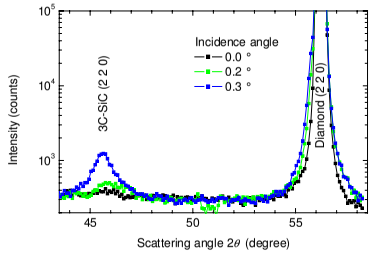

Fig. 3: Grazing incidence grazing exit diffraction of material implanted at 900 °C: radial scan in <110> direction.

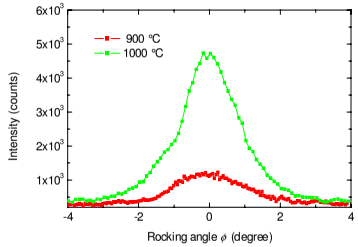

Fig. 4: Grazing incidence grazing exit diffraction: angular scan across 3C-SiC(220).

Concluding it may be stated that the implantation temperature influences in an essential way the structure of the SiC nanocrystals as well as the matrix material.

IBS of 3C-SiC is more efficient at 1000 °C: the amount of crystalline 3C-SiC is 2.2 times higher; the diameter of the crystallites is 11 nm, they are strained by -4.8x10^{-3} and have a mosaicity FWHM of 1.7°. IBS at 900 °C produces smaller crystallites with a diameter of 8 nm, a higher strain of -7.5x10^{-3} and a wider mosaicity of 2.4°.

At 1000 °C the diamond matrix nearly completely relaxes immediately during the implantation process.

ROBL-CRG	**Experiment title:** **Real-time studies of the ITO film structure and resistivity behavior during annealing**	**Experiment number:** **IH-SI-142**
Beamline: BM 20	**Date of experiment:** from: 15.02.2004 to: 17.02.2004	**Date of report:** 09.07.2004
Shifts: 6	**Local contact(s):** Mrs. Valentina Cantelli	*Received at ROBL:* *12.07.04*

Names and affiliations of applicants (* indicates experimentalists):

V. Cantelli*, FZ Rossendorf, IIM, Dresden, Germany

N. Shevchenko*, FZ Rossendorf, IIM, Dresden, Germany

A. Rogozin*, FZ Rossendorf, IIM, Dresden, Germany

M. Vinnichenko, IIM, Dresden, Germany

Report:

Amorphous tin-doped indium oxide (ITO) films were produced by reactive pulsed middle frequency dual magnetron sputtering on Si(100) substrates covered with 500 nm SiO_2 [1]. The aim of this work is a real-time *in-situ* investigation of the structure evolution and resistivity of the ITO films during annealing in vacuum. The samples were characterized by *in-situ* synchrotron XRD analysis and simultaneous four-point probe measurements at the ROssendorf Beam Line (ROBL). The experiments are performed at non-isothermal (T-ramp: 2.5 – 10 K/min) and isothermal (temperature range of 210–240°C) annealing modes.

The direct observation of the structure evolution reveals a rapid crystallisation within the temperature range 240–280°C at non-isothermal annealing. The heating rate does not influence notably the temperature of the crystallisation onset (T_{cr} = 240 ± 12°C). However, the crystallisation rate increases with an enhancement of the heating rate.

The isothermal annealing experiments show, that an increase of the annealing temperature leads to a decrease of the incubation or delay time and total time of amorphous-to-crystalline transformation (Fig. 1(a)). The XRD data were analyzed to determine the kinetic parameters of crystallisation using the Kolmogorov–Johnson–Mehl-Avrami equation [$f \sim 1\text{-}exp(-kt^n)$]. A linear fit of the function $-ln(1\text{-}f)$ plotted *versus* the annealing time on a double-logarithmic scale, yields the kinetic exponent n, as indicated by Fig. 1(b). Probably, n~2 reveals a two-dimensional crystallisation process with constant growth rate (site saturation mode).

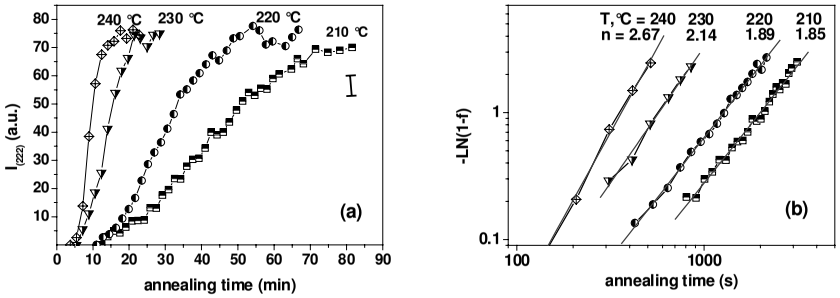

Fig. 1: Integral intensity of the In_2O_3 (222) peak (**a**), and function $-ln(1\text{-}f)$ (**b**) *versus* the annealing time at different isothermal annealing temperatures.

The activation energy was estimated from an Arrhenius relationship of the form $U=U_0\,exp\text{-}(Q/k_BT)$, where U is a crystallisation rate. The activation energy for crystallisation of these ITO films was found to be Q = 1.44 ± 0.14 eV.

The observed temperature or time dependences of the resistivity (not shown here) indicate several stages of its behavior [2]. The resistivity depends non-linearly on the crystalline fraction. Even in the amorphous stage the resistivity significantly decreases with increasing temperature or annealing time, likely due to a relaxation of distorted In-O bonds in the amorphous phase and, therefore, a free electron density enhancement by the creation of oxygen vacancies. The rapid crystallisation leads to a further decrease of the resistivity most probably due to Sn donor activation.

References

[1] A.I. Rogozin, M.V. Vinnichenko, A. Kolitsch, W. Möller, J. Vac. Sci. Technol. **A22(2)** (2004) 349-355

[2] A. Rogozin, N. Shevchenko, M. Vinnichenko, F. Prokert, A. Cantelli, A. Kolitsch, W. Möller, APL **85(2)** (2004) 212-214

ESRF	**Experiment title:** Crystallization of Ni-Ti thin film Shape Memory Alloy (SMA)	**Experiment number:** ME-474
Beamline: BM 20	**Date of experiment:** from: 05.02.2003 to: 09.02.2003	**Date of report:** 01.03.2003
Shifts: 12	**Local contact(s):** Dr. Norbert Schell	*Received at ESRF:* *18.07.03*

Names and affiliations of applicants (* indicates experimentalists):

*Francisco M. Braz Fernandes, *Rui M. S. Martins, *Rui J. C. Silva

CENIMAT – Centro de Investigação de Materiais

Campus da FCT/UNL, 2829-516 MONTE DE CAPARICA, PORTUGAL

1. Thin films production

NiTi thin films were deposited on Si(100) wafers using sputtering dc technique. The chemical composition of the target material was 44 wt% Ni – 56 wt% Ti, i.e. 49 at% Ni – 51 at%Ti (60 x 232 x 2 mm). The substrates used for the deposition of the Ni-Ti thin films were (i) Si(100) oxidized wafers and (ii) polysilicon thin films deposited on Si(100) oxidized wafers. The thickness of the sputtered Ni-Ti films ranged from 1.4 μm to 1.6 μm (D3: 70 mm, D4: 40 mm; 5.75 W/cm^2, P_{Ar} = 1 mTorr). The temperature range covered for the crystallization studies was from room temperature to 430ºC.

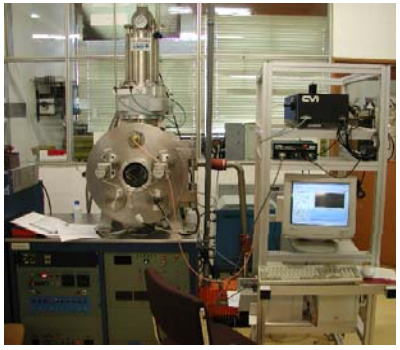

Fig. 1 – Dc sputtering equipment.

Designation	Position on the sample holder	Substrate/Target distance (mm)
D3M93	**a)**	70
D3M47	**b)**	70
D3064	**a)**	70
D35104	**a)**	70
D4M64	**a)**	40
D4M68	**b)**	40
D4044	**a)**	40

a) sample located inside the vertical projection of the target on the substrate

b) sample located outside the vertical projection of the target on the substrate (~ 25 mm from the edge)

2. GIXRD *in situ* annealing

Samples of 10x10 mm^2 were cut to be analysed by GIXRD at ROBL. The annealing of the films took place under vacuum (pressures ranging from 4×10^{-8} to 2×10^{-6} mbar). The grazing incidence angle was 1º.

3. Results[1]

Fig. 2 shows the diffraction patterns of the NiTi thin films during and after crystallization (RT).

[1] presented at "Materiais 2003" and submitted for publ. in Mat. Sci. For. (*In-situ* GIXRD characterization of the crystalli-zation of Ni-Ti sputtered thin films; R.M.S. Martins, R.J.C. Silva, F.M.Braz Fernandes, L. Pereira, P.R. Gordo, M.J.P. Maneira, N. Schell).

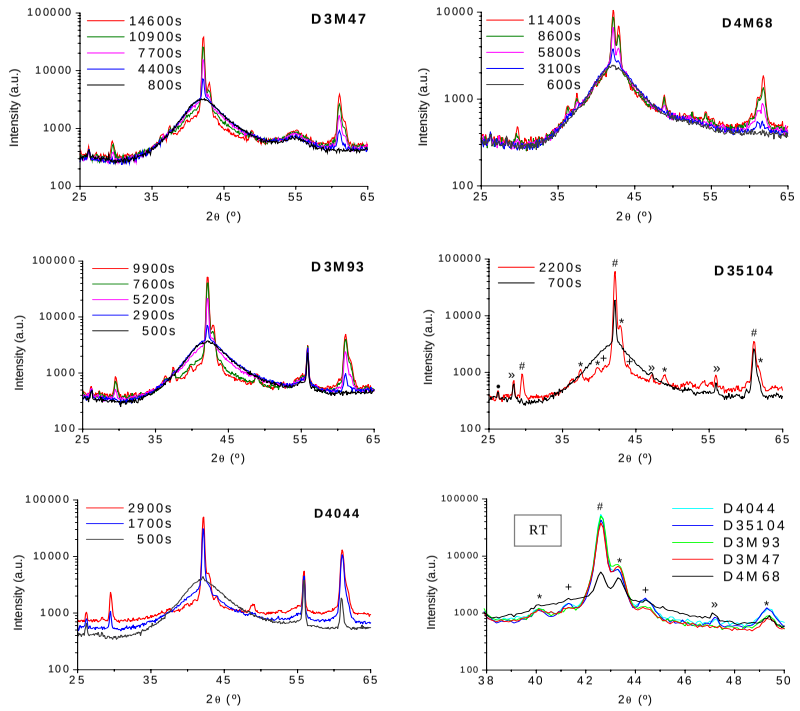

Fig. 2 – GIXRD patterns of dc and rf sputtered films at crystallization temperature and at RT after crystallization (# B2, * Ni_4Ti_3, + Ni_3Ti_2, • SiO_2, » Si).

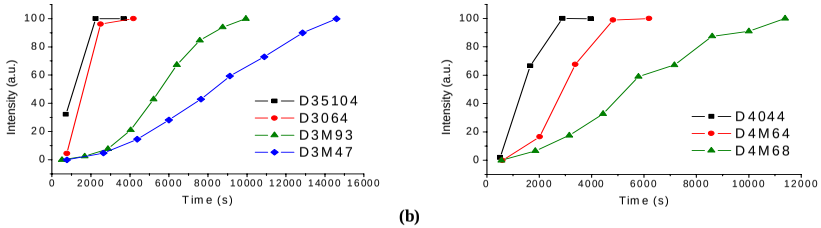

(a) **(b)**

Fig. 3 – Crystallization evolution represented by the integrated intensity of the (110) austenite peak versus time during annealing at 430ºC for the distance target/substrate of (a) 70 mm, (b) 40 mm.

4. Discussion

From the kinetic results, we observe that the **crystallization is significantly enhanced by:**

- **the presence of an intermediate film of polysilicon**
- **the fact that the sample lies within the limits of the vertical projection of the target on the substrate**.

During crystallization, ***Ni_3Ti_2 and Ni_4Ti_3 precipitate*** (as it is also reported by other authors). Using the distance target/substrate of 40 mm instead of 70 mm gives:

- no significant change of the kinetics for the depositions on polysilicon
- a significant change for the deposition on the Si(100) wafer (no intermediate polysilicon).

ROBL-CRG	**Experiment title:** Chalcopyrite thin films on Si substrates	**Experiment number:** ME-586
Beamline: BM 20	**Date of experiment:** from: 10.05.2003 to: 13.05.2003	**Date of report:** 28.08.2003
Shifts: 9	**Local contact(s):** Dr. Norbert Schell	*Received at ROBL:* *29.08.03*

Names and affiliations of applicants (* indicates experimentalists):

Dr. J. Kräußlich*[1)] Dr. H. Metzner[2)]
DP F. Wunderlich*[1)] Dr. Th. Hahn[2)]
DP J. Cieslak*[2)] Dr. U. Kaiser[2)]
Prof. K. Goetz[1)] Prof. W. Witthuhn[2)]

Friedrich-Schiller-University of Jena, [1)] Institute of Optics and Quantumelectronics, [2)] Institute of Solid-State Physics, Max-Wien-Platz 1, 07743 Jena, Gemany

Report

$CuGaS_2$ thin film epitaxially grown on Si(111)

J. Kräußlich, J. Cieslak, Th. Hahn, H. Metzner, U. Kaiser, W. Wunderlich, W. Witthuhn, K. Goetz

The aim of the experiment has been to characterise $CuGaS_2$ thin films epitaxially grown on Si(111) substrates by means of high resolution x-ray diffraction methods (HRXRD). Data concerning the characteristics of the epitaxial growth, the crystallographic orientation of the thin film crystallites to the substrate as well as the numerical evaluation of the in-plane lattice parameter **a** of the epitaxially grown $CuGaS_2$ are of special interest for the thin film producer to optimize the technological growth process as well as the research and development of optoelectronic devices.

Within the chalcopyrite family, the sulphur based compounds $CuMS_2$ (M=In, Ga, Al) have attracted much interest in recent years because they show a direct wide band-gap covering from E_{gap} = 1.53 eV ($CuInS_2$) over **E_{gap} = 2.43 eV ($CuGaS_2$)** to E_{gap} = 3.49 eV ($CuAlS_2$). Therefore they are particularly suitable for optoelectronic as well as photovoltaic applications. The epitaxial growth of $CuInS_2$ on Si was already demonstrated [1], while CuGaS2 was hitherto grown epitaxially on the compound semiconductor substrates GaAs and GaP only [2]. Recently, our efforts to epitaxial growth of CuGaS2 (CGS) thin films on Si(111) substrates using the three-sources-molecular beam epitaxy (MBE) were successful [3].

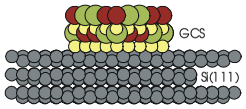

The structure of the grown CGS films was studied by means of high resolution transmission electron microscopy (HRTEM), selected area electron diffraction (SAED) and high resolution x-ray diffraction (HRXRD).

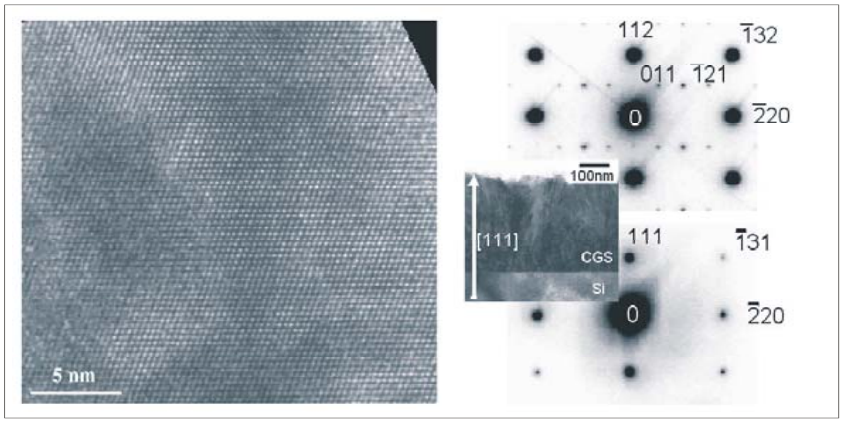

Fig. 1: [110] cross-section HRTEM image showing perfectly grown regions of CGS on Si(111).

Fig. 2: Selected area electron diffraction pattern of the [11-4]-zone axis of CGS on Si(111) showing chalcopyrite ordering (h+k+l=2n).

The XRD measurements have been carried out to check the crystallographic phase, to find out the crystallographic orientation of the grown CGS films in relation to the substrate as well as to determine the real lattice parameter **a** and **c** of the epitaxially grown $CuGaS_2$. A part of the measurements, which predominantly used the reflection mode, were accomplished at the home institute using a 18 kW rotation unit x-ray generator as radiation source. Whereas the measurements which predominantly used the transmission mode were carried out using synchrotron radiation at the ESRF (CRG beamline ROBL). The used high-resolution x-ray diffractometers were equipped with an Eulerian cradle. This made possible the x-ray diffraction investigation by using symmetric, asymmetric and oblique crystal reflection adjustments (Figs 3, 4, 5).

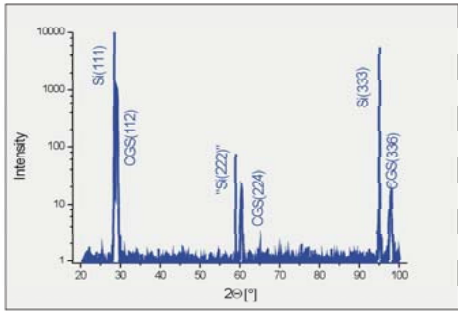

Fig. 3: Large area ω/2Θ-diffraction pattern of the CGS film grown on Si(111). Besides the n•(111)-reflections of the Si substrate, only higher orders of CGS(112)-reflections appear. Hence, there is not any polycrystalline phase. This suggests an epitaxial growth of CGS with predominant [112] growth direction. Note that $d_{(112)}$CGS < $d_{(111)}$Si.

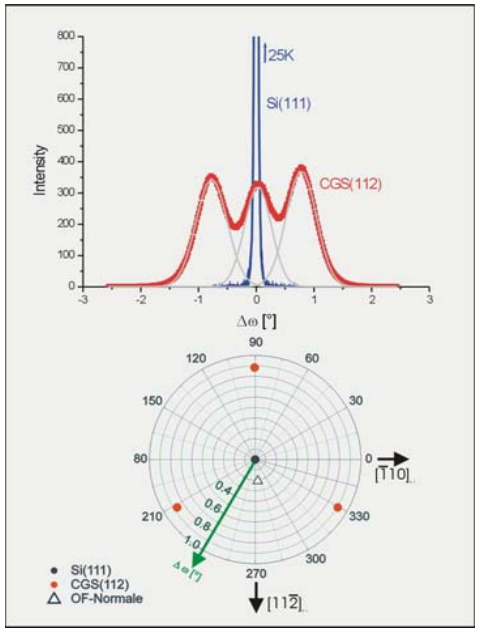

Fig. 4: Rocking curve (ω-scan) recorded with the CGS(112)-reflection. The ´threefold necking´ of the CGS peak is caused by rotation twins of CGS domains, which are preferentially grown with small angle difference (0.8°) to the wafer normal, respectively to the Si[111]-direction as shown in the stereographic projection. Threefold is their preferred lateral tilting, resp. orientated to the three inclined <001>-directions of the Si(111)-wafer.

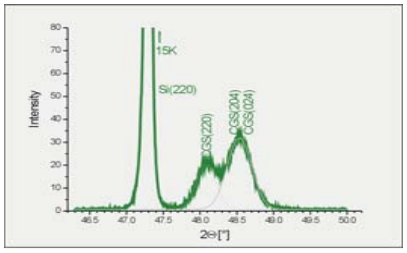

Fig. 5: ω/2Θ-diffraction pattern recorded with the asymmetric (204)/(024)- respectively (220)-reflections of CGS and the (220)Si-reflection for comparison only. The splitting of the (220)- and (204)/(024)-CGS reflections reveal the tetragonal chalcopyrite structure of the CGS thin film grown on Si(111).

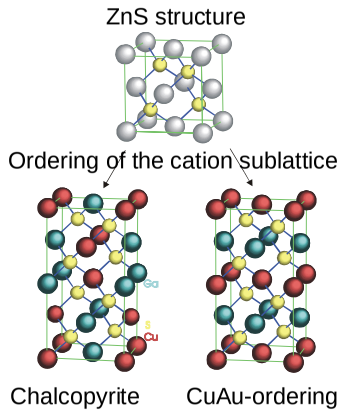

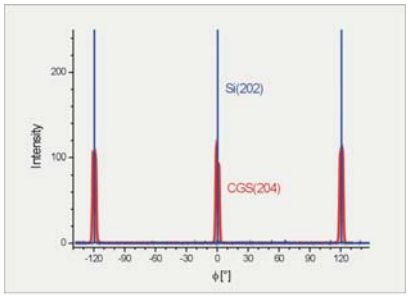

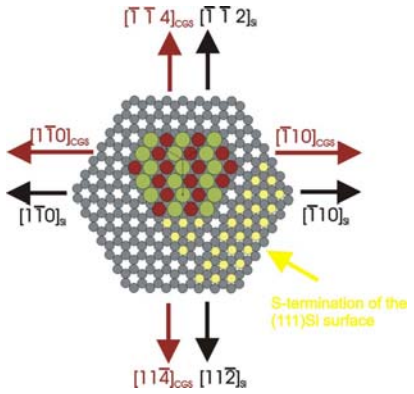

Fig. 6: Φ-scan recorded with the inclined (204)/(024)/(220)-reflections of CGS and {202}-reflection of Si for comparison. The Φ-rotation was accomplished around the surface-normal of the Si(111) substrate.

The diffractogram reveals the lateral orientation relation of the grown CGS thin film in respect to the Si(111) lattice. From this follows the lateral epitaxial relation as shown in the schema on the right. Lateral epitaxial relation of the CGS thin films grown on Si(111) substrates: $[001]_{CGS} \parallel <001>_{Si}$.

Despite the usage of the 6°-off-axis (111)Si wafer as substrate, it was found that the CGS thin films also grew epitaxially. The crystallographic relationship of CGS thin film and Si-substrate is given by the preferred alignment of the $[112]_{CGS}$-direction (growth direction) toward the $[111]_{Si}$-direction with an angle difference of ≈ 0.8° (normal relation) and the $[001]_{CGS}$-direction toward the inclined $<001>_{Si}$-axis. The CGS thin film is obviously composed of 120°-rotation twins due to three-fold symmetry of the Si(111) wafer surface.

We thank all members of the ROBL beamline team, especially Dr. Schell and A. Bauer, for all the helpful support at the time of execution of this experiment.

[1] Th. Hahn, H. Metzner, B. Plikat, M. Seibt; Appl. Phys. Lett. **72** (1998) 2733
[2] S. Shirakata, S. Chichibu; J. Appl. Phys. **87** (2000) 3793
[3] H. Metzner, Th. Hahn, J. Cieslak, U. Grossner, U. Reislöhner, W. Witthuhn, R. Goldhahm, J. Eberhardt, G. Gobsch, J. Kräußlich; Appl. Phys. Lett. **81** (2002) 156

ESRF	**Experiment title:** ***In situ*** **XRD study of sputtered Ni-Ti SMA (Shape Memory Alloy) thin films**	**Experiment number:** **ME-584**
Beamline: BM 20	**Date of experiment:** from: 16.07.2003 to: 22.07.2003	**Date of report:** 19.08.2003
Shifts: 18	**Local contact(s):** Dr. Norbert Schell	*Received at ESRF:* *20.08.03*

Names and affiliations of applicants (* indicates experimentalists):

F.M. Braz Fernandes*, **Rui M.S. Martins***, **Rui J. C. Silva***: CENIMAT – Centro de Investigação de Materiais, Campus da FCT/UNL, 2829-516 Monte de Caparica, PORTUGAL

N. Schell*, FZR, ROBL-CRG at ESRF, B.P. 220, F – 38043, Grenoble, FRANCE

Report:

Deposition of useful Ni-Ti thin films has been problematic due to compositional sensitivity. According to Ho *et al.* [1], the chemical composition of Ni-Ti sputtered films may deviate by up to 2 at% (lower Ti) when compared to the target composition. A more robust procedure is clearly desirable, and sputtering using multiple targets is an obvious solution. Preliminary studies performed by other researchers [2] indicate that the excessive roughening of Ni targets during service affects the vapor flux at constant power and suggest that Ni-Ti is a better target source than pure elements. In continuation of earlier work done at ROBL (Exp. **20_02_608**), experimental ***in-situ*** **studies of the structural evolution during co-sputtering using NiTi and Ti targets** were carried out.

EXPERIMENTAL

The deposition chamber is described in detail in reference [3]. For the *in-situ* studies (incident x-rays monochromatized to 18.367 keV / λ = 0.675 Å), two different scattering geometries were used: (1) Bragg-Brentano large-angle scattering (XRD) and (2) low-angle specular reflectivity with information on film thickness and surface roughness.

Further experimental parameters were: base pressure < 3×10^{-6} mbar, target material Ni-Ti (49 at% Ni – 51 at%Ti) and pure Ti (99.999%), sputter gas Ar (99.9996%) at a pressure of 3.5×10^{-3} mbar. The substrate temperature varied from 460ºC to 480ºC during deposition.

RESULTS

Table 1: Parameters used for the *in-situ* sputtering deposition.

Sample	*Power (W)*		*Substrate*	*Bias (V)*	*Deposition procedure*	*Annealing (min)*
	NiTi	*Ti*				
8	40	40	Poly Si / Si(100)	0	Ti deposition (28 min) / NiTi deposition (2 h 10 min)	80
9	40	-	Poly Si / Si(100)	-45	NiTi deposition (2 h)	65
10	40	40	Si(100)	-45	4 × (6 min Ti deposition + 30 min NiTi deposition)	78
11	40	5	Si(100)	-45	4 x (35 min NiTi + Ti co-sputtering / 25 min annealing)	85
12	40	5	Si(100)	0		90
13	80	5	Si(100)	0	1 h 30 min (NiTi + Ti co-sputtering)	46 at 470ºC 100 at 545ºC

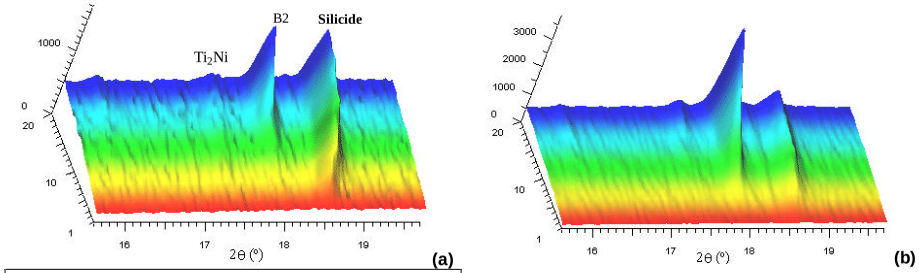

Fig. 1: *In-situ* XRD study during co-sputtering deposition and during annealing (steps of ≈ 7.5 min). *Samples:* (a) 11; (b) 12; (c) 13.

The experimental results show that:

- a bias (-45 V) gives rise to a significant change of the peak area ratio B2(110) / B2(200); the **first layers of B2 stack preferentially on (h00) planes**; **when no bias is applied, (110) stacking prevails over (h00)**, (**Fig. 2** - a, b);

- the **FWHM changes** significantly during deposition and remains quite stable during annealing (at 470ºC); this trend is more noticeable when no bias is applied.

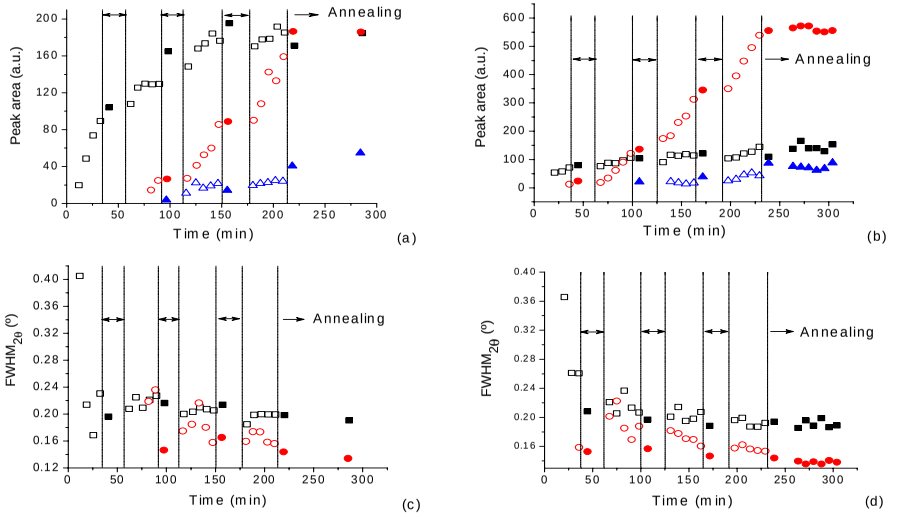

Fig. 2: Area and $FWHM_{2\theta}$ of *in-situ* XRD peaks recorded during deposition (co-sputtering NiTi + Ti) of *sample 11* (a, c) and *sample 12* (b, d), *versus* time. ()/(■) **Ti_2Ni** (deposition/annealing); (○)/(●) **B2**; (8) (7) **Silicide**.

This series of first experiments on the *in-situ* study of co-sputtering shows that it is possible to follow the structural evolution of sputtered thin films along the deposition process, using the facilities of the ROBL beamline.

REFERENCES

[1] K. Ho, K. Mohanchandra, and G. Carman, Thin Solid Films, **413** (2002), p. 1.

[2] C. Shih, B. Lai, H. Kahn, and S. Philips, IEEE Journal of Micromechanical Systems, **10** (1) (2001), p. 69.

[3] W. Matz, N. Schell, W. Neumann, J. Bottiger, and J. Chevallier, Rev. Sci. Instrum., **72** (2001), p. 3344.

ESRF	**Experiment title:** X-ray diffraction studies on stress-released cubic boron nitride thin films	**Experiment number:** ME-706
Beamline: BM 20	**Date of experiment:** from: 12.10.2003 to: 15.10.2003	**Date of report:** 03.02.2004
Shifts: 9	**Local contact(s):** Dr. Norbert Schell	*Received at ESRF:* *05.02.04*

Names and affiliations of applicants (* indicates experimentalists):
*Dr. R. Gago, FZR, IIM, Dresden, Germany
*B. Abendroth, FZR, IIM, Dresden, Germany

Report

The aim of this work was to investigate the mechanisms of ion-induced stress relaxation in magnetron sputtered cubic boron nitride (cBN) films. The stress relaxation was achieved by simultaneous medium energy (2-10 keV) Ar/N_2 ion bombardment during the growth process[1]. The relaxation process was verified by measuring *in-situ* the level of macroscopic stress (substrate curvature method) during growth. The purpose of x-ray diffraction (XRD) measurements was to study the stress relaxation at a microscopic scale and discern the mechanisms involved in the process.

a) Experiment:

A set of samples with different degree of ion induced damage, as quantified by the number of displacements per atom (dpa), were prepared at the home laboratory. A sample grown without medium-energy ion bombardment was used as a reference for cBN with high compressive stress (-9 GPa). The macroscopic stress decreases with the number of dpa and ranges from -2.5 to -1.6 GPa for the samples measured at the ESRF (between 0.6 and 1.2 dpa).

Grazing incidence diffraction (GID) geometry was chosen to minimize the signal coming from the single crystal Si(100) substrate. The wavelength of the incidence x-ray beam was set at 1.2 Å (10.332 keV) and the angle of incidence (θ) at 0.2°, slightly above the critical angle (α_c=0.19°) to enhance the scattered x-rays intensity. For each sample, in-plane (2ω) and out-of-plane (2θ) scans were performed, which allows to map the state of biaxial stress in the films.

b) Results:

Figure 1 shows the in-plane (a) and out-of-plane (b) diffraction patterns. In the in-plane geometry, the Bragg peaks related to the hBN(002) and cBN(111) reflections are observed. The hBN signal comes mainly from the seed layer necessary for nucleation of cBN. The hBN(002) peak vanishes in the out-of-plane geometry due to the preferential orientation of this buffer layer with the c-axis parallel to the substrate. A preferential (111) in-plane texture of the cBN grains is observed for the non-irradiated sample. This texture decreases with the introduction of medium-energy ion bombardment.

Figure 2 shows the lattice parameters obtained from Figure 1. For comparison, the d(111) tabulated value of polycrystalline cBN[2] is also included (dashed line). The lattice parameter is larger in the out-of-plane than in in-plane direction, indicating a pronounced biaxial state of compressive stress. Even with the presence of compressive stress, the in-plane d(111) values of our samples are larger than the powder reference value. This is most likely due to the nanocrystalline structure and incorporation of defects as a result of the deposition process. The cBN grains are elongated parallel to the film surface, with a size of ~3 nm out-of-plane and 6 nm in-plane. Despite the ion-bombardment, the FWHM of the Bragg peaks remains the same for all the samples studied, indicating no amorphisation of the cBN phase.

In the case of post-annealing at 900°C of a sample with 1.2 dpa (performed at the home laboratory), the analysis shows a complete relaxation of the lattice with equal in-plane and out-of-plane lattice parameters. The obtained d(111) value can be considered as a reference for stress-free cBN films produced by magnetron sputtering. In the case of medium-energy ion bombardment, the in-plane and out-of-plane lattice parameters approach the value of the annealed sample with increasing the ion induced damage as a signature of the stress relaxation.

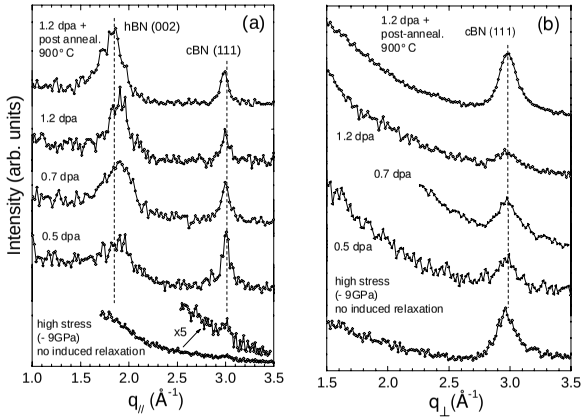

Figure 1. In-plane (a) and out-of-plane (b) diffraction pattern of cBN thin films with different stress relaxation as result of the growth under different induced damage by Ar/N_2 medium-energy ions. The in-plane spectrum of the non released sample shows a very low intensity due to the extreme small film thickness of only 30 nm.

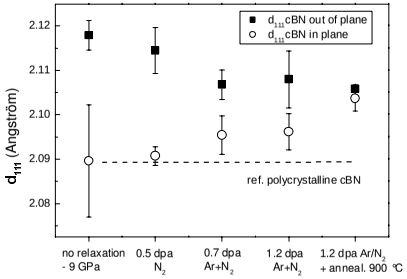

Figure 2. cBN (111) lattice spacing measured in in-plane and out-of-plane geometry for samples with different degree of ion-induced damage and stress relaxation. For comparison the values of polycrystalline cBN, a non relaxed cBN thin film and a cBN thin film that is stress free after annealing at 900°C are shown.

c) Final remarks and out-look:

XRD measurements with a lab-source (Cu-Kα, λ=1.54 Å) were not successful due to the low scattering cross-section of B and N, the nanocrystallinity of the samples and the low film thickness (< 0.5 µm). In view of the above results, the use of synchrotron radiation is clearly justified. However, even when using synchrotron radiation, the set-up has to be chosen carefully (scattering from air,…) to detect such a weak signal.

In conclusion, it can be stated that the observed ion-induced stress relaxation takes place at a microscopic scale. The main path is strain release in the cBN grains and not phase transformation to hBN. In addition, the cBN grains are stable against the ion bombardment, since no signs of amorphisation could be detected.

For future measurements, it would be interesting to performed in-depth studies due to the layered structure of the films. We might also gain some additional information with *in-situ* annealing experiments. Finally, the use of an ID beamline or, at least, operation mode with "Uniform Filling" mode is suggested to compensate the large acquisition time required for this kind of films.

Acknowledgments: We would like to thank Dr. F. Eichhorn for the XRD analysis at FZR and fruitful discussions regarding the preparation of this experiment and posterior data evaluation.

REFERENCES:

[1] Abendroth et al. Thin Solid Films 447-448 (2004) 131; [2] JCPDS pattern 25-1033.

ESRF	**Experiment title:** ***In situ* stress state analysis during thermal cycling of Ni-Ti Shape Memory Alloy**	**Experiment number:** **ME-705**
Beamline: BM 20	**Date of experiment:** from: 30.10.2003 to: 04.11.2003	**Date of report:** 29.02.2004
Shifts: 15	**Local contact(s):** Dr. Norbert Schell	*Received at ESRF:* *02.07.04*

Names and affiliations of applicants (* indicates experimentalists):

F.M. Braz Fernandes*, **Andersan dos Santos Paula***, **João Canejo***: CENIMAT – Centro de Investigação de Materiais, Campus da FCT/UNL, 2829-516 Monte de Caparica, PORTUGAL

N. Schell*, FZR, ROBL-CRG at ESRF, B.P. 220, F – 38043, Grenoble, FRANCE

Report:

The aim of the experiment was to follow the microstrain/microstress evolution during annealing of Ni-Ti shape memory alloy subject to different thermomechanical treatments. As this type of structural evolution is accompanied by changes in the preferential orientation, the conditions for the *in-situ* determination of pole figures were also tested. This type of study is relevant to the envisaged applications, because of the anisotropic response of the shape memory effect.

Experiment

A series of samples in different thermomechanical conditions have been studied using the Be-dome furnace installed on the 6-circle goniometer of the BM20 beamline. The samples were extracted from a 2 mm thick plate supplied by Memory-Metalle GmbH, the chemical composition being 49 at% Ni –51 at% Ti; *in-situ* annealing has been carried out up to 700ºC, under a vacuum better than 10^{-6} mbar. The temperature control of the sample was done by a thermocouple in contact with the sample's upper surface. The wavelength of the incident beam was set at 1.54 Å. The pole figures have been determined for $-45º<\phi<+45º$ and $-60º<\chi<0º$, the rolling direction (RD) being aligned with $\phi = -45º$.

Results

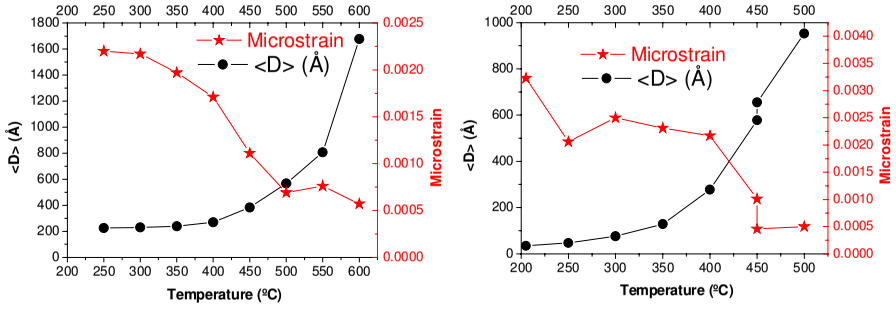

Fig. 1: Coherency domain length <D> and microstrain as a function of annealing temperature for the (a) as-received sample and (b) quenched from 500ºC, followed by 40% deformation (rolling).

Between 300 and 500ºC there is a significant change of the microstrains and the coherency domain length (Fig. 1), as well as the type of preferential orientation of the samples that have been studied (Fig. 2).

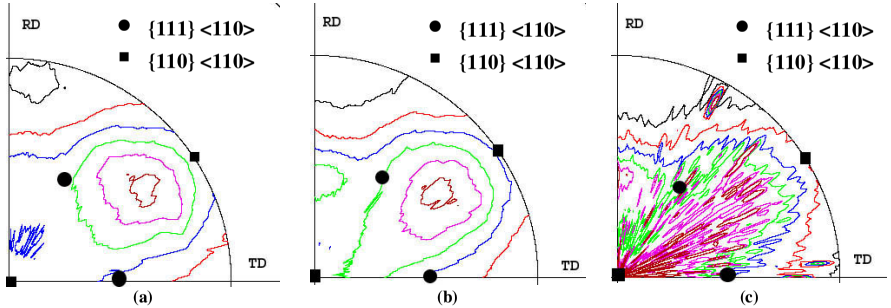

Fig. 2: {110} pole figures of B2 phase for material as received during annealing at (a) 150ºC, (b) 400ºC, (c) 500ºC.

It has been identified the presence of Ti_2Ni already in the as received material before any treatment (Fig. 3). The corresponding peaks are not detected at room temperature, where the martensite phase (B19') is stable, because of the superposition of the peaks Ti_2Ni / B19'. Only after heating the sample into the austenitic (B2) field the Ti_2Ni peaks can be detected. But, at the end of the annealing at 700ºC, the Ti_2Ni peaks have significantly increased, denoting a precipitation during annealing (Fig. 4).

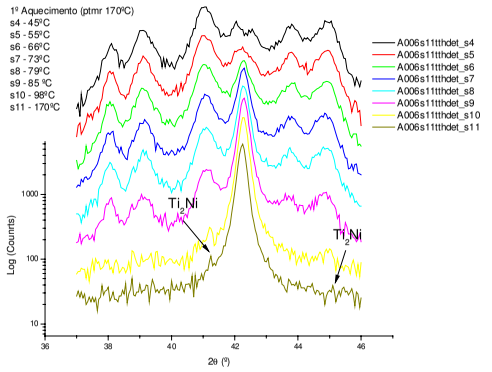

Fig. 3: Spectra sequence showing the gradual transformation of martensite (B19') into austenite (B2) during heating (from top to bottom) before annealing at 700ºC.

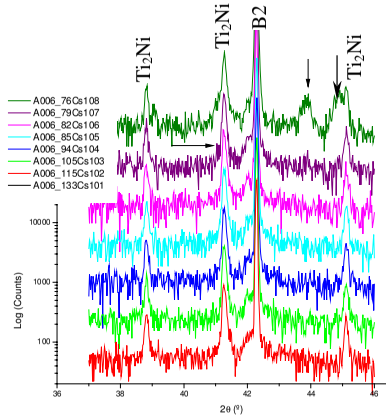

Fig. 4: Spectra sequence illustrating the start of formation of B19' (marked by →) during cooling after the material has been annealed at 700ºC.

Discussion

The only high temperature texture determination for polycrystalline Ni-Ti that is reported in the literature [1] has been made at 120ºC. In this study we have tested the feasibility of high temperature pole figures determination in BM20 and we have shown that there is a relation between the preferential orientation change and the structural evolution taking place during annealing. It is thus very interesting to continue this study by evaluating the evolution of the preferential orientation during annealing and correlating it with the other structural changes that are taking place.

REFERENCES

[1] *Texture Development and Anisotropic Behaviour in a Ti-45Ni-5Cu (at.%) Shape Memory Alloy*; Lie Zhao; PhD Thesis, University of Twente, Oct 1997.

ESRF	**Experiment title:** **Strain and texture investigation across a crack in an experimentally deformed granite sample**	**Experiment number:** **ME-708**
Beamline: BM 20	**Date of experiment:** from: 12.02.2004 to: 15.02.2004	**Date of report:** 24.11.2004
Shifts: 9	**Local contact(s):** Dr. Norbert Schell	*Received at ROBL:* *24.11.04*

Names and affiliations of applicants (* indicates experimentalists):

K. Walther*,[1], A. Frischbutter[1], P. Mikula*,[2], C. Scheffzük*,[1]

[1] GeoForschungsZentrum Potsdam, Dept. 5.3, Telegrafenberg, 14772 Potsdam, Germany

[2] Nuclear Physics Institute, 25068 Rez near Prague, Czech Republic

Report

Hypervelocity collisions of solid materials are one of the fundamental processes taking place in the solar system. The steadily increasing number of terrestrial impact craters discovered is an expression of the importance of shock deformation on Earth as well. During an impact-event kinetic energy is released instantly and locally concentrated, causing the formation of spherically spreading shock waves. A shock wave is a discontinuous compression wave which travels with supersonic velocity and causes the material engulfed by the shock wave to move behind the front at a somewhat lower velocity than the shock front (Stöffler *et al*., 1994). The extreme physical conditions of pressure, temperature and strain imposed by transient shock waves lead to vaporization, melting and produce unique effects in rocks and minerals at pressure levels ranging from 2-100 GPa. (for instance shatter cones, planar deformation features (PDF), high pressure polymorphs, diaplectic glasses, localized melt veins *etc*.). The composite and heterogeneous nature of rocks, which is the rule rather than the exception in nature, has a profound effect on the characteristics of shock metamorphism too. Experiments carried out with rocks strongly differ in mechanical and compositional features. In this experiment ***we investigated especially phenomena relating the effects of shock metamorphism on strain/stress distributions***.

The samples under investigation consisted of ***two rock types: quartzite and dunite***. The quartzite (from Oberschöna, Germany) is quite pure in composition (98.8 % SiO_2) and strongly foliated. The average grain size of quartz is 230 µm. The dunite comes from Åheim (Norway), has an average grain size of 187 µm and can be seen as equigranular. The rock dominantly consists of olivine (89.1 %), the residue is mainly pyroxene and phlogopite/serpentine. The olivine has a Fo_{96} (forsterite) composition.

From both materials cylinders were made of 15 mm in diameter and 10 mm in length, cutted into halves along the axes of the cylinders, polished and fitted together to a cylindrical sample. This sample was put into a steel jacket. At room temperature the detonation of a high explosive accelerated a plate of ARMCO-iron of 4 mm thickness which impacts the jacket (Stöffler *et al*., 1994), where the sample was located. The ***peak pressure was about 34 GPa within the sample***. The experiment was performed for a perpendicular interface arrangement with respect to the shock wave front (Fig. 1). After the shock the sample was 8 mm in height and about 18 mm Ø. The shock recovery experiments were performed at the Fraunhofer-Institut für Kurzzeitdynamik (Ernst-Mach-Institut, Freiburg im Breisgau, Germany) (Kenkmann *et al*., 2000).

The deformed sample was investigated for ***microstructures*** using ***optical-***, electron- (***SEM***) and transmission electron microscopy (***TEM***). Neither those methods, nor synchrotron radiation diffraction gave any signs of high pressure phases of quartz-like coesite or shistovite.

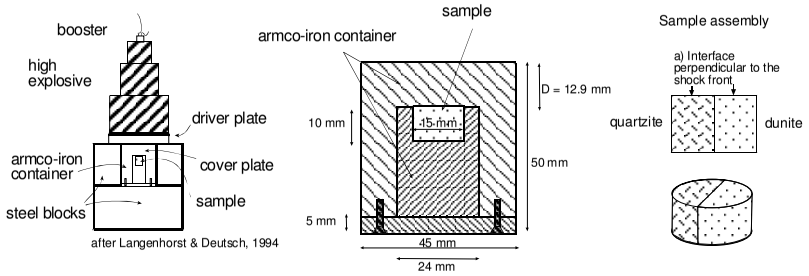

Fig. 1: Experimental set-up for the shock loading experiments.

At ROBL (BM20) ***the texture of both phases*** of the sample was investigated. Using an incident beam of 17 keV (nearly the wavelength of Mo radiation) a slice of 1 mm thickness could be investigated in ***transmission geometry***. First a ***2-dim. CCD*** detector was used with an entrance window of 64 x 64 mm^2 (SMART-detector, Bruker, Madison, USA) with a resolution of 512 x 512 pixels. The sequence of the observed Debye-Scherrer rings was very, very dense, i.e. the resolution too poor for obtaining a gap of about ten pixels between two neighbouring rings. This gap is required for proper background correction. 2D-detectors of this (relatively) small sizes and resolution seems to be useful only for samples with high crystal symmetry.

A next attempt was made using a large image plate (***MAR3500-detector***). The effective size of the image plate was 350 mm in diameter and therefore yielding a resolution of 3500 x 3500 pixels. A drawback of image plates is a too long read-out time in the order of a few minutes. In our experiments, where no dynamical processes took place, an image plate could be used without restriction. The detector was provided by the detector pool of the ESRF. The MAR3500-detector was mounted on a desk, thus the centre of the detector was about 25 mm above the centre of the beamline. The beam itself was guided inside of a conical tube in order to prevent background due to air scattering, the front window of the tube was 2 mm in diameter. Furthermore, in order to have sufficient grain statistics, the sample was permanently moved by a sample spinner.

Besides rings, belonging to the sample and having their centre 25 mm below the centre of the detector, additionally rings were observed, which are concentric to the centre of the detector. Control experiments with closed filters showed absolutly "empty" frames indicating, therefore, that the ***artifical rings*** are not caused by an overexposition or damage by other users. A method for the correction of the artifical rings in the 2d-frames has to be worked out.

The authors (K.W., A.F. and C.S.) are grateful to the ESRF for providing measuring time and to the staff of the ROBL beamline for their excellent support.

References

D. STÖFFLER AND F. LANGENHORST, *Shock metamorphism of quartz in nature and experiment: I. Basic observation and theory,* Meteoritics **29** (1994) 155-181.

T. KENKMANN, U. HORNEMANN, AND D. STÖFFLER, *Experimental generation of shock-induced pseudotachylites*, Meteoritics and Planetary Science **35** (2000) 1275-1290.

ESRF	**Experiment title:** ***In-situ*** **XRD study of sputtered Ni-Ti SMA (Shape Memory Alloy) thin films (cont.)**	**Experiment number:** **ME-814**
Beamline: BM 20	**Date of experiment:** from: 03.03.2004 to: 09.03.2004	**Date of report:** 12.08.2004
Shifts: 18	**Local contact(s):** Dr. Norbert Schell	*Received at ESRF:* *16.08.04*

Names and affiliations of applicants (* indicates experimentalists):

F.M. Braz Fernandes*, **Rui J.C. Silva***, **Márcia Silva***: CENIMAT – Centro de Investigação de Materiais, Campus da FCT/UNL, 2829-516 Monte de Caparica, PORTUGAL

N. Schell*, Rui M.S. Martins*: FZR, ROBL-CRG at ESRF, B.P. 220, F – 38043, Grenoble, FRANCE

Report:

Previous experiments at ROBL (**20_02_608 and ME-584**) were carried out using separate NiTi and Ti targets, where the power applied to each magnetron was kept constant. This new series of experiments was intended to make the *in-situ* study of the structural evolution during co-sputtering using NiTi and Ti targets with the power applied to the Ti magnetron being changed during the deposition process in order to actively design the film composition.

EXPERIMENTAL

The experimental conditions used were the same as those of the previous series of experiments. All the depositions were made on Si(100) substrates.

sample	*Power (W)*		*Bias (V)*	*Annealing (min)*
	NiTi	*Ti*		
S18	40	30 min (Ti 8W) + 30 min (Ti 20W) + 34 min (Ti 30W) + 66 min (only NiTi)	0	16
S19	40	44 min (Ti 20W) + 40 min (Ti 30W) + 45 min (only NiTi) + 40 min (annealing) + 40 min (only NiTi, substrate at 600°C)	0	21.5
S20	40	42 min (Ti 8W) + 37 min (Ti 20W) + 43 min (only NiTi)	-45	29
S21	40	44 min (Ti 20W) + 45 min (Ti 30W) + 39 min (only NiTi)	0	96

Table 1 – Deposition conditions.

RESULTS

The 3D plot capability of the program XOP has been used to follow the structural evolution of the films during the deposition as the power of the Ti magnetron was being changed (Fig. 1).

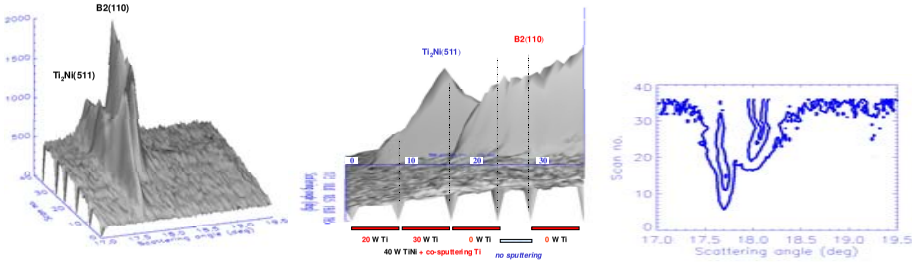

(a) (b) (c)

Fig. 1: 3D plot of the peak intensity (a, b) and 2D intensity contour level (c) during deposition of sample S19.

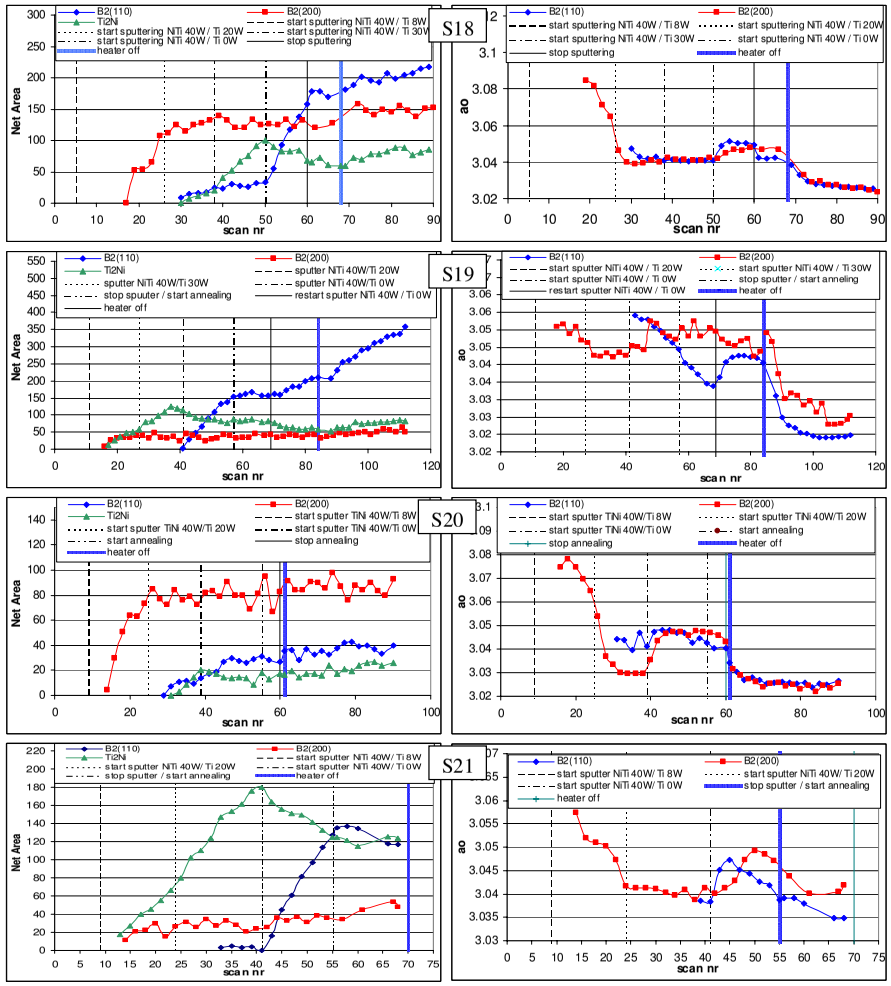

(a) (b)

Fig. 2: (a) Net area of the B2(110) and B2(200) and $Ti_2Ni(511)$peaks. (b) B2 lattice parameter calculated from (110) and (200).

SUMMARY

The results (comp. Fig. 2) show that:

- there is clearly a ***different variation of the intensity peaks for different powers*** applied to the Ti magnetron,
- under these deposition conditions, the ***B2 phase always started by stacking onto (200) planes*** and, when the (110) stacking was started, the (200) peak intensity was stabilized,
- significant ***stress relaxation processes*** are taking place ***during deposition*** as seen by the significant changes of the lattice parameter as calculated from $d_{(110)}$ and $d_{(200)}$..

CONCLUSIONS

The sputter chamber installed on the 6-circle-goniometer of ROBL proves to be a very efficient instrument to follow the deposition process.

ESRF	**Experiment title:** Oxide growth on iron single crystals	**Experiment number:** ME-816
Beamline: BM 20	**Date of experiment:** from: 13.07.2004 to: 19.07.2004	**Date of report:** 19.11.2004
Shifts: 15	**Local contact(s):** Dr. Norbert Schell	*Received at ESRF:* *19.11.04*

Names and affiliations of applicants (* indicates experimentalists):

Anke Pyzalla[1]*, Walter Reimers[2], Michael Skornia[2]*, Pedro Augusto Souza e Silva[1]

[1] TU Wien, Institute of Material Science and Technology, Karlsplatz 13-308, A-1040 Wien, Austria

[2] TU Berlin, Institute for Material Science and Technologies, Ernst-Reuter-Platz 1, D-10587 Berlin, Germany

Report:

Introduction

Materials are subjected to high temperature corrosion in numerous technical processes and environments such as turbines, engines, catalysers and power stations. Essential for the high temperature corrosion resistance of a material is its ability to build up a dense surface layer. A dense surface layer protects the substrate by barring the diffusion between the corrosive environment and the reactant and, thus, by decreasing the corrosion rate /Schütze 1988, Schütze 1991/. If the substrate is subjected to both mechanical and thermo–chemical-loading, a further condition for high temperature oxidation resistance is the adhesion of the surface layer to the substrate and the integrity of the surface layer. Further conditions are layer stability in the corrosive environment, a low partial pressure of the chemical compound in the surface layer and the durability of the surface layer against contaminations of the substrate surface. Last but not least the surface layer has to withstand mechanical stresses, which are caused by the growth of the oxide and in many cases also by external mechanical loading.

Originally and even until a few years ago strains in oxide layers were estimated by the Pilling-Bedworth-Ratio (PBR) /Pilling *et al.* 1923/. But, in many cases not even a qualitative connection exists between the PBR and the internal stresses /e.g. Baxter *et al.* 1983/. In many metal/oxide systems the mechanisms for strain formation in oxides have not been totally clarified yet, since this can only be determined by *in-situ* strain analyses. Experimental results indicate that the morphology and the texture of the oxide layer strongly influence its strain/stress state /Gnäupel-Herold *et al.* 1997, Corkovic *et al.* 2003/. The residual strain/stress state after oxidation and cooling differs from the strain/stress state in the oxide layers at high temperature, since additional stresses are formed during cooling as a result of the differences in the thermal expansion coefficients of the oxide layer and the metallic substrate. These cooling stresses often lead to oxide spalling.

Oxide layers on iron/steel substrates contain several sub-layers and thus, their strain state is more complicated. The aim of the experiments was an *in-situ* study of oxide layer growth on iron and the evolution of its strain/stress. In order to enable a systematic study of the influence of layer epitaxy and texture on the strain/stress state the investigations concentrated on single crystal iron substrates. The layer morphology, texture and strain/stress state in these layers was compared to oxide layers on coarse and fine-grained iron substrates.

Experimental Details

We used a ***halogen lamp furnace*** with a flat bottom plate that fits into the diffractometer at BM 20. The furnace was built at TU Berlin. The oxidation experiments were performed at ***ambient pressure***, with ***ambient oxygen partial pressure***. In order to see both the phase, texture and internal stress development in layers with and without Wuestite (FeO), we chose ***450°C and 650°C as oxidation temperatures***.

The samples were ***Armco iron samples and iron single crystals in <100> orientation***. Two samples of the originally fine grained Armco iron were heat treated in order to induce grain growth. All samples were ground and polished prior to the oxidation experiment.

In this early stage of layer growth the phase evolution and the internal stresses were studied in ***grazing incidence diffraction***. For internal stress evaluation the LIBAD method /van Acker 1996/ is used. In the later stage of layer growth the stresses within the different sublayers were be determined using the $\sin 2\psi$ – method working in an ***Ω–geometry***. Measurements at room temperature after the oxidation experimetn will reveal the strain/stress state changes due to cooling. In the oxide layers on iron/steel these depend on the thickness of the sublayers, since the oxides (FeO, Fe_2O_3, Fe_3O_4) and the substrate have different thermal expansion coefficients.

Results

The experiments revealed that the slowliest oxide layer growth occurs on the single crystals and the fastest oxide growth occurs on the fine grained substrates. Oxide growth was substantially faster at 650°C than at 450°C. The oxide layers appear to be strongly textured.

Internal stress analyses showed that strong compressive internal stress evolved in the hematite, while the magnetite contained usually tensile internal stresses. The magnitude of the internal stresses depends both on the oxidation temperature and the oxidation time. Dominant sources of the internal stresses presumably are epitaxial growth of the layers, the incorporation of new oxide in the magnetite and especially in the hematite and, in the case of oxidation at 600°C, also wuestite formation.

Residual stresses after cooling are dominated by the thermal expansion misfit of the oxides and the substrate.

Most of the data is still under evaluation and will be incorporated in this reported as soon as possible.

References

/Baxter *et al.* 1983/ Baxter, D.J., Natesan, K., *Mechanical considerations in the degradation of structural materials in aggressive environments at high temperatures*, Rev. High Temp. Mater. **5** (1983) 149-250

/Corkovic *et al.* 2003/ Corkovic, S., Pyzalla, A., *In-situ stress analyses during high temperature oxidation of mild steel and grey cast iron*, Materials and Corrosion, *in print*

/Gnäupel – Herold *et al.* 1997/ Gnäupel-Herold, T., Reimers, W., *Residual stresses in oxide scales on nickel- and TiAl-substrates*, Proc. ICRS **5**, Linköping, Sweden (1997) 952-957

/Pilling *et al.* 1923/ Pilling, N., Bedworth, E.J., *The oxidation of metals at high temperatures*, Inst. Met. **29** (1923) 529-594

/Schütze 1988/ Schütze, M., *Stresses and decohesion of oxide scales*, Mater. Sci. Technol. **4** (1988) 407-414

/Schütze 1991/ Schütze, M., *Die Korrosionsschutzwirkung oxidischer Deckschichten unter thermisch-chemisch-mechanischer Werkstoffbeanspruchung*, Habilitation, RWTH Aachen und Verlag Gebrüder Bornträger, Berlin (1991)

/van Acker 1996/ van Acker, K., *Internal stress states in cold worked metals and in metal matrix composites*, dissertation, Katholieke Universiteit Leuven, Belgien (1996)

ESRF	**Experiment title:** Characterization of Cu(In/Ga)S_2 thin films using GID	**Experiment number:** SI-1031
Beamline: BM 20	**Date of experiment:** from: 07.05.2004 to: 11.05.2004	**Date of report:** 18.11.2004
Shifts: 12	**Local contact(s):** Valentina Cantelli	*Received at ESRF:* *18.11.04*

Names and affiliations of applicants (* indicates experimentalists):

Dr. J. Kräußlich*[1)], Dr. H. Metzner[2)], Dr. Th. Hahn*[2)], Dr. U. Kaiser[2)], DP J.Cieslak*[2)], Prof. W. Witthuhn[2)], Prof. K. Goetz[1)]

Friedrich-Schiller-University of Jena, [1)] Institute of Optics and Quantumelectronics, [2)] Institute of Solid-State Physics, Max-Wien-Platz 1, 07743 Jena, Gemany

REPORT

Within the chalcopyrite family the sulphur based compounds $CuMS_2$ (M=In, Ga, Al) have attracted much interest in recent years because they show a **direct** wide band-gap covering from E_{gap} = 1.53 eV ($CuInS_2$) over E_{gap} = 2.43 eV ($CuGaS_2$) to E_{gap} = 3.49 eV ($CuAlS_2$) [**Fig. 1**]. Therefore, they are particularly suitable for optoelectronic as well as photovoltaic applications. The epitaxial growth of $CuInS_2$ (**CIS**) on Si(111) and Si(001) was already demonstrated [1, 2] while $CuGaS_2$ was hitherto grown epitaxially on GaAs(001), GaP(001) and Si(001) only [3, 4]. Recently, our group demonstrated the epitaxial growth of $CuGaS_2$ (**CGS**) thin films on Si(111) substrates using the three-sources-molecular beam epitaxy (MBE) [5]. Our recent work focused on the heteroepitaxial growth of quaternary $CuIn_{(1-x)}Ga_xS_2$ (**CIGS**) thin films on Si(111) substrates by means of molecular-beam epitaxy. By variation of the Ga/In contents, evaluated by *x*, a nearly perfect lateral lattice match between epitaxial layer and substrate can be achieved [**Fig. 2**][6]. The *in-situ* analysis of the growing thin film using electron diffraction via LEED or RHEED already indicates the epitaxial growth of $CuIn_{(1-x)}Ga_xS_2$. However, more detailed information concerning the structural perfection of the grown layers will be won using the *ex-situ* methods of high-resolution transmission electron microscopy (HRTEM) and x-ray diffraction (HRXRD).

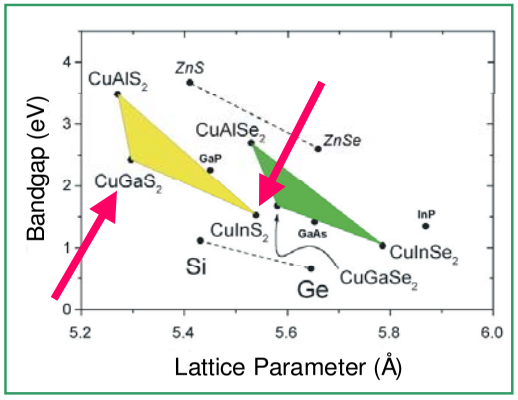

Lattice Parameter

a_{CGS} = 5.3474 Å
c_{CGS} = 10.4743 Å
→ c/a = 1.9588

a_{CIS} = 5.5228 Å
c_{CIS} = 11.1329 Å
→ c/a = 2.0158

a_{Si} = 5.43098 Å

Fig. 1: Bandgap *versus* lattice parameter for the chalcopyrite family $CuMS_2$ (M=In, Ga, Al).

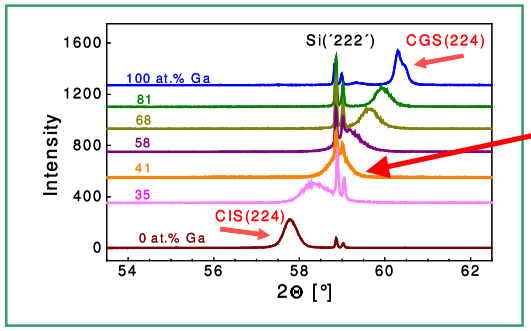

Fig. 2: XRD Θ-2Θ scans of epitaxial $CuIn_{(1-x)}Ga_xS_2$ films on Si(111) in vicinity of the forbidden 222-reflection of Si. The 224-film-reflections shift to higher scattering angles with increasing Ga content x. For x ≈ 0.41 the reflections of the film and substrate coincide. The diffraction pattern series were recorded with a conventional homebound x-ray diffraction set-up using CuKα1,2 radiation. Therefore, the double $Kα_{1,2}$ peaks of the forbidden 222-reflection of Si arise.

X-ray diffraction executed in the usual Θ/2Θ-mode, with a wafer orientation for the symmetric reflection on lattice planes parallel to the surface give only information concerning the lattice parameter normal to the wafer surface and, therefore, also to the thin film, whereas the x-ray diffraction in transmission mode gives information on the crystallographic **in-plane parameters** both of the crystalline substrate and the epitaxially grown $CuIn_{(1-x)}Ga_xS_2$ thin film. In this case we have also the possibility to compare directly the adequate thin film reflections to those of the substrate, arising during the same run. This is very useful for a high precision Bragg angle calibration**.**

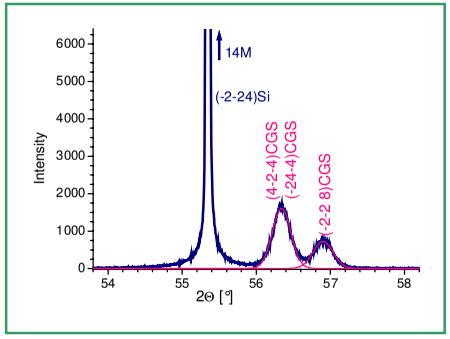

Fig. 3: HRXRD scan in transmission mode of epitaxial CGS films on Si(111). The diffractogram shows the splitting up of the adequate CGS thin film reflections. This is caused by two effects: first, the grown CGS film is characterized by a parameter relation of c/2 ≠ a and second, by a formation of 120°-rotation-twins (see **Fig. 4**).

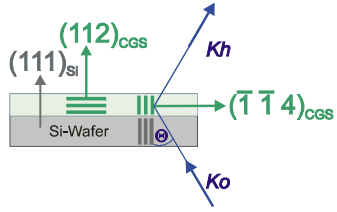

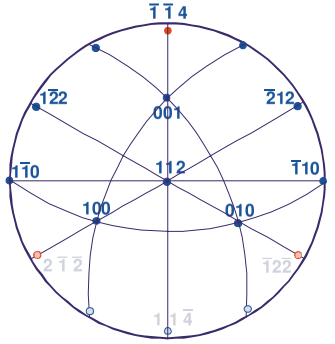

Fig. 4: Stereographic projection of CGS in respect of the [112] pole.

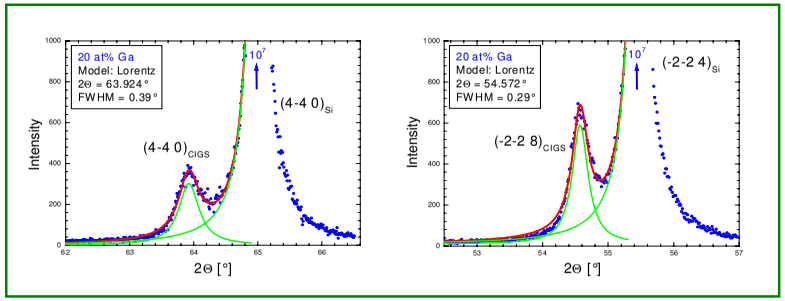

Fig. 5: HRXRD scan in transmission mode of epitaxial $CuIn_{(1-x)}Ga_xS_2$ films on Si(111). With the Ga content x ≈ 0.20, no lateral lattice match between epitaxial layer and substrate is observed, and no splitting of the adequate thin film reflections can be recognized. Hence, we have a lattice parameter relation of c/2 ≈ a. The 4-40-reflection of CIGS results in a lattice parameter $a_{CIGS(x=20)}$ = 0.5513(4) nm.

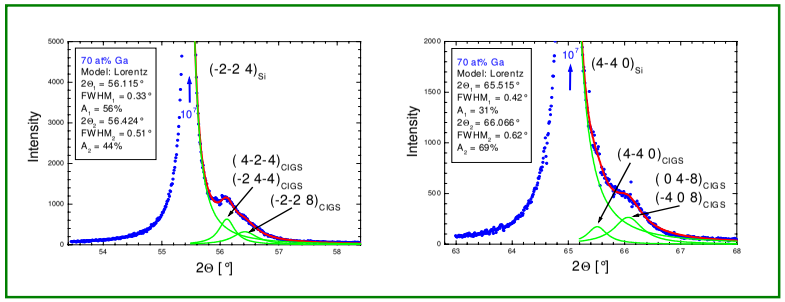

Fig. 6: HRXRD scan in transmission mode of epitaxial $CuIn_{(1-x)}Ga_xS_2$ films on Si(111). With the Ga content of x ≈ 0.70, no lateral lattice match between epitaxial layer and substrate is to be observed. Here, however, the profile analysis of the measured reflection results in a splitting up of the adequate thin film reflections (**see also Fig. 4**). Hence, we have here once again a lattice parameter relation of c/2 ≠ a. The 4-40-reflection of CIGS results in a lattice parameter $a_{CIGS(x=70)}$ = 0.5390(4) nm.

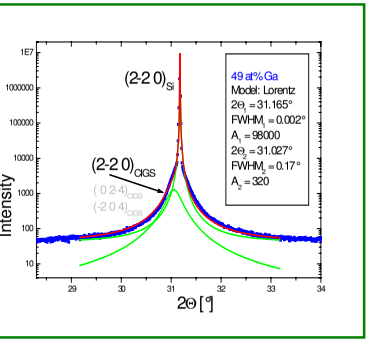

Fig. 7: HRXRD scan in transmission mode of epitaxial $CuIn_{(1-x)}Ga_xS_2$ films on Si(111). With the Ga content of x ≈ 0.49, no separation of the thin film and substrate reflections is to be observed. Hence, we have also in-plane a lattice match between the epitaxially grown CIGS thin film on the Si(111) substrate. However, in this case it is nearly impossible to evaluate significant in-plane lattice parameters of the grown CIGS thin film using profile analysis of the superimposed thin film and substrate reflections. But the precise knowledge of the thin film in-plane lattice parameters depending on the depth and thickness of the grown thin film is of interest to determine the inherent strain. We hope with HRXRD measurements in the GID mode, just as well for $CuIn_{(1-x)}Ga_xS_2$ films with x ≈ 0.49, to separate the thin film reflection from those of the substrate. Then, it will be possible to determine also the inherent strain components of the epitaxially grown CIGS thin film.

[1] H. Metzner, Th. Hahn, J.-H. Bremer, J. Conrad, Appl. Phys. Lett. **69**, 1900 (1996)
[2] Th. Hahn, H. Metzner, B. Plikat, M. Seibt, Appl. Phys. Lett. **72**, 2733 (1998)
[3] K. Oishi, S. Kobayashi, F. Kaneko, J. Crystal Growth **153**, 158 (1995)
[4] S. Shirakata, S. Chichibu, J. Appl. Phys. **87**, 3793 (2000)
[5] H. Metzner, Th. Hahn, J. Cieslak, *et al.*, Appl. Phys. Lett. **81**, 156 (2002)
[6] H. Metzner, Th. Hahn, J. Cieslak, *et al.*, J. Phys. Chem. Solids, *in press*